

**Application of metal oxide-carbon  
nanocomposites and metal-organic  
frameworks (MOFs) for highly sensitive  
electrochemical sensors**

**Weiwei Qiu**

**September, 2020**

**Shimane University, Japan**



# **Application of metal oxide-carbon nanocomposites and metal-organic frameworks (MOFs) for highly sensitive electrochemical sensors**

## **CONTENTS**

Abstract of the Thesis	1
1. General Introduction	5
1.1 Introduction of electrochemical sensor	6
1.2 Introduction of metal oxide/carbon composites	13
1.3 Introduction of the functionalization of MOFs	14
1.4 Application of the functionalization of metal-oxide and MOFs in electrochemical sensors	21
1.5 The research significance and main contents	22
1.6 Reference	24
2. Application of metal-oxide nanocomposites for highly sensitive electrochemical sensors	32
2-1 Synthesis of porous nanododecahedron Co <sub>3</sub> O <sub>4</sub> /C and its application for nonenzymatic electrochemical detection of nitrite	33
2-1.1 Introduction	34
2-1.2 Experimental	37
2-1.3 Results and Discussion	38
2-1.4 Conclusions	61
2-1.5 References	62
2-2 Synthesis of ZrO <sub>2</sub> /C using UiO-67 as template and its high sensitivity for heavy metal ions	65
2-2.1 Introduction	66
2-2.2 Experiment section	70
2-2.3 Results and discussion	72
2-2.4 Conclusion	95
2-2.5 References	96
2-3 Yolk-shell-structured SnO <sub>2</sub> -C and poly-tyrosine composite films as an impedimetric “Signal-Off” sensing platform for transgenic soybean screening	99
2-3.1 Introduction	100
2-3.2 Experimental	104

2-3.3 Results and Discussion	107
2-3.4 Conclusions	138
2-3.5 References	139
3. Application of metal-organic frameworks (MOFs) for highly sensitive electrochemical sensors	142
3-1 Flexible flower-like MOF of $\text{Cu}_2(\text{trans-1,4-cyclohexanedicarboxylic acid})_2$ as the electroactive matrix material for label-free and highly sensitive sensing of thrombin	143
3-1.1 Introduction	144
3-1.2 Experimental	148
3-1.3 Results and Discussion	150
3-1.4 Conclusion	172
3-1.5 Reference	173
3-2 A strategy for the construction of a reusable electrochemical aptasensor using UiO-66 as signal amplified platform	175
3-2.1 Introduction	176
3-2.2 Experimental	178
3-2.3 Results and Discussion	181
3-2.4 Conclusions	203
3-2.5 References	204
4. General Conclusion and Scope	207
4.1 General Conclusions	208
4.2 Scope	212
Acknowledgments	214
Appendix	
List of Figures	215
List of Tables	222
List of Schemes	224
List of Publications	225

## **Abstract of the Thesis**

Electrochemical sensor plays an important role in the research of analytical chemistry because of its sensitivity, rapidity, low cost, portable detection device, low energy consumption and easy miniaturization and integration. It has been applied in many fields, such as biomedicine, environmental protection, electrochemical catalysis, and so on. Recently, the functionalization of metal-oxide and MOFs had been attracted wide attention based on their excellent performance, and take part in the construction of electrochemical sensor is one of their most promising applications, their intervention provides a broad space for the development of electrochemical sensors in the direction of practicality, miniaturization, intelligence and multi-function, they can effectively realize the immobilization of biomolecules and chemical molecules, signal amplification, and high-throughput on-line real-time monitoring of the electrochemical sensor. Therefore, the application of the functional metal-oxide and MOFs provides a new strategy for the study of biomolecules and chemical molecules in the electrochemical sensing field.

**Chapter 1:** The brief introduce of electrochemistry; the functionalization of metal-oxide and MOFs were described. Moreover, some questions of the previous studies were pointed out and the significance and purpose of this study were stressed.

**Chapter 2:** The functionalization of metal-oxide and their application in electrochemical sensors.

2-1 Porous nanododecahedron of  $\text{Co}_3\text{O}_4/\text{C}$  nanocomposites was synthesized by calcination of the Co-based MOF (ZIF-67) in air at  $400\text{ }^\circ\text{C}$  and was used for fabricating a highly sensitive and low oxide potential nitrite ion ( $\text{NO}_2^-$ ) sensor. The structure and morphology characterization show that ZIF-67 behaves as an ideal sacrificial template and converted to  $\text{Co}_3\text{O}_4/\text{C}$  with regular shape. Electrochemical analysis shows that the excellent electrocatalysis performance toward the oxidation of  $\text{NO}_2^-$  based on the synergy of  $\text{Co}_3\text{O}_4$  and carbon in the nanocomposite. At  $\text{NO}_2^-$  concentration from 2 nM to 8 mM, a fast response time within 3 s is revealed and 1.21 nM of ultralow detection limit is achieved as the steady-state current signal linear increase. Using the nanocomposite acts as an electrochemical sensing material for determination of  $\text{NO}_2^-$  in the real samples, the results are satisfactory.

2-2 A thin nanosheet structure of  $\text{ZrO}_2/\text{C}$  was prepared using UiO-67 with a flat cuboid structure as precursor. The peculiar and fluffy structures endowed materials with high surface areas that tremendously improved the adsorption capacity of

electrode materials for heavy metal ions. Thus,  $ZrO_2/C$  as an electrode material was used to simultaneous detection of Pb(II) and Cd(II) in 0.1 M HAc-NaAc buffer by differential pulse anodic stripping voltammetry (DPASV). Under the optimal conditions, the results showed that prepared sensor has the high sensitivity, good stability and low interference of the detection for two metal ions, and the limit detections for Pb(II) and Cd(II) of 0.007  $\mu\text{M}$  and 0.019  $\mu\text{M}$  were estimated, respectively. Furthermore, it was also successfully applied for the detection of trace Pb(II) and Cd(II) in real water samples with a satisfactory result.

2-3 The yolk-shell structured  $\text{SnO}_2\text{-C}$  nanospheres have been prepared by a hydrothermal reaction of  $\text{SnCl}_2\cdot 2\text{H}_2\text{O}$  and glucose, followed by carbonization under 500 °C in air condition. Then an inorganic/organic hybrid film bearing  $\text{SnO}_2\text{-C}$  and polytyrosine (pTyr) is fabricated by electro-polymerization of  $\text{SnO}_2\text{-C}$  modified electrode in tyrosine solution. The modified electrode is utilized as a supporting platform for covalent immobilization of cauliflower mosaic virus 35s (CaMV35s) promoter gene fragments to construct an electrochemical DNA sensor. Chronocoulometric experiments show that the loading density of probe DNA (pDNA) and hybridization efficiency are determined to be as high as  $4.54\times 10^{13}$  strands  $\text{cm}^{-2}$  and 83.2%, respectively. Upon hybridization with target DNA (tDNA), the probe DNA that lied flat on the electrode surface through hydrogen bonding with pTyr is erected, reducing the charge repulsion and steric hindrance for  $[\text{Fe}(\text{CN})_6]^{3-/4-}$  diffusion. So a “signal-off” response strictly dependent on hybridization reaction is achieved in electrochemical impedance spectroscopy. The response mechanism is predicted by theoretical calculation. Owing to the high probe density and hybridization efficiency of the sensor, a wide kinetic linear ranging from 1.0 aM to 100 pM and an ultralow detection limit of 0.53 aM for target sequence are obtained. The biosensor also presents high recognition ability toward the DNA samples extracted from real transgenic and non-transgenic soybeans, showing great promising of the biosensor for facile monitoring of transgenic product.

**Chapter 3:** The functionalization of metal-organic frameworks (MOFs) and their application in electrochemical sensors

3-1 A flexible metal-organic framework (MOF) of  $\text{Cu}_2(\text{trans-1,4-cyclohexanedicarboxylic acid})_2$  ( $\text{Cu}_2(\text{CHDC})_2$ ) has been synthesized by a facile hydrothermal method. The physical characterization experiments show that the

$\text{Cu}_2(\text{CHDC})_2$  presents unique flower-like shape, large surface area and high electroactivity. Then gold nanoparticles (AuNPs)/ $\text{Cu}_2(\text{CHDC})_2$  modified electrode was prepared and utilized as an electroactive matrix for thrombin aptamer immobilization. The electrochemical assay shows that the AuNPs can effectively enhance the electrochemical signal of the  $\text{Cu}_2(\text{CHDC})_2$ . Upon the binding of the electrode-confined aptamer with the thrombin, the electrochemical signal of the  $\text{Cu}_2(\text{CHDC})_2$  decreases obviously due to the change of the microenvironment of the sensing interface. Thus a label-free electrochemical sensing strategy for thrombin was realized. The aptasensor displays excellent performance with wide linear range, ultralow detection limit of 0.01 fM (S/N=3), and favorable specificity. Also, the aptasensor was applied for determination of thrombin in the human serum samples, and the satisfactory results are obtained. The results imply that the proposed sensor can be potentially used for the early diagnosis of disease and clinical monitoring.

3-2 Direct, strong and specific coordination between  $\text{Zr}^{4+}$  and phosphate group ( $-\text{PO}_4^{3-}$ ) provides new avenue to construct Zr-MOF-based high-performance electrochemical biosensors. In this work, a rational, sensitive and reusable electrochemical aptasensing strategy for Ochratoxin A (OTA) was proposed using *in-situ* coordination-assembled UiO-66 as signal amplification platform in the design, the OTA aptamer was pre-hybridized with supporting strands that immobilized on the gold electrode surface. Then the classic Zr-MOF of UiO-66 was *in-situ* immobilized on the terminal of OTA aptamer through coordination between  $\text{Zr}^{4+}$  and  $5'-\text{PO}_4^{3-}$  modified on OTA aptamer. Furthermore, the signal probe with electroactive tag of methylene blue was *in-situ* assembled on UiO-66 also by the Zr-O-P bond. Because of large surface area and rich active sites of  $\text{Zr}^{4+}$ , the comparative assay shows that the UiO-66 greatly enhances the analytical performance of the aptasensor. A wide range from 0.1 fM to 2.0  $\mu\text{M}$  and an ultralow detection limit of 0.079 fM (S/N = 3) for target OTA were achieved. In addition, because the aptasensor was designed on the basis of the auxiliary strand-based competitive binding strategy, 11 times reusability of the aptasensor can be realized in accompany with the detection process. The aptasensor can also be applied for detection of OTA in the red wine sample, demonstrating a promising prospect of the biosensor for food safety monitoring.

**Chapter 4:** Conclusions and scope of these studies were described.

**Chapter 1**  
**General Introduction**

## **1.1 Introduction of electrochemical sensor**

Electrochemistry is a science that studies the relationship between electricity and chemical reactions [1-5]. Electrochemical sensor is an independent integrated device, which is connected to the data acquisition and processing system through chemically modified elements and electrochemical signal sensor elements to effectively provide accurate analytical information [6-8]. Electrochemical sensor plays an important role in the research of analytical chemistry because of its sensitivity, rapidity, low cost, portable detection device, low energy consumption and easy miniaturization and integration [9, 10]. It has been applied in many fields, such as biomedicine, environmental protection, electrochemical catalysis, and so on [11-13]. Fig. 1.1 shows the traditional electrochemical sensing equipment, three-electrode electrochemical workstation.

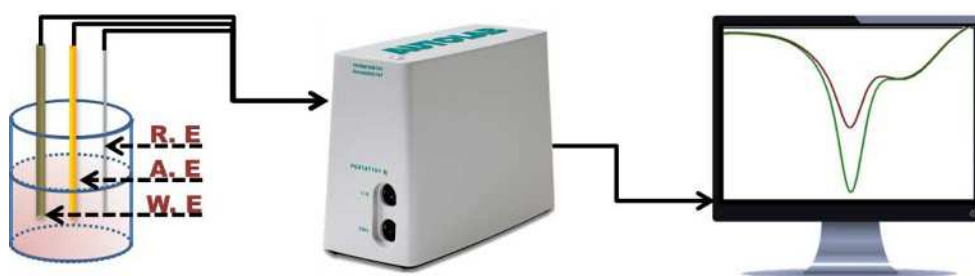


Fig. 1.1 Schematic diagram of three-electrode electrochemical workstation

### **1.1.1 Application of Electrochemical Sensor in Biological Field**

As one of the earliest biosensors, electrochemical biosensors mainly use solid electrodes as basic electrodes, fix bioactive substances as molecular identifiers on the electrode surface, and then capture target molecules to the electrode surface through the specific recognition between biomolecules [14-16]. The basic electrode converts the concentration signal into a measurable electrical signal such as potential, current, resistance or capacitance as the response signal, thus realizing the quantitative or qualitative analysis of the target analyte, the principle is shown in Fig. 1.2 [17-19]. Electrochemical biosensor has the advantages of high sensitivity, easy miniaturization and can be detected in complex system samples, so it has been widely used in clinical diagnosis [20], food industry [21], agriculture [22], environmental pollutants [23] and other fields. According to the different bio-sensitive molecules immobilized on the electrode surface, the electrochemical biosensors can be categorized into electrochemical immunosensors [24, 25], electrochemical aptamer sensors [26, 27], electrochemical DNA sensors [28, 29], electrochemical enzyme sensors [30, 31] and so on [32, 33]. In addition, with the development of material science, electrochemical biosensors have been applied for the rapid detection of small biological molecules through modifying catalytic materials on the electrodes [34, 35].

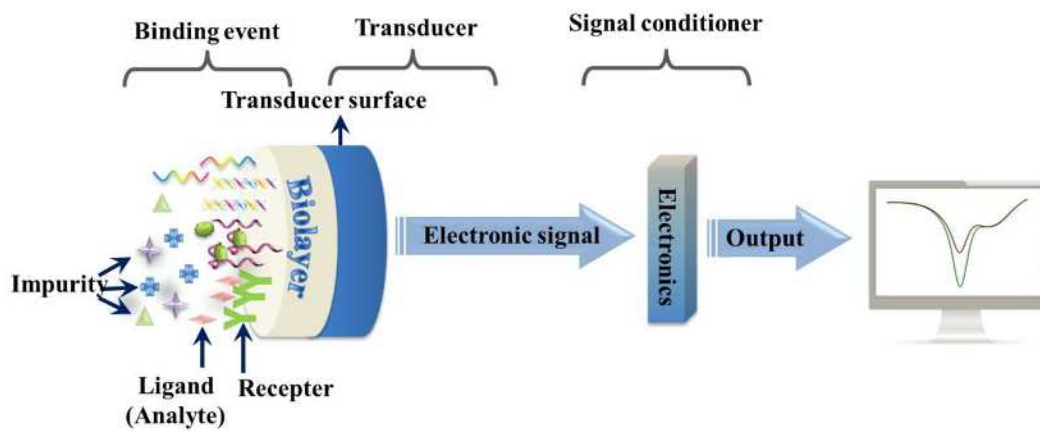


Fig. 1.2 Schematic diagram of the principle of electrochemical biosensor

### **1.1.1.1 Electrochemical immunosensor**

Electrochemical immune biosensor is an integrated device for quantitative or semi-quantitative analysis of targets based on the principle of antigen-antibody specific reaction [36-38]. The molecular recognition part of immunosensor containing antigens and antibodies is connected with electrochemical sensing elements to convert the analyte concentration signals into corresponding electrical signals [39, 40]. Using the electrochemical detection method, a linear relationship between the signal and the analyte to be measured in a certain concentration range can be achieved, to realize the analysis and determination of the target molecules [41, 42]. In recent years, electrochemical immunosensor has been attracted wide attention. For example, our group used the unique zero-dimensional structure and highly active aldehyde group of a novel fullerene derivative, 2-(4-Formylphenyl) [60] fulleropyrrolidine (FPD) as an electrode material for the construction of an impedimetric immunosensor for human chorionic gonadotrophin (HCG) [43]. Omidi et al. proposed an electrochemical immunosensor for ultrasensitive detection of carcinoembryonic antigen based on gold and silver bio/nano-hybrids [44].

### **1.1.1.2 Electrochemical aptamer biosensor**

In 1990, Gold et al [45] and Szostak et al [46] independently established nucleic acid molecular libraries, and gradually developed an exponentially enriched ligand phylogenetic technique (SELEX). A segment of ssDNA or ribonucleic acid (RNA) can be screen from the nucleic acid molecular library that can efficiently and specifically bind to target molecules, that is, nucleic acid aptamer [47, 48]. The selected aptamers are reorganized by complementary base pairs in the sequence, static electricity and hydrogen bonds, combined with the diversity of ssDNA structure and spatial conformation, and a variety of three-dimensional spatial structures, such as hairpins [49], stem rings [50], pseudoknot pockets [51] or G quadruplets [52] can be obtained. These three-dimensional structures are the basis for the binding of nucleic acid aptamers to specific regions of the target substance, which are combined by the accumulation of “pseudo-base pairs” [53], hydrogen bonding [54], static electricity [55], and so on. As a new type of recognition macromolecule, nucleic acid aptamer

has higher stability and selectivity than traditional biological antibody, because of the biological antibody is easily denatured by temperature, pH and other conditions [56, 57]. The specific advantages of the nucleic acid aptamer are as follows [58-62]: (1) It is not limited by immunogenicity, and has a wide application for more target molecules. (2) The aptamer is fast synthesized and easy modified. (3) In different working environments, nucleic acid aptamers can form different spatial conformations with high specificity from the target molecule. (4) It is easy to be preserved at room temperature and recoverable at high temperature. (5) The affinity of the aptamer can be expanded continuously, and the SELEX screening process is a process of continuous enrichment, so the affinity of DNA sequence to the target molecule is also gradually enhanced. Because of the above advantages, nucleic acid aptamers are widely used in clinical diagnosis and rapid detection of food safety. Wang et al. proposed a sensitive and reusable thrombin aptasensor through the in situ assembly strategy based on the electroactive L-cys–Cu<sup>2+</sup> tag and the signal enhancing platform of AuNPs [63]. Wei and his coworkers prepared an electrochemical aptasensor for aflatoxin B1 based on smart host-guest recognition of  $\beta$ -cyclodextrin polymer [64]. Fahimeh Jalali et al. synthesized Cu-MOF-graphene oxide (Cu-MOF-GO) nanocomposite, and used it as redox probe in an electrochemical aptasensor for sensitive detection of Mucin 1 [65].

### **1.1.1.3 Electrochemical enzyme sensor**

Electrochemical enzyme sensor, also known as enzyme electrode, is the earliest, most mature and commercialized biosensor [66-68]. The principle of this kind of biosensor is that the enzyme is fixed on the electrode, then the biomolecules undergo chemical changes under the catalysis of enzyme, and the analyte to be measured is indirectly determined by recording the changes through the signal converter [69-71]. So, the electrochemical enzyme sensor has attracted the attention of the majority of researchers, and the related research work has made rapid progress. Hasan Bagheri et al. fabricated a novel biosensor for paraoxon detection based on the acetylcholinesterase (AChE) modified Ce/UiO-66@MWCNTs matrix [72]. Miroslav Fojta et al. present a rapid electrochemical enzyme-linked DNA hybridization assay using disposable pencil graphite electrodes (PeGE) to detect target DNA (tDNA) sequences in DNA fragments amplified by polymerase chain reaction

[73]. However, due to the shortcomings of electrochemical enzyme sensors, such as harsh experimental conditions and difficult preservation of enzymes [74, 75], non-enzyme electrochemical biosensors have been gradually developed.

#### **1.1.1.4 Non-enzyme electrochemical biosensors**

In recent years, non-enzyme electrochemical biosensors have attracted wide attention of scientists because of their many characteristics, including simple preparation, high sensitivity, low production cost, miniaturization compatibility and so on [76, 77]. It has also achieved certain achievements in the detection of many biological small molecules, such as uric acid [78], glucose [79, 80], neurotransmitters [81, 82], hydrogen peroxide [83, 84], etc.

#### **1.1.2 Application of electrochemical sensors in the field of environmental monitoring**

With the rapid development of the world economy, it not only improves people's quality of life, but also brings a series of negative effects, among which the problem of environmental pollution is becoming more and more serious, which brings a great threat to human health and development. Electrochemical sensor plays an important role in environmental monitoring because of its simple equipment, low cost and high sensitivity [85, 86].

##### **1.1.2.1 Electrochemical sensors for monitoring heavy metal cations**

Heavy metals cations, they are toxic and then destroy the biological systems when their concentration exceeds the natural levels [87, 88]. It was urgently to search for a sensitive, rapid and simple analytical method for monitoring heavy metals ions in food, supplies and biological systems. And the electrochemical sensors have widely applied for detecting heavy metals based on its inherent advantages [89]. For examples, Wang et al. presented a novel  $\text{Pb}^{2+}$  electrochemical sensor based on the composite consisting of two-dimensional (2D) flake-shaped MOF of Mn(TPA) (TPA

= terephthalic acid) and single walled carbon nanotubes (SWCNTs) [90]. The zeolitic imidazolate framework ZIF-8 was synthesized and utilized for stripping voltammetric analysis of  $\text{Hg}^{2+}$ ,  $\text{Cu}^{2+}$ ,  $\text{Pb}^{2+}$  and  $\text{Cd}^{2+}$  [91].

### **1.1.2.2 Electrochemical sensors for inorganic anions and their salts in the environment**

In industry, nitrite ( $\text{NO}_2^-$ ) and sulfite ( $\text{SO}_3^{2-}$ ) are widely used as colorants and preservatives.  $\text{NO}_2^-$  can oxidize low-methemoglobin to methemoglobin, making it lose the ability to transport oxygen, thus causing poisoning [93, 94]. When  $\text{SO}_3^{2-}$  is excessive, people have allergic reactions such as headache, nausea, dizziness and asthma. Therefore, the rapid monitoring of  $\text{NO}_2^-$  and  $\text{SO}_3^{2-}$  in food is also of great significance. For examples, our group synthesized porous nanododecahedron of  $\text{Co}_3\text{O}_4/\text{C}$  and used it as electrode material for fabricating a highly sensitive and low overpotential sensor of  $\text{NO}_2^-$  [95]. Thangamuthu et al. reported a construction of COOH-functionalized, multiwall carbon nanotubes (HOOC-MWCNT) modified GCE for simultaneous estimation of  $\text{SO}_3^{2-}$  and  $\text{NO}_2^-$  under neutral condition [96].

### **1.1.2.3 Monitoring of organic pollutants in the environment by electrochemical sensors**

In addition, phenols, benzene and amines are important organic environmental pollutants and important environmental monitoring objects [97, 98]. The real-time and rapid response ability of electrochemical sensors is widely used to monitor the pollution of organic compounds in the environment. For examples, Yang et al. covalently immobilized  $\text{Cu}_3(\text{btc})_2$  at chitosan-electroreduced graphene oxide hybrid film and applied it for simultaneous detection of dihydroxybenzene isomers [99]. Maruf Ahmed et al. proposed an electrochemical amine sensor based on a hexagonal nanotablets structure of ZnO [100].

## **1.2 Introduction of metal oxide/carbon composites**

Some nanomaterials, such as non-precious metals (including iron, nickel, cobalt, and

so on) and their oxides have high specific surface area, excellent electrocatalytic activity, low cost, and the ability of facilitating electron transfer at a lower overpotential, so they are widely used as sensing materials [101-103]. Unfortunately, the optimal synthetic conditions and suitable template of synthesis still unsolved, some of porous metal oxide products cannot keep the pristine morphology features of the precursor template [104]. Most seriously, pure metal oxide still faces disadvantage of poor conductivity and lack of stability during the detecting process. And then, several advancements had confirmed that formation of metal oxide-carbon nanocomposites using of the additional-conductive species (graphene, carbon nanotubes, etc.) is a great method to solve the problem [105]. For example, Kim and co-workers synthesized a hybrid  $\text{Co}_3\text{O}_4$ /graphene material to enhance the electronic conductivity of  $\text{Co}_3\text{O}_4$  [106]. Tian and co-workers designed a compound  $\text{Co}_3\text{O}_4$ -carbon porous nanowire arrays (named as  $\text{Co}_3\text{O}_4$ -CNA) through pyrolyzation of the metal-organic framework (MOF) [107].

### **1.3 Introduction of the functionalization of MOFs**

In the past two decades, metal-organic frameworks (MOFs), also known as porous coordination polymer (PCPs), has experienced explosive growth. MOFs have a wide application prospect in the fields of catalysis [108], gas storage and separation [109], luminescence [110], drug release [111] and so on. The reasons for the wide application of MOF include: 1) the analyte can be concentrated to a high level on the high specific surface area, which improves the detection sensitivity; 2) specific functional sites (open metal sites, Lewis acid/basic sites and adjustable aperture) can achieve unprecedented selective recognition through host-guest interaction or size exclusion; 3) flexible porosity or skeleton can increase regeneration and recycling by reversible absorption and release of matrix; 4) the shape and size of the channel are selective to the shape and size of the synthetic object; 5) the source of selectivity is the specific chemical interaction between molecules. The interaction between guest molecule and MOFs are realized by hydrogen bond,  $\pi$ - $\pi$  interaction, exoteric metal sites and van der Waals force [112, 113].

Although MOF materials have excellent performance and are considered as an ideal material for electrode surface modification, but efficient signal transduction is still

one of the main challenges for MOF electrochemical sensors. Only part of MOF can satisfy the need of electrochemical sensing and is used as advanced electrode materials. In order to broaden the practical application of MOF as electrode materials and improve its conductivity, redox activity and biocompatibility, more and more researchers pay attention to the design and preparation of the functionalization of MOFs [114, 115].

The functionalization of MOFs with novel structures and more diverse types and functions can be derived from MOFs due to its abundant metal centers, functional groups of active organic ligands, regular controllable holes and tunnels, unsaturated metal sites and a variety of guest molecules [116, 117]. Compared with the original MOFs, the functionalization of MOFs have more advantages, such as higher electrical conductivity, better stability, uniform distribution of active materials, and so on. In recent years, the research on the functionalization of MOFs has achieved exciting results [118, 119]. There are mainly two kinds of MOFs-derived materials: one is MOFs functionalization through combining with various functional materials, including metal nanoparticles (MNPs) [120], carbon nanostructures [121], polymers [122] and biomolecules [123] and so on. The other is the derivative materials obtained by controlling the reaction conditions using MOFs or MOFs composites as templates [124, 125]. The familiar MOFs-derived materials are showed in Fig. 1.3.

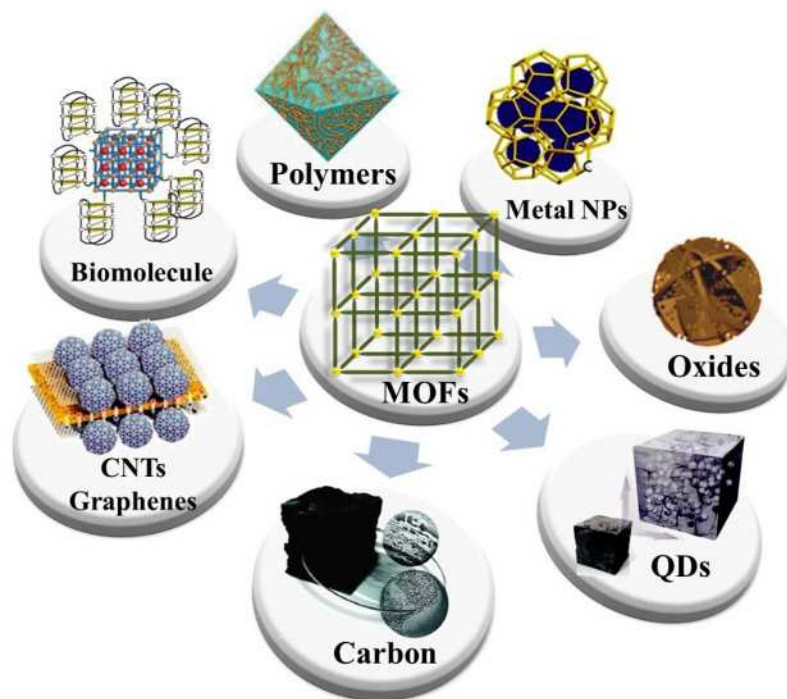


Fig. 1.3 Schematic diagram of the mainly MOFs-derived materials [126]

### **1.3.1 The functionalization of MOFs based on compounding with functional materials**

#### **1.3.1.1 MOFs/Carbon materials**

Common carbon materials, include graphite oxide (GO) [127], graphene (GN) [128], carbon nanotubes (CNT) [129] and porous carbon (PC) [130], they all have good stability and conductivity and easy to post-functionalized. The polar functional groups such as hydroxyl group, epoxy group, carboxyl group and amino group with rich charge on the carbon materials surface can be pretreated, which can provide abundant sites for the growth of MOFs, it is recognized as an excellent carrier for immobilizing MOFs. At the same time, it can also be used as a medium for electron transfer to improve the electrical conductivity of the composites. Wang et al. one-pot synthesized a flower-like graphene@HKUST-1 (SGO@HKUST-1) for enzyme-free detection of hydrogen peroxide in biological samples [131]. Ansari et al. prepared a functionalized Cu-MOF@CNT hybrid by a simple ultrasonication technique and applicability in supercapacitors [132].

#### **1.3.1.2 MNPs/MOFs materials**

MOFs have attracted wide attention as a carrier of catalysts because of its large specific surface area, well-arranged pores and unique chemical properties. Metal nanoparticles (MNPs) can be well fixed on MOFs by different synthesis methods, including physical mechanical methods, chemical redox methods, electrodeposition, and so on [133, 134]. At the same time, the pore structure and large specific surface area of MOFs can effectively increase the load of MNPs on the MOFs surface and improve the contact rate between reactants and MNPs/MOFs-derived materials, so as to promote the catalytic efficiency. For example, a reliable and non-invasive electrochemical immunosensor for nuclear matrix protein 22 (NMP22) was presented based on reduced 17rapheme oxide-tetraethylenepentamine (rGO-TEPA) and gold nanoparticles-platinum nanoparticles-metal organic frameworks (AuNPs-PtNPs-MOFs) nanomaterial [135].

### 1.3.1.3 Biomolecule/MOFs materials

In order to solve the problems of poor structural stability, faint bioavailability and poor pharmacokinetics of some MOFs, the post-synthetic modification of the external surface of MOFs not only weakens these shortcomings, but also introduces the necessary functions for MOF NPs, such as enhancing structural stability, improving cell uptake and biomarker targeting, *etc.*[136], especially biological macromolecules, including lipids [137], peptides [138], nucleic acids [139], are particularly attractive surface modification ligands due to they have special chemical adaptation and difficultly diffused into MOFs pores. Among the existing methods of post-modification of MOFs on the external surface, two common methods of direct bonding between the ligand and the outer surface of MOFs have been attracted attention (Fig. 1.4): 1) covalent surface functionalization and 2) coordination surface functionalization. For example, Lin and co-workers bound the protease trypsin onto  $\text{Cr}_3\text{O}(\text{H}_2\text{O})_3(\text{BDC-NH}_2)_3$  [MIL-88B-NH<sub>2</sub>(Cr)] via an endogenous terminal amino group to afford a reusable bovine serum albumin digestion system [140]. Chang et al. prepared a nucleic acid-functionalized metal-organic framework-based homogeneous electrochemical biosensor for simultaneous detection of multiple tumor biomarkers [141]. Mirkin et al. [142] made use of the strong coordination between phosphate and Zr-metal ions to realize the surface functionalization of UiO-66 nanoparticles with terminal modified phosphate DNA, and used it as a probe to detect cellular endotoxin. This research result has important guiding significance for the rational design and synthesis of metal-organic polymer nucleic acid surface functionalization and its application in biosensor.

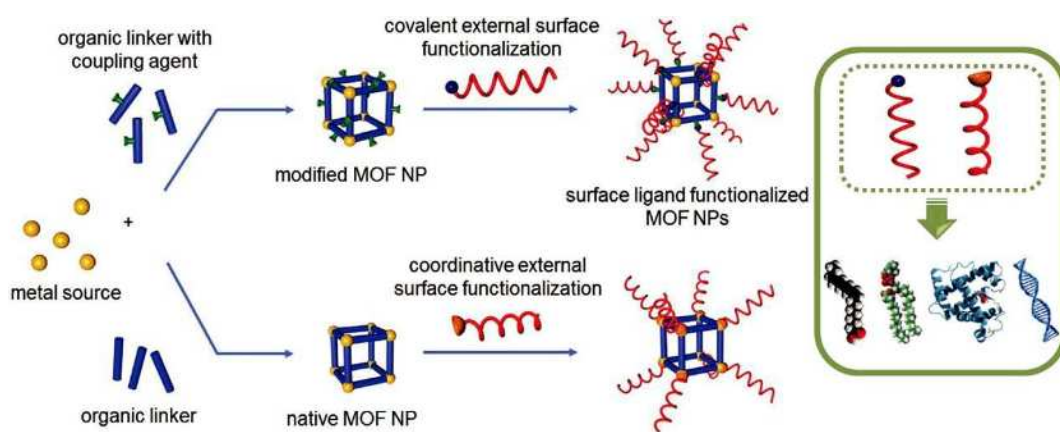


Fig. 1.4 Schematic illustration of postsynthetic modification of MOFs external surfaces through covalent bonds (top) and coordinative bonds (bottom) on the MOFs surface [136].

#### **1.3.1.4 Other composite MOFs-derived materials**

Due to the high mechanical strength and good stability of organic polymer molecules, the composites with MOFs can not only resist solvent, but also respond to external light, heat or pH under certain conditions, which has more potential application [143, 144]. Gamage et al prepared the composite material of polystyrene grafted in MOF-5 and used it for the adsorption of CO<sub>2</sub> [145].

The versatility of MOFs is further enriched by MOF@MOF composites. By means of epitaxial growth or seed growth, a different layer of MOF was grown on the surface of MOF as a core as a shell to form a heteroepitaxial MOF@MOF crystal with core-shell structure [146, 147].

#### **1.3.2 Functionalization using MOFs as template**

Based on MOFs structure has diverse metal sources (metal ions or metal clusters) and carbon sources (organic ligands), the synthesis of advanced functional materials using MOFs as precursors, including nano-porous carbon and metal oxide nanomaterials, is a new hot spot in the research and development of new functional materials.

##### **1.3.2.1 Porous carbon**

When MOFs is used as template and calcined in inert gas, the organic ligands in MOFs structure can be directly carbonized into porous carbon [148, 149]. Compared with the traditional template method, this method has obvious advantages: (1) no need for external carbon sources; (2) the carbon source is stable and not easy to volatilize in the carbonization process because of MOFs is a kind of crystal material, thus ensuring the high-efficiency of the conversion process; (3) different morphologies and sizes of porous carbon can be designed and synthesized due to the structure diversity of MOFs; (4) the synthesis procedure is simple and there is no template removal process.

### 1.3.2.2 Metal oxide (MO<sub>x</sub>) and metal oxide/carbon (MO<sub>x</sub>/C)

In addition to porous carbon, MO<sub>x</sub> and metal oxide/carbon (MO<sub>x</sub>/C) are also important MOFs-derived materials [150, 151]. Synthesis of MO<sub>x</sub> and MO<sub>x</sub>/C using MOFs as template has the following advantages: (1) the MOFs template method can synthesize MO<sub>x</sub> or MO<sub>x</sub>/C by simple steps without extra protective agent, which simplifies the synthesis step and avoids the interference caused by external reagents; (2) the MOFs precursor of general using has the advantages of cheap raw materials, high conversion yield and mass production; (3) the most importance is that the morphology of MOFs is various and controllable, so that the particle size and morphology of MO<sub>x</sub> or MO<sub>x</sub>/C also can be controlled indirectly, and MO<sub>x</sub> or MO<sub>x</sub>/C with various shapes can be prepared. Therefore, Xu et al. used MIL-88(Fe) as the sacrificial template, a spindle like mesoporous structures of Fe<sub>2</sub>O<sub>3</sub> with a surface area of 75 m<sup>2</sup> g<sup>-1</sup> were obtained and tested as anode material for lithium batteries (LBs) [152]. In addition, the MO<sub>x</sub>/C composites can effectively improve the conductivity of materials due to the synergy of between MO<sub>x</sub> and carbon [153-155].

## 1.4 Application of the functionalization of metal-oxide and MOFs in electrochemical sensors

Electrochemical sensor is one of the most promising application fields of the functionalization of metal-oxide and MOFs, and its intervention provides a broad space for the development of electrochemical sensors [156-159]. The electrode materials with excellent characters including high sensitivity, low detection limit, fast response, wide linear range of detection, high selectivity, good functionality and stability, *etc.* can efficient promote the analytical performance of electrochemical sensor. Then, functionalized metal oxides and MOFs well meet these requirements due to its high surface activity, large specific surface area, stability structure and incomplete coordination of surface atoms. In addition, functionalized metal oxides and MOFs have more active sites, higher catalytic activity and stronger adsorption capacity on their surface, so that the immobilization of biomolecules and chemical molecules, signal amplification, and high-throughput on-line real-time monitoring of the electrochemical sensor can be realized. Therefore, using functionalized metal oxides

and MOFs as advanced functional electrode material expect to provide a new strategy for the study of electrochemical sensing application.

## 1.5 The research significance and main contents

With the rapid development of nanotechnology, functional nanomaterials have several incomparable excellent properties. Among them, functionalized metal oxides and MOFs is especially suitable for the immobilization of sensitive molecules, preconcentration of the target molecule, signal amplification due to its large specific surface area, high surface reaction activity, high catalytic efficiency and strong adsorption capacity. So, it has important application prospect in tumor detection, biological separation, biomedical imaging, ultra-sensitive detection of proteins, small molecules and organic pollutants. Based on the above reasons, it is of great significance to develop a rational signal amplification sensing construction strategy bases on the functionalized metal oxides and MOFs to improve the development of a novel electrochemical sensor.

On this basis, the main idea of this paper is put forward.

Chapter 2:

2-1: Based on a ZIF-67 template, we prepared porous nanododecahedron of  $\text{Co}_3\text{O}_4/\text{C}$  which includes high surface area, fast charge/mass transport and low overpotential. All these virtues of the nanocomposite material are beneficial to play a novel and remarkable nonenzymatic electrochemical sensing material for  $\text{NO}_2^-$  (Scheme 1). Then, the prepared sensor is used for  $\text{NO}_2^-$  detection in the real samples, the satisfactory results are obtained.

2-2: A thin nanosheet structure of  $\text{ZrO}_2/\text{C}$  was prepared using UiO-67 with a flat cuboid structure as precursor. The peculiar and fluffy structures endowed materials with high surface areas that tremendously improved the adsorption capacity of electrode materials for heavy metal ions. Thus,  $\text{ZrO}_2/\text{C}$  as an electrode material was used to simultaneous detection of Pb(II) and Cd(II) by differential pulse anodic stripping voltammetry (DPASV). The results showed that prepared sensor has the high sensitivity, good stability and low interference of the detection for two metal

ions.

2-3: An inorganic-organic hybrid material consisting SnO<sub>2</sub>-C yolk-shell nanospheres and poly-Tyrosine (pTyr) has been developed for DNA biosensor fabrication. Electrochemical experiments show that the existence of SnO<sub>2</sub>-C in the hybrid matrix remarkably enhances the effective surface area, and the pTyr not only provides abundant carboxyl groups for covalent bonding with pDNA, but also its 4'-hydroxyl group shows hydrogen bonding with the base groups of pDNA. When tDNA was hybridized with the probe DNA, the "signal-off" response in electrochemical impedance spectroscopy (EIS) measurement is obtained. The reason is likely related to the change of the state and environment of the biosensor surface before and after hybridization reaction. An ultralow detection limit of 0.53 aM for CaMV35s promoter gene is achieved. Meanwhile, it potentially becomes a convenient tool of PCR-free TG sequences analysis for medical, public, and environmental purposes.

### Chapter 3:

3-1: A flexible metal-organic framework (MOF) of Cu<sub>2</sub>(*trans*-1,4-cyclohexanedicarboxylic acid)<sub>2</sub> (Cu<sub>2</sub>(CHDC)<sub>2</sub>) with a flower-like shape was synthesized by a facile hydrothermal method. Then a signal-off aptasensor using thrombin as the target model was constructed that Cu<sub>2</sub>(CHDC)<sub>2</sub> as the signal platform and in-situ electrodeposited gold nanoparticles as signal amplification and aptamer immobilization matrix. The proposed thrombin aptasensor displays excellent performance and the results imply that the proposed sensor can be potentially used for the early diagnosis of disease and clinical monitoring.

3-2: A rational, sensitive and reusable electrochemical aptasensing strategy for Ochratoxin A (OTA) was proposed using *in-situ* coordination-assembled UiO-66 as signal amplification platform in the design, the comparative assay shows that the UiO-66 greatly enhances the analytical performance of the aptasensor. In addition, because the aptasensor was designed on the basis of the auxiliary strand-based competitive binding strategy, the excellent reusability of the aptasensor can be realized in accompany with the detection process.

## 1.6 Reference

- [1] P. J. Garnett, and D. F. Treagust, *J. Res. Sci. Teach.*, **29**, 121 (1992).
- [2] F. Nasirpour, pringer, *Cham.* 43 (2017).
- [3] G. Tsaparlis, *Isr. J. Chem.*, **59**, 478 (2019).
- [4] M. Sato, T. Ohgiyama and J. S. Clements, *IEEE Trans. Ind. Appl.*, **32**, 106 (1996).
- [5] Q. Pang, X. Liang, C. Y. Kwok and L. F. Nazar, *Nat. Energy*, **1**, 1 (2016)..
- [6] V. Vogiazzi, A. de la Cruz, S. Mishra, V. Shanov, W. R. Heineman and D. D. Dionysiou, *ACS Sens.*, **4**, 1151 (2019).
- [7] G. Maduraiveeran, M. Sasidharan and V. Ganesan, *Biosens. Bioelectron.*, **103**, 113 (2018).
- [8] F. Xie, X. Cao, F. Qu, A. M. Asiri and X. Sun, *Sens. Actuators, B*, **255**, 1254 (2018).
- [9] T. Kaneta, W. Alahmad, and P. Varanusupakul, *Appl. Spectrosc. Rev.*, **54**, 117 (2019).
- [10] C. Roggo and J. R. van der Meer, *Curr. Opin. Biotechnol.*, **45**, 24-33 (2017).
- [11] J. Nai and X. W. Lou, *Adv. Mater.*, **31**, 1706825 (2019).
- [12] A. Zhao, J. She, D. Manoj, T. Wang, Y. Sun, Y. Zhang and F. Xiao, *Sens. Actuators, B*, 127861 (2020).
- [13] A. Karimi, S. Andreescu and D. Andreescu, *ACS Appl. Mater. Interfaces*, **11**, 24725 (2019).
- [14] G. Marrazza, I. Chianella and M. Mascini, *Anal. Chim. Acta*, **387**, 297 (1999).
- [15] N. J. Ronkainen, H. B. Halsall and W. R. Heineman, *Chem. Soc. Rev.*, **39**, 1747 (2010).
- [16] E. O. Blair and D. K. Corrigan, *Biosens. Bioelectron.*, **134**, 57 (2019).
- [17] D. Grieshaber, R. MacKenzie, J. Vörös and E. Reimhult, *Sens.*, **8**, 1400 (2008).
- [18] J. B. B. Rayappan, N. Nesakumar, L. R. Bhat, M. B. Gumpu, K. J. Babu and A. Jayalatha JBB, *Bioelectrochem. Interface Eng.*, 431 (2019)..
- [19] L. Tian, K. Qian, J. Qi, Q. Liu, C. Yao, W. Song and Y. Wang, *Biosens. Bioelectron.*, **99**, 564 (2018).
- [20] L. Wang, Q. Xiong, F. Xiao and H. Duan, *Biosens. Bioelectron.*, **89**, 136 (2017).
- [21] N. F. Silva, J. M. Magalhães, C. Freire and C. Delerue-Matos, *Biosens. Bioelectron.*, **99**, 667 (2018).

- [22] V. V. Uslu and G. Grossmann, *Curr. Opin. Plant Biol.*, **29**, 138 (2016).
- [23] P. Ramnani, N. M. Saucedo and A. Mulchandani, *Chemosphere*, **143**, 85 (2016).
- [24] W. Wen, , X. Yan, , C. Zhu, , D. Du and Y. Lin, *Anal. Chem.*, **89**, 138 (2017).
- [25] S. A. Lim and M. U. Ahmed, *RSC Adv.*, **6**, 24995 (2016).
- [26] S. Patskovsky, A. M. Dallaire and M. Meunier, *Sens. Actuators, B*, **222**, 71 (2016).
- [27] Z. W. Peng, D. Yuan, Z. W. Jiang and Y. F. Li, *Electrochim. Acta*, **238**, 1 (2017).
- [28] T. Kulikova, A. Porfireva, G. Evtugyn and T. Hianik, *Sens.*, **19**, 469 (2019).
- [29] Q. Hu, J. Kong, D. Han, L. Niu and X. Zhang, *ACS Sens.*, **4**, 235 (2019).
- [30] Y. Jiang, N. Chu and R. J. Zeng, *J. Cleaner Prod.*, **232**, 1371 (2019).
- [31] S. Chinnathambi and G. J. W. Euverink, *Sens. Actuators, B*, **264**, 38 (2018).
- [32] J. Ma, L. Xue, M. Zhang, C. Li, Y. Xiang, P. Liu and G. Li, *Biosens. Bioelectron.*, **127**, 194 (2019).
- [33] T. E. Lin, S. Rapino, H. H. Girault and A. Lesch, *Chemical science*, **9**, 4546 (2018).
- [34] J. Zou, S. Wu, Y. Liu, Y. Sun, Y. Cao, , J. P. Hsu and J. Jiang, *Carbon*, **130**, 652 (2018)..
- [35] G. Maduraiveeran, M. Sasidharan and V. Ganesan, *Biosens. Bioelectron.*, **103**, 113 (2018).
- [36] M. F. Diouani, , O. Ouerghi, , A. Refai, , K. Belgacem, C. Tlili, , D. Laouini and M. Essafi, *Mater. Sci. Eng. C*, **74**, 465 (2017).
- [37] T. Xu, B. Chi, J. Gao, M. Chu, W. Fan, M. Yi and C. Mao, *Anal. Chim. Acta*, **977**, 36 (2017).
- [38] Z. Tao, J. Du, Y. Cheng and Q. Li, *Int J Electrochem Sci*, **13**, 1413 (2018).
- [39] H. Jin, R. Gui, J. Yu, W. Lv and Z. Wang, *Biosens. Bioelectron.*, **91**, 523 (2017).
- [40] F. Farshchi, M. Hasanzadeh and A. Mokhtarzadeh, *J. Mol. Recognit.*, e2825 (2019).
- [41] K. Y. Goud, S. K. Kailasa, V. Kumar, Y. F. Tsang, K. V. Gobi and K. H. Kim, *Biosens. Bioelectron.*, **121**, 205 (2018).
- [42] W. Dang, Y. Sun, H. Jiao, L. Xu and M. Lin, *J. Electroanal. Chem.*, **856**, 113592 (2020).
- [43] W. Qiu, F. Gao, J. Chen, L. Xie and Q. Wang, *Sens. Actuators, B*, **231**, 376 (2016).
- [44] S. A. Nakhjavani, H. Afsharan, B. Khalilzadeh, M. H. Ghahremani, S. Carrara

- and Y. Omid, *Biosens. Bioelectron.*, **141**, 111439 (2019).
- [45] C. Tuerk and L. Gold, *Sci.*, **249**, 505 (1990).
- [46] M. Famulok and J. W. Szostak, *Angew. Chem., Int. Ed. Engl.*, **31**, 979 (1992).
- [47] T. Wang, C. Chen, L. M. Larcher, R. A. Barrero and R. N. Veedu, *Biotechnol. Adv.*, **37**, 28 (2019).
- [48] K. S. Park, *Biosens. Bioelectron.*, **102**, 179 (2018).
- [49] I. Jeddi and L. Saiz, *Sci. Rep.*, **7**, 1 (2017).
- [50] J. M. O'Hara, D. Marashi, S. Morton, L. Jaeger and W. W. Grabow, *Nanomaterials*, **9**, 378 (2019).
- [51] P. P. Seelam, A. Mitra and P. Sharma, *RNA*, **25**, 1274 (2019).
- [52] Y. Wu, L. Zou, S. Lei, Q. Yu and B. Ye, *Biosens. Bioelectron.*, **97**, 317 (2017).
- [53] X. Ren, A. D. Gelinis, I. von Carlowitz, N. Janjic and A. M. Pyle, *Nat. Commun.*, **8**, 1 (2017).
- [54] F. Aboul-ela, *Future Med. Chem.*, **2**, 93 (2010).
- [55] J. Shu, Z. Qiu, Q. Zhou and D. Tang, *Chem. Commun.*, **55**, 3262 (2019).
- [56] M. ur Rahman, J. Wang, H. Xia, J. Liu and Q. Bai, *Chem. Eng. J.*, 123561 (2019).
- [57] Y. Feng, H. Wang, S. Zhang, Y. Zhao, J. Gao, Y. Zheng and S. Ma, *Adv. Mater.*, **31**, 1805148 (2019).
- [58] A. Villalonga, A. M. Pérez-Calabuig and R. Villalonga, *Anal. Bioanal. Chem.*, 1 (2020).
- [59] T. Wang, C. Chen, L. M. Larcher, R. A. Barrero and R. N. Veedu, *Biotechnol. Adv.*, **37**, 28 (2019).
- [60] H. Xiong, J. Yan, S. Cai, Q. He, D. Peng, Z. Liu and Y. Liu, *Int. J. Biol. Macromol.*, **132**, 190 (2019).
- [61] Q. Zhao, J. Tao, J. S. Uppal, H. Peng, H. Wang and X. C. Le, *TrAC, Trends Anal. Chem.*, **110**, 401 (2019).
- [62] M. Panigaj, M. B. Johnson, W. Ke, J. McMillan, E. A. Goncharova, M. Chandler and K. A. Afonin, *ACS nano*, **13**, 12301 (2019).
- [63] J. Song, S. Li, F. Gao, Q. Wang and Z. Lin, *Chem. Commun.*, **55**, 905 (2019).
- [64] S. S. Wu, M. Wei, W. Wei, Y. Liu and S. Liu, *Biosens. Bioelectron.*, **129**, 58 (2019).
- [65] Z. Hatami, F. Jalali, M. A. Tabrizi and M. Shamsipur, *Biosens. Bioelectron.*, **141**, 111433 (2019).

- [66] G. Selvolini, M. Lettieri, L. Tassoni, S. Gastaldello, M. Grillo, C. Maran and G. Marrazza, *Talanta*, **203**, 49 (2019).
- [67] I. Morkvenaite-Vilkonciene, A. Ramanaviciene, A. Kisieliute, V. Bucinskas and A. Ramanavicius, *Biosens. Bioelectron.*, 141, 111411 (2019).
- [68] T. Monteiro and M. G. Almeida, *Crit. Rev. Anal. Chem.*, 49, 44 (2019).
- [69] Y. Liu, L. Yao, L. He, N. Liu and Y. Piao, *Sens.*, **19**, 1619 (2019).
- [70] I. S. Kucherenko, O. O. Soldatkin, D. Y. Kucherenko, O. V. Soldatkina and S. V. Dzyadevych, *Nanoscale Adv.*, **1**, 4560 (2019).
- [71] N. Loew, W. Tsugawa, D. Nagae, K. Kojima and K. Sode, *Sens.*, **17**, 2636 (2017).
- [72] E. Mahmoudi, H. Fakhri, A. Hajian, A. Afkhami and H. Bagheri, *Bioelectrochemistry*, **130**, 107348 (2019).
- [73] J. Špaček, E. Eksin, L. Havran, A. Erdem and M. Fojta, *J. Electroanal. Chem.*, 113951 (2020).
- [74] S. Y. Tee, C. P. Teng and E. Ye, *Mater. Sci. Eng.: C*, **70**, 1018 (2017).
- [75] H. Zhu, L. Li, W. Zhou, Z. Shao and X. Chen, *J. Mater. Chem. B*, **4**, 7333 (2016).
- [76] Y. Yang, H. Zhang, C. Huang, D. Yang and N. Jia, *Biosens. Bioelectron.*, **89**, 461-467 (2017).
- [77] S. Wu, N. Tan, D. Lan, C. T. Au and B. Yi, *Sens.*, **18**, 3464 (2018).
- [78] Z. Shi, X. Li, L. Yu, X. Wu, J. Wu, C. Guo and C. M. Li, *Biosens. Bioelectron.*, **141**, 111421 (2019).
- [79] J. Chen, P. He, H. Bai, H. Lei, K. Liu, F. Dong and X. Zhang, *J. Electroanal. Chem.*, **784**, 41 (2017).
- [80] X. Tang, B. Zhang, C. Xiao, H. Zhou, X. Wang and D. He, *Sens. Actuators, B*, **222**, 232 (2016)
- [81] J. M. Moon, N. Thapliyal, K. K. Hussain, R. N. Goyal and Y. B. Shim, *Biosens. Bioelectron.*, **102**, 540 (2018).
- [82] S. He, P. He, X. Zhang, X. Zhang, K. Liu, L. Jia and F. Dong, *Anal. Chim. Acta*, **1031**, 75 (2018).
- [83] S. Wu, N. Tan, D. Lan, C. T. Au and B. Yi, *Sens.*, **18**, 3464 (2018) .
- [84] B. Liu, X. Wang, Y. Zhai, Z. Zhang, H. Liu, L. Li and H. Wen, *J. Electroanal. Chem.*, **858**, 113804 (2020).
- [85] R. Waditee-Sirisattha, H. Kageyama and T. Takabe, Halophilic microorganism

- resources and their applications in industrial and environmental biotechnology. *AIMS Microbiol.*, **2**, 42 (2016).
- [86] Y. Si, A. Y. Zhang, C. Liu, D. N. Pei and H. Q. Yu, *Water Res.*, **157**, 30 (2019).
- [87] Z. Fu and S. Xi, *Toxicol. Mech. Methods*, **30**, 167 (2020).
- [88] K. Rehman, F. Fatima, I. Waheed and M. S. H. Akash, *J. Cell. Biochem.*, **119**, 157 (2018).
- [89] J. Liao, F. Yang, C. Z. Wang and S. Lin, *Sens. Actuators, B*, **271**, 195 (2018).
- [90] F. Cai, Q. Wang, X. Chen, W. Qiu, F. Zhan, F. Gao and Q. Wang, *Biosens. Bioelectron.*, **98**, 310 (2017).
- [91] Y. Chu, F. Gao, F. Gao and Q. Wang, *J. Electroanal. Chem.*, **835**, 293 (2019).
- [92] X. Shu, Y. Wang, J. Cui, G. Xu, J. Zhang, W. Yang and Z. Chen, *J. Alloys Compd.*, **753**, 731 (2018).
- [93] B. K. Maiti, L. B. Maia, I. Moura and J. J. Moura, *Chem.-Eur. J.*, **25**, 4309 (2019).
- [94] V. S. Manikandan, B. Adhikari and A. Chen, *Analyst*, **143**, 4537 (2018).
- [95] W. Qiu, H. Tanaka, F. Gao, Q. Wang and M. Huang, *Adv. Powder Technol.*, **30**, 2083 (2019).
- [96] V. Sudha, S. M. S. Kumar and R. Thangamuthu, *J. Alloys Compd.*, **749**, 990 (2018).
- [97] Y. Liu, Q. Xie, X. Li, F. Tian, X. Qiao, J. Chen and W. Ding, *Environ. Sci.: Processes Impacts*, **21**, 9 (2019).
- [98] S. Yadav and R. Chandra, *Environ. Monit. Assess.*, **190**, 581 (2018).
- [99] Y. Yang, Q. Wang, W. Qiu, H. Guo and F. Gao, *J. Phys. Chem. C*, **120**, 9794 (2016).
- [100] M. Ahmed, R. Zhao, B. Hayytov, Y. Shang, J. Li and J. Du, *Chin. Chem. Lett.*, (2020).
- [101] M. A. Subhan, P. C. Saha, M. M. Rahman, J. Ahmed, A. M. Asiri, M. Al-Mamun, *New J. Chem.* **42**, 872 (2018).
- [102] S. Selvarajan, A. Suganthi, M. Rajarajan, *Ultrason. Sonochem.* **41**, 651 (2018).
- [103] H. Liu, L. Weng, C. Yang, *Microchim Acta.* **1** (2017).
- [104] Y. Lü, W. Zhan, Y. He, Y. Wang, X. Kong, Q. Kuang, L. Zheng, *ACS Appl Mater Interfaces.* **64**, 186 (2014).
- [105] C. Yan, G. Chen, X. Zhou, J. Sun, C. Lv, *Adv Funct Mater.* **26**, 1428 (2016).
- [106] L. T. Anh, A. K. Rai, T. V. Thi, J. Gim, S. Kim, V. Mathew, J. Kim, *J Mater Chem A Mater.* **2**, 6966 (2014).

- [107] T. Y. Ma, S. Dai, M. Jaroniec, S. Z. Qiao, *J. Am. Chem. Soc.* **136**, 13925 (2014).
- [108] A. Herbst and C. Janiak, *CrystEngComm*, **19**, 4092 (2017).
- [109] M. Bonneau, C. Lavenn, P. Ginet, K. I. Otake and S. Kitagawa, *Green Chem.*, **22**, 718 (2020).
- [110] Y. Zhao, M. Y. Wan, J. P. Bai, H. Zeng, W. Lu and D. Li, *J. Mater. Chem. A*, **7**, 11127 (2019).
- [111] X. Gao, R. Cui, M. Zhang and Z. Liu, *Mater. Lett.*, **197**, 217 (2017).
- [112] X. Zhang, Z. Zhang, J. Boissonault and S. M. Cohen, *Chem. Commun.*, **52**, 8585 (2016).
- [113] P. Karthik, R. Vinoth, P. Zhang, W. Choi, E. Balaraman and B. Neppolian, *ACS Appl. Energy Mater.*, **1**, 1913 (2018) .
- [114] C. Wang, L. Sun, L. Lv, L. Ni, S. Wang and P. Yan, *Inorg. Chem. Commun.*, **18**, 75 (2012).
- [115] H. Furukawa, K. E. Cordova , M. Okeeffe, O. M. Yaghi, *Science*, **341**, 1230444 (2013).
- [116] H. Yang and X. Wang, *Adv. Mater.*, **31**, 1800743 (2019).
- [117] B. Z hu, D. Xia and R. Zou, *Coord. Chem. Rev.*, **376**, 430 (2018).
- [118] X. Ma, X. Zhao, J. Sun, D. Li and X. Yang, *RSC Adv.*, **6**, 7728 (2016).
- [119] Z. J. Wang, L. J. Han, X. J. Gao and H. G. Zheng, *Inorg. Chem*, **57**, 5232 (2018).
- [120] Q. Yang, Q. Xu and H. L. Jiang, *Chem. Soc. Rev.*, **46**, 4774 (2017).
- [121] M. H. Yap, K. L. Fow and G. Z. Chen, *Green Energy Environ.*, **2**, 218 (2017) .
- [122] S. He, H. Wang, C. Zhang, S. Zhang, Y. Yu, Y. Lee and T. Li, *Chem. Sci.*, **10**, 1816 (2019).
- [123] S. Kempahanumakkagari, V. Kumar, P. Samaddar, P. Kumar, T. Ramakrishnappa and K. H. Kim, *Biotechnol. Adv.*, **36**, 467 (2018).
- [124] G. Cai, W. Zhang, L. Jiao, S. H. Yu and H. L. Jiang, *Chem.*, **2**, 791 (2017).
- [125] M. L. Hu, M. Y. Masoomi and A. Morsali, *Coord. Chem. Rev.*, **387**, 415 (2019).
- [126] W. Xia, A. Mahmood, R. Zou, Q. Xu, *Energy Environ. Sci.*, **8**, 1837 (2015).
- [127] Y. Liu, M. Zhu, M. Chen, L. Ma, B. Yang, L. Li and W. Tu, *Chem. Eng. J.*, **359**, 47 (2019).
- [128] K. Fu, R. Zhang, J. He, H. Bai and G. Zhang, *Biosens. Bioelectron.*, **143**, 111636 (2019).

- [129] H. Niu, Y. Liu, B. Mao, N. Xin, H. Jia and W. Shi, *Electrochim. Acta*, **329**, 135130 (2020).
- [130] G. Zheng, M. Chen, H. Zhang, J. Zhang, X. Liang, M. Qi and J. Yin, *Surf. Coat. Technol.*, **359**, 384 (2019).
- [131] Q. Wang, Y. Yang, F. Gao, J. Ni, Y. Zhang and Z. Lin, *ACS Appl. Energy Mater.*, **8**, 32477 (2016).
- [132] S. N. Ansari, M. Saraf, A. K. Gupta and S. M. Mobin, *Chem.-Asian J.*, **14**, 3566 (2019).
- [133] B. Li, J. G. Ma and P. Cheng, *Small*, **15**, 1804849 (2019).
- [134] J. Su, S. Yuan, T. Wang, C. Lollar, J. L. Zuo, J. Zhang and H. C. Zhou, *Chem. Sci.*, **11**, 1918 (2020).
- [135] S. Zhao, Y. Zhang, S. Ding, J. Fan, Z. Luo, K. Liu and G. Zang, *J. Electroanal. Chem.*, **834**, 33 (2019).
- [136] S. Wang, C. M. McGuirk, A. d'Aquino, J. A. Mason and C. A. Mirkin, *Adv. Mater.*, **30**, 1800202 (2018).
- [137] J. H. Deng, Y. Q. Wen, J. Willman, W. J. Liu, Y. N. Gong, D. C. Zhong and H. C. Zhou, *Inorg. Chem.*, **58**, 11020 (2019).
- [138] J. Liang, F. Mazur, C. Tang, X. Ning, R. Chandrawati and K. Liang, *Chem. Sci.*, **10**, 7852 (2019).
- [139] Y. H. Zhou, Z. Zhang, M. Patrick, F. Yang, R. Wei, Y. Cheng and J. Gu, *Dalton Trans.*, **48**, 8044-8048 (2019).
- [140] Y. H. Shih, S. H. Lo, N. S. Yang, B. Singco, Y. J. Cheng, C. Y. Wu and C. H. Lin, *ChemPlusChem*, **77**, 982 (2012).
- [141] J. Chang, X. Wang, J. Wang, H. Li and F. Li, *Anal. Chem.*, **91**, 3604 (2019).
- [142] S. Wang, C. M. McGuirk, M. B. Ross, S. Wang, P. Chen, H. Xing and C. A. Mirkin, *J. Am. Chem. Soc.*, **139**, 9827 (2017).
- [143] R. Lin, L. Ge, H. Diao, V. Rudolph and Z. Zhu, *ACS Appl. Mater. Interfaces*, **8**, 32041 (2016).
- [144] R. Lin, B. V. Hernandez, L. Ge and Z. Zhu, *J. Mater. Chem. A*, **6**, 293 (2018).
- [145] N. D. H. Gamage, K. A. McDonald and A. J. Matzger, *Angew. Chem., Int. Ed.*, **55**, 12099 (2016).
- [146] M. Lu, Y. Deng, Y. Li, T. Li, J. Xu, S. W. Chen and J. Wang, *Anal. Chim. Acta* (2020).
- [147] L. Li, Y. Xu, D. Zhong and N. Zhong, *Colloids Surf., A*, **586**, 124255 (2020).

- [148] D. M. Reinoso, U. Diaz and M. A. Frechero, *Mater. Today Chem.*, **14**, 100188 (2019).
- [149] W. Jiang, J. Pan and X. Liu, *J. Power Sources*, **409**, 13 (2019).
- [150] Y. Li, Y. Xu, W. Yang, W. Shen, H. Xue and H. Pang, *Small*, **14**, 1704435 (2018).
- [151] A. Li, B. Qian, M. Zhong, Y. Liu, Z. Chang and X. H. Bu, *Mater. Chem. Front.*, **3**, 1398 (2019).
- [152] X. Xu, R. Cao, S. Jeong and J. Cho, *Nano Lett.*, **12**, 4988 (2012).
- [153] J. Zhou, Y. Dou, A. Zhou, L. Shu, Y. Chen and J. R. Li, *ACS Energy Lett.*, **3**, 1655 (2018).
- [154] H. Liu, X. Liu, S. Mu, S. Wang, S. Wang, , L. Li and E. P. Giannelis, *Catal. Sci. Technol.*, **7**, 1965 (2017).
- [155] Y. C. Wang, W. B. Li, L. Zhao and B. Q. Xu, *Phys. Chem. Chem. Phys.*, **18**, 17941 (2016).
- [156] C. S. Liu, J. Li and H. Pang, *Coord. Chem. Rev.*, **410**, 213222 (2020).
- [157] Z. Zhao, J. Ding, R. Zhu and H. Pang, *J. Mater. Chem. A*, **7**, 15519 (2019).
- [158] Y. Xue, S. Zheng, H. Xue and H. Pang, *J. Mater. Chem. A*, **7**, 7301 (2019).
- [159] L. Liu, Y. Zhou, S. Liu and M. Xu, *ChemElectroChem*, **5**, 6 (2018).

## **Chapter 2**

### **The functionalization of metal-oxide and their application for electrochemical sensors**

**2-1 Synthesis of porous nanododecahedron  $\text{Co}_3\text{O}_4/\text{C}$  and its application for nonenzymatic electrochemical detection of nitrite**

## 2-1.1 Introduction

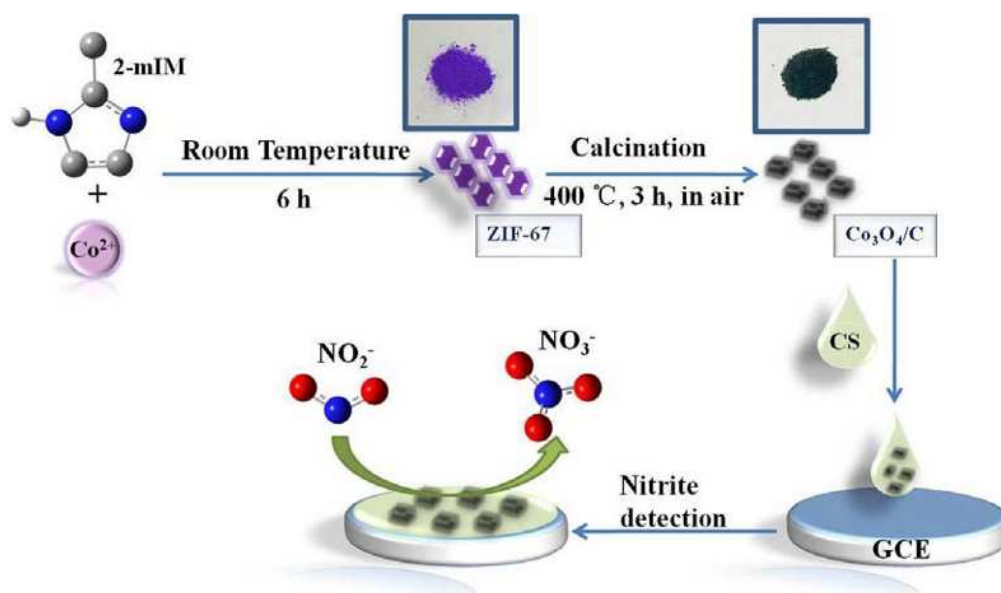
Nitrite ions ( $\text{NO}_2^-$ ) are general toxic inorganic pollutants existing in our live such as soil, water, food, and even physiological systems [1]. Excessive amount of  $\text{NO}_2^-$  makes against to the human body, for example  $\text{NO}_2^-$  can combine with hemoglobin to lead to a serious syndrome; and even convert into nitrosamine, which will induce hypertension and cancer [2]. Therefore, it is urgently to find a fast response monitor for toxic  $\text{NO}_2^-$ . Accordingly, many technologies have been developed to detect  $\text{NO}_2^-$  based on different principles, such as chromatography [3], spectrophotometry [4], spectrofluorimetry [5], chemiluminescence [6], and electrochemical biosensors [7]. Among them, the electrochemical method possesses outstanding performance including rapidity, sensitivity, convenience, cost-cheap, and so on. Hence, the fabrication of electrochemical  $\text{NO}_2^-$  sensor has been paid more attentions [8]. However, using the bare glassy carbon electrode (GCE) as sensing electrode, the redox potential of  $\text{NO}_2^-$  is high, which will cause interference with other ions in the detect process. In order to overcome the disadvantage, nanomaterials are applied to lower overpotential for detecting  $\text{NO}_2^-$  and to improve its sensitivity and selectivity [9].

Some inorganic nanomaterials, such as non-precious metals (including iron, nickel, and cobalt) and their oxides and sulfides have high specific surface area, excellent electrocatalytic activity, low cost, and the ability of facilitating electron transfer at a lower overpotential, so they are widely used as sensing materials [10-12]. Among them,  $\text{Co}_3\text{O}_4$  is one of the most fascinating semiconductors and has been extensive applied to many fields such as electrode materials in heterogeneous catalysts [13], lithium-ion battery and supercapacitors [14-16], and sensing materials [17, 18]. So far,  $\text{Co}_3\text{O}_4$  porous nanostructures with various morphologies including nanospheres, nanorods, nanotubes and flowers are obtained based on pyrolysis Co-based carbonates [19], coordination complex [20], hydroxide [21, 22]. Unfortunately, the optimal synthetic conditions and suitable template of synthesis still unsolved, some of porous  $\text{Co}_3\text{O}_4$  products cannot keep the pristine morphology features of the precursor template [17]. Most seriously, pure  $\text{Co}_3\text{O}_4$  still faces disadvantage of poor conductivity and lack of stability during the detecting process. And then, several advancements had confirmed that formation of  $\text{Co}_3\text{O}_4$ -carbon nanocomposites using

of the additional-conductive species (graphene, carbon nanotubes, etc.) is a great method to solve the problem [16]. For example, Kim and co-workers synthesized a hybrid  $\text{Co}_3\text{O}_4$ /graphene material to enhance the electronic conductivity of  $\text{Co}_3\text{O}_4$  [23]. Tian and co-workers designed a compound  $\text{Co}_3\text{O}_4$ -carbon porous nanowire arrays (named as  $\text{Co}_3\text{O}_4$ -CNA) through pyrolyzation of the metal-organic framework (MOF) [24].

In the synthesis of novel nanomaterials, MOFs are frequently used as sacrificial templates or precursors, due to its excellent porous structure and abundant elemental composition [25]. In MOFs scaffolds, the uniform distribution metal oxide nanoparticles formed resulting from the periodic repeated arrays of metal nodes and carbon species formed resulting from organic motifs [26]. Our purpose is to synthesize the uniform distribution metal oxide and carbon composite electrode materials, and use their synergy to achieve excellent catalytic performance. Herein, the  $\text{Co}_3\text{O}_4$ /C nanoparticles with high surface area and excellent conductivity were prepared via a facile way based on Co-based MOF as the precursors.

Based on a ZIF-67 template [27], we prepared porous nanododecahedron of  $\text{Co}_3\text{O}_4$ /C which includes high surface area, fast charge/mass transport and low overpotential. All these virtues of the nanocomposite material are beneficial to play a novel and remarkable nonenzymatic electrochemical sensing material for  $\text{NO}_2^-$  (Scheme 2-1.1). Then, the prepared sensor is used for  $\text{NO}_2^-$  detection in the real samples, the satisfactory results are obtained.



Scheme 2-1.1 Schematic synthesis of  $\text{Co}_3\text{O}_4/\text{C}$  and its application as a nonenzymatic electrocatalyst for nitrite

## 2-1.2 Experimental

### 2-1.2.1 Reagents and apparatus

Cobalt nitrate hexahydrate ( $\text{Co}(\text{NO}_3)_2 \cdot 6\text{H}_2\text{O}$ ), sodium nitrite ( $\text{NaNO}_2$ ), sodium nitrate ( $\text{NaNO}_3$ ), and ascorbic acid (AA) were provided by Guangdong Xilong Chemical Co., Ltd (China). 2-methylimidazole (mIM, 99%), dopamine (DA), and glucose (Glu) were acquired from Aladdin Reagent Co., Ltd (China). The macrophages were obtained from Jiangsu KeyGEN BioTECH Co., Ltd. (China). Hydrogen peroxide ( $\text{H}_2\text{O}_2$ ), uric acid (UA), and chitosan (CS) were provided by Hengmao Chemical Reagent Co. Ltd. (China). All the other chemicals were of analytical reagent grade. All the electrochemical experiments were executed in  $\text{N}_2$ -saturated NaAc-HAc buffer (pH 4.5).

Transmission electron microscope (TEM) was performed by Tecnai G2 F20 (USA). Scanning electron microscopy (SEM) was evaluated using JSM-60-10LA (Japan). X-ray diffraction (XRD) was carried out by a Rigaku D/MAX-RB diffractometer with  $\text{Cu K}\alpha$  radiation (Japan). Nitrogen adsorption-desorption isotherms were determined by Belsorp-MAX (USA). X-ray photoelectron spectroscopy (XPS) was performed using Axis Ultra instrument (U.K.). The CHI 660E electrochemical workstation (China) with the standard three-electrode configuration (working electrode: a modified GCE; counter electrode: Pt wire; reference electrode: Ag/AgCl electrode) was carried out for electrochemical measurements.

### 2-1.2.2 Preparation of $\text{Co}_3\text{O}_4/\text{C}$ nanocomposite

$\text{Co}_3\text{O}_4/\text{C}$  nanocomposite was synthesized through a facile process involving the synthesis of ZIF-67 nanododecahedron and the pyrolysis was performed at 400 °C in air (Scheme 2-1.1). According to a previous report [20], the ZIF-67 nanododecahedron as sacrificial template was fabricated by a simple precipitation reaction in aqueous solution at room temperature. Typically, 3 mL of 1.55 mM  $\text{Co}(\text{NO}_3)_2 \cdot 6\text{H}_2\text{O}$  aqueous solution and 20 mL of 67.1 mM 2-methylimidazole aqueous solution were mixed, and the formed suspension was stirred at room temperature for 6

h. Subsequently, the purple products were filtered off and washed with distilled-water and alcohol for several times and dried at 80 °C in vacuum for 24 h. Then, as-prepared ZIF-67 precursor was calcined at 400 °C in air for 3 h with a heating speed of 10 °C·min<sup>-1</sup>. As a result, the purple powder was converted into the black powder by calcination at 400 °C and the final product was named as Co<sub>3</sub>O<sub>4</sub>/C. In order to reveal the key factor for the formation mechanism of dodecahedron nanoparticles, calcination was carried out at 300 °C, 400 °C and 500 °C in air for 3 h.

### **2-1.2.3 Fabrication of the Co<sub>3</sub>O<sub>4</sub>/C-CS/GCE modified electrode.**

To prepare the modified electrode, a bare GCE was burnished with alumina slurry and then in turn ultrasonically washed in distilled-water and ethanol for 5 min. 1 mg of Co<sub>3</sub>O<sub>4</sub>/C nanocomposite was dispersed into 1 mL water for 30 min by ultraphonic. Then, the prepared suspension was mixed with 75.0% acetic acid solution including 0.3 wt% CS until a well-dispersed solution was achieved. After that, 10 μL of the uniform mixture solution was cast on the polished GCE and then dried naturally, the modified electrode (Co<sub>3</sub>O<sub>4</sub>/C-CS/GCE) was obtained. Also, the CS/GCE and Co<sub>3</sub>O<sub>4</sub>/C/GCE were fabricated via the same way.

## **2-1.3 Results and Discussion**

### **2-1.3.1 Characterizations of products**

The XRD pattern (Fig. 2-1.1A) reveals that the obtained precursor is ZIF-67, because all the diffraction peaks correspond to the standard CCDC card of ZIF-67 (CCDC No.: 671073). Fig. 2-1.1B displays the XRD pattern of the calcined products of ZIF-67 at different temperatures. From the results, the products calcined at 400 °C and 500 °C exhibit main intense diffraction peaks indexed to the (111), (220), (311), (400), (422), (511), and (440) of Co<sub>3</sub>O<sub>4</sub> (PDF No. 74-2120). Moreover, no impurity phase is observed. While the (111) peak of Co<sub>3</sub>O<sub>4</sub> at 19° is disappeared (the orange dashed inset Fig. 2-1.1B) when the product was obtained at 300 °C. The reason may be due to the fact that the ZIF-67 precursor calcined at lower temperature cannot

transform into  $\text{Co}_3\text{O}_4$  completely. In addition, the calcined products obtained at 500 °C have sharp and strong diffraction peaks compared to that calcined at 400 °C. This implies that the primary crystallites turn bigger in size and the higher calcination temperature improves the crystallinity of this material. This result is confirmed at the TEM images.  $\text{N}_2$  adsorption-desorption isotherms were performed to clarify the specific surface area of the  $\text{Co}_3\text{O}_4$  products and are shown in Fig. 2-1.1C. The adsorption isotherms of the samples obtained at 300 °C (curve violet) and 400 °C (curve green) show a steep rise at a relative pressure more than 0.8, suggesting the presence of mesopores [28]. The sample obtained at 500 °C exhibits typical type II adsorption isotherm, indicating the product is non-porous (curve wine) [29]. The specific surface area of the products formed at 300 °C, 400 °C and 500 °C was estimated from the BET method to be 54.4, 77.3, 49.9  $\text{m}^2\text{g}^{-1}$ , respectively. Note that, the specific surface area of  $\text{Co}_3\text{O}_4$  obtained at 400 °C is higher than those of the control samples obtained at 300 °C and 500 °C. Therefore, the porous  $\text{Co}_3\text{O}_4/\text{C}$  with high surface area is likely to enhance its performance in electrochemical application [30, 31].

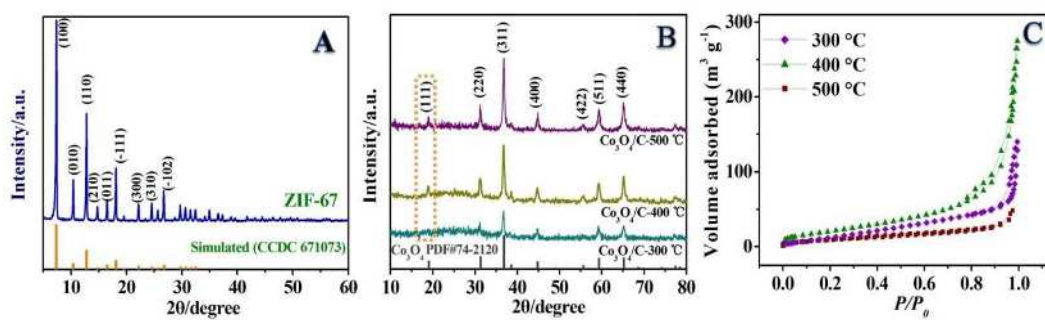


Fig. 2-1.1 (A) XRD pattern of ZIF-67, (B) XRD pattern, and (C)  $\text{N}_2$  adsorption-desorption isotherms of  $\text{Co}_3\text{O}_4/\text{C}$  obtained at 300 °C, 400 °C, 500 °C.

The morphology of the synthetic ZIF-67 particles was revealed by SEM and a dodecahedron structure is observed in Fig. 2-1.2A [32]. The TEM images of the samples calcined at 300 °C, 400 °C and 500 °C in an air atmosphere show the influence of calcination temperature on product morphology and the results are displayed in Fig. 2-1.2B-D. As the ZIF-67 was calcined at 400 °C, it can be clearly seen that the product is highly porous, fluffy, homogeneous and a structured dodecahedron (Fig. 2-1.2C). On contrary, when the material was treated at 300 °C, no porous structure is found and non-transparent products are observed from Fig. 2-1.2B, suggesting that the ZIF-67 cannot completely convert into metal oxide at lower pyrolysis temperature. When the pyrolysis temperature was increased to 500 °C, the porous structure entirely collapsed (Fig. 2-1.2D). So, the results suggest that calcination of 400 °C is the optimal temperature to remain the MOF structure and to achieve the formation of uniform porous structure. The results may be attributed to the following reasons: when pyrolysis temperature reaches or exceeds the decomposition temperature of the MOFs precursors, organic ligands and other guest molecules in the ZIF-67 precursors are burned out in air and releases the gases including CO<sub>2</sub>, H<sub>2</sub>O, and NO<sub>x</sub> [17]. At an appropriate decomposition temperature of 400 °C, the conversion process of the precursor is relatively facile, thus the materials of regular structure and porous is formed. With increasing the pyrolysis temperature, the gases, such as H<sub>2</sub>O, CO<sub>2</sub>, and NO<sub>x</sub>, release fast at high temperatures and the porous structure collapses during the decomposition process. However, the precursors have not been thoroughly calcined at a low temperature, so that there are not enough gases to release, and failure to form the porous structure. Then, the products have maximum porosity and minimum structural damage at the optimal calcination temperature of 400 °C.

By TEM description, more morphological information of the Co<sub>3</sub>O<sub>4</sub> porous nanododecahedron formed at 400 °C is revealed. As shown in Fig. 2-1.2E, a survey on an individual porous nanododecahedron shows that the materials are made up of numerous primary crystallites of about 13 nm in size (yellow dotted line). As evidence, the lattice fringes are displayed via the high resolution TEM (HRTEM) image (Fig. 2-1.2F). Two sets of lattice fringes, both with a spacing of 0.28 nm and 0.24 nm are observed, matching well with the (220) and (311) planes in the product formed at 400 °C.

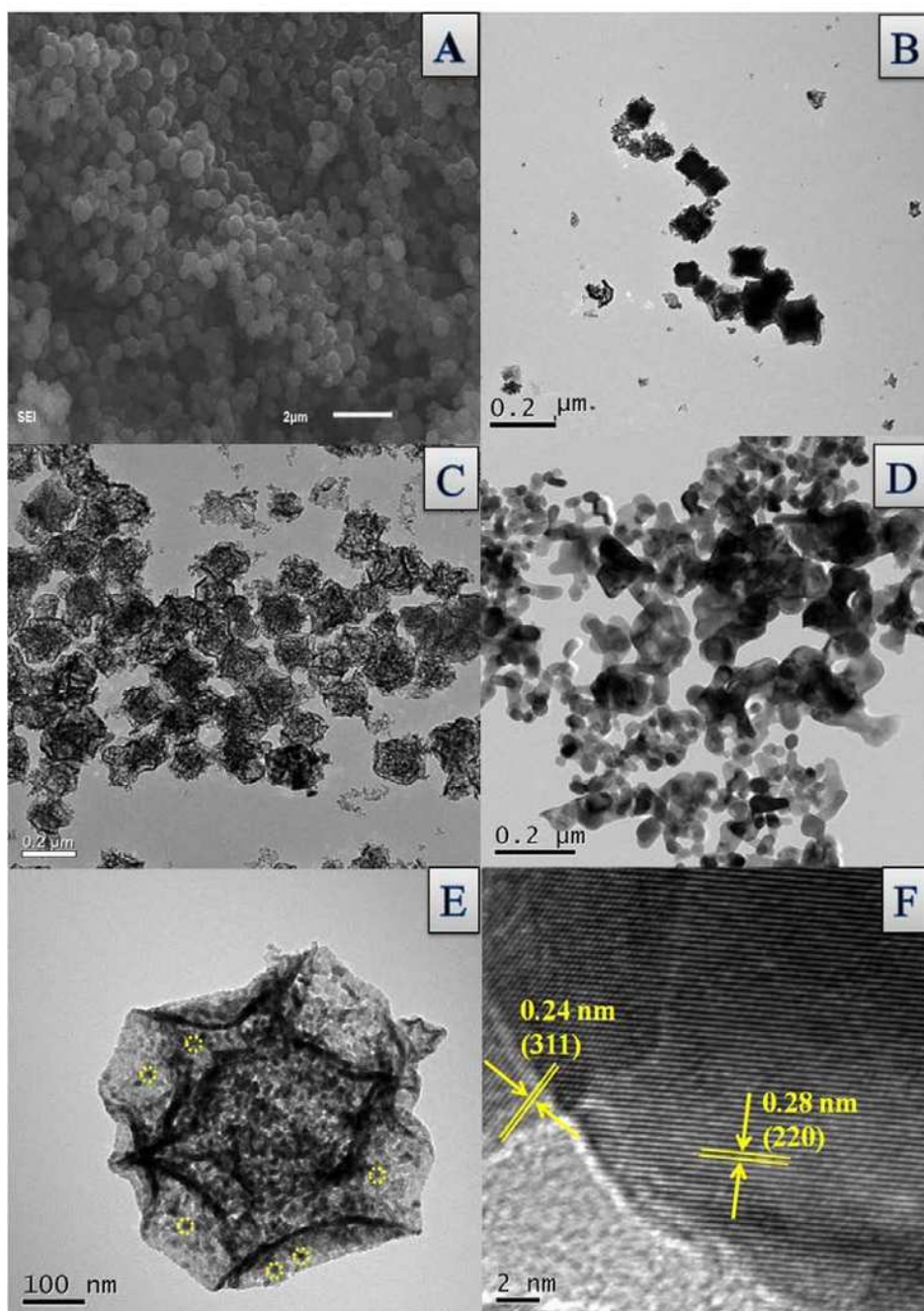


Fig. 2-1.2 SEM images of (A) ZIF-67, and Low-magnification TEM images  $\text{Co}_3\text{O}_4$  products obtained at (B) 300 °C, (C, E) 400 °C, and (D) 500 °C. (F) HRTEM image of  $\text{Co}_3\text{O}_4$  formed at 400 °C.

The nature of the surface electronic state and the chemical elemental composition of  $\text{Co}_3\text{O}_4$  obtained at  $400\text{ }^\circ\text{C}$  were explored through XPS characterization and the results are displayed in Fig. 2-1.3. As seen in Fig. 2-1.3A, the full XPS spectrum testifies the presence of Co, O and C on the surface of the prepared nanomaterial, so the nanomaterial composed of  $\text{Co}_3\text{O}_4$  and carbon was named  $\text{Co}_3\text{O}_4/\text{C}$ . The Co 2p spectrum of  $\text{Co}_3\text{O}_4/\text{C}$  particles is displayed in Fig. 2-1.3B. Two binding energy at 794.9 eV and 779.8 eV in line with the peaks corresponding to Co  $2p_{1/2}$  and Co  $2p_{3/2}$  spin-orbit of  $\text{Co}_3\text{O}_4$  are observed [33]. In addition, a weak satellite peak is obviously found at 789.8 eV, which is a key feature of  $\text{Co}_3\text{O}_4$  crystallite [34]. The O 1s spectrum presents in Fig. 2-1.3C is useful for the structural identification of  $\text{Co}_3\text{O}_4$ . The peak at 531.6 eV is assigned to the  $\text{O}^{2-}$  ions in oxygen-deficient regions of the  $\text{Co}_3\text{O}_4$  (oxygen vacancies,  $\text{O}_\text{V}$ ) matrix, while the binding energy of O 1s at 529.8 eV is considered to be the lattice oxygen ( $\text{O}_\text{L}$ ) in the  $\text{Co}_3\text{O}_4$  crystallite [17]. In Fig. 2-1.3D, the C 1s spectrum has been divided into two peaks. The main binding energy at 284.6 eV is identified as C–C bond, while the peak at 286.5 eV is derived from C–O bond [35]. The formation of the C–O bond can be due to structural defects on the edge of unsaturated carbon at high temperature, which easily form oxygen-containing groups because of reacting with the physically adsorbs oxygen when being exposes to air.

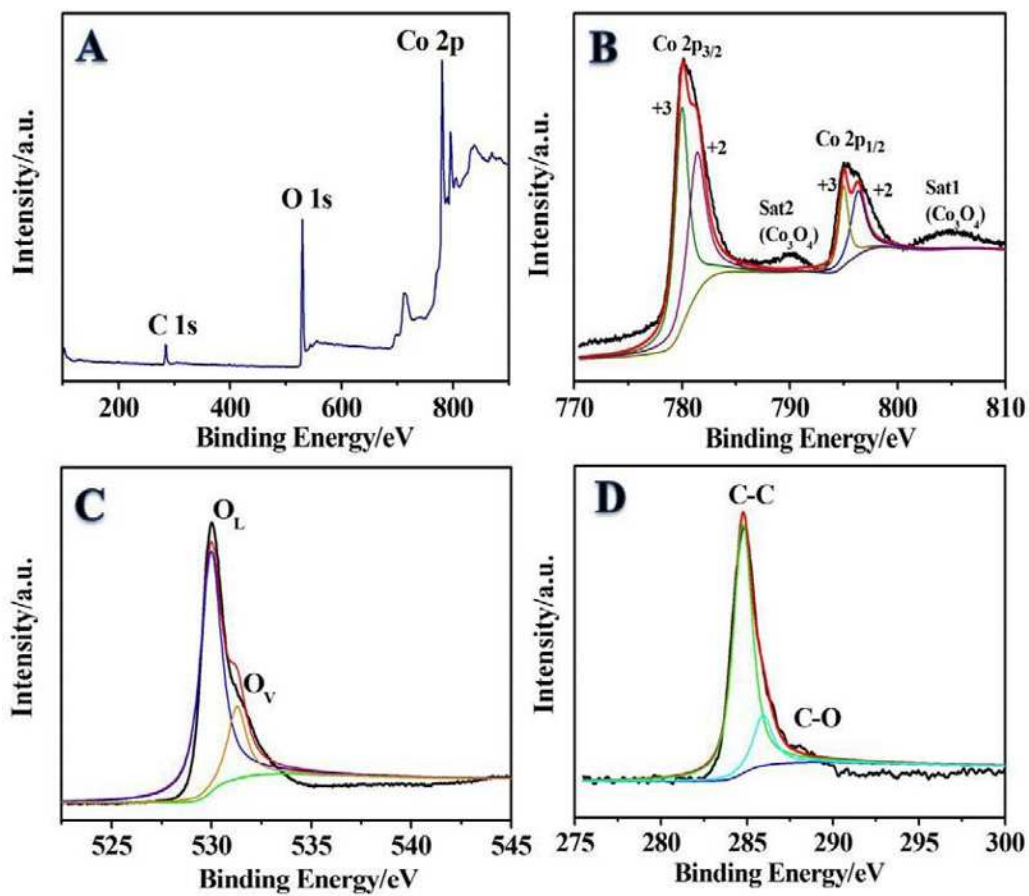


Fig. 2-1.3 (A) Full XPS spectrum of  $\text{Co}_3\text{O}_4/\text{C}$  prepared at  $400\text{ }^\circ\text{C}$ . Result of curve fitting of (B) Co 2p, (C) O 1s, and (D) C 1s spectra.

### 2-1.3.2 Optimization of experiment conditions

The conductivity of the  $\text{Co}_3\text{O}_4$  products calcined at different temperatures was investigated by cyclic voltammograms (CV) and electrochemical impedance spectroscopy (EIS) using  $[\text{Fe}(\text{CN})_6]^{3-/4-}$  as electrochemical probe. As shown in Fig. 2-1.4A, the  $\text{Co}_3\text{O}_4/\text{C}$  possesses the highest redox current (curve b), suggesting that the  $\text{Co}_3\text{O}_4/\text{C}$  has the best conductivity. The excellent conductivity performance of  $\text{Co}_3\text{O}_4/\text{C}$  is due to its highly porous structure and the presence of conductive carbon. At the low calcined temperature, the MOFs template decomposed incompletely and the chemical activation of the product is limited, resulting in the low electrochemical response (curve a). When the higher calcination temperature was adopted, the product collapsed during calcination, so the porous structure vanished and the active sites decreased, resulting in the decrease of the electrochemical response (curve c). Therefore,  $\text{Co}_3\text{O}_4/\text{C}$  obtained at 400  $^{\circ}\text{C}$  is identified as the optimal sensing material. Meanwhile, the electrochemical behavior of modified electrode was characterized by EIS (inset Fig. 2-1.4A), which has been known to monitor the electron transfer process at the interface. The results show that the value of electron transfer resistance ( $R_{\text{et}}$ ) on the  $\text{Co}_3\text{O}_4/\text{C}$  modified surface is 88.5  $\Omega$  (red dots). However, after anchoring  $\text{Co}_3\text{O}_4$ -300  $^{\circ}\text{C}$  and  $\text{Co}_3\text{O}_4$ -500  $^{\circ}\text{C}$  on GCE, the  $R_{\text{et}}$  values are increased to 105.6  $\Omega$  (black dots) and 160.1  $\Omega$  (green dots), respectively, further testifying the  $\text{Co}_3\text{O}_4/\text{C}$  can effectively facilitate the electron transfer process of the composite film and the presence of carbon material in the composite can effectively enhance the electronic conductivity of the material, as well as analytical signal of the sensor.

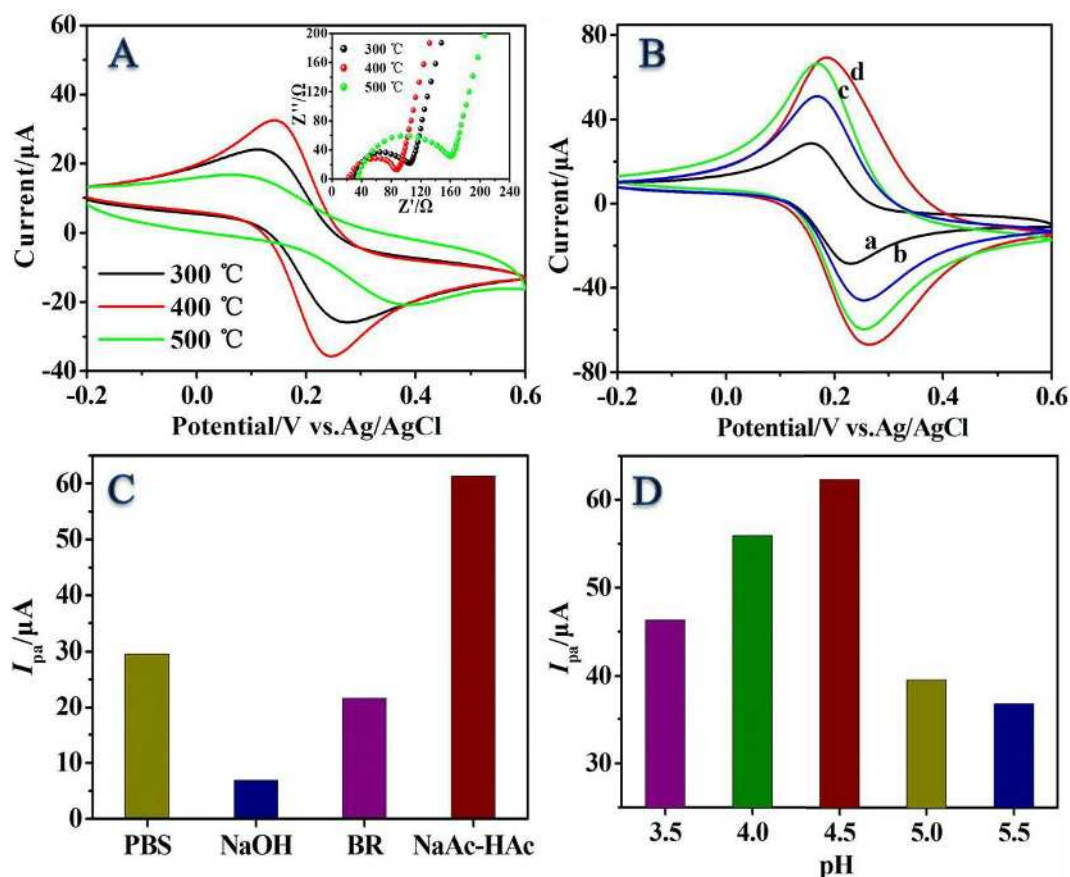


Fig. 2-1.4 (A) CVs for three products were obtained at 300 °C (a), 400 °C (b), and 500 °C (c) modified GCE in the solution of 1 mM  $\text{Fe}(\text{CN})_6^{3-/4-}$  containing 0.1 M KCl, inset: EIS characterization for different modified GCE. (B) CVs of the GCE before (a) and after modification with different volume ratio of  $\text{Co}_3\text{O}_4/\text{C}$  nanoparticles to CS in the composite membrane (b-d). (C) Histograms of oxidation peak current ( $I_{pa}$ ) of  $\text{Co}_3\text{O}_4/\text{C}$  for  $\text{NO}_2^-$  in the solution of PBS, NaOH, B-R and NaAc-HAc. (D) Histograms of oxidation peak current ( $I_{pa}$ ) of  $\text{Co}_3\text{O}_4/\text{C}$  for  $\text{NO}_2^-$  versus pH values of NaAc-HAc buffer.

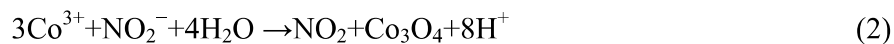
The experimental parameters are important factors for the sensitivity of the sensor, such as the volume ratio of  $\text{Co}_3\text{O}_4/\text{C}$  and CS, the species of the supporting electrolyte and its pH values. At the first, the conductivity of different volume ratio of  $\text{Co}_3\text{O}_4/\text{C}$  nanoparticles to CS in the composite film was investigated by CV analysis. The CVs of bare GCE (curve a) and the electrodes modified with mixture solution of  $\text{Co}_3\text{O}_4/\text{C}$  and CS at various volume ratio of 1:1 (curve b), 1:2 (curve c) and 1:3 (curve d) in the solution of 1.0 mM  $[\text{Fe}(\text{CN})_6]^{3-/4-}$  with 0.1 M KCl are showed in Fig. 2-1.4B, the redox peaks of bare GCE are lower than those on the other modified electrodes, indicating that the prepared nanocomposites have an excellent electrical conductivity. Relatively, the strongest current is observed at the modified electrode for the ratio of 1:2, suggesting that the volume of  $\text{Co}_3\text{O}_4/\text{C}$  to CS has the optimal electrocatalysis at this ratio.

The species of the supporting electrolyte and its pH values were further investigated. The histograms of the oxidation peak currents ( $I_{\text{pa}}$ ) of  $\text{Co}_3\text{O}_4/\text{C}$  for  $\text{NO}_2^-$  in various electrolytes including PBS, NaOH, B-R and NaAc-HAc are showed in Fig. 2-1.4C. It is found that, in comparison with PBS, NaOH and B-R supporting electrolytes at the same concentration and pH value, the largest  $I_{\text{pa}}$  is achieved in NaAc-HAc buffer. So, in the following experiment NaAc-HAc buffer is chosen as the supporting electrolyte. For the best sensing performance, the effect of the pH values of the buffer on the oxidation response of  $\text{NO}_2^-$  was explored. Fig. 2-1.4D displays the histograms of the oxidation peak currents ( $I_{\text{pa}}$ ) of the pH values of NaAc-HAc buffer ranging from 3.5 to 5.5 for  $\text{NO}_2^-$ . It is observed that current response of  $\text{NO}_2^-$  increases as pH value increases from 3.5 to 4.5 and then decreases at 5.0. The result of the low current response at low pH value may be due to unstableness of  $\text{NO}_2^-$  in a strongly acidic medium [36]. Accordingly, NaAc-HAc buffer of pH value 4.5 is chose as the optimal acidity.

### **2-1.3.3 Electrochemical behaviors of $\text{Co}_3\text{O}_4/\text{C}$ and its electrocatalytic toward $\text{NO}_2^-$**

Under the optimal conditions, the electrocatalytic capacity of  $\text{Co}_3\text{O}_4/\text{C}$  for  $\text{NO}_2^-$  was analyzed by CV and chronoamperometry (CA) technologies. Fig. 2-1.5 shows the CVs of GCE (A), CS/GCE (B), and  $\text{Co}_3\text{O}_4/\text{C}$ -CS/GCE (C) in NaAc-HAc buffer

without (a) and with (b) 1.0 mM  $\text{NO}_2^-$  and the electrocatalytical responses at different concentration of  $\text{NO}_2^-$  (D). For GCE and CS/GCE, it is found that when 1.0 mM  $\text{NO}_2^-$  was added into the blank NaAc-HAc buffer, the ignored oxidation current responses in CV are observed. This fact indicates that the GCE and the CS film have no electrocatalytic performance for  $\text{NO}_2^-$ . Interestingly, when  $\text{Co}_3\text{O}_4/\text{C-CS}/\text{GCE}$  is applied for  $\text{NO}_2^-$  oxidation (Fig. 2-1.5C), a remarkable irreversible oxidation current signal of  $\text{NO}_2^-$  appears, and meanwhile the responses gradually increase with increasing  $\text{NO}_2^-$  concentration (Fig. 2-1.5D). The changes suggest that the  $\text{Co}_3\text{O}_4/\text{C}$  has outstanding electrocatalysis activity for  $\text{NO}_2^-$  oxidation. According to previous report [37], the mechanism of electrochemical oxidation of  $\text{NO}_2^-$  on the prepared sensor can be described two steps including oxidation process and the rapid disproportionation process. The whole electrocatalytic process happening at the  $\text{Co}_3\text{O}_4/\text{C-CS}/\text{GCE}$  is proposed as follow:



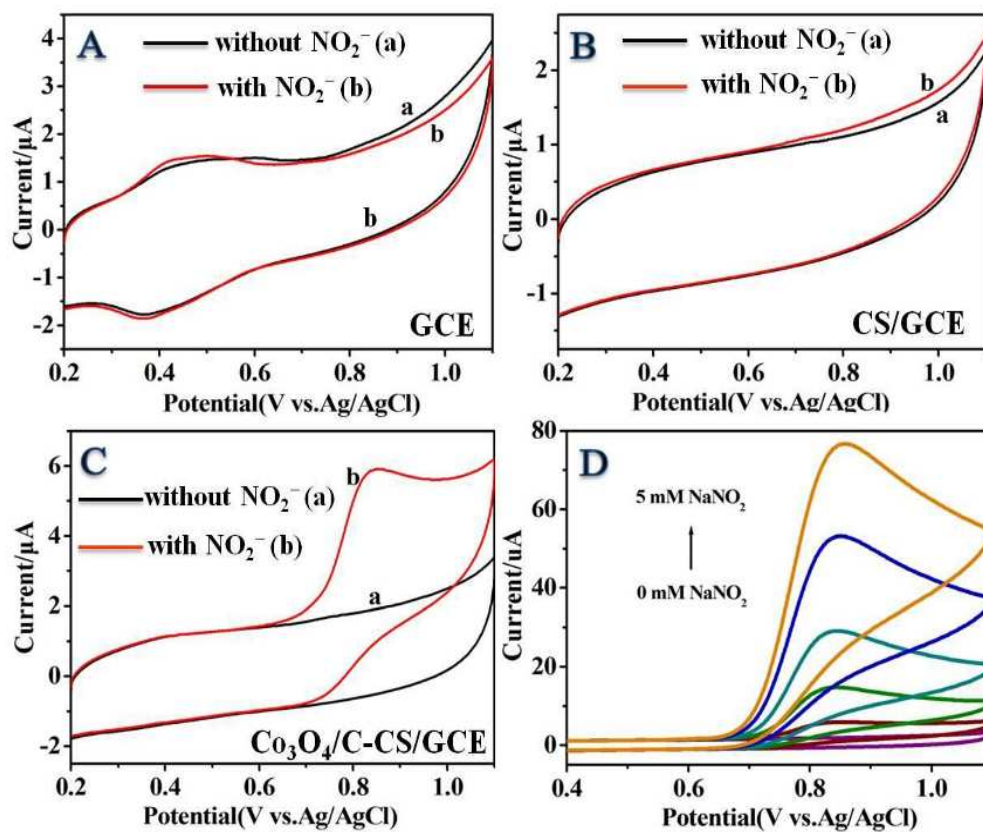


Fig. 2-1.5 CVs of GCE (A), CS/GCE (B), and  $\text{Co}_3\text{O}_4/\text{C-CS/GCE}$  (C) in NaAc-HAc (pH 4.5) buffer without (a) and with (b) 1.0 mM  $\text{NO}_2^-$ . (D)  $\text{Co}_3\text{O}_4/\text{C-CS/GCE}$  measured in NaAc-HAc (pH 4.5) containing various concentrations of  $\text{NO}_2^-$ .

The CV profiles of the Co<sub>3</sub>O<sub>4</sub>/C-CS/GCE at various scan rates are revealed in the supporting electrolyte with 0.2 mM NO<sub>2</sub><sup>-</sup> (Fig. 2-1.6A). It can be found that the oxidation responses for NO<sub>2</sub><sup>-</sup> linear increased with the square root of the scan rate (inset Fig. 2-1.6A), indicating the NO<sub>2</sub><sup>-</sup> oxidation procedure on the Co<sub>3</sub>O<sub>4</sub>/C-CS/GCE is controlled by the diffusion process [38].

By chronoamperometry (CA), the electrocatalytic parameter and electrochemical kinetic of Co<sub>3</sub>O<sub>4</sub>/C toward NO<sub>2</sub><sup>-</sup> were inspected. The CA curves of Co<sub>3</sub>O<sub>4</sub>/C-CS/GCE with various NO<sub>2</sub><sup>-</sup> concentrations ranging from 0 to 2.4 mM in NaAc-HAc (pH 4.5) are expressed in Fig. 2-1.6B. The linear of diffusion coefficient (*D*) for the catalytical current was calculated by the following Cottrell's equation:

$$I_{\text{cat}} = nFAD^{1/2}C_0\pi^{-1/2}t^{-1/2} \quad (4)$$

Where, *I*<sub>cat</sub> is the catalytical response for NO<sub>2</sub><sup>-</sup> at Co<sub>3</sub>O<sub>4</sub>/C-CS/GCE, *n* is number of electrons, *F* is Faraday constant, *A* is electrode area, and *t* is elapsed time. From the CA curves, *I*<sub>cat</sub> versus *t*<sup>-1/2</sup> plots were inferred and showed in Fig. 2-1.6C. According to Cottrell's equation, the average value of *D* for NO<sub>2</sub><sup>-</sup> was estimated to be 5.928×10<sup>-5</sup> cm<sup>2</sup> s<sup>-1</sup> in this system, which is similar to the theoretical value [39].

Meanwhile, the oxidation current is controlled by the electrocatalytic rate for NO<sub>2</sub><sup>-</sup> at intermediate time points. Accordingly, the catalytic rate constant (*K*<sub>cat</sub>) was determined using the equation [40]:

$$I_{\text{cat}}/I_L = (\pi K_{\text{cat}} C_0 t)^{1/2} \quad (5)$$

Where, *I*<sub>cat</sub> and *I*<sub>L</sub> are the responses with and without NO<sub>2</sub><sup>-</sup> on Co<sub>3</sub>O<sub>4</sub>/C-CS/GCE, respectively. Base on the slope of the *I*<sub>cat</sub>/*I*<sub>L</sub> versus *t*<sup>1/2</sup> plot (Fig. 2-1.6D), the value of *K*<sub>cat</sub> was determined as 1.02×10<sup>5</sup> M<sup>-1</sup> s<sup>-1</sup>, which is excellent than the previously studied results on Ag-AFS/GCE [41] and [Mn<sub>2</sub><sup>IV</sup>O<sub>2</sub>(phen)<sub>2</sub>(H<sub>2</sub>O)<sub>2</sub>]/Nafion/GCE [42], confirming that the Co<sub>3</sub>O<sub>4</sub>/C-CS has an outstanding electrocatalytic activity for NO<sub>2</sub><sup>-</sup>.

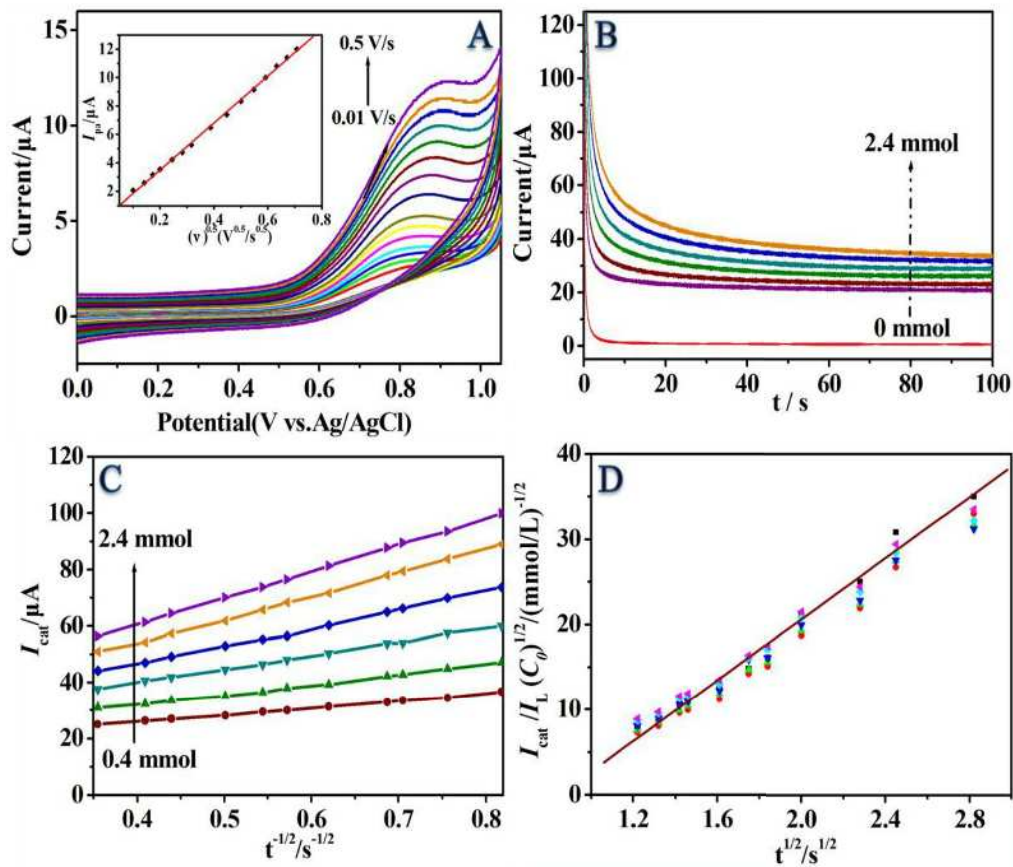


Fig. 2-1.6 (A) CV responses of the  $\text{Co}_3\text{O}_4/\text{C-CS}/\text{GCE}$  investigated in the buffer solution with 0.2 mM  $\text{NO}_2^-$  at various  $v$ . Inset: Plot of  $I_{pa}$  vs.  $v^{1/2}$ . (B) Chronoamperograms of  $\text{Co}_3\text{O}_4/\text{C-CS}/\text{GCE}$  without and with different  $\text{NO}_2^-$  concentrations in NaAc-HAc (pH 4.5) analyzed at 0.85 V. (C) Plots of  $I_{cat}$  vs  $t^{-1/2}$ . (D) Plot of  $I_{cat}/I_L$  vs.  $t^{1/2}$ .

### 2-1.3.4 Chronoamperometric detection of $\text{NO}_2^-$

As we all know that the applied potential is another key factor for the sensitivity and stability of sensors in chronoamperometry technology. Then, the optimal applied potential of the sensor for detecting  $\text{NO}_2^-$  is discussed in the following work. Under the various applied potentials, successive addition of  $\text{NO}_2^-$  in NaAc-HAc (pH 4.5), the  $I-t$  curves of  $\text{Co}_3\text{O}_4/\text{C-CS}/\text{GCE}$  are observed. From Fig. 2-1.7A, the slopes of the  $I-t$  curves increase with the potential increases from 0.65 to 0.85 V and then decreases at 0.90 V, suggesting the sensor has the optimal sensitivity at the applied potential of 0.85 V. At the optimal potential, a real-time amperometric  $I-t$  curve with unremitting injections of various concentrations of  $\text{NO}_2^-$  into NaAc-HAc (pH 4.5) on the biosensor of  $\text{Co}_3\text{O}_4/\text{C-CS}/\text{GCE}$  is presented in Fig. 2-1.7B. The inset a of the figure shows the enhancement of the catalytic current in the low concentration of  $\text{NO}_2^-$  on the sensor, testifying the excellent electrocatalytic performance of the nanocomposite. Meanwhile, inset b of the figure reveals the response attained maximum steady-state response within 3 s after injection of  $\text{NO}_2^-$ , suggesting the sensor has ultrafast electrocatalytic response for  $\text{NO}_2^-$ . The expression may be due to the speedy adsorption, penetration, and electrocatalytic reaction of sensing layer for  $\text{NO}_2^-$ . The corresponding calibration curve for  $\text{NO}_2^-$  is displayed in Fig. 2-1.7C. In the figure, two linear ranging from 2.0 nM to 1.0 mM and from 1.0 to 8.0 mM are obtained, respectively, and the ultralow limit of detection was identified to be 1.21 nM. The two regression equations for  $\text{NO}_2^-$  following:

$$I (\mu\text{A}) = 7.35C (\text{mM}) + 0.320 (r = 0.998)$$

$$I (\mu\text{A}) = 7.00C (\text{mM}) + 0.582 (r = 0.999)$$

From two regression equations, the sensor sensitivity of  $108.3 \mu\text{A cm}^{-2} \text{mM}^{-1}$  and  $108.0 \mu\text{A cm}^{-2} \text{mM}^{-1}$  were achieved at low and high concentration region, respectively. It can be found that the sensitivity is slightly superior at the low concentration, the reason of the phenomenon may be attributed to all  $\text{NO}_2^-$  on the sensor surface were catalyzed immediately because of abundant active sites at low concentration of  $\text{NO}_2^-$ , and lead to a higher sensitivity [26]. But with increasing the concentration, the catalytic process is changed to the coefficient of  $\text{NO}_2^-$  adsorption and catalytic activation on the sensor surface, then resulting in a lower sensitivity because of competitive effects [28]. Additionally, it is noted that the catalytic current

shows slightly unstable when the  $\text{NO}_2^-$  concentration was higher than 8 mM. The reason of the result is the high concentration of  $\text{NO}_2^-$  on the active sites of the sensor surface is saturated. Comparing with the previously reports, the analytical performance of the prospective sensor is superior and the comparative results are listed in Table 2-1.1. According the results, the excellent performance of the prepared sensor is explained by the following reasons: on the one hand the materials possess high catalytic performance and the excellent electronic conductivity for  $\text{NO}_2^-$  electro-oxidation. On the other hand, the porous structure of material leads to large surface area to improve the catalytic active site for  $\text{NO}_2^-$  on the sensing interface.

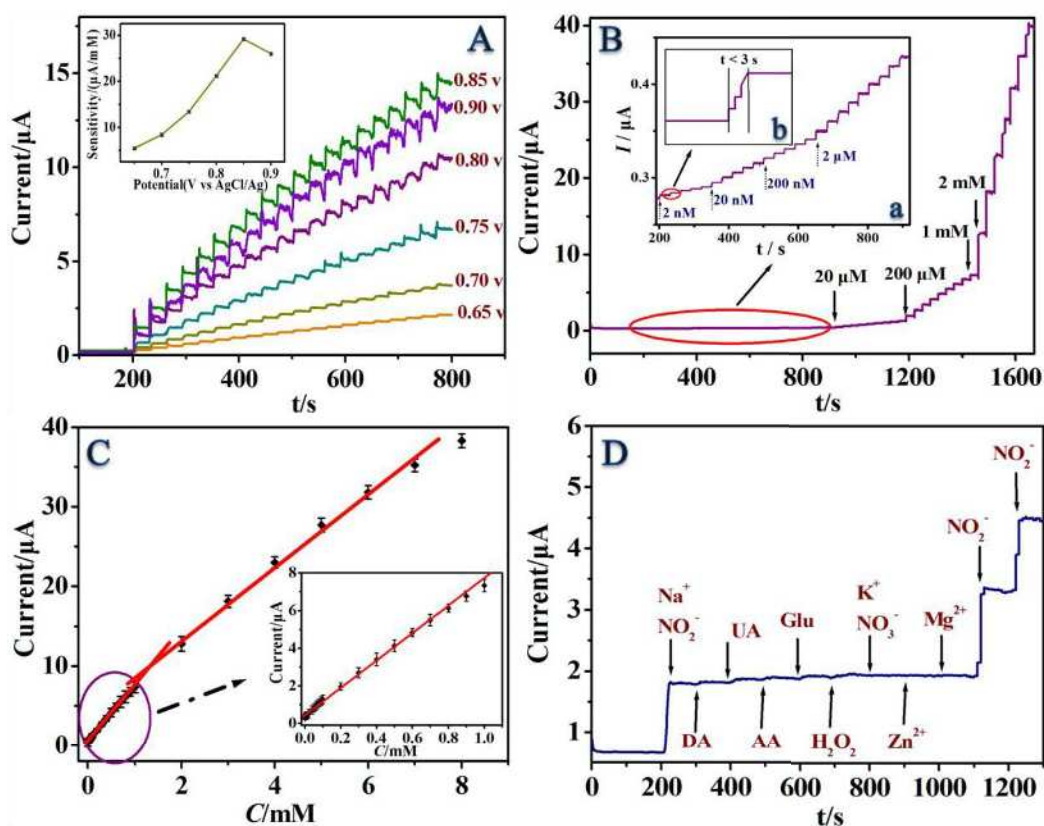


Fig. 2-1.7 (A) Chronoamperometric currents of the  $\text{Co}_3\text{O}_4/\text{C-CS}/\text{GCE}$  upon unremitting injections of  $0.05 \text{ mM NO}_2^-$  in  $\text{NaAc-HAc}$  ( $\text{pH } 4.5$ ) at various potentials. (B) Chronoamperometric responses of the  $\text{Co}_3\text{O}_4/\text{C-CS}/\text{GCE}$  upon unremitting injections of  $\text{NO}_2^-$  at the applied potential of  $0.85 \text{ V}$ . Inset a is the amplified  $I-t$  curve in the low concentration of  $\text{NO}_2^-$ . Inset b is response time of the sensor upon injection of  $\text{NO}_2^-$ . (C) Calibration plots for the  $\text{Co}_3\text{O}_4/\text{C-CS}/\text{GCE}$  with  $\text{NO}_2^-$  concentrations of  $2.0 \text{ nM}$  to  $1.0 \text{ mM}$  and  $1.0$  to  $8.0 \text{ mM}$ . The inset displays an amplified calibration curve with  $\text{NO}_2^-$  concentrations ranging from  $2.0 \text{ nM}$  to  $1.0 \text{ mM}$ . (D) Amperometric response of  $\text{Co}_3\text{O}_4/\text{C-CS}/\text{GCE}$  to  $0.05 \text{ mM NO}_2^-$  in the presence of  $0.1 \text{ mM DA}$ ,  $\text{UA}$ ,  $\text{AA}$ ,  $\text{Glu}$ ,  $\text{H}_2\text{O}_2$ ,  $\text{NO}_3^-$ ,  $\text{Na}^+$ ,  $\text{K}^+$ ,  $\text{Mg}^{2+}$ ,  $\text{Zn}^{2+}$ .

Table 2-1.1 Comparisons of Analytical Performance of  $\text{NO}_2^-$  on Electrode Modified with Different Materials<sup>a</sup>

Electrode	Technique	Detection limit (nM)	Linear range ( $\mu\text{M}$ )	Sensitivity ( $\mu\text{A } \mu\text{M}^{-1} \text{cm}^{-2}$ )	Refs.
MWCNTs–TiN/Cyt c	CA	1.4	1-2000	121.5	[43]
rGO/AgNPs/poly(PyY)	CA	12	0.1-1000	13.5	[44]
Cu-MOF/rGO	CA	33	3-40 000	43.74	[45]
Pd/RGO	CV	15.64	0.04-108	7.672	[46]
$\text{Fe}_2\text{O}_3$ /RGO	DPV	15	0.05-780	0.204	[47]
Au/MWCNT	DPV	0.01	0.05-250	2.5815	[48]
Au-Pd/rGO/GCE	CA	0.02	0.05-1000	-	[49]
$\alpha\text{-Fe}_2\text{O}_3$ NPs-ZnONRs	DPV	0.015	1-1250	131.2	[50]
$\text{Co}_3\text{O}_4$ /rGO	CA	140	1-380	-	[51]
$\text{CoO}_x$ /CNT	CA	300	0.5-250	-	[52]
$\text{Co}_3\text{O}_4$ /C	CA	1.21	0.002-8000	108.3	This work.

Cyt c: cytochrome c; PyY: pyronin Y.

### 2-1.3.5 Interference, Reproducibility and Stability Study

The excellent selectivity is also an important standard for the prospective sensor, the effect of disturbing species which possibly coexists with  $\text{NO}_2^-$  on the response of the sensor was assessed. Fig. 2-1.7D shows the interference measurement at the applied potential of 0.85 V with continuous additions of 0.05 mM  $\text{NO}_2^-$ , 0.1 mM dopamine (DA), 0.1 mM uric acid (UA), 0.1 mM ascorbic acid (AA), 0.1 mM glucose (Glu), 0.1 mM  $\text{H}_2\text{O}_2$ , 0.1 mM  $\text{KNO}_3$ , 0.1 mM  $\text{Mg}^{2+}$ , 0.1 mM  $\text{Zn}^{2+}$  and 0.05 mM  $\text{NaNO}_2$  in NaAc-HAc (pH 4.5) solution. Obviously, a clear  $I-t$  response increased is revealed by injection of 0.05 mM  $\text{NO}_2^-$  into the blank buffer solution. And comparison with the response of  $\text{NO}_2^-$ , the  $I-t$  responses of other interfering species on the sensor were negligible. This result confirmed that  $\text{Co}_3\text{O}_4/\text{C-CS}/\text{GCE}$  possesses great selectivity for the electrochemical detection of  $\text{NO}_2^-$  in a complicated environment.

In addition, the stability of the biosensor was inspected. The amperometric response of the assay stability is expressed in Fig. 2-1.8A. The result shows that still 81.6 % of the current response is kept over a long period of 10000 s, suggesting the stability is excellent in the assay process. Moreover, the prepared sensor was stored at ambient environment and monitored every other day via chronoamperometric method. The result (inset, Fig. 2-1.8A) shows that only 3.84% of the initial  $I-t$  response of the sensor toward  $\text{NO}_2^-$  was lost after 4 weeks, which confirms its qualified long-term stability. Subsequently, when five  $\text{Co}_3\text{O}_4/\text{C-CS}/\text{GCE}$  were prepared at the same conditions and used to detect 0.05 mM  $\text{NO}_2^-$ , the relative standard deviation (RSD) value was estimated to be 2.17% (Fig. 2-1.8B). As shown from inset in Fig. 8B, repeatability of the sensor was evaluated with one electrode detected 0.05 mM  $\text{NO}_2^-$  seven times, the RSD value of 2.09% was obtained. Therefore, all the results suggest the  $\text{Co}_3\text{O}_4/\text{C-CS}/\text{GCE}$  is reliable for  $\text{NO}_2^-$  sensing due to its excellent stability, reproducibility and repeatability. The excellent performance also meant that the prepared sensor is promising to be applied for monitoring  $\text{NO}_2^-$  in real samples.

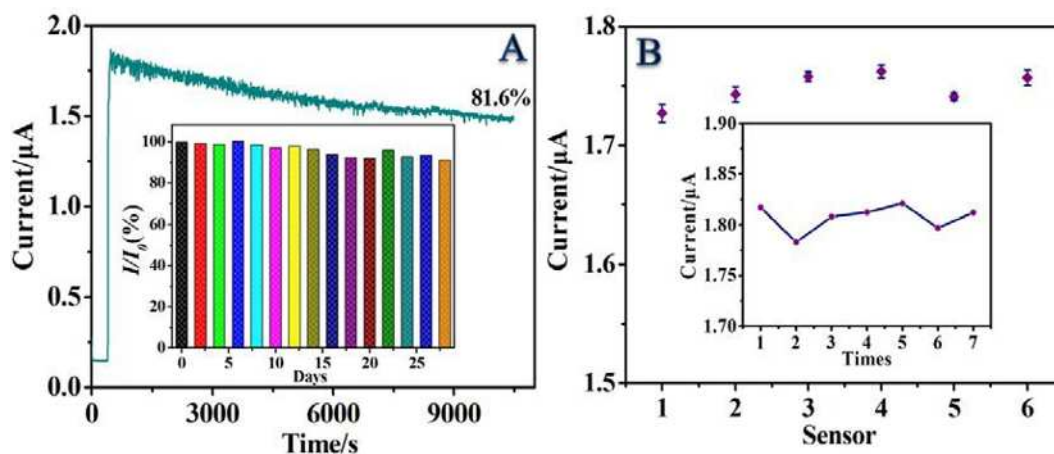


Fig. 2-1.8 (A) Amperometric current with 0.05 mM NO<sub>2</sub><sup>-</sup> over a long time-period of 10000 s. Inset: the stability of the sensor to NO<sub>2</sub><sup>-</sup> measured every other day for 4 weeks. (B) Reproducibility of five Co<sub>3</sub>O<sub>4</sub>/C-CS/GCEs for detection of 0.05 mM NO<sub>2</sub><sup>-</sup>. Inset: Repeatability of Co<sub>3</sub>O<sub>4</sub>/C-CS/GCE for detection 0.05 mM NO<sub>2</sub><sup>-</sup> seven times.

### 2-1.3.6 Real Sample Analysis

In order to verify the practicability of the sensor, the prepared sensor was utilized to monitor  $\text{NO}_2^-$  in real samples, including soil leaching liquid, macrophage supernate (nitrite is the main metabolism product of macrophage), using standard additions method. The diluted soil leaching liquid was added into the blank buffer, followed by standard concentration of  $\text{NO}_2^-$  was injected. Instead of soil leaching liquid, the same operation was performed for macrophage supernate. The amperometric curves are shown in Fig. 2-1.9, and according to the standard addition plot as depicted in the inset of Fig. 2-1.9, the content of  $\text{NO}_2^-$  in the soil leaching liquid and macrophage supernate were estimated to be 6.70 and 1.69  $\mu\text{M}$  by extrapolating the curve to  $y=0$ , respectively, which were close to the High performance ion chromatography (HPIC) results (6.49 and 1.62  $\mu\text{M}$ ). As shown in Table 2-1.2, the recovery values for three additions are between 97.8 and 102.2% for soil leaching liquid, 98.2 and 101.3% for macrophage supernate, respectively, suggesting the approach is feasible for detecting  $\text{NO}_2^-$  in complex environment.

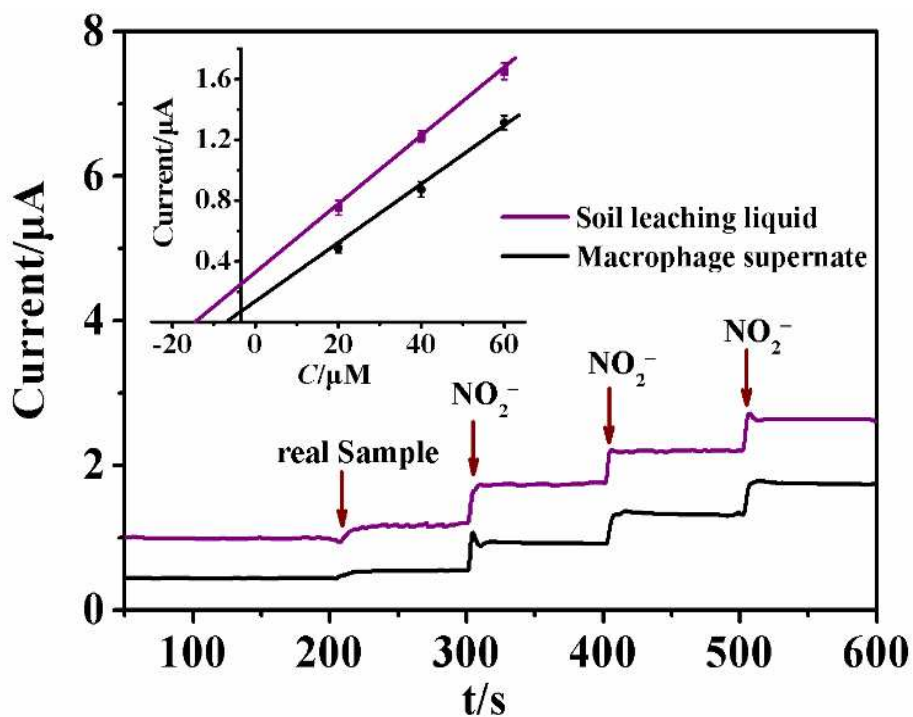


Fig. 2-1.9 Chronoamperometric responses recorded at  $\text{Co}_3\text{O}_4/\text{C-CS}/\text{GCE}$  upon injection of real samples and followed by continuous injections of  $0.02 \text{ mM NO}_2^-$  in HAc-NaAc (pH 4.5) buffer

Table 2-1.2 Recovery data for NO<sub>2</sub><sup>-</sup> determination in real samples on  
Co<sub>3</sub>O<sub>4</sub>/C-CS/GCE

Sample	Added ( $\mu\text{M}$ )	Found ( $\mu\text{M}$ )	Recovery (%)	RSD (%) (n=3)	HPIC ( $\mu\text{M}$ )	Er (%)
	0.00	6.70	-	1.92	6.49	+3.2
Soil leaching	20.00	20.44	102.2	3.41	-	-
liquid	40.00	39.11	97.8	2.17	-	-
	60.00	60.43	100.7	4.11	-	-
	0.00	1.69	-	2.49	1.62	+4.3
Macrophage	20.00	19.63	98.2	3.13	-	-
supernatant	40.00	40.51	101.3	2.51	-	-
	60.00	59.51	99.2	2.97	-	-

## 2-1.4 Conclusions

In summary, nanododecahedron porous  $\text{Co}_3\text{O}_4/\text{C}$  was synthesized by a simple method of calcining ZIF-67. The physical characterization was revealed by TEM, XRD, BET, XPS, and so on. The results testify that ZIF-67 acts as a key role in controlling the morphology of  $\text{Co}_3\text{O}_4$  particles and provides carbon source in the product at appropriate temperature. The fluffy and porous structure of  $\text{Co}_3\text{O}_4/\text{C}$  nanocomposite promotes the transport of  $\text{NO}_2^-$  within sensing interface and the high analytical performances for  $\text{NO}_2^-$  are ascribed the synergic effects of the high conductivity from carbon and the excellent electrocatalytic performance from  $\text{Co}_3\text{O}_4$ . Electrochemical assays demonstrate that the  $\text{Co}_3\text{O}_4/\text{C}$  nanocomposite owns outstanding performance for detecting  $\text{NO}_2^-$ , a wide linear range (from 2 nM to 8 mM) and the ultralow detection limit of 1.21 nM were obtained. In addition, the  $\text{Co}_3\text{O}_4/\text{C}$  expresses outstanding selectivity, sensitivity, and feasibility for detecting  $\text{NO}_2^-$  in the real samples.

## 2-1.5 References

- [1] Y. Haldorai, J. Y. Kim, A. E. Vilian, N. S. Heo, Y. S. Huh, Y. K. Han, *Sens Actuators B Chem.*, **227**, 92 (2016).
- [2] A. Butler, *J Ethnopharmacol.*, **167**, 105 (2015).
- [3] S. Chamandust, M. R. Mehrasebi, K. Kamali, R. Solgi, J. Taran, F. Nazari, M. J. Hosseini, *Int J Food Prop.*, **19**, 1983 (2016).
- [4] Y. Jiao, J. Yu, Y. Yang, *Water Sci. Technol.: Water Supply*, ws2017010 (2017).
- [5] Q. Wang, S. Ma, H. Huang, A. Cao, M. Li, L. He, *Food Control.*, **63**, 117 (2016).
- [6] R. K. Foreman, M. Segura-Noguera, D. M. Karl, *Mar Chem.*, **186**, 83 (2016).
- [7] H. Liu, K. Guo, J. Lv, Y. Gao, C. Duan, L. Deng, Z. Zhu, *Sens Actuators B Chem.*, **238**, 249 (2017).
- [8] Y. Wan, Y. F. Zheng, H. T. Wan, H. Y. Yin, X. C. Song, *Food Control.*, **73**, 1507 (2017).
- [9] S. Zhang, B. Li, Q. Sheng, J. Zheng, *J Electroanal Chem.*, **769**, 118 (2016).
- [10] M. A. Subhan, P. C. Saha, M. M. Rahman, J. Ahmed, A. M. Asiri, M. Al-Mamun, *New J. Chem.*, **42**, 872 (2018).
- [11] S. Selvarajan, A. Suganthi, M. Rajarajan, *Ultrason. Sonochem.*, **41**, 651 (2018).
- [12] H. Liu, L. Weng, C. Yang, *Microchim Acta.*, 1 (2017).
- [13] C. Gao, Q. Meng, K. Zhao, H. Yin, D. Wang, J. Guo, H. Zhao, *Adv Mater.*, **28**, 6485 (2016).
- [14] Q. Liao, N. Li, S. Jin, G. Yang, C. Wang, *ACS Nano.*, **9**, 5310 (2015).
- [15] X. Zhou, X. Shen, Z. Xia, Z. Zhang, J. Li, Y. Ma, Y. Qu, *ACS Appl Mater Interfaces.*, **7**, 20322 (2015).
- [16] C. Yan, G. Chen, X. Zhou, J. Sun, C. Lv, *Adv Funct Mater.*, **26**, 1428 (2016).
- [17] Y. Lü, W. Zhan, Y. He, Y. Wang, X. Kong, Q. Kuang, L. Zheng, *ACS Appl Mater Interfaces.*, **64**, 186 (2014).
- [18] X. Dong, Y. Su, T. Lu, L. Zhang, L. Wu, Y. Lv, *Sens Actuators B Chem.*, **258**, 349 (2018).
- [19] T. Zhu, J. S. Chen, X. W. Lou, *J Mater Chem.*, **20**, 7015 (2010).
- [20] B. Geng, F. Zhan, C. Fang, *J Mater Chem.*, **18**, 4977 (2008).
- [21] W. Du, R. Liu, Y. Jiang, *J Power Sources.*, **227**, 101 (2013).
- [22] J. Xiao, C. Chen, J. Xi, Y. Xu, F. Xiao, S. Wang, S. Yang, *Nanoscale.*, **7**, 7056

- (2015).
- [23] L. T. Anh, A. K. Rai, T. V. Thi, J. Gim, S. Kim, V. Mathew, J. Kim, *J Mater Chem A Mater.*, **2**, 6966 (2014)
- [24] T. Y. Ma, S. Dai, M. Jaroniec, S. Z. Qiao, *J. Am. Chem. Soc.*, **136**,13925 (2014).
- [25] Y. V. Kaneti, J. Tang, R. R. Salunkhe, X. Jiang, A. Yu, K. C. W. Wu, Y. Yamauchi, *Adv Mater.*, **29**, 1604898 (2017).
- [26] H. Yang, S. J. Bradley, A. Chan, G. I. Waterhouse, T. Nann, P. E. Kruger, S. G. Telfer, *J. Am. Chem. Soc.*, **138**, 11872 (2016).
- [27] R. Banerjee, A. Phan, B. Wang, C. Knobler, H. Furukawa, M. O'Keeffe, O. Yaghi, *Science*, **319**, 939 (2008) .
- [28] Q. Wang, Y. Yang, F. Gao, J. Ni, Y. Zhang, Z. Lin, *ACS Appl Mater Interfaces.*, **8**, 32477 (2016).
- [29] A. B. Fuertes, M. C. Arbestain, M. Sevilla, J. A. Maciá-Agulló, S. Fiol, R. López, F. Macias, *Soil Research.*, **48**, 618 (2010).
- [30] F. Meng, Z. Fang, Z. Li, W. Xu, M. Wang, Y. Liu, X. Guo, *J Mater Chem A Mater.*, **1**, 7235 (2013).
- [31] J. Tang, S. Wu, T. Wang, H. Gong, H. Zhang, S. M. Alshehri, Y. Yamauchi, *ACS Appl Mater Interfaces.*, **8**, 2796 (2016).
- [32] X. Qian, Q. Ren, X. Wu, J. Sun, H. Wu, J. Lei, *ChemistrySelect.*, **3**, 657 (2018).
- [33] T. Zhai, L. Wan, S. Sun, *Adv Mater.*, **29**,1604167 (2017).
- [34] L. An, W. Huang, N. Zhang, X. Chen, D. Xia, *J Mater Chem A Mater.*, **2**, 62 (2014).
- [35] Q. Pang, J. Tang, H. Huang, X. Liang, C. Hart, K. C. Tam, L. F. Nazar, *Adv Mater.*, **27**,6021 (2015).
- [36] M. Amjadi, J. Hassanzadeh, J. L. Manzoori, *Microchim Acta.*, **181**,851 (2014).
- [37] H. Kominami, K. Kitsui, Y. Ishiyama, K. Hashimoto, *RSC Adv.*, **4**,51576 (2014).
- [38] F. Gao, X. Cai, X. Wang, C. Gao, S. Liu, F. Gao, Q. Wang, *Sens Actuators B Chem.*, **186**,380 (2013).
- [39] C. W. Kung, T. H. Chang, L. Y. Chou, J. T. Hupp, O. K. Farha, K. C. Ho, *Electrochem commun.*, **58**,51 (2015).
- [40] S. A. Bhat, S. A. Pandit, M. A. Rather, G. M. Rather, N. Rashid, P. P. Ingole, M. A. Bhat, *New J. Chem.*, **41**,8347 (2017).
- [41] P. K. Sonkar, V. Ganesan, *J Solid State Electrochem.*, **19**,2107 (2015).

- [42] W. B. Machini, M. F. Teixeira, *Sens Actuators B Chem.*, **217**,58 (2015).
- [43] Y. Haldorai, S. K. Hwang, A. I. Gopalan, Y. S. Huh, Y. K. Han, W. Voit, K. P. Lee, *Biosens. Bioelectron.*, **79**,543 (2016).
- [44] K. Da ci, M. Alanyalıo lu, *ACS Appl Mater Interfaces.*, **8**, 2713 (2016).
- [45] M. Saraf, R. Rajak, S. M. Mobin, *J Mater Chem A Mater.*, **4**,16432 (2016).
- [46] Y. Zhang, Y. Zhao, S. Yuan, H. Wang, C. He, *Sens Actuators B Chem.*, **185**, 602 (2013).
- [47] S. Radhakrishnan, K. Krishnamoorthy, C. Sekar, J. Wilson, S. J. Kim, *Appl Catal B.*, **148**, 22 (2014).
- [48] A. Afkhami, F. Soltani-Felehgari, T. Madrakian, H. Ghaedi, *Biosens. Bioelectron.*, **51**, 379 (2014).
- [49] S. S. Li, Y. Y.Hu, A. J. Wang, X. Weng, J. R. Chen, J. J. Feng, *Sens Actuators B Chem.*, **208**, 468 (2015).
- [50] R. Ahmad, M. S. Ahn, Y. B. Hahn, *Adv Mater Interfaces.*, **4**, 1700691 (2017).
- [51] Y. Haldorai, J. Y. Kim, A. E. Vilian, N. S. Heo, Y. S. Huh, Y. K. Han, *Sens Actuators B Chem.*, **227**, 92 (2016).
- [52] Z. Meng, B. Liu, J. Zheng, Q. Sheng, H. Zhang, *Microchim Acta.*, **175**, 251 (2011).

**2-2 Synthesis of ZrO<sub>2</sub>/C using UiO-67 as template and its high sensitivity for heavy metal ions**

## 2-2.1 Introduction

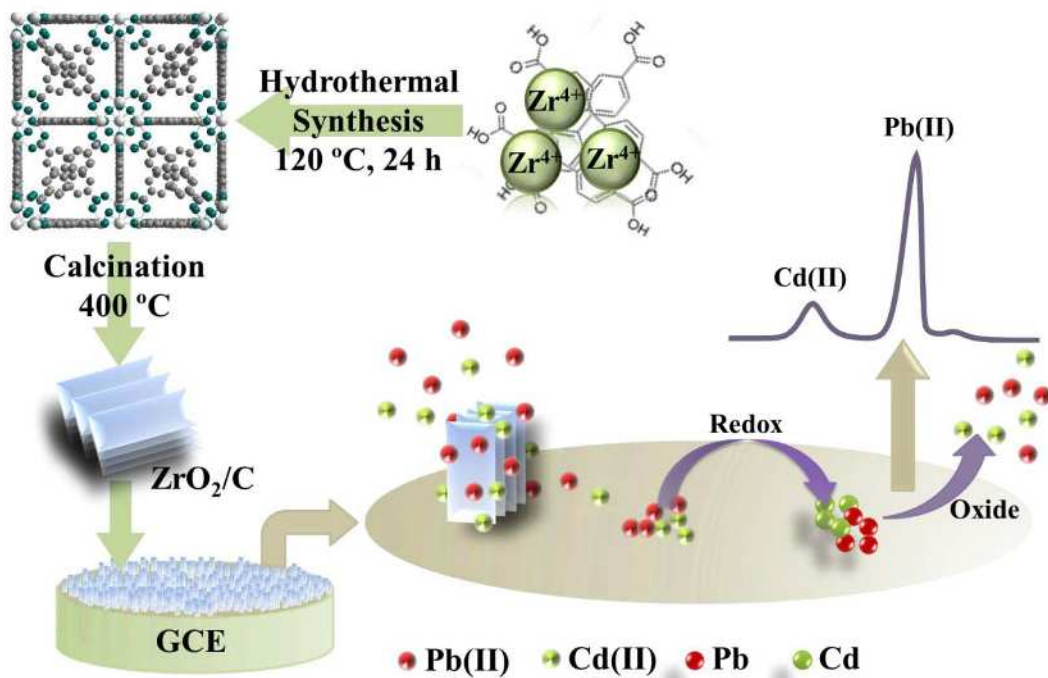
In many fields, heavy metal ions act important roles, including organometallic reactions, catalysis and biochemistry [1, 2]. However, when the concentration of heavy metals exceeds the natural levels, they will become toxic and then destroy the biological systems [3, 4]. The toxicity of heavy metal ions is mainly due to their tough and efficient coordination ability with bioactive groups. Lead ion (Pb(II)), the heavy metal ions that universally existed in agricultural and industrial wastewater, making a threat to living things and human beings [5, 6]. Cadmium ion (Cd(II)) was another lethal heavy metal ion towards bacteria and microorganisms, it causes severely environmental and health problems [7, 8]. Long-term touching high level concentration of Pb(II) and Cd(II) would cause a series of lesion, such as cancer, kidney disease, and imperceptible negative effects on intelligence and metabolism. Thus, it is urgently to search for a sensitive, rapid, and simple analytical method for monitoring heavy metal ions in food, supplies and biological systems.

So far, there are many proficient methods to detect heavy metal ions, such as atomic absorption spectroscopy (AAS) [9], inductively coupled plasma atomic emission spectrometry (ICP) [10], and inductively coupled plasma mass spectrometry (IC) [11]. However, these spectrometric methods are expensive and not suitable for in situ analysis due to the ponderous and complicated instruments [12]. On the contrary, the electrochemical method because of their excellent sensitivity, short analysis time, portability, and low-cost had been adopted as an efficient method to fast monitor heavy metal ions [13, 14]. In all the electrochemical methods, electrochemical different pulse anodic stripping voltammetry (DPASV) provided a powerful performance for the determination of heavy metal ions, it can realize simultaneously analyze concomitant heavy metal ions [15, 16]. The utilization of the nanomaterials modified electrodes amazing improves the efficiency of accumulating target analytes, and the development of high-performance electrode modified materials is very important to improve the sensitivity of electrochemical sensors [17, 18].

As is well-known, metal oxides, as high performance electrode materials, have attracted wide attention based on its many inherent advantages, including excellent electrocatalytic activity, good mechanical stability, large specific surface area and low-cost, and so on [19-21]. Zirconium dioxide ( $\text{ZrO}_2$ ) [22, 23], a kind of transition metal oxide, it has been widely applied in many fields due to its excellent chemical resistance, good mechanical strength, highly biocompatible and good thermal stability. It is widely used in many fields, including solid electrolyte [24], thermal barrier coating [25], electro-optic material and fuel cell technology [26, 27], biological sensor [28] and thermoluminescence UV dosimeter [29]. For example, M. Mansouri et al. [30] synthesized NiO-doped ZnO- $\text{ZrO}_2$  nanoparticles and applied it for the photocatalytic degradation of Reactive Blue 81 (RB81). Zhou and his coworker used  $\text{ZrO}_2$  as a bifunctional catalyst approach to improve the electrochemical activity of electrodes for the vanadium flow batteries (VFB) [31]. However,  $\text{ZrO}_2$  also presents some shortcomings, such as aggregation morphology, poor conductivity, *etc.* Therefore, it is urgent to develop a new strategy to improve the conductivity of  $\text{ZrO}_2$ , and enhance its specific surface area. In order to solve this problem, a novel synthesis method of using Zr-based MOFs as sacrificial template or precursor is proposed due to the advantages of MOFs, such as good porous structure, regular morphology and rich metal nodes. Therefore, a composite of  $\text{ZrO}_2$  and carbon nanocomposite ( $\text{ZrO}_2/\text{C}$ ) with controllable shape and excellent properties were obtained by calcining Zr-based MOFs at appropriate temperature [32, 33].

UiO-67 is a kind of Zr-based MOFs nanomaterial, it is obtained by connecting  $\text{Zr}_6\text{O}_4(\text{OH})_4$  inorganic cornerstones with 4,4'-biphenyl-dicarboxylate (BPDC) as linker. It has large pore size and high specific surface area attribute to its long linker of 4, 4'-biphenyldicarboxylate [34]. Using UiO-67 as a sacrificial template is expected to produce desired  $\text{ZrO}_2/\text{C}$  nanocomposite with high specific surface area and strong adsorption capacity. In this paper, a thin nanosheet structure of  $\text{ZrO}_2/\text{C}$  was prepared using UiO-67 with a flat cuboid structure as precursor. The peculiar and fluffy structures endowed materials with high surface areas that tremendously improved the adsorption capacity of electrode materials for detecting heavy metal ions. Thus, the

ZrO<sub>2</sub>/C as an ideal electrode material was applied to simultaneous detection of Pb(II) and Cd(II) in 0.1 M HAc-NaAc buffer by DPASV. Scheme 2-2.1 expresses the model of adsorption-release of the stripping behaviors for heavy metal ions on the nanomaterial modified electrode [20]. The results show that the developed sensor has excellent analytical performance for the simultaneous detection of two metal heavy ions. Furthermore, it was also successfully applied for the detection of trace Pb(II) and Cd(II) in real water samples with a satisfactory result.



Scheme 2-2.1 Schematic diagram for ZrO<sub>2</sub>/C synthesis and the adsorption-release model illustrating the electrochemical stripping behaviors

## 2-2.2 Experiment section

### 2-2.2.1 Reagents and apparatus

Potassium chloride (KCl), potassium ferricyanide ( $K_3Fe(CN)_6$ ), potassium ferrocyanide ( $K_4Fe(CN)_6$ ), magnesium nitrate ( $Mg(NO_3)_2$ ), sodium nitrate ( $NaNO_3$ ), potassium nitrate ( $KNO_3$ ), zinc nitrate ( $Zn(NO_3)_2$ ), nickel nitrate ( $Ni(NO_3)_2$ ), chromium nitrate ( $Cr(NO_3)_3$ ), iron nitrate ( $Fe(NO_3)_3$ ), barium nitrate ( $Ba(NO_3)_2$ ), calcium nitrate ( $Ca(NO_3)_2$ ), lead nitrate ( $Pb(NO_3)_2$ ), cadmium nitrate ( $Cd(NO_3)_2$ ), N,N-Dimethylformamide (DMF), formic acid and acetate buffer (HAc-NaAc) were obtained from Guangdong Xilong Chemical Co., Ltd. (China); zirconium tetrachloride ( $ZrCl_4$ ), 4,4-biphenyl dicarboxylic acid ( $H_2BPDC$ ) was provided by Aladdin Reagent Co., Ltd. (China). Nafion (5 wt.% solution in low aliphatic alcohols) was purchased from Aldrich (China). All aqueous solutions were prepared in ultrapure water, which was obtained from a Milli-Q water purifying system (18  $M\Omega \cdot cm$ ). All the chemicals were of analytical grade and used without further purification.

Powder X-ray diffraction (XRD) patterns of the materials were obtained from a Rigaku Miniflex-II diffractometer with a Ni-filtered Cu  $K\alpha$  radiation (30 kV and 15 mA, Japan). Nitrogen adsorption-desorption isotherms were determined by Belsorp-MAX (Japan). Morphology of the UiO-66 was recorded on JEOL JSM-5600F Field-Emission Scanning Electron Microscopy (SEM, Japan). Electrochemical measurements were carried out on a CHI 660E electrochemical analyzer (China) in connection with a conventional three-electrode system: a GCE ( $\Phi=3$  mm) modified with different materials was used as the working electrode, Ag/AgCl electrode as the reference electrode, and Pt wire as the counter electrode.

### 2-2.2.2 Synthesis of ZrO<sub>2</sub>/C nanomaterials

UiO-67 was synthesized via solvothermal reaction method [35]. ZrCl<sub>4</sub> (233.0 mg, 1.0 mmol) and H<sub>2</sub>BPDC (242.2 mg, 1.0 mmol) were dissolved in 15 mL N,N-dimethylformamide (DMF). The mixture solution was moved to a 30 mL vial and 7.0 mL formic acid was added to the reaction mixture. After brief sonication, the solution was heated at 120 °C for 24 h in oil bath to yield UiO-67 nanoparticles. After cooling to the room temperature, the resulting precipitate was washed with DMF and acetone several times and dried under vacuum at room temperature for 1 h. Then the obtained white powder was stirred in 100 mL dichloromethane (CH<sub>2</sub>Cl<sub>2</sub>) for 24 h to removal of residual DMF from UiO-67 holes. Finally, the cleaned product was filtered and washed with CH<sub>2</sub>Cl<sub>2</sub> several times and dried at 80 °C for 1 h in vacuum.

Then, as-prepared UiO-67 precursor was calcined at 400 °C in air for 3 h with a heating speed of 10 °C·min<sup>-1</sup>. As a result, the white powder was converted into the brown powder by calcination at 400 °C and the final product was named as ZrO<sub>2</sub>/C. In addition, in order to reveal the effect of calcination temperature on the morphology and properties of the product, calcination was also carried out at 200 °C, 300 °C, and 500 °C in air for 3 h, and the corresponding product was named as UiO-67-200, UiO-67-300, UiO-67-500.

### 2-2.2.3 Fabrication of the ZrO<sub>2</sub>/C/Nafion modified GCE

The ZrO<sub>2</sub>/C/Nafion composite was prepared by dispersing 1 mg of ZrO<sub>2</sub>/C into 1 mL water, obtained a homogeneous dispersion after sonicating at 100 W for 1 h. Then, 5 μL 90% Nafion solution was added into suspension with sonicating for 30 min, the composite of ZrO<sub>2</sub>/C/Nafion was obtained. Prior to modification, the bare GCE was polished to a mirror-like surface sequentially with 1.0, 0.3, and 0.05 μm α-Al<sub>2</sub>O<sub>3</sub> and then rinsed ultrasonically with water, ethanol, and water. After purification, the electrode was dried under a purity N<sub>2</sub> stream. Then, 10 μL of ZrO<sub>2</sub>/C/Nafion

suspension was dropped onto the electrode surface. After dryness at air temperature, the modified electrode was cautiously rinsed with water to remove loosely attached  $\text{ZrO}_2/\text{C}/\text{Nafion}$ . Thus, the composite of  $\text{ZrO}_2/\text{C}/\text{Nafion}$  modified GCE ( $\text{ZrO}_2/\text{C}/\text{Nafion}/\text{GCE}$ ) was obtained. For comparison, the UiO-67/Nafion, UiO-67-200/Nafion, UiO-67-300/Nafion, UiO-67-500/Nafion and Nafion modified GCE were prepared at the similar process.

#### **2-2.2.4 Electrochemical measurements**

Differential pulse anodic stripping voltammetry (DPASV) is normally used for the electrochemical monitoring of heavy metal ions under optimized conditions. Pb(II) and Cd(II) were deposited at the potential of  $-1.2$  V for 270 s by the reduction of Pb(II) and Cd(II) in 0.1 M NaAc-HAc buffer (pH 4.5), the anodic stripping (reoxidation of metal to metal ions) of electrodeposited metal was performed in the potential range of  $-1.0$  to  $-0.2$  V. In order to maintain the sensitivity of sensor, the modified electrode was regenerated in fresh stirred supporting electrolyte by electrolysis at  $+0.4$  V for 100 s after each measurement to remove the previous residual Pb and Cd from the electrode surface.

### **2-2.3 Results and discussion**

#### **2-2.3.1 Structure and morphologic characterization**

Fig. 2-2.1A shows the XRD patterns of UiO-67 nanoparticles. All of the diffraction peaks of UiO-67 are well consistently indexed to the simulated of UiO-67 [36], indicating the UiO-67 was successfully synthesized. For the sake of investigating the textural properties such as surface area and pore volume of UiO-67, the Brunner-Emmet-Teller (BET) surface area and pores volume measurements of the sample were identified by  $\text{N}_2$  adsorption-desorption isotherms. Fig. 2-2.1B shows the typical  $\text{N}_2$  adsorption-desorption isotherms at 77 K and the Barrett-Joyner-Halenda

(BJH) desorption pore size distribution of UiO-67. As can be seen that the material exhibits a typical type I curve, indicating that the presence of microporous in the sample. According to the corresponding pore size distribution curve and the crystal structure (inset of Fig. 2-2.1B), the pore size of the tetrahedral cages of 1.22 nm (violet ball) and the octahedral cages of 1.62 nm (green ball) was achieved, respectively, which is well corresponded to the previously reported results [37]. From the BET method, the specific surface area of the product was estimated to be 1350.07  $\text{m}^2\text{g}^{-1}$ , which suggests that the UiO-67 has high specific surface area.

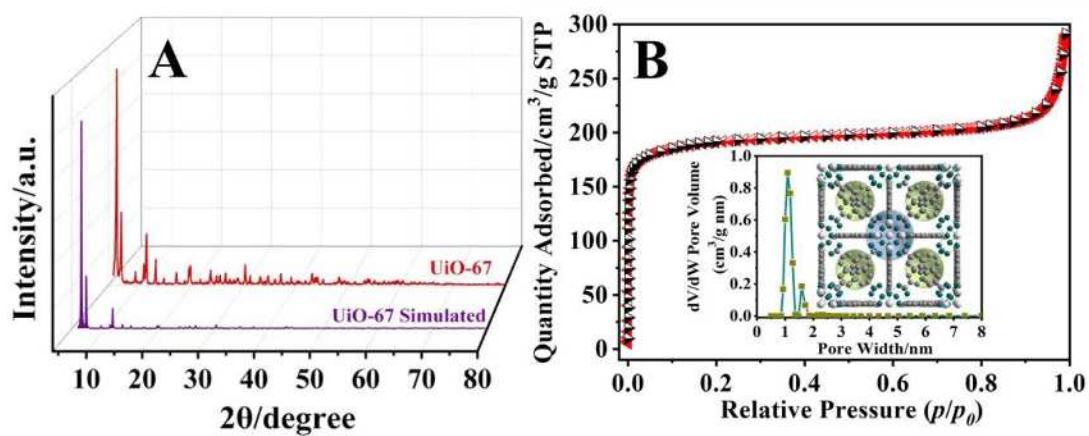


Fig. 2-2.1 (A) XRD pattern (A) and N<sub>2</sub> adsorption-desorption isotherms (B) of UiO-67 nanoparticles.

Fig. 2-2.2A displays the comparison of the XRD pattern between the UiO-67 and the calcined products of UiO-67 at different temperatures. From the results, the XRD pattern of the product calcined at 200 °C (curve b) is almost the same as that of UiO-67 (curve a), indicating that the crystal form of UiO-67 has no obvious change at low temperature. The XRD pattern shows that the crystal form of the calcined product changes with the increase of calcination temperature. At the calcination temperature of 300 °C, the obvious diffraction peak of UiO-67 disappears (curve c), indicating that the MOF structure of UiO-67 has gradually disintegrated during the calcination process. When the calcination temperature increase to 400 °C and 500 °C (curve d and curve e), all feature diffraction peaks of UiO-67 disappear, instead the intense diffraction peaks indexed to the (111), (200), (220), and (311) are observed, which is in well agreement with the indexed diffraction peak of ZrO<sub>2</sub> (PDF No.:49-1642), indicating that UiO-67 has been gradually transformed into ZrO<sub>2</sub> crystalline phase in high heating temperature. In addition, compared with the diffraction peaks of the calcined products obtained at 400 °C and 500 °C, respectively, more sharp and stronger diffraction peaks of the product obtained at high temperature can be observed. This result indicates that the higher the calcination temperature leads to larger crystal size and higher crystallinity of the material.

Fig. 2-2.2B displays the SEM image of the UiO-67 and a flat cuboid structure is observed. The obtained cuboid UiO-67 nanoparticle is about 2 μm, 1 μm and 100 nm in length, width and height, respectively, and the smooth surface is observed at any planes. The SEM images of the samples calcined at 200 °C, 300 °C, 400 °C and 500 °C show the influence of calcination temperature on the morphology of the product, and the results are displayed in Fig. 3-3.2C-F. As the UiO-67 was calcined at 200 °C, it can be obviously observed that the morphology of the produce hardly changes compare with that of UiO-67, indicating the low temperature is difficult to effect on the change of product morphology (Fig. 2-2.2C). When the material was treated at 300 °C, an obviously change exhibites, the side of the cuboid expands and splits into innumerable flakes (Fig. 2-2.2D). The calcination temperature further increases to 400 °C, it can be clearly found that the cuboid structure of the material is

obviously cracked into a thin sheet and a fluffy structure was achieved (Fig. 2-2.2E). The result suggests that the fluffy structure was obtained when the enough gases release from the MOF at the appropriate decomposition temperature of UiO-67 [38]. However, when the material was treated at 500 °C, the fluffy structure disappear, it can be found that all the flakes melt into blocks at high temperature (Fig. 2-2.2F).

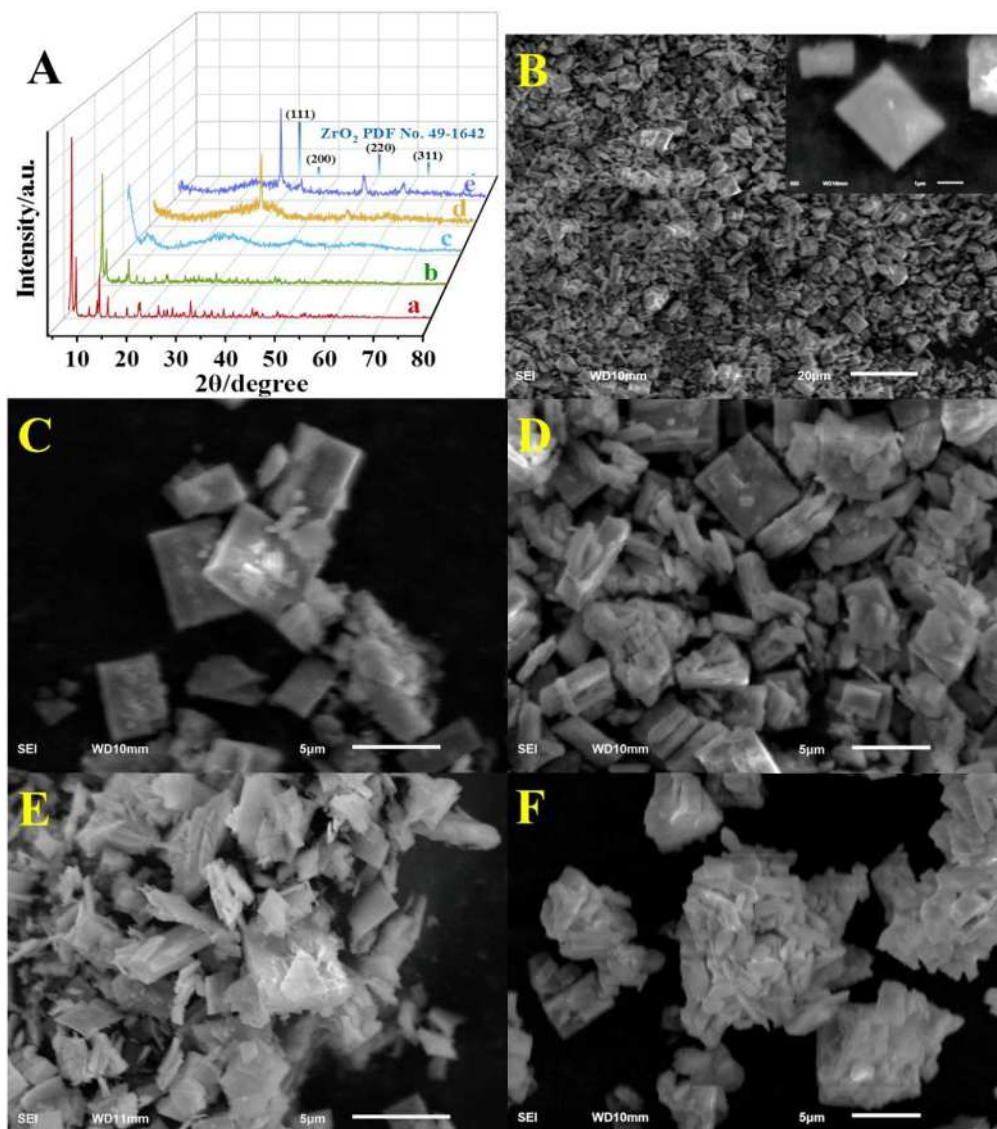


Fig. 2-2.2 (A) XRD pattern of UiO-67 (a), UiO-67-200 (b), UiO-67-300 (c), ZrO<sub>2</sub>/C (d), UiO-67-500 (e) and SEM images of UiO-67 (B), UiO-67-200 (C), UiO-67-300 (D), ZrO<sub>2</sub>/C (E), UiO-67-500 (F).

The chemical elemental composition and the surface electronic state of ZrO<sub>2</sub>/C were investigated through XPS characterization and the results are showed in Fig. 2-2.3. From the complete XPS spectrum (Fig. 2-2.3A), it can be found that the presence of Zr, C and O on the surface of the material. Fig. 2-2.3B shows the Zr 3d spectrum of ZrO<sub>2</sub>/C nanosheet. Two binding energies at 182.3 and 184.7 eV are observed, which are consistent with the peaks corresponding to Zr 3d<sub>3/2</sub> and Zr 3d<sub>5/2</sub> spin-orbit of ZrO<sub>2</sub>, respectively. The binding energy at 184.7 eV is identified as Zr-O bonding, and the peak locates at 182.3 eV corresponds to the chemical bond of the compound between Zr, C and O elements [39]. In figure 2-2.3C, two binding energies are observed in the C 1s spectrum. The peak at 284.7 eV is attributed to C–C bond, and the binding energy at 289.0 eV confirmed to C-O bonding, it may be derived from the structural defects on the edge of unsaturated carbon at high temperature or the residues of carboxyl groups in intermediates. The O 1s spectrum expresses two features in ZrO<sub>2</sub>/C composites (Fig. 2-2.3D). The feature peak at 530.1 eV is considered to be the Zr-O bonds, and the binding energy of O 1s at 531.7 eV is assigned to C-O bonding.

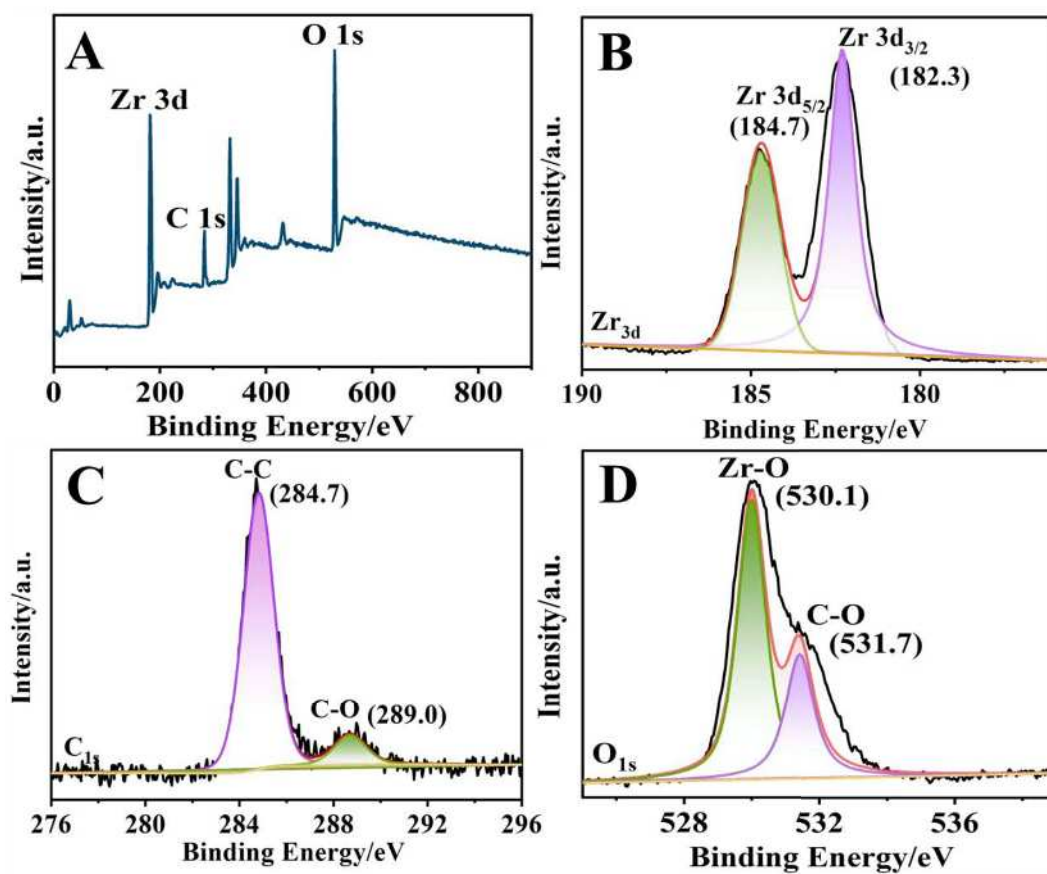


Fig. 2-2.3 (A) Full XPS spectrum of  $\text{ZrO}_2/\text{C}$  prepared at  $400\text{ }^\circ\text{C}$ . Result of curve fitting of (B) Zr 3d, (C) C 1s, and (D) O 1s spectra.

### 2-2.3.2 Electrochemical stripping voltammetric behaviour of the different electrodes

Fig. 2-2.4A presents the DPASV analytical characteristics of the 1.0  $\mu\text{M}$  each of Pb(II) and Cd(II) on bare (a), Nafion (b), UiO-67-200/Nafion (c), UiO-67-300/Nafion (d),  $\text{ZrO}_2/\text{C}/\text{Nafion}$  (e), UiO-67-500/Nafion (f), and UiO-67/Nafion (g) modified GCE in 0.1 M HAc-NaAc buffer (pH 4.5). The inconspicuous peaks are observed on bare GCE (curve a) in the potential range of  $-1.0$  to  $-0.2$  V, when the exploration process was executed for 60 s at  $-1.0$  V in buffer solution. On the contrary, the various DPASV responses for target metal ions were obtained on the different modified GCE. Obviously, compared to other modified electrodes, the sharpest and the highest peak currents for two target metal ions are observed on the  $\text{ZrO}_2/\text{C}/\text{Nafion}/\text{GCE}$  (curve e), which is attributed to the strong adsorption ability of  $\text{ZrO}_2/\text{C}$  with fluffy structure and the synergistic effect between  $\text{ZrO}_2$  and carbon effectively promotes the electron transfer. Two strong peaks at the potential of  $-0.54$  V and  $-0.78$  V are observed, respectively, which can be attributed to the stripping process of reduced Pb(II) and Cd(II) based on the peak potentials. The sufficient distance between the stripping peaks of the two ions also indicates that the two ions can be detected simultaneously without interfering with each other. So, the  $\text{ZrO}_2/\text{C}/\text{Nafion}/\text{GCE}$  was chosen as an effective platform for simultaneous detection of Pb(II) and Cd(II) in the following experiment based on the high surface area and the fluffy structure of the  $\text{ZrO}_2/\text{C}$  and the film formation of Nafion. Fig. 2-2.4B displays the histogram of stripping peak currents ( $I_p$ ).

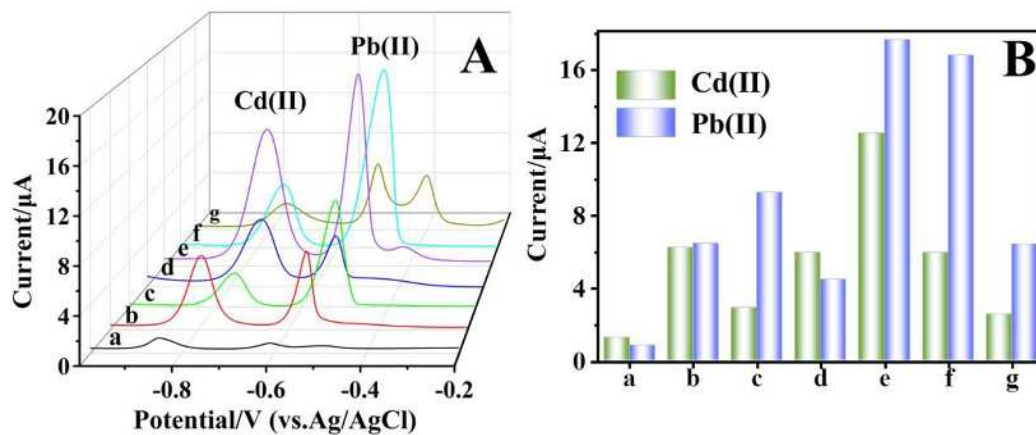


Fig. 2-2.4 DPASV responses (A) and histogram of stripping peak currents ( $I_p$ ) (B) for 1.0  $\mu\text{M}$  each of Pb(II) and Cd(II) on bare (a), Nafion (b), UiO-67-200/Nafion (c), UiO-67-300/Nafion (d), ZrO<sub>2</sub>/C/Nafion (e), UiO-67-500/Nafion (f), and UiO-67/Nafion (g) modified GCE in 0.1 M HAc-NaAc buffer (pH 4.5).

### 2-2.3.3 Optimization of experimental conditions

In order to obtain maximum detection sensitivity for trace heavy metal ions with ZrO<sub>2</sub>/C/Nafion/GCE, the voltammetric parameters (pH value, deposition potential, and deposition time) were optimized in 0.1 M HAc-NaAc buffer containing 1.0 μM Pb(II) and Cd(II). The pH value is one of the important assay factors, thus, it was necessary to select a proper pH value to carry out the following experiment. In order to avoid the hydrolysis of metal ions, the weak acid solution was selected. The influence of pH value on voltammetric response was investigated in the pH range from 3.5 to 5.5 in 0.1 M HAc-NaAc buffer. As shown in Fig. 2-2.5A, with the pH changes from 3.5 to 4.5, the peak current for Pb(II) and Cd(II) both increase, the maximum response was obtained at pH 4.5. When the pH value increase to 5.0, the stripping peak current of Pb(II) and Cd(II) both declined violently. So, pH 4.5 in 0.1 M HAc-NaAc buffer was selected for the stripping measurements.

In the stripping voltammetry analysis, the choice of the optimal deposition potential was vital to achieve the best sensitivity. Then, the influence of the deposition potential on the peak current after 60 s accumulation was investigated in the potential range from -1.3 to -0.7 V in 0.1 M HAc-NaAc buffer (pH 4.5), the results were shown in Fig. 2-2.5B. With the deposition potential shifted from -1.3 to -0.7 V, the peak currents for Pb(II) and Cd(II) increase at first and then decrease, and a maximum response is obtained at potential -1.2 V. And then when deposition potentials exceed -1.3 V was employed, a descending tendency on the response was observed for both Pb(II) and Cd(II). Thus, -1.2 V was chosen as the optimal deposition potential for the subsequent experiment.

The deposition time is another important factor about the sensitivity of the detection for heavy metal ions. So, the optimum deposition times were also explored and the variety of peak currents on the deposition time for two target metal ions was described in Fig. 2-2.5C. With the extension of deposition time from 30 s to 270 s, the signal of the stripping peak currents of Pb(II) and Cd(II) slowly increase. For the stripping peak

currents of Pb(II) enhanced with the increase of the deposition time varying from 30 up to 240 s and then followed a descending trend. While the time extends to 270 s, the stripping peak current of Cd(II) reaches to a constant. Attribute to the ideal deposition time of two metals, 240 s was chosen as the optimum deposition time.

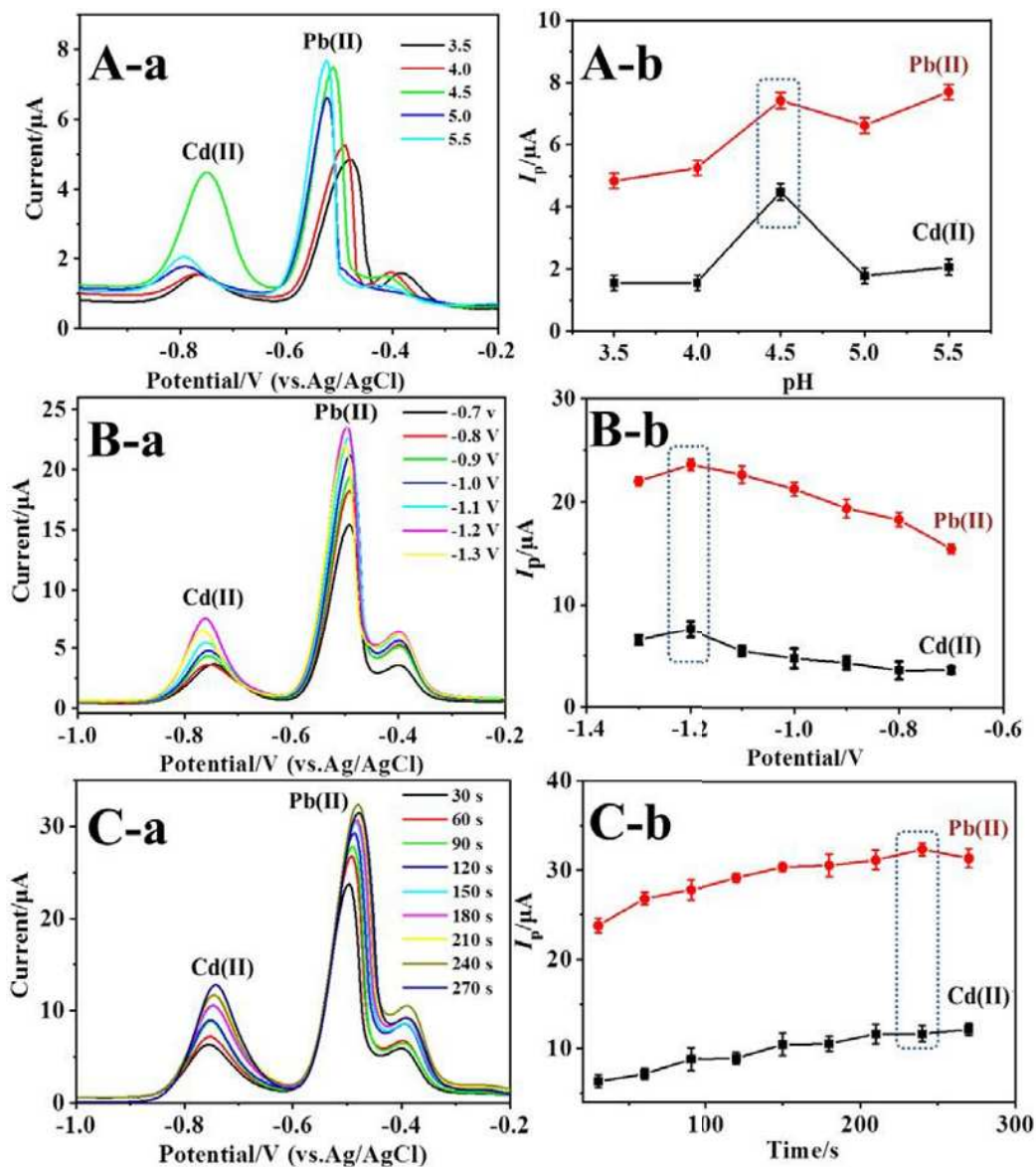


Fig. 2-2.5 The DPASV responses (a) and point plots of stripping peak currents ( $I_p$ ) (B) of pH value of 0.1 M HAc-NaAc buffer (A), deposition potential (B), and deposition time (C) of the  $ZrO_2/C/Nafion/GCE$  for 1.0  $\mu$ M each of Pb(II) and Cd(II).

#### **2-2.3.4 Simultaneous determination of Pb(II) and Cd(II) using ZrO<sub>2</sub>/C/Nafion/GCE**

Under the optimal experimental conditions, the quantitative analysis of Pb(II) and Cd(II) were determined simultaneously on the ZrO<sub>2</sub>/C/Nafion/GCE by DPASV. However, mutual interference between the metal ions is a common problem existing in detection of several metal ions simultaneously. Thus, the mutual interferences between Pb(II) and Cd(II) at the sensor of ZrO<sub>2</sub>/C/Nafion/GCE were discussed before the quantitative analysis. When maintain the concentration of Cd(II) at 0.5 μM but increasing the concentration of Pd(II) from 0.1 to 1.2 μM, seen from Fig. 2-2.6A, the stripping peak current of Pd(II) gradually increased with increasing the concentration of Pd(II), while the peak current of Cd(II) only tiny increasing. Similarly, the responses of Cd(II) linearly increase with its concentration increase from 0.1 to 1.2 μM in the presence of 0.5 μM Pb(II), and the peak current of Pb(II) also slight increasing (Fig. 2-2.6B), this result may be due to the formation of Pb-Cd intermetallic film during the deposition process, which increases the sensitivity for Pb(II) [40]. When the concentration of Cd(II) reaches to a certain high value, the peak current of Pb(II) tendes to stability, this result might be due to the advantage of competition absorption for high concentration of Cd(II) was dominated at the moment. Thus, all the results testify that the formation of Pb-Cd intermetallic film slightly improves the sensitivity for heavy metal ions, but no mutual interference between Pb(II) and Cd(II) exists on the ZrO<sub>2</sub>/C/Nafion/GCE when the simultaneous detection for two target metal ions.

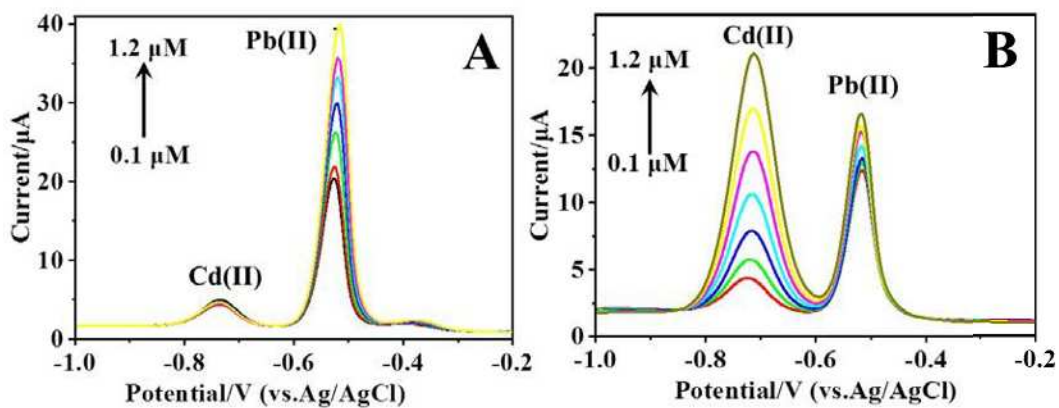


Fig. 2-2.6 DPASV response of the ZrO<sub>2</sub>/C/Nafion/GCE at 0.1, 0.2, 0.4, 0.5, 0.8, 1.0 and 1.2 μM Pb(II) in the presence of 0.5 μM Cd(II) (A), and 0.1, 0.2, 0.4, 0.5, 0.8, 1.0 and 1.2 μM Cd(II) in the presence of 0.5 μM Pb(II) (B) in 0.1 M HAc-NaAc buffer (pH 4.5).

The results of simultaneously analyzing of Pb(II) and Cd(II) were shown in Fig. 2-2.7A, and the diacritical stripping peaks at potentials of  $-0.54$  and  $-0.73$  V for Pb(II) and Cd(II) were discovered for both target metal ions, respectively. Fig. 2-2.7A shows the DPASV response for Pb(II) and Cd(II) at different concentrations. A well-defined peaks increase for Pb(II) is observed at potentials of approximately  $-0.54$  V with increasing the concentration of the metal ions from  $0.01 \mu\text{M}$  to  $2.0 \mu\text{M}$ . The regression equation of  $I_{pa}/\mu\text{A}=60.6C/\mu\text{M}+0.868$  at low concentrations (from  $0.01 \mu\text{M}$  to  $0.1 \mu\text{M}$ ) and  $I_{pa}/\mu\text{A}=22.4C/\mu\text{M}+8.365$  at high concentration (from  $0.2 \mu\text{M}$  to  $2.0 \mu\text{M}$ ) are displayed in Fig. 2-2.7B, and the correlation coefficient of  $0.992$  and  $0.998$  were achieved, respectively. And the limit of detection for Pb(II) of  $0.007 \mu\text{M}$  was identified ( $\sigma=3$ ). Meanwhile, the distinct peak current of Cd(II) was detected at potentials of approximately  $-0.73$  V, and the peak signal is proportional increased to the concentration of Cd(II) from  $0.05 \mu\text{M}$  to  $5.0 \mu\text{M}$  (Fig. 2-2.7B). The regression equations for Cd(II) were  $I_{pa}/\mu\text{A}=10.7C/\mu\text{M}+0.767$  at low concentrations (from  $0.05 \mu\text{M}$  to  $1.0 \mu\text{M}$ ) and  $I_{pa}/\mu\text{A}=6.48C/\mu\text{M}+6.42$  at high concentration (from  $1.5 \mu\text{M}$  to  $5.0 \mu\text{M}$ ), with the corresponding correlation coefficients of  $0.991$  and  $0.998$ , respectively. And the limit of detection for Cd(II) was estimated to be  $0.019 \mu\text{M}$  ( $\sigma=3$ ). As a summary,  $\text{ZrO}_2/\text{C}/\text{Nafion}/\text{GCE}$  displays a low detection limit of  $0.019 \mu\text{M}$  for Cd(II) and  $0.007 \mu\text{M}$  for Pb(II), which are lower than the respective values of  $3 \text{ ppb}$  ( $0.027 \mu\text{M}$ ) and  $10 \text{ ppb}$  ( $0.048 \mu\text{M}$ ) in drinking water permitted by the World Health Organization (WHO). The analytical performance of the sensor has been compared with many materials in electrochemical detection for Pb(II) and Cd(II) were listed in Table 2-2.1.

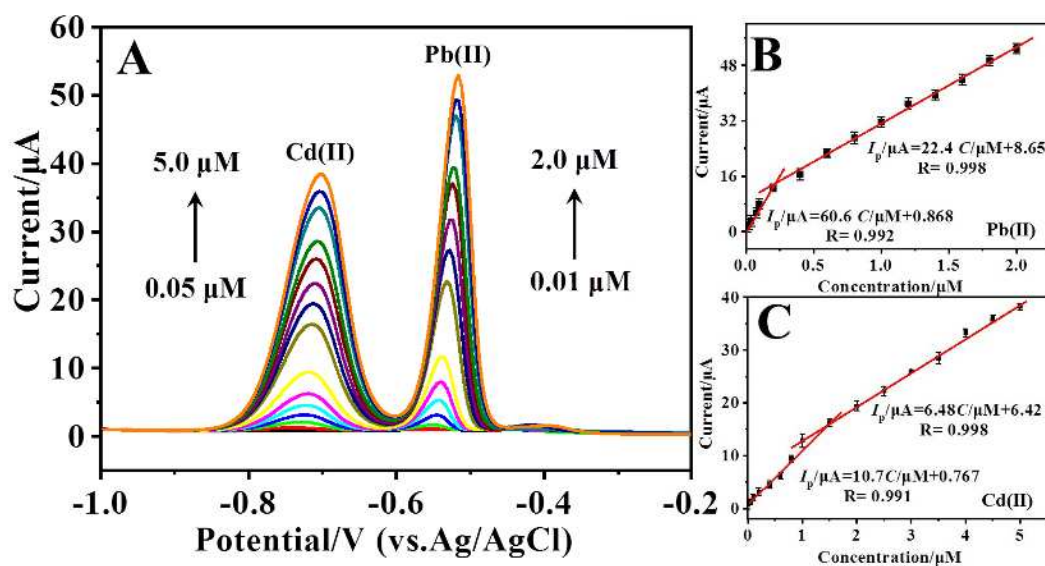


Fig. 2-2.7 (A) DPASV response for the simultaneous analysis of Pb(II) and Cd(II) in the different concentration from 0.01 to 2.0 μM and 0.05 to 5.0 μM on ZrO<sub>2</sub>/C/Nafion/GCE in 0.1 M HAc-NaAc buffer (pH 4.5), (B) The calibration curves of Pb(II), (C) the calibration curves of Cd(II).

Table 2-2.1 Comparison of the proposed sensors for the determination of Pb(II) and Cd(II).

Electrode	Method	Linear ranges ( $\mu\text{M}$ )	Determination limit( $\mu\text{M}$ )	Reference
Nafion/AuNPs-CD-GS/GCE	DPV	Pb(II) 0.19–5.8	0.051	[41]
		Cd(II) 0.36–10.7	0.27	
BiONPs-CS-GCE	DPASV	Pb(II) 0.4–2.8	0.15	[42]
		Cd(II) 0.8–5.6	0.05	
NiO/GCE	SWASV	Pb(II) 0.2–1.2	0.08	[43]
		Cd(II) 0.2–1.2	0.07	
BOC/GCE	SWASV	Pb(II) 0.048–0.24	0.019	[44]
		Cd(II) 0.089–0.44	0.038	
GC/ErGO/GCE	SWASV	Pb(II) 0.072–0.51	0.072	[45]
		Cd(II) 0.134–0.94	0.134	
GCE/SWCNTs/Biomass	DPASV	Pb(II) 0.02–2.0	0.01	[46]
		Cd(II) 0.2–0.99	0.1	
ZrO <sub>2</sub> /C/Nafion/GCE	DPASV	Pb(II) 0.001–7.0	0.007	This work.
		Cd(II) 0.001–5.0	0.019	

Notes: AuNPs: gold nanoparticles; CD: cyclodextrin; GS: graphene; DPV: differential pulse voltammetry; CS: chitosan; DPASV: differential pulse anodic stripping voltammetry; SWASV: square wave anodic stripping voltammetry; BOC: bismuth oxycarbide; ErGO: electrochemically reduced graphene; SWCNT: single walled carbon nanotubes.

### 2-2.3.5 Evaluation of selectivity and stability

In order to investigate the selectivity of the sensor for Pb(II) and Cd(II) simultaneous detection under the optimized conditions. The interference study was carried out by adding some possible interfering metal ions, including Na(I), K(I), Zn(II), Ni(II), Cr(II), Fe(III), Ba(II), and Ca(II) in 5 fold excess with analytes, into a standard solution containing 1  $\mu\text{M}$  Pb(II) and 2.5  $\mu\text{M}$  Cd(II) ions, the DPASV responses are shown in Fig. 2-2.8A. Fig. 2-2.8B shows the signals change on the histogram of stripping peak currents ( $I_p$ ) were within  $\pm 7.6\%$  for two metal ions. The results indicated that this prepared sensor has satisfactory selectivity.

The stability of ZrO<sub>2</sub>/C/Nafion/GCE was investigated in repetitive experiment for 14 times by DPASV. The DPASV responses of 0.5  $\mu\text{M}$  Pb(II) and Cd(II) on the sensor after 14 successive scans were shown in Fig. 2-2.8C. The results show that the stripping peak currents on ZrO<sub>2</sub>/C/Nafion/GCE were nearly steady and relative standard deviation (RSD) values of 3.96 % and 2.67% for Pb(II) and Cd(II) were achieved, respectively (Fig. 2-2.8D). All of results indicate that ZrO<sub>2</sub>/C/Nafion/GCE exhibits excellent selectivity and stability for the target metal ions determination.

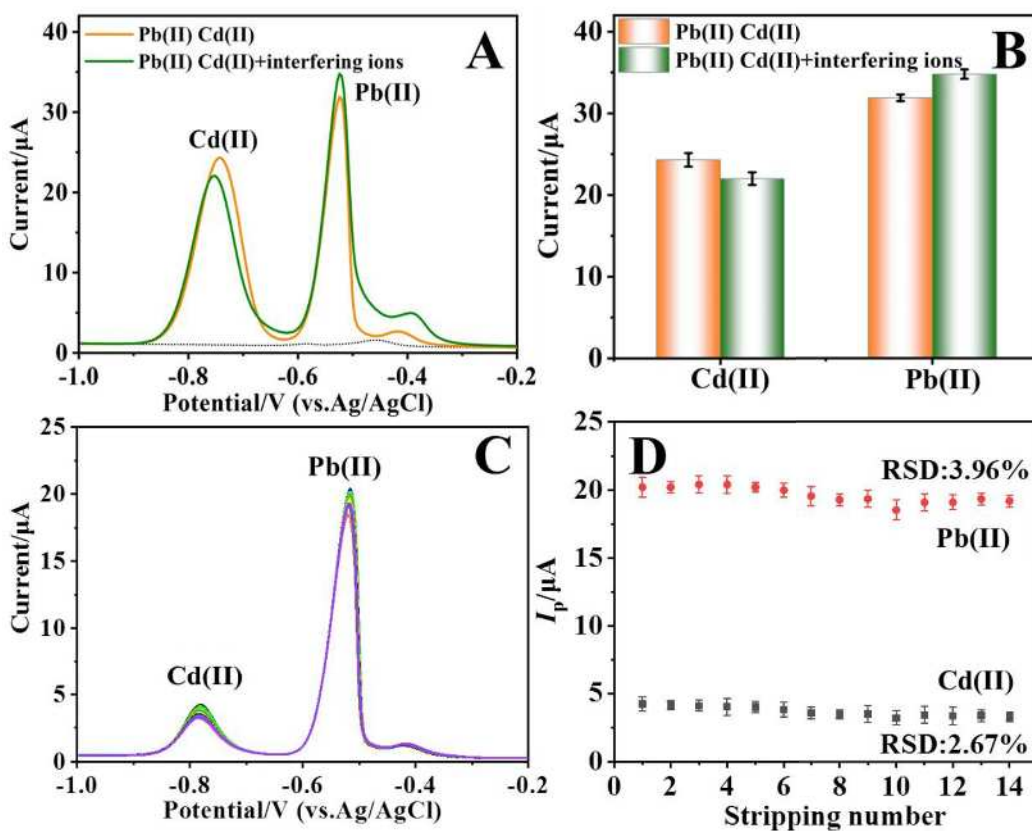


Fig. 2-2.8 DPASV responses (A) and histogram of stripping peak currents ( $I_p$ ) (B) of interference experiments for simultaneous detection of Pb(II) and Cd(II) without (curve orange) and with (curve green) different metal ions (5-fold concentration) under optimal conditions. DPASVs responses (C) and the point plot of stripping peak currents ( $I_p$ ) (D) for simultaneous detection of 0.5  $\mu\text{M}$  Pb(II) and Cd(II) on the  $\text{ZrO}_2/\text{C}/\text{Nafion}/\text{GCE}$  in 0.1 M HAc-NaAc buffer (pH 4.5)

### 3-3.3.6 Real sample analysis

For the purpose of practical application of the prospective electrode, an application on real water sample had been executed. The standard addition method was adopted to simultaneously determine Pb(II) and Cd(II) in three different real water samples. Fig. 2-2.9 shows the detection results of three different real water samples. It can be found that when the real sample was injected into the blank solution, two weak peaks (purple curve) at the potential of -0.78 and -0.58 V are observed on the three samples, indicating a certain amount of Pb(II) and Cd(II) present in real samples. Then, by adding three concentrations of standard samples to real samples, respectively, it can be seen that the stripping peaks of the two metal ions increases with the increase of ion concentration. Based on linearly equation, the concentration and recovery of Pb(II) and Cd(II) in the three samples are listed in Table 2-2.2. From the results, the content of Pb(II) and Cd(II) in the three real water samples was estimated to be 0.0119 and 0.0227  $\mu\text{M}$ , 0.0262 and 0.0283  $\mu\text{M}$ , 0.0204 and 0.0178  $\mu\text{M}$ , respectively, and the recoveries for Pb(II) and Cd(II) were 94.5-106% and 94.7-104%, respectively. The results indicate that the proposed electrode was efficiently applied to simultaneous monitor the heavy metal ions of Pb(II) and Cd(II) in the real water samples.

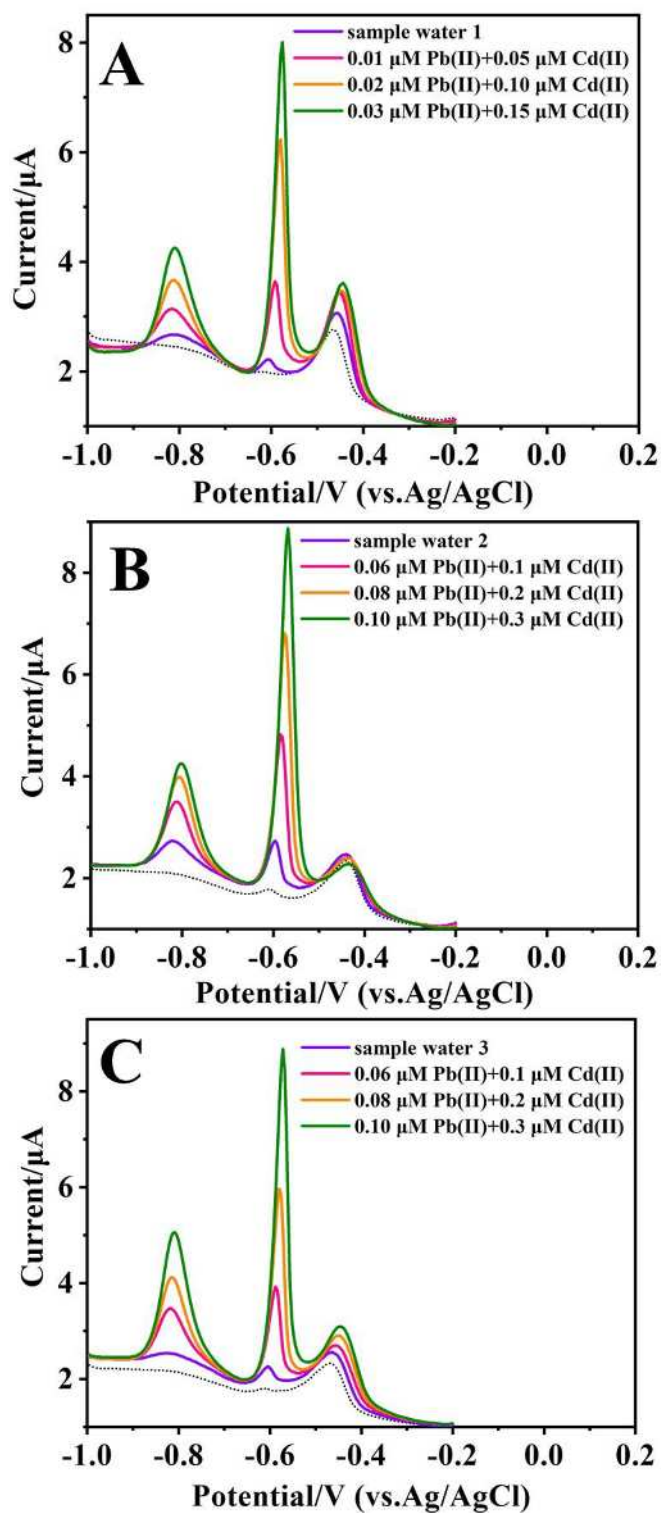


Fig. 2-2.9 DPASV responses recorded at  $\text{ZrO}_2/\text{C}/\text{Nafion}/\text{GCE}$  upon injection of real samples and followed by continuous injections of Pb(II) and Cd(II) in HAc-NaAc (pH 4.5) buffer.

Table 2-2.2 Determination of Pb(II) and Cd(II) in different water samples

(n = 3).

Sample	Added/ $\mu\text{M}$	Found/ $\mu\text{M}$	Recovery/%	
Sample 1	sample	0.0119		
	Pb(II)	0.06	0.0567	94.5
		0.08	0.0847	106
		0.10	0.0973	97.3
Sample 2	sample	0.0227		
	Cd(II)	0.1	0.101	101
		0.2	0.199	99.6
		0.3	0.304	101
Sample 3	sample	0.0262		
	Pb(II)	0.06	0.0587	97.8
		0.08	0.0795	99.4
		0.10	0.10	100
Sample 4	sample	0.0283		
	Cd(II)	0.1	0.0998	99.8
		0.2	0.203	102
		0.3	0.293	97.8
Sample 5	sample	0.0204		
	Pb(II)	0.06	0.0579	96.5
		0.08	0.0824	103
		0.10	0.102	102
Sample 6	sample	0.0178		
	Cd(II)	0.1	0.0947	94.7
		0.2	0.193	96.4
		0.3	0.311	104

## 2-2.4 Conclusion

In summary, a thin nanosheet shape of  $ZrO_2/C$  were synthesized by hydrothermal method and thermal treatment, the composite of  $ZrO_2/C$  and Nafion was prepared and acts as an adsorbed sensing material to fabricated an electrochemical sensor of simultaneously detection for Pb(II) and Cd(II). An excellent analysis performance including high sensitivity, good stability and low interference were achieved based on the large surface area and high adsorbed ability of the  $ZrO_2/C$ . The real water samples were also analyzed and the satisfied results were achieved, suggesting the sensor has a great potential applications of the simultaneously detection for Pb(II) and Cd(II) in the real samples.

## 2-2.5 References

- [1] E. Tahmasebi, M. Y. Masoomi, Y. Yamini and A. Morsali, *Inorg. Chem.*, **54**, 425 (2015).
- [2] Y. Zou, X. Wang, A. Khan, P. Wang, Y. Liu, A. Alsaedi and X. Wang, *Environ. Sci. Technol.*, **50**, 7290 (2016).
- [3] A. S. Ayangbenro and O. O. Babalola, *Int. J. Environ. Res. Public Health*, **14**, 94 (2017).
- [4] X. Wu, S. J. Cobbina, G. Mao, H. Xu, Z. Zhang and L. Yang, *Environ. Sci. Pollut. Res.*, **23**, 8244 (2016).
- [5] Y. Cheng, C. Yang, H. He, G. Zeng, K. Zhao and Z. Yan, *J. Environ. Eng.*, **142**, C4015001 (2016).
- [6] P. Ajitha, K. Vijayalakshmi, M. Saranya, T. Gomathi, K. Rani, P. N. Sudha and A. Sukumaran, *Int. J. Biol. Macromol.*, **104**, 1469 (2017).
- [7] M. R. Awual, *J. Environ. Chem. Eng.*, **7**, 103378 (2019).
- [8] B. Li, L. Yang, C. Q. Wang, Q. P. Zhang, Q. C. Liu, Y. D. Li and R. Xiao, *Chemosphere*, **175**, 332 (2017).
- [9] A. A. Wasim, S. Naz, M. N. Khan and S. Fazalurrehman, *Pak. J. Anal. Environ. Chem.*, **20**, 67 (2019).
- [10] Y. Yamini and M. Safari, *Microchem. J.*, **143**, 503 (2018).
- [11] T. T. Shih, C. C. Hsieh, Y. T. Luo, Y. A. Su, P. H. Chen, Y. C. Chuang and Y. C. Sun, *Anal. Chim. Acta*, **916**, 24 (2016).
- [12] B. Bansod, T. Kumar, R. Thakur, S. Rana and I. Singh, *Biosens. Bioelectron.*, **94**, 443 (2017).
- [13] S. Lee, J. Oh, D. Kim and Y. Piao, *Talanta*, **160**, 528 (2016).
- [14] W. Yi, Z. He, J. Fei and X. He, *RSC adv.*, **9**, 17325 (2019).
- [15] Y. Zhang, C. Li, Y. Su, W. Mu and X. Han, *Inorg. Chem. Comm.*, **111**, 107672 (2020).
- [16] N. T. Lieu, C. Van Hoang, P. T. T. Le and L. T. Giang, *Vietnam J. Chem.*, **57**, 379 (2019).
- [17] P. Yan, S. Zhang, C. Zhang, Z. Liu and A. Tang, *Microchim. Acta*, **186**, 706

- (2019).
- [18] N. T. Lieu, C. Van Hoang, P. T. T. Le and L. T. Giang, *Vietnam J. Chem.*, **57**, 379 (2019).
- [19] C. Wei, S. Sun, D. Mandler, X. Wang, S. Z. Qiao and Z. J. Xu, *Chem. Soc. Rev.*, **48**, 2518 (2019).
- [20] J. Liao, F. Yang, C. Z. Wang and S. Lin, *Sens. Actuators, B*, **271**, 195 (2018).
- [21] L. Wang, Z. Wei, M. Mao, H. Wang, Y. Li and J. Ma, *Energy Storage Mater.*, **16**, 434 (2019).
- [22] M. J. Rushton, I. Ipatova, L. J. Evitts, W. E. Lee and S. C. Middleburgh, *RSC adv.*, **9**, 16320 (2019).
- [23] P. Saharan, P. Bansal, G. R. Chaudhary and A. K. Sharma, *J. Nanosci. Nanotechnol.*, **19**, 7221 (2019).
- [24] H. C. Chen, D. J. Jan, J. H. Lin and M. C. Wang, *Sol. Energy Mater. Sol. Cells*, **203**, 110158 (2019).
- [25] V. V. Okovity, O. G. Devoino, V. A. Okovity and V. M. Astashinsky, *Sci. Tech.*, **15**, 193 (2016).
- [26] H. J. Kim, Y. G. Kang, H. G. Park, K. M. Lee, S. Yang, H. Y. Jung and D. S. Seo, *Liq. Cryst.*, **38**, 871 (2011).
- [27] B. Mecheri, A. Iannaci, A. D'Epifanio, A. Mauri and S. Licoccia, *ChemPlusChem*, **81**, 80 (2016).
- [28] M. Arvand, S. Elyan and M. S. Ardaki, *Sens. Actuators, B*, **281**, 157 (2019).
- [29] J. A. Nieto, *Appl. Radiat. Isot.*, **138**, 35 (2018).
- [30] A. Nodehi, H. Atashi and M. Mansouri, *J. Dispersion Sci. Technol.*, **40**, 766 (2019).
- [31] H. Zhou, Y. Shen, J. Xi, X. Qiu and L. Chen, *ACS Appl. Mater. Interfaces*, **8**, 15369 (2016).
- [32] L. Oar-Arteta, T. Wezendonk, X. Sun, F. Kapteijn and J. Gascon, *Mater. Chem. Front.*, **1**, 1709 (2017).
- [33] Y. F. Huang, X. Y. Sun, S. H. Huo, Y. Li and C. Zhong, *Appl. Surf. Sci.*, **466**, 637 (2019).
- [34] X. Zhu, B. Li, J. Yang, Y. Li, W. Zhao, J. Shi and J. Gu, *ACS Appl. Mater. Interfaces*, **7**, 223 (2015).
- [35] B. Wang, H. Huang, X. L. Lv, Y. Xie, M. Li and J. R. Li, *Inorg. Chem.*, **53**, 9254

- (2014).
- [36] S. Liu, Z. Yue and Y. Liu, *Dalton Trans.*, **44**, 12976 (2015).
- [37] M. J. Katz, Z. J. Brown, Y. J. Colón, P. W. Siu, K. A. Scheidt, R. Q. Snurr and O. K. Farha, *Chem. Comm.*, **49**, 9449 (2013).
- [38] W. Qiu, H. Tanaka, F. Gao, Q. Wang and M. Huang, *Adv. Powder Technol.*, **30**, 2083 (2019).
- [39] R. Liu, C. Yan, C. Zhang, Y. Cao and X. Long, *Adv. Appl. Ceram.*, **115**, 6 (2016).
- [40] L. Durai, A. Gopalakrishnan and S. Badhulika, *J. Electroanal. Chem.*, 113937 (2020).
- [41] X. Qin, D. Tang, Y. Zhang, Y. Cheng, F. He, Z. Su and H. Jiang, *Int. J. Electrochem. Sci.*, **15**, 1517 (2020).
- [42] C. Hao, Y. Shen, J. Shen, K. Xu, X. Wang, Y. Zhao and C. Ge, *Microchim. Acta*, **183**, 1823 (2016).
- [43] X. Li, H. Wen, Q. Fu, D. Peng, J. Yu, Q. Zhang and X. Huang, *Appl. Surf. Sci.*, **363**, 7 (2016).
- [44] Y. Zhang, C. Li, Y. Su, W. Mu and X. Han, *Inorg. Chem. Comm.s*, **111**, 107672 (2020).
- [45] J. Pizarro, R. Segura, D. Tapia, S. Bollo and P. Sierra-Rosales, *Electroanalysis*, **31**, 2199 (2019)
- [46] M. Dali, K. Zinoubi, A. Chrouda, S. Abderrahmane, S. Cherrad and N. Jaffrezic-Renault, *J. Electroanal. Chem.*, **813**, 9 (2018).

**2-3 Yolk-shell-structured SnO<sub>2</sub>-C and poly-tyrosine composite films as an impedimetric “Signal-Off” sensing platform for transgenic soybean screening**

### **2-3.1 Introduction**

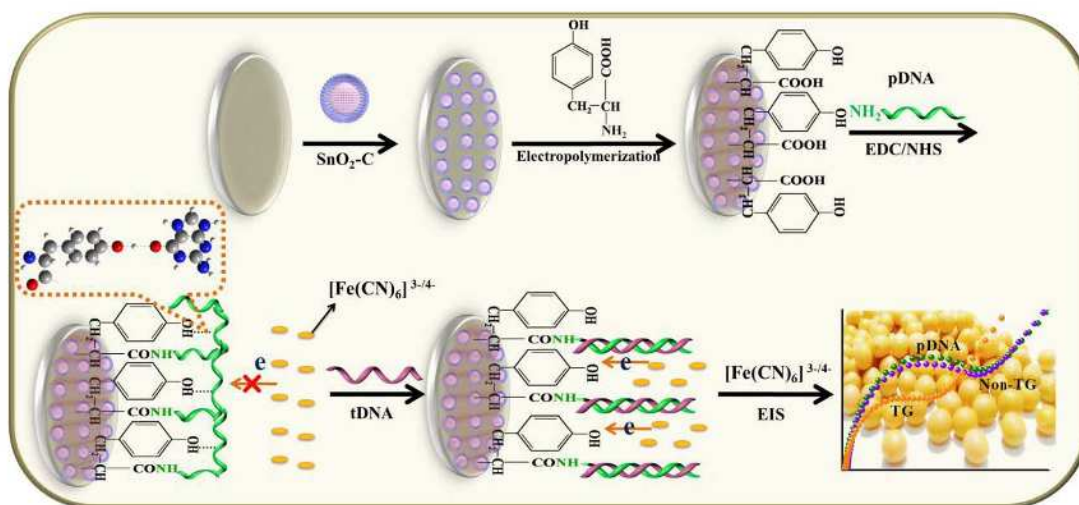
Transgenic technology brings great benefits in agriculture field, but also raises serious social and ethical concerns because of its potential environmental risk and allergenicity to human health [1, 2]. Transgenic soybean is one of the most distributed transgenic crops that nearly occupy 50% of the global biotechnology area. Up to date, there are several technologies to detect transgenic soybean, such as enzyme-linked immune sorbent assays (ELISA) and polymerase chain reaction (PCR) [3], and so on. However, these strategies suffer from some disadvantages such as expensive and sophisticated instrumentation, poisonous reagents, time-consuming, and the complicated operation [4]. To contrast, the electrochemical approach presents the advantages of quick response, low cost, cheap instrument, easy for micromation and portability [5-8], and therefore receives considerable interest for DNA analysis.

The immobilization of probe DNA (pDNA) on a supporting interface is a vital step for the construction of an electrochemical biosensor. The ideal mobilization strategy will be of great benefit to improve accuracy, sensitivity, and lifetime of the biosensor. Usually, the design of the immobilization interface defers to the following rules: (1) good electronic conductivity to induce intense response signal; (2) high surface area to allow the attachment of pDNA with high density; (3) appropriate functional group and active sites for tight grating of pDNA. In order to satisfy these requirements simultaneously, the hybrid materials containing inorganic materials with highly electronic conductivity and large surface area, and organic polymers with rich functional group have been frequently developed [9-11]. Poly-tyrosine (pTyr) is a kind of favorable polymer for the nanomaterial modification since its merits of rich functional groups, good electrochemical property, and excellent biocompatibility [12]. In recent years, it also receives considerable attention in biosensor construction for the electroanalysis of various biomolecules example for norepinephrine [13], dopamine [14], and melanocyte [15]. However, as far as our knowledge, the use of pTyr as a platform for DNA immobilization and hybridization detection has not been mentioned yet.

Stannic oxide ( $\text{SnO}_2$ ), an important *n*-type binary semiconductor nanomaterial, has been widely applied in the field of environmental protection, photochemistry, solar cells, and lithium batteries anodes [16, 17]. The nanosized  $\text{SnO}_2$  with different shapes have also been exploited as the electrode materials for electrochemical sensor fabrication due to their large surfaces area, high biocompatibility, and chemical stability. For example, Al-Hada's group reported an electrochemical sensor for Gram-positive B based on pure  $\text{SnO}_2$  nanopowder [18]. Huang et al. have prepared ultrathin  $\text{SnO}_2$  nanosheets and utilized its highly reactive exposed (110) surface for sensitive analysis of As(III) [19]. Unfortunately, the pure  $\text{SnO}_2$  nanomaterials will weaken their performance during electrochemical application, attributing to its nature of low electronic/ionic conductivity and easy aggregation between nanoparticles [20]. One of the most effective approaches to resolve this problem is to prepare its composite with carbon material. For example, Zhou et al. have synthesized hollow core-shell  $\text{SnO}_2/\text{C}$  fibers and used them as highly stable anodes for Lithium-ion batteries [21]. Wang et al. synthesized the  $\text{SnO}_2$ /reduced graphene oxide nanocomposite and applied it as electrode material for detecting  $\text{NO}_2$  [22]. Singh et al. also prepared  $\text{SnO}_2/\text{g-C}_3\text{N}_4$  by wet chemical method and applied it to study for rhodamine-B degradation [23]. In these reports, the carbon materials are believed to act as two significant roles. First, its elastic nature makes it very effective to improve the mechanical stability and prevents the aggregation of the  $\text{SnO}_2$ . Second, it also increases the electronic conductivity of the composite material.

In this work, the  $\text{SnO}_2$ -C composite with unique yolk-shell nanosphere structure has been prepared via a solvothermal approach coupling with thermal treatment. The resulting composite has uniformly distributed metal oxide and carbon because they come from the same precursor. The result shows that the nanocomposite not only effectively ensures structural integrity, but also boosts the electrical conductivity and surface area. To explore its application, a functional organic film of poly-tyrosine (pTyr) is electrochemically fabricated on  $\text{SnO}_2$ -C modified glassy carbon electrode (GCE). The presence of pTyr has two important effects for DNA biosensor construction in this work. First, its exposed carboxyl groups can be utilized as a

scaffold for pDNA immobilization, and secondly, its 4'-hydroxyl group (-OH) shows hydrogen bonding with the base groups of pDNA. This action makes the pDNA overlying on the modified electrode surface, resulting in high electrochemical impedance. After the pDNA is reacted with target DNA (tDNA) to generate rigid duplex structure, the DNA strands erect on the sensor surface, and facilitates  $[\text{Fe}(\text{CN})_6]^{3-/4-}$  to diffuse to the electrode surface. Thus, a decreased impedance value is achieved. Being contrast to the most impedimetric “signal-on”-based sensing strategies, a novel electrochemical sensing mechanism based on “signal-off” signal variation is presented in this work (Scheme 2-3.1). The response mechanism of the biosensor is proposed under the assistance of theoretic calculation. Also, thanks to the high surface area of the  $\text{SnO}_2\text{-C}$  and good bio-functionality of the pTyr film in the composite membrane, the biosensor displays excellent analytical performance in hybridization detection. When the developed biosensor is used to detect specific transgenic DNA fragment, cauliflower mosaic virus 35s (CaMV35s) that extracted from transgenic soybean samples, satisfactory results are achieved, showing good reliability of the biosensor for transgenic product monitoring.



Scheme 2-3.1 Schematic illustration for preparation procedure of DNA biosensor and its application for monitoring transgenic soybean sample.

## 2-3.2 Experimental

### 2-3.2.1 Reagents and apparatus

Tyrosine (Tyr), Tris (hydroxymethyl aminomethane) (Tris) were provided by Aladdin Reagent Company (China). 1-ethyl-3-(3-dimethylaminopropyl) carbodiimide (EDC) and N-hydroxysulfosuccinimide (NHS) were purchased from Sigma-Aldrich Co., Ltd. (China). Stannous chloride dihydrate ( $\text{SnCl}_2 \cdot 2\text{H}_2\text{O}$ ), glucose, citric acid and ethylenediaminetetraacetic acid (EDTA) were obtained from Xilong Chemical Co., Ltd. (China). Phosphate buffer saline (PBS) was supplied by Shanghai KangYi Instruments Co., Ltd. (China). The transgenic (TG) soybean power sample was donated by Xiamen Import and Export Commodity Inspection and Quarantine Bureau (China). All the other chemicals were of analytical reagent grade and purchased commercially. Doubly distilled water was used throughout the experiments.

The synthetic oligonucleotide fragments including amino modified probe sequence (pDNA): 5'-NH<sub>2</sub>-(CH<sub>2</sub>)<sub>6</sub>-TCT TTG GGA CCA CTG TCG-3' that derived from CaMV35s promoter gene, complementary target DNA (tDNA): 5'-CGA CAG TGG TCC CAA AGA-3', one-base-mismatch target (1MT): 5'-CGA CAG TGG TCC CAA CGA-3', three-base-mismatch target (3MT): 5'-CGA CAA TGG CCC CAA CGA-3', and non-complementary sequence (NC): 5'-GCA TCG AGC GAG CAC GTA-3' were synthesized by Shanghai Sangon Bioengineering Co., Ltd. (China).

All DNA fragments (10 μM) were prepared by dissolving in pH 8.0 TE buffer containing 10 μM Tris and 1.0 mM EDTA. All the DNA solutions were kept at -20 °C when not in use.

Scanning electron microscope (SEM) was recorded on JSM-60-10LA (Japan). Transmission electron microscopy (TEM) was determined by Tecnai G2 F20 (USA). The X-Ray powder Diffraction (XRD) pattern was performed using a Rigaku D/MAX-RB diffractometer (Japan). For the X-ray photoelectron spectroscopy (XPS) analysis, a Kratos AXIS 165 multitechnique electron spectrometer (Britain) was used.

The fluorescence assay was performed by Quant Studio (TM) 6 Flex (USA). Electrochemical measurements were measured on a CHI 660E electrochemical analyzer (China) in connection with a conventional three-electrode system: a modified glassy carbon disk electrode (GCE) with the geometric area of  $0.031 \text{ cm}^2$  was used as the working electrode, Ag/AgCl (3 M KCl) electrode as the reference electrode and Pt wire as the counter electrode.

### **2-3.2.2 Preparation of yolk-shell structured SnO<sub>2</sub>-C nanospheres**

In a typical synthesis, 3.6 mmol (0.80 g) SnCl<sub>2</sub>·2H<sub>2</sub>O, 36 mmol (7 g) glucose and 14 mmol (1.5 g) citric acid were mixed in 70 mL water. Then, the solution was adjusted to pH~7 using NH<sub>3</sub>H<sub>2</sub>O (30 wt%), which was followed by transferring into a autoclave, and heated at 170 °C for 3 h in an oven. Afterward, the reaction solution was cooled naturally, and the black intermediate product (SnO<sub>2</sub>@C) was obtained. The product was rinsed with redistilled water and anhydrous ethanol, respectively, and then dried in vacuum at 80 °C for 24 h. Finally, the sample was calcined in air at 500 °C for 3 h to achieve the final yolk-shell structured SnO<sub>2</sub>-C nanospheres.

### **2-3.2.3 Electrochemical fabrication of pTyr on SnO<sub>2</sub>-C modified GCE**

The fabrication of pTyr on SnO<sub>2</sub>-C modified GCE was achieved through the physical casting coupled with electro-polymerization. First, the GCE was mechanically cleaned with alumina slurry, and then washed under ultrasonication with ethanol and water. Followed by, a homogeneous suspension was obtained through dispersing 1.0 mg of synthesized SnO<sub>2</sub>-C in 10 mL water by ultrasonication. Thereafter, 10 μL suspension was dropped on the GCE and stand in air to dry. The SnO<sub>2</sub>-C modified electrode (SnO<sub>2</sub>-C/GCE) was electrochemically scanned for 18 cycles in the mixture of 0.1 M KCl and 0.1 mM Tyr at scan rate of  $0.1 \text{ V s}^{-1}$  within potential window from

0 to +1.8 V. When the electrochemical polymerization was finished, the pTyr/SnO<sub>2</sub>-C modified electrode (pTyr/SnO<sub>2</sub>-C/GCE) was obtained upon further rinsing with water.

#### **2-3.2.4 Fabrication of sensor surface and hybridization reaction**

Attribute to the functional carboxylic group of the pTyr film on the prepared electrode surface, the amino-modified pDNA was anchored on pTyr/SnO<sub>2</sub>-C/GCE surface via a classic EDC/NHS-based covalent coupling method. In details, the pTyr/SnO<sub>2</sub>-C/GCE was immersed into a mixture solution of 25 mM PBS, 8 mM NHS and 5 mM EDC for 20 min, and then moved to 1.0 mL TE buffer including 0.1 μM amino-modified pDNA at normal temperature for 12 h. The physically adsorbed DNA on the electrode was removed by sufficiently rinsed with TE buffer and water, and the pDNA modified electrode (pDNA/pTyr/SnO<sub>2</sub>-C/GCE) was obtained.

The hybridization reaction was carried out through incubation of the pDNA/pTyr/SnO<sub>2</sub>-C/GCE in 100 μL analyte solution at 42 °C for 25 min, the nonspecifically adsorbed DNA was eliminated by rinsing with TE buffer.

#### **2-3.2.5 Preparation of DNA sample from real soybeans**

The DNA from soybeans was first extracted according to the instruction of DePure Plant DNA kit (Double helix gene technology Co., Ltd., Guangzhou). Then the extracted DNA was digested by the digestion mixture solution of 1 μL ice-cold restriction enzyme Hind III, 2 μL TE buffer (pH 8.0) and 16 μL water. The mixture was devitalized the enzyme at 37 °C for 60 min, and heating at 80 °C for 20 min. Finally, the DNA in the mixture was denatured in 100 °C for 5 min to achieve single strands DNA, and then diluted 10 times for the following electrochemical analysis. To testify the reliability of the biosensor, the extracted DNA was amplified by PCR at 63 °C for 60 min, and then analyzed by the homoiothermy fluorescence method [24].

### 2-3.2.6 Quantum Chemical Computation

The binding energy of the four bases and pTyr was performed with the Gaussian 09 package and conducted by B3LYP/6-31+G(d) basis set of the density functional theory (DFT) [25].

## 2-3.3 Results and Discussion

### 2-3.3.1 Physical characterization of the yolk-shell SnO<sub>2</sub>-C nanospheres

Fig. 2-3.1A presents the typical XRD patterns of the SnO<sub>2</sub>@C precursor and its calcinated product. From the figure, it can be obtained that the precursor sample shows reflection peaks at 26.58, 33.88, 37.95, 51.75, 54.76 and 61.89°, which is well assigned to the (110), (101), (200), (210), (220) and (310) lattice planes of the tetragonal SnO<sub>2</sub> (PDF card No. 41-1445). Besides, a broad peak centered at 23.02° is visible, indicating that vast disorder carbon is generated from glucose during the hydrothermal reaction [26]. After calcining, all the peaks corresponding to SnO<sub>2</sub> become sharp and intense, suggesting that the crystallinity of the sample changes better. It is noticeable that no characteristic peak of C is observed in the XRD pattern of the SnO<sub>2</sub>-C, suggesting that the carbon exists in the composite as an amorphous form.

The chemical composition and valence states of the elements in SnO<sub>2</sub>-C were confirmed by XPS. Fig. 2-3.1B-C shows the C 1s, O 1s and Sn 3d core level spectra of the SnO<sub>2</sub>-C, respectively. As shown in Fig. 2-3.1B for the C 1s XPS spectra, two peaks are observed. The peak of 284.8 eV is attributed to graphitic layers in the form of C-C or C=C, and the peak of 289.0 eV is assigned to the group of C-O. The C-O is likely derived from the structural defects at the edges of unsaturated carbon [27]. The O 1s core-level spectrum (Fig. 2-3.1C) shows a strong peak at 530.3 eV, which is attributed to O atoms embed in SnO<sub>2</sub> lattice. For the Sn spectra shown in Fig. 2-3.1D,

two satellite peaks for Sn 3d<sub>5/2</sub> and Sn 3d<sub>3/2</sub> are displayed at 486.4 and 494.8 eV, respectively. The difference of binding energy between the Sn 3d<sub>5/2</sub> and Sn 3d<sub>3/2</sub> peaks is determined to be 8.4 eV, suggesting the presence of Sn (IV) oxide in the samples [28].

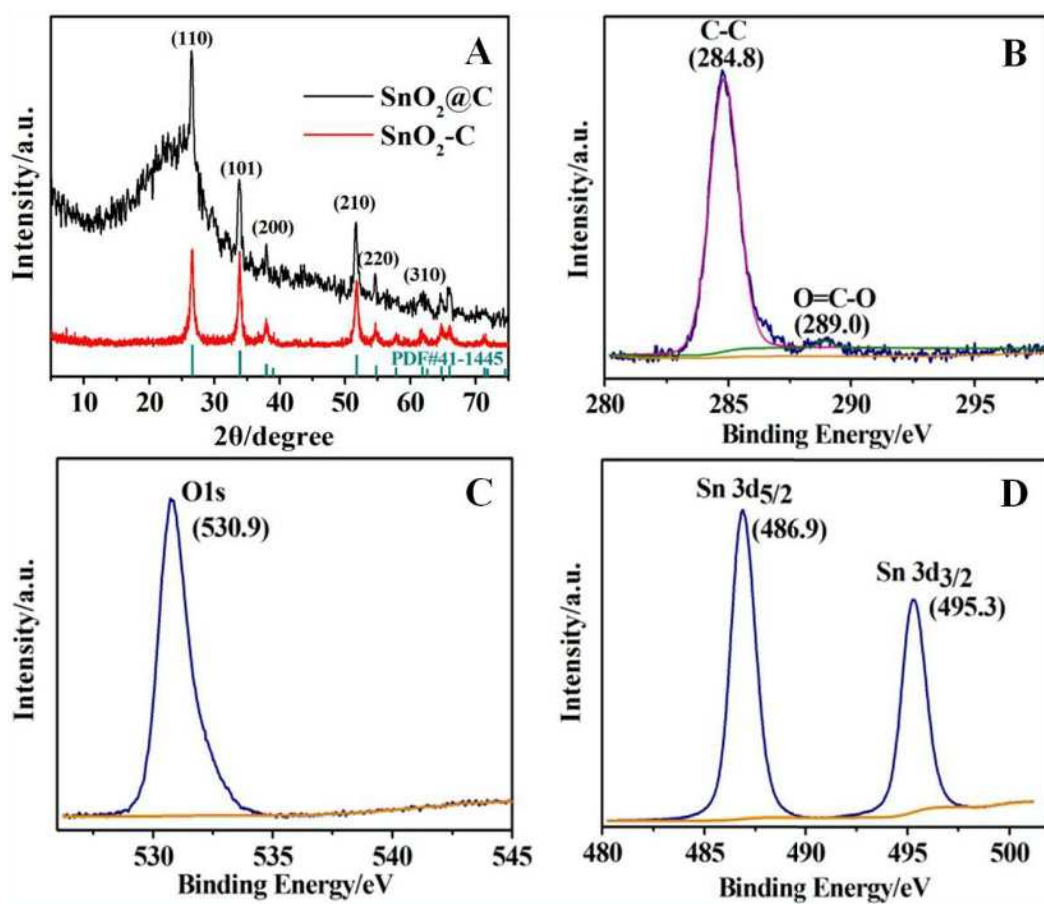


Fig. 2-3.1 (A) XRD patterns of SnO<sub>2</sub>-C and its precursor, (B) C 1s, (C) O 1s and (D) Sn 3d XPS spectra of SnO<sub>2</sub>-C.

The morphology of the materials was revealed by SEM and TEM. The SEM image of SnO<sub>2</sub>@C (Fig. 2-3.2A) displays that the precursor presents regular spheres with smooth surface. On the contrary, the surface of the calcined product is fluffy and rough, as displayed in Fig. 2-3.3A and Fig. 2-3.3B. The low-magnification SEM as shown in Fig. 2-3.3A suggests that the size of the spheres is from 0.9 μm to 2.0 μm in diameters. From the broken spheres as indicated by the arrows, a smaller sphere is clearly observed to be encapsulated inside the outer spheres, which demonstrates that the SnO<sub>2</sub>-C possesses the yolk-shell structure. The magnified SEM image (Fig. 2-3.3B) shows that the surface of each sphere consisted of the small nanoparticles with the average diameter of 16 nm. Such a feature endows the yolk-shell structured nanospheres a high surface area.

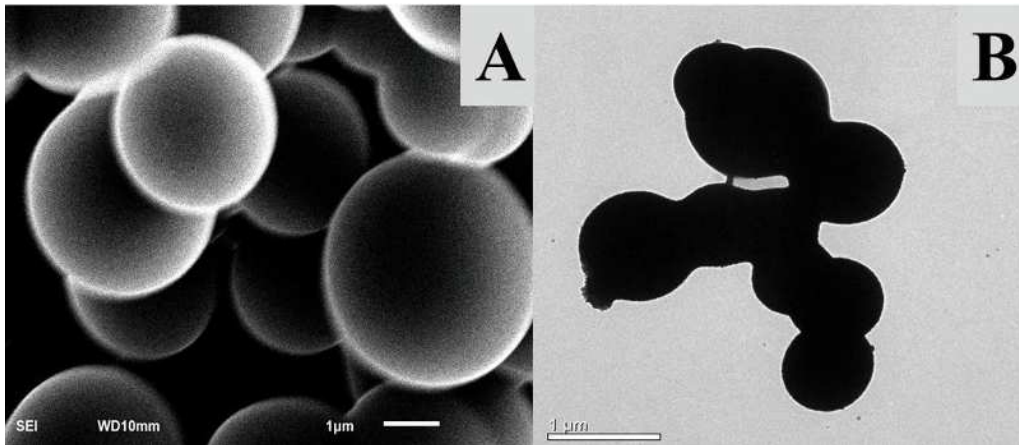


Fig. 2-3.2 SEM(A) and TEM(B) images for SnO<sub>2</sub>-C precursor

TEM image can provide a visualized method to expose the interior structure of the nanospheres by showing difference between the hollow and solid parts. The TEM image of SnO<sub>2</sub>-C (Fig. 2-3.3C) shows that the dark center is surrounded with bright shell, which is well consistent with the typical nature of the yolk-shell structure. In contrast, the TEM image of SnO<sub>2</sub>@C precursor shows deep black as whole (Fig. 2-3.2B). So, it can be concluded that the calcination procedure is a critical step for the formation of yolk-shell structured SnO<sub>2</sub>-C. The average diameter of the inner yolk was estimated to be about 600 nm and the outer shell is thin, with an average thickness of around 30 nm. Higher magnification of TEM image as displayed in Fig. 2-3.3D confirms that the shell is formed by small nanoparticles with an average size of around 16 nm. And this value is very close to the average crystallite size of ~17.6 nm as obtained from the aforementioned XRD characterization. An HRTEM image of SnO<sub>2</sub>-C nanospheres is shown in Fig. 2-3.3E. From the result, the interplanar spacing of 0.228 nm, 0.267 nm, 0.326 nm and 0.333 nm are determined, which are in good consistence with lattice planes of (110), (101), (200), and (111) of the SnO<sub>2</sub>, respectively.

Based on energy-dispersive X-ray (EDX) spectroscopy, more information about the elemental distribution within the nanospheres was provided from elemental mapping. From Fig. 2-3.3F, it is found that the Sn, O, and C elements are homogeneously distributed around the nanospheres, and the results of EDX mapping display that the elemental distribution of yolk (yellow dotted cycle) and shell (blue dotted cycle) is totally identical, *i.e.*, suggesting that both the yolk and the shell are constituted by carbon and SnO<sub>2</sub>. From the EDX spectra, the molar ratio of C, O, and Sn of yolk (Fig. 2-3.4A) and shell (Fig. 2-3.4B) for the SnO<sub>2</sub>-C nanospheres are determined to be about 39.4:45.4:15.2 and 40.2:43.3:16.5, respectively, which verifies the identical composition of the yolk and shell during the synthesis process.

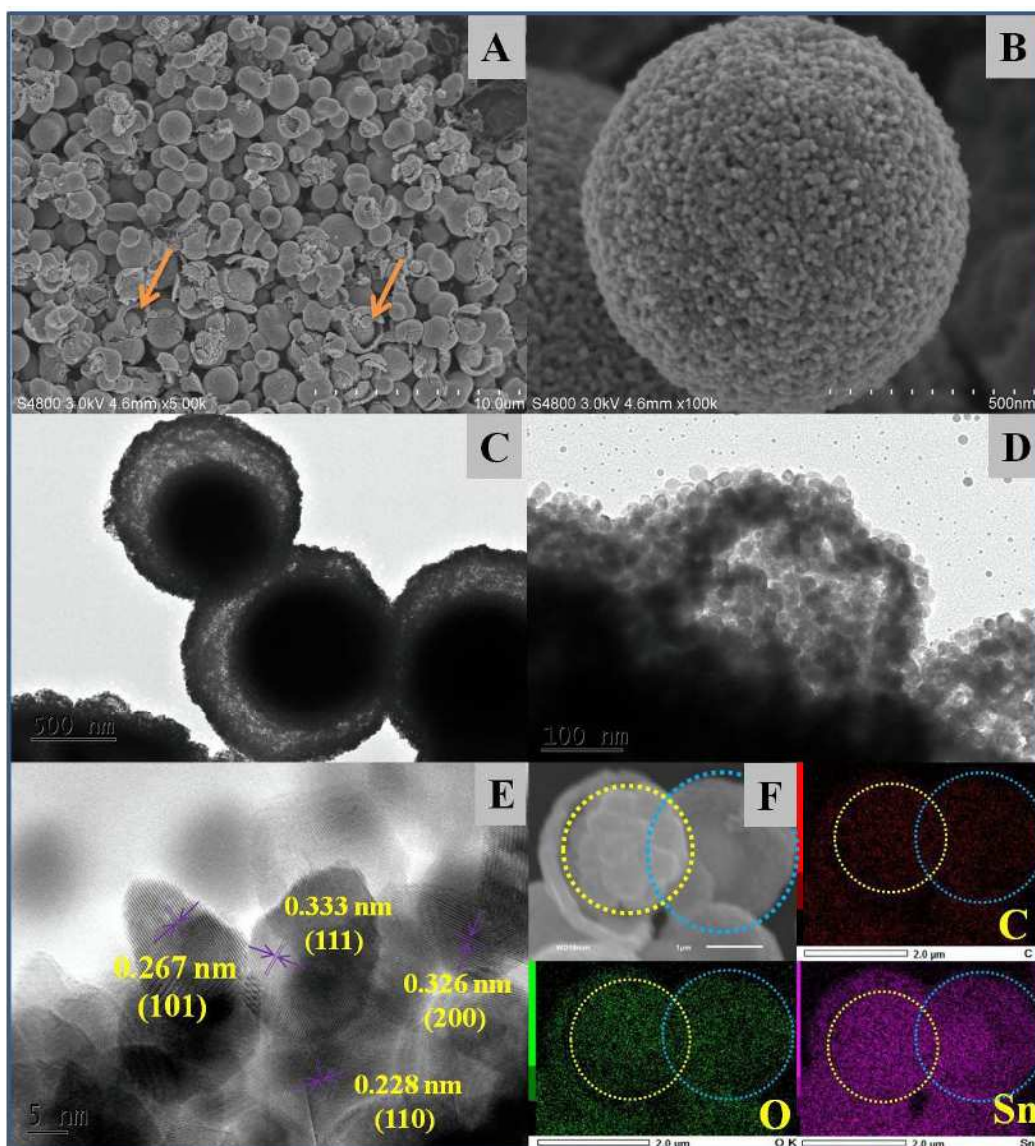


Fig. 2-3.3 SEM images (A-B), TEM images (C-D), and HRTEM image (E) for yolk-shell  $\text{SnO}_2\text{-C}$  structure nanospheres, EDX element mapping (F) of  $\text{SnO}_2\text{-C}$  nanospheres reveals the elemental distribution of C, O, and Sn.

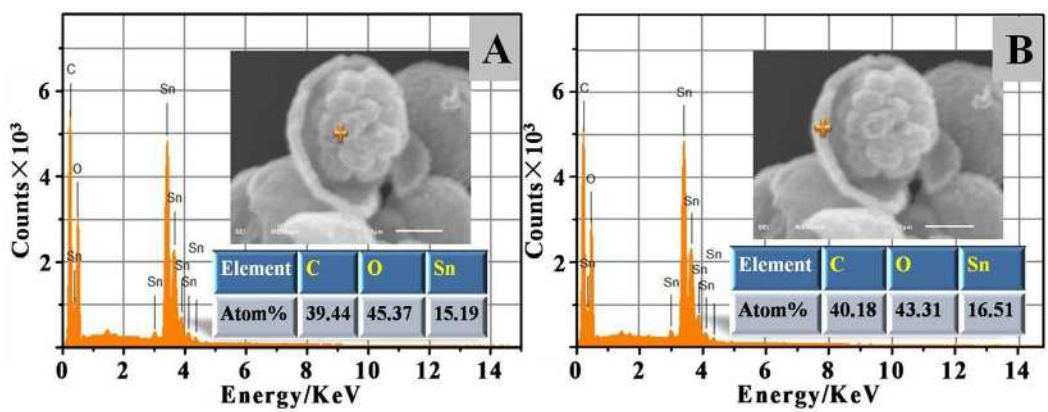


Fig. 2-3.4 EDX spectra of yolk (A) and shell (B) for SnO<sub>2</sub>-C nanospheres

### 2-3.3.2 Electrochemical characterization and probe surface density calculation

The pTyr/SnO<sub>2</sub>-C modified electrode was fabricated by physical coating of SnO<sub>2</sub>-C coupling with electrochemical preparation of pTyr in Tyr solution. The electrosynthesis process and the mechanism discussion on the formation of pTyr are displayed in Fig. 2-3.5A. Fig. 2-3.5A shows the successive CVs of SnO<sub>2</sub>-C/GCE in 1×10<sup>-4</sup> M Tyr solution. As seen, the reduction peak at 0.51 V and the oxidation peak at 1.40 V enhances gradually with increase of scan cycles, which reflects the continual formation of the polymerized film on the SnO<sub>2</sub>-C modified surface. When the sweep segments reach to 36<sup>th</sup>, both of the peaks achieve stability, indicating that the organic film have been saturated at SnO<sub>2</sub>-C/GCE. According to literature [29, 30], the electropolymerized mechanism of pTyr on the SnO<sub>2</sub>-C surface can be speculated as the process as displays in Fig. 2-3.5B: First, the electro-oxidation of the monomers produces radicals. Then, these radicals go through ortho coupling reactions, producing non-soluble polyphenol-like compounds, which are then physically adsorbed to the electrode surface. For comparison, the bare GCE was also utilized as a substrate for successive CV scan in 0.1 mM Tyr solution. From the result (inset of Fig. 2-3.5A), it can be found that both the reduction and oxidation peaks were much smaller than those on SnO<sub>2</sub>-C/GCE. These changes suggest that Tyr is harder to get polymerization reaction on bare GCE than on SnO<sub>2</sub>-C/GCE, which can be assigned to the good electro-conductive property and large surface area of the modified SnO<sub>2</sub>-C.

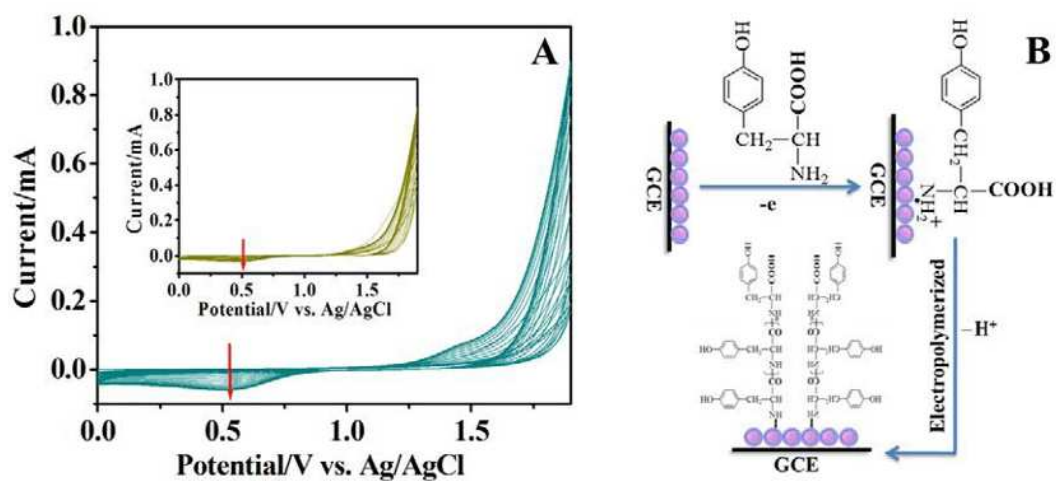


Fig. 2-3.5 (A) Continuously scanned CVs of SnO<sub>2</sub>-C/GCE and GCE (inset) in the mixture solution of  $1.0 \times 10^{-4}$  M Tyr and 0.1 M KCl with the scan rate of  $100 \text{ mV s}^{-1}$ . (B) Proposed growth mechanism of pTyr on SnO<sub>2</sub>-C by electro-polymerization.

Then the pTyr/SnO<sub>2</sub>-C/GCE was applied as a supporting platform for the fixation of amino-terminated pDNA to construct a DNA sensing interface. The layer-by-layer fabrication process of the biosensor are verified by CV (Fig. 2-3.6A) and EIS (Fig. 2-3.6B) in [Fe(CN)<sub>6</sub>]<sup>3-/4-</sup>. In the CV experiments, it is observed that a pair of well-defined redox peaks in [Fe(CN)<sub>6</sub>]<sup>3-/4-</sup> solution on bare GCE (curve a). Upon modification of GCE with the synthesized SnO<sub>2</sub>-C, it is found that the redox peaks in [Fe(CN)<sub>6</sub>]<sup>3-/4-</sup> solution (curve c) enhanced greatly, and the formal potential negatively shifted. Meanwhile, compared with bare GCE, the background current on the modified electrode is increased significantly. All these indicate increase of effective surface area and electro conductivity of the electrode by SnO<sub>2</sub>-C. When pTyr was further electro-synthesized on SnO<sub>2</sub>-C/GCE and tested under the same conditions, it is found that peak currents of [Fe(CN)<sub>6</sub>]<sup>3-/4-</sup> decrease obviously in comparison with SnO<sub>2</sub>-C/GCE (curve d), which suggest that pTyr had been successfully formed on SnO<sub>2</sub>-C/GCE, and the negatively charged -COOH on the polymer surface prevents the approaching of the electroactive [Fe(CN)<sub>6</sub>]<sup>3-/4-</sup> anion by the electrostatic repulsion. Interestingly, when pTyr was directly electrosynthesized on GCE without pre-modification of SnO<sub>2</sub>-C layer, the redox peaks of [Fe(CN)<sub>6</sub>]<sup>3-/4-</sup> become very small with an obviously increased peak-to-peak separation (curve b), suggesting the electrochemical response of [Fe(CN)<sub>6</sub>]<sup>3-/4-</sup> on pTyr/GCE is almost seriously suppressed. Such a difference of electrochemical responses between pTyr/GCE and pTyr/SnO<sub>2</sub>-C/GCE confirmed that the SnO<sub>2</sub>-C can be acted as an excellent substrate to improve the electro-polymerization of pTyr by its large surface area and good electro-conductivity.

Then based on derivative functional group of -COOH on pTyr, the pTyr/SnO<sub>2</sub>-C/GCE was applied as a matrix for the covalent immobilization of amino-modified probe DNA (pDNA) via EDC/NHS crosslink reaction. The CV result of [Fe(CN)<sub>6</sub>]<sup>3-/4-</sup> on the DNA modified electrode is displayed as curve e of Fig. 2-3.6A. As seen, the redox peaks of [Fe(CN)<sub>6</sub>]<sup>3-/4-</sup> decrease obviously as compared to those on pTyr/SnO<sub>2</sub>-C/GCE, suggesting pDNA had been successfully anchored on pTyr/SnO<sub>2</sub>-C/GCE. The reason for the decrease of redox peaks upon modification of DNA can be assigned to the interfering of negatively charged phosphate backbone on the pDNA for the effective diffusion of electro-negative [Fe(CN)<sub>6</sub>]<sup>3-/4-</sup> to the electrode surface [31].

In this work, the fabrication process of the sensing interface was also characterized by EIS and the obtained Nyquist plots are presented in Fig. 2-3.6B. An equivalent circuit model was utilized for fitting of impedance results (Fig. 2-3.6B, inset), where  $R_s$  is the solution resistance,  $Q_{dl}$  is the double-layer capacitance,  $R_{ct}$  represents the charge transfer resistance at the electrode/electrolyte interface,  $W$  is the Warburg impedance due to mass transfer to the electrode surface. The fitting results (solid lines) display that the equivalent circuit model is consistent with the real experimental data (dotted curves). The values of all the elements in the equivalent circuit model are listed in Table 2-3.1. It can be found that the bare GCE has a small  $R_{ct}$  value of  $4.48 \times 10^2 \Omega$  (curve a). After anchoring SnO<sub>2</sub>-C nanospheres on GCE, the  $R_{ct}$  value is reduced to  $2.13 \times 10^2 \Omega$  (curve c), which demonstrates that the SnO<sub>2</sub>-C nanospheres accelerate the electron transfer kinetics of the electrode surface as a well-behaved electron transfer channel. The  $R_{ct}$  value on pTyr/GCE is found to be as large as  $6.09 \times 10^3 \Omega$  (curve b), which is one-order larger than the bare GCE, suggesting the electron transfer process of  $[\text{Fe}(\text{CN})_6]^{3-/4-}$  is seriously inhibited by the single-component polymer film of pTyr. However, on pTyr/SnO<sub>2</sub>-C/GCE, the  $R_{ct}$  value is decreased to  $2.04 \times 10^3 \Omega$  (curve d), further testifying the SnO<sub>2</sub>-C nanospheres can effectively facilitate the electron transfer process of the composite film. Upon immobilization of pDNA on pTyr/SnO<sub>2</sub>-C/GCE, the  $R_{ct}$  value increases to  $4.95 \times 10^3 \Omega$  due to the electrostatic repulsion between negatively charged phosphate skeletons of DNA and  $[\text{Fe}(\text{CN})_6]^{3-/4-}$  ions (curve e). Therefore, both the CV and EIS experiments confirm that the pTyr/SnO<sub>2</sub>-C nanocomposite can be used as a highly powered electrochemical platform for bioprobe immobilization.

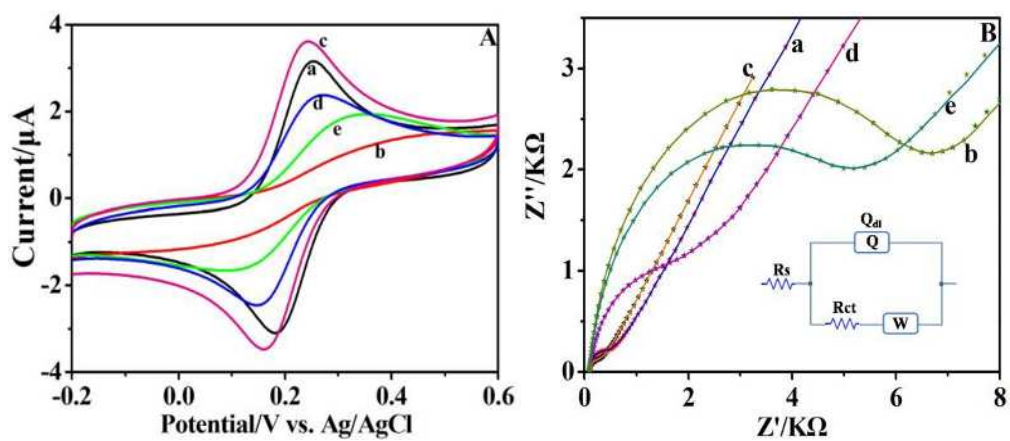


Fig. 2-3.6 Cyclic voltammograms (A) and Nyquist diagrams (B) of 1.0 mM  $[\text{Fe}(\text{CN})_6]^{3-/4-}$  (1:1) with 0.1 M KCl at bare GCE (a), pTyr/GCE (b),  $\text{SnO}_2\text{-C}$ /GCE (c), pTyr/ $\text{SnO}_2\text{-C}$ /GCE (d), and pDNA/pTyr/ $\text{SnO}_2\text{-C}$ /GCE (e). Inset in image B shows the equivalent circuit diagram of the modified electrodes.

Table 2-3.1 Values of the equivalent circuit elements obtained by fitting the experimental results for the different modified electrodes

Electrode	$R_s$ ( $\Omega \text{ cm}^2$ )	$Q_{dl}$ ( $\mu\text{F cm}^2$ )	$n$	$R_{ct}$ ( $\Omega \text{ cm}^2$ )	$W$ ( $\text{m}\Omega \text{ cm}^2$ )
GCE	87.94	4.489	0.800	448.9	0.286
pTyr/GCE	90.95	10.50	0.800	6093	0.360
SnO <sub>2</sub> -C/GCE	93.17	4.293	0.800	213.0	0.294
pTyr/SnO <sub>2</sub> -C/GCE	99.52	14.75	0.866	2035	0.255
pDNA/pTyr/SnO <sub>2</sub> -C/GCE	94.37	12.84	0.800	4945	0.338

In addition, for a biosensing interface, it has been proved that much more capture probe on the sensing interface will lead to higher capacity of the device to capture the target [32]. Therefore in this work, in order to quantify the contribution of SnO<sub>2</sub>-C material for enhancing the loading amount of pDNA strands, the probe density on both pTyr/GCE and pTyr/SnO<sub>2</sub>-C/GCE were calculated and compared through the classic CC method using RuHex as the indicator [33]. It is known that RuHex cations can electrostatically absorb on the negatively charged phosphate groups of oligonucleotide through a stoichiometric approach, thereby allowing the quantitative analysis of the surface-confined DNA via determining the amount of absorbed RuHex. In the CC assay, the charge ( $Q$ ) as a function of time ( $t$ ) is given by the following integrated Cottrell expression:

$$Q = (2nFAD_0^{1/2}t^{1/2}C_0^*)/\pi^{1/2} + Q_{dl} + nFA\Gamma_0 \quad (1)$$

where  $n$  is the electron of number per RuHex for reduction,  $A$  is the electrode area (cm<sup>2</sup>),  $Q_{dl}$  is the capacitive charge (C),  $D_0$  is the diffusion coefficient (cm<sup>2</sup> s<sup>-1</sup>),  $C_0^*$  is the bulk concentration of RuHex (mol cm<sup>-3</sup>).  $\Gamma_0$  represents the amount of RuHex adsorb on the electrode surface. The surface coverage of pDNA is then converted to the loading density ( $\Gamma_{DNA}$ , strands cm<sup>-2</sup>) using the following relationship:

$$\Gamma_{DNA} = \Gamma_0 (z/m)N_A \quad (2)$$

where  $z$  is the charge of the RuHex,  $m$  is the number of nucleotides in one pDNA strand, and  $N_A$  is the Avogadro's number. The CC test was carried out in Tris-HCl (pH 8.0) containing 50 μM RuHex.

Fig. 2-3.7A shows the CCs of pDNA/pTyr/SnO<sub>2</sub>-C/GCE in 10 mM Tris-HCl (pH 8.0) in the absence (a) and presence of 50 μM RuHex (b). The charge difference ( $\Delta Q$ ) is identified to be 1.31 μC from the intercept difference of two CC curves. Accordingly, the surface density ( $\Gamma_{DNA}$ ) of pDNA on the biosensor interface is determined to be  $4.54 \times 10^{13}$  strands cm<sup>-2</sup>. Under the same conditions, the surface density ( $\Gamma_{DNA}$ ) of pDNA on the interface of pDNA/pTyr/GCE is obtained to be  $1.59 \times 10^{13}$  strands cm<sup>-2</sup>. This result shows that the loading amount of pDNA on pTyr/SnO<sub>2</sub>-C/GCE is about 3-fold larger than that on pTyr/GCE, revealing that the SnO<sub>2</sub>-C nanocomposite acts as

a vital role to increase the loading amount of the pDNA by its surface area effect. Such a high surface density of pDNA is also higher than the previously reported DNA biosensors such as  $8.83 \times 10^{12}$  strands  $\text{cm}^{-2}$  on TPA/CS- $\text{Fe}_2\text{O}_3$  [34], and  $1.05 \times 10^{13}$  strands  $\text{cm}^{-2}$  on gold nanoparticles [35].

What's more, the probe electrode was interacted with excess amount of tDNA, and the DNA strands on the hybridized electrode were also measured by CC in RuHex solution, the  $\Delta Q$  of 2.40  $\mu\text{C}$  and the DNA density of  $8.33 \times 10^{13}$  strands  $\text{cm}^{-2}$  were estimated, respectively. Then, an outstanding hybridization efficiency of 83.2% was achieved. For comparison, the  $\Delta Q$  and DNA density on the pDNA/pTyr/GCE (Fig. 2-3.7B) were calculated to be 0.87  $\mu\text{C}$  and  $3.02 \times 10^{13}$  strands  $\text{cm}^{-2}$ , respectively, yielding a hybridization efficiency of only 68.3%. The improved hybridization efficiency on pDNA/pTyr/ $\text{SnO}_2\text{-C}$ /GCE on comparison with pDNA/pTyr/GCE can be explained by the following reason: when pDNA immobilized on pTyr that directly electro-polymerized on GCE, the probe strands curly, and the large steric hindrance inhibits the effective diffusion of tDNA to electrode surface. However, on pDNA/pTyr/ $\text{SnO}_2\text{-C}$ /GCE, the unique yolk-shell structure and large surface area of  $\text{SnO}_2\text{-C}$  enables the immobilized pDNA on the sensing interface having broad space to accommodate the tDNA for hybridization (Fig. 2-3.7C), resulting in higher hybridization efficiency.

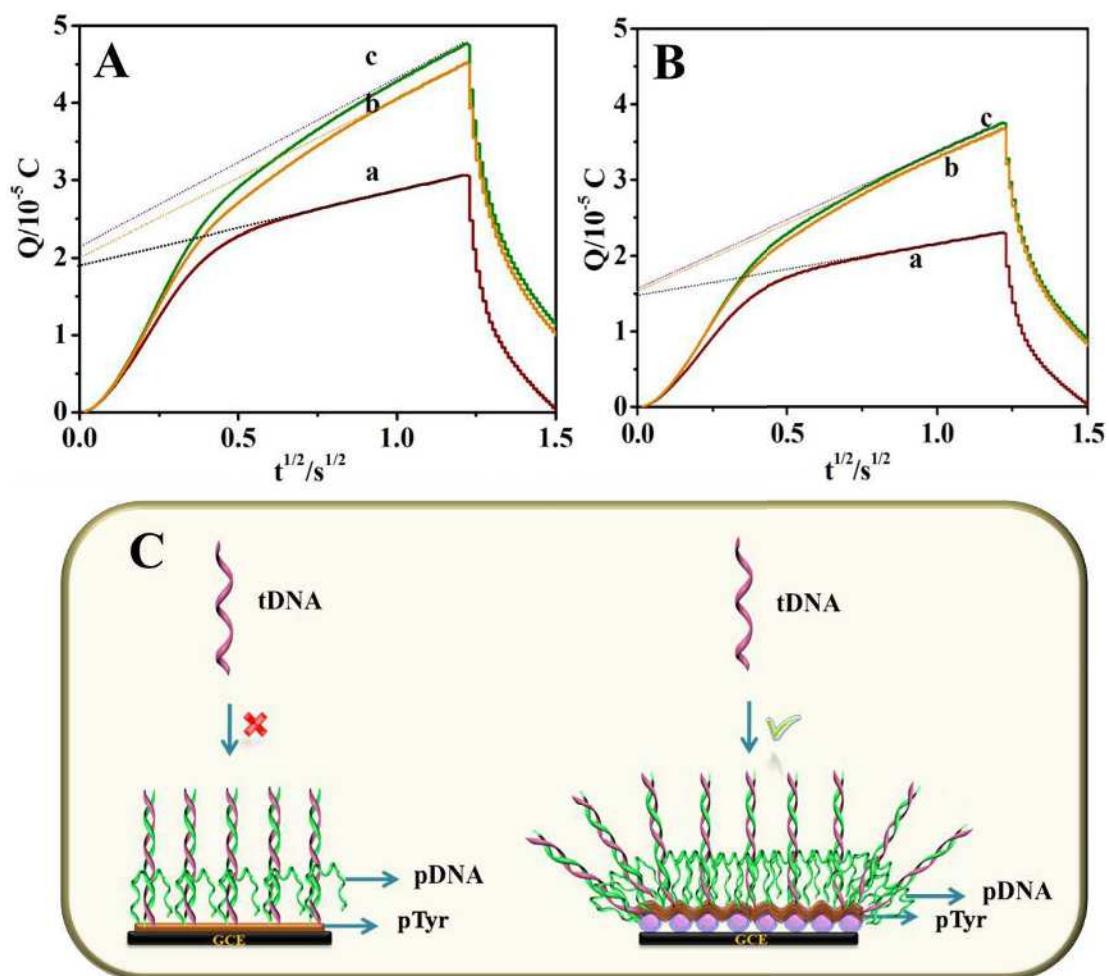


Fig. 2-3.7 (A) Chronocoulometric curves of pDNA/pTyr/SnO<sub>2</sub>-C/GCE in 10 mM pH 8.0 Tris-HCl without (a) and with (b) 50  $\mu\text{M}$  RuHex. The chronocoulometric curve (c) is pDNA/pTyr/SnO<sub>2</sub>-C/GCE after hybridization with 0.1 nM tDNA in 10 mM pH 8.0 Tris-HCl with 50  $\mu\text{M}$  RuHex. (B) The same test was matched at pDNA/pTyr/GCE. (C) Schematic illustration of larger surface to accommodate the tDNA for hybridization.

### 2-3.3.3 Sensing performance of the biosensor

The experimental conditions including coating amount of SnO<sub>2</sub>-C, immobilization time of capture pDNA on pTyr/SnO<sub>2</sub>-C/GCE, and hybridization time ( $t_H$ ) and hybridization temperature ( $T_H$ ) with tDNA are optimized and evaluated by EIS in this work. In order to obtain the optimal conductivity, the cast amount of SnO<sub>2</sub>-C on the surface electrode was first studied. The relationship between the  $R_{et}$  values versus the cast amount of SnO<sub>2</sub>-C ( $V_{SnO_2-C}$ ) on the electrode surface is showed in Fig. 2-3.8A. From the figure, it is observed that the value of  $R_{et}$  stepped down with increase of the cast amount of SnO<sub>2</sub>-C, suggesting electronic conductivity of the electrode is enhanced gradually with increase of modified SnO<sub>2</sub>-C. When the cast amount is 10  $\mu$ L, the  $R_{et}$  value reaches to the smallest value and enlarges again with increase of the cast amount likely due to blockage of electron transfer by the thick film. So 10  $\mu$ L is chosen as the best modification amount of SnO<sub>2</sub>-C.

The optimal immobilization time of capture pDNA on pTyr/SnO<sub>2</sub>-C/GCE was investigated by immersing the pTyr/SnO<sub>2</sub>-C/GCE into pDNA solution for different time in the range from 2 to 14 h. The result shows that the response signal ( $R_{et}$ ) enhances with time increasing from 2 to 12 h (Fig. 2-3.8B), and then the value of  $R_{et}$  hardly changes with further increase of the reaction time, indicating the immobilization of pDNA on the electrode is saturated. Thus, 12 h is used as the optimal immobilization time.

The influences of the hybridization time ( $t_H$ ) and temperature ( $T_H$ ) on the  $R_{et}$  were also evaluated. Fig. 2-3.8C shows the relationship of  $R_{et}$  values versus  $t_H$  of pDNA/pTyr/SnO<sub>2</sub>-C/GCE upon hybridization with  $1.0 \times 10^{-11}$  M complementary target DNA (tDNA) at 40 °C. From the figure, it can be obtained that the  $R_{et}$  values decrease when  $t_H$  increases from 0 min to 25 min, proving that increasing amounts of tDNA are captured by pDNA. When the hybridization time is more than 25 min, the  $R_{et}$  is almost constant, indicating the finish of the hybridization reaction. So, 25 min is chosen as the optimal hybridization time in the following test. The effect of hybridization temperature on the hybridization reaction was tested in the temperature range from 32 to 50 °C, and the result is shown in Fig. 2-3.8D. As seen, the plot of  $R_{et}$

versus  $T_H$  level off when  $T_H$  is beyond 42 °C, suggesting optimal hybridization performance between tDNA and pDNA under this temperature. Therefore, 42 °C is employed as the optimal hybridization temperature in the subsequent experiments.

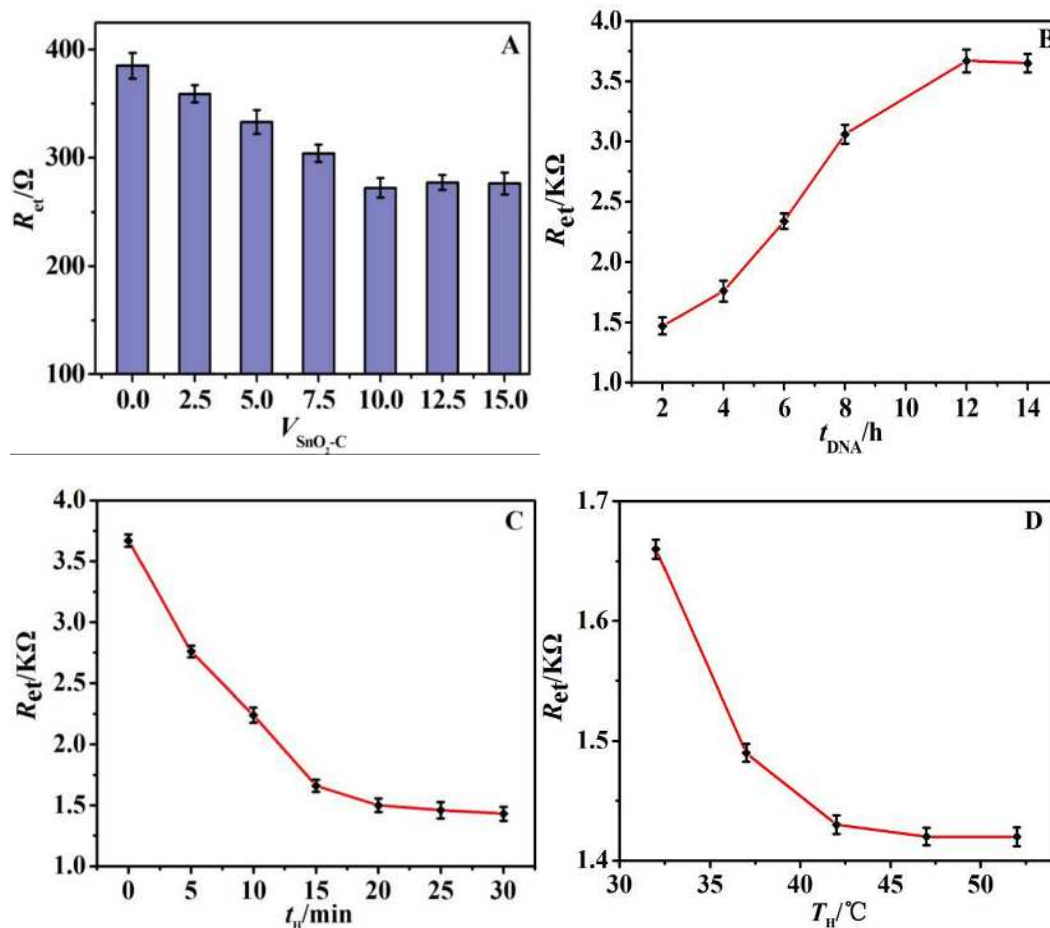


Fig. 2-3.8 Effect of (A) amount of  $SnO_2-C$ , (B) immobilization time ( $t_{DNA}$ ) of pDNA at pTyr/ $SnO_2-C$ /GCE, (C) hybridization time ( $t_H$ ), (D) hybridization temperature ( $T_H$ ) of tDNA on pDNA/pTyr/ $SnO_2-C$ /GCE on the  $R_{et}$ . The electrolyte is a 1.0 mM  $[Fe(CN)_6]^{3-/4-}$  (1:1) with 0.1 M KCl. The Hybridization concentration of tDNA is 10 pM.

Then the performance of the biosensor was studied through reaction with tDNA with different concentrations under the optimal conditions. Fig. 2-3.9A displays the Nyquist plots of the biosensor upon interaction with different concentrations of tDNA increasing from 1.0 aM to 100 pM. The results show that, with increasing of the tDNA concentration in the hybridization solution, the obtained  $R_{et}$  value decreases gradually. When the difference values ( $\Delta R_{et}$ ) between  $R_{et}$  at pDNA modified electrode before and after hybridizing was adopted as the analytical signals, it is found that  $\Delta R_{et}$  values varies as the logarithm of tDNA concentrations ( $\lg C$ ) in a wide range from 1.0 aM to 100 pM with a linear equation of  $\Delta R_{et}/K\Omega=0.564\lg(C/M)+11.31$ ,  $R^2=0.997$  (Fig. 2-3.9B), and the detection limit was 0.53 aM using  $3\sigma/s$ , where  $\sigma$  was the standard deviation of the blank solution with 11 parallel measurements and  $s$  is the slope of the linear relationship. Table 2-3.2 lists the comparison results of analytical performance including the linear ranges and detection limits of DNA biosensors based on different polymer. From the results, it is found that a low limit of detection is achieved on the prepared DNA biosensor, confirming that our biosensor displays an excellent performance, which may be derived from the synergic effect of pTyr providing abundant functional groups for tight immobilization of pDNA and SnO<sub>2</sub>-C with large surface area to enhance loading amount of pDNA. Additionally, the excellent performance can also be attributed to a “signal-off” response that strictly depends on the hybridization reaction. The mechanism can be explained by the change of the state and environment of the biosensor surface before and after hybridization reaction (Fig. 2-3.9C): before hybridization with tDNA, the unhybridized pDNA presents high flexibility, and overlies on the pTyr/SnO<sub>2</sub>-C layer via the hydrogen bonding between the exposed bases on pDNA and the free 4'-hydroxyl group (-OH) of the pTyr.

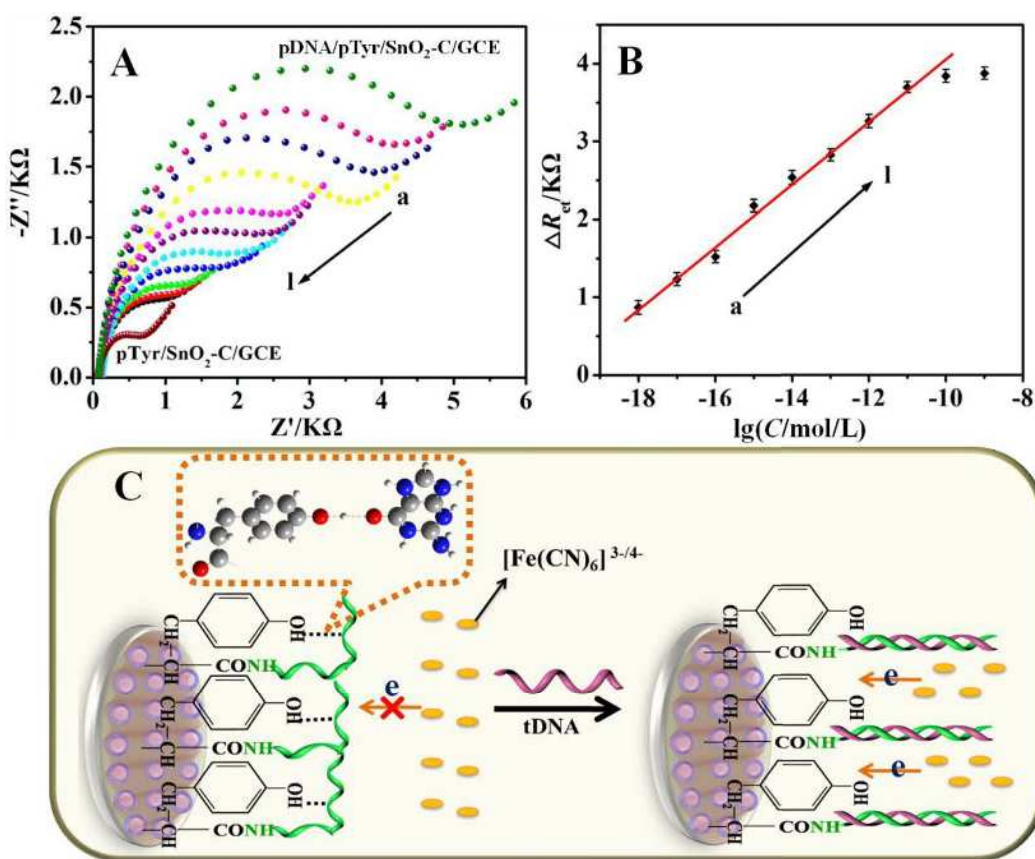


Fig. 2-3.9 (A) Nyquist diagrams of pDNA/pTyr/SnO<sub>2</sub>-C/GCE before (a) and after hybridization with 1.0 aM (b), 10 aM (c), 100 aM (d), 1.0 fM (e), 10 fM (f), 100 fM (g), 1.0 pM (h), 10 pM (i), 100 pM (j), 1.0 nM (k) tDNA in 1.0 mM [Fe(CN)<sub>6</sub>]<sup>3-/4-</sup> (1:1) with 0.1 M KCl solution. (B) The calibration curve for  $\Delta R_{et}$  values versus the logarithm of tDNA concentrations ( $\lg C$ ). (C) The illustration of the hydrogen bonding effect before and after hybridization reaction.

Table 2-3.2 Analytical performance of DNA biosensors designed with different inorganic material or organic polymer composites as probe immobilization matrix

Electrode materials	Indicator	Method	Linear range (M)	LOD (M)	Ref.
Fe <sub>3</sub> O <sub>4</sub> /r-GO	Lable-free	DPV	1.0×10 <sup>-17</sup> –1.0×10 <sup>-8</sup>	2.0×10 <sup>-18</sup>	[36]
MB-Mediated CSDP/HRCA	MB	DPV	1.0×10 <sup>-17</sup> –1.0×10 <sup>-11</sup>	8.9×10 <sup>-18</sup>	[37]
AP1/AP2/Au	[Ru(NH <sub>3</sub> ) <sub>6</sub> ] <sup>3+</sup>	DPV	2.0×10 <sup>-18</sup> –1.0×10 <sup>-11</sup>	2.0×10 <sup>-18</sup>	[38]
AuNCs/GR/Au	KCl	LSV	2.0×10 <sup>-17</sup> –2.0×10 <sup>-11</sup>	5.7 ×10 <sup>-17</sup>	[39]
PEDOT-Citrate/Ni <sup>2+</sup> /Peptide	[Fe(CN) <sub>6</sub> ] <sup>3-/4-</sup>	DPV	1.0×10 <sup>-16</sup> –1.0×10 <sup>-10</sup>	3.0×10 <sup>-17</sup>	[40]
PANHS/rGO/GCE	[Fe(CN) <sub>6</sub> ] <sup>3-/4-</sup>	EIS	1.0×10 <sup>-18</sup> –1.0×10 <sup>-10</sup>	3.5×10 <sup>-19</sup>	[41]
nanoMoS <sub>2</sub> /CPE	Lable-free	DPV	1.0×10 <sup>-16</sup> –1.0×10 <sup>-10</sup>	1.7×10 <sup>-17</sup>	[42]
AuNP/hemin-rGO/GCE	hemin-rGO	DPV	1.0×10 <sup>-18</sup> –1.0×10 <sup>-13</sup>	1.4×10 <sup>-19</sup>	[43]
N-G/Au/GCE	[Fe(CN) <sub>6</sub> ] <sup>3-/4-</sup>	DPV	1.0×10 <sup>-14</sup> –1.0×10 <sup>-7</sup>	3.1×10 <sup>-15</sup>	[44]
NG-Fe <sub>3</sub> O <sub>4</sub> NPs	MB	DPV	1.0×10 <sup>-14</sup> –1.0×10 <sup>-7</sup>	2.2×10 <sup>-15</sup>	[45]
pTyr/SnO <sub>2</sub> -C/GCE	[Fe(CN) <sub>6</sub> ] <sup>3-/4-</sup>	EIS	1.0×10 <sup>-18</sup> –1.0×10 <sup>-10</sup>	5.3×10 <sup>-19</sup>	This work.

rGO: Reduced Graphene oxide; MB: methyleneblue; CSDP: circular strand displacement polymerization; HRCA: hyperbranched rolling circle amplification; AP1: auxiliary probe 1; AP2: auxiliary probe 2; GR: graphene; PEDOT: poly(3,4-ethylenedioxythiophene); PANHS: 1-pyrenebutyric acid-N- hydroxysuccinimide ester; CPE: carbon paste electrode; N-G: nitrogen-doped graphene

In order to study the detailed hydrogen bonding situation between the hydroxyl terminal of tyrosine and bases of DNA, the binding energies ( $E_B$ ) of various bases (including adenine (A), cytosine (C), thymine (T), guanine (G)) to the hydroxyl-terminated tyrosine monomer were studied by DFT calculations according to the formula of  $E_B = E_{\text{base-Tyr}} - (E_{\text{base}} + E_{\text{Tyr}})$  [25], where  $E_{\text{base-Tyr}}$  is the stabilization energy of the various bases interacting with Tyr,  $E_{\text{base}}$  is the stabilization energy of the bases and  $E_{\text{Tyr}}$  is the stabilization energy of Tyr. The negative and positive values of the  $E_B$  mean the effective and un-effective bonding between the hydroxyl-terminated of tyrosine monomers and bases. The calculated models and results are displayed in Fig. 2-3.10. Clearly, the negative  $E_B$  (-1.04 keV) is only obtained for the interaction between G base and Tyr. The result suggests that the single-stranded DNA probes lie on electrode surface through hydrogen bonding of G base with hydroxyl-terminated of pTyr film.

Thus, a layer of thick DNA molecule membrane with dense negative charges is formed on the sensor surface. This prevents the diffusion of electroactive  $[\text{Fe}(\text{CN})_6]^{3-/4-}$  from bulk solution to the electrode surface because of stereo-hindrance effect and electrostatic repulsion. However, when the pDNA is hybridized with tDNA, the double-helix pDNA-tDNA structure was formed, the lying pDNAs are driven to erect perpendicular to the electrode surface attribute to the rigid structure of the double-stranded DNA. Because the erected double-stranded DNA has relatively low steric hindrance and high hydrophilicity in comparison with single-stranded DNA, the  $[\text{Fe}(\text{CN})_6]^{3-/4-}$  molecules are easier to diffuse from the bulk solution to the electrode surface along the interspace between double-stranded DNAs, leading to lower  $R_{\text{ct}}$  values. Obviously, the mechanism of the propositional sensor is a typical “signal-off” impedimetric process. Currently, most impedimetric biosensors are based on a “signal-on” mechanism, i.e., the impedance signal enhancement correlates with the analyte concentration. However, in this type of sensing mechanism, the nonspecific adsorption of the other substances may also induce an increase of impedance values, leading to a false position result. In contrast, the “signal-off” characteristic presents in this work is strictly dependent on the hybridization-induced changes in configuration and charge density, refuse the false position result and resulting in a higher accuracy.

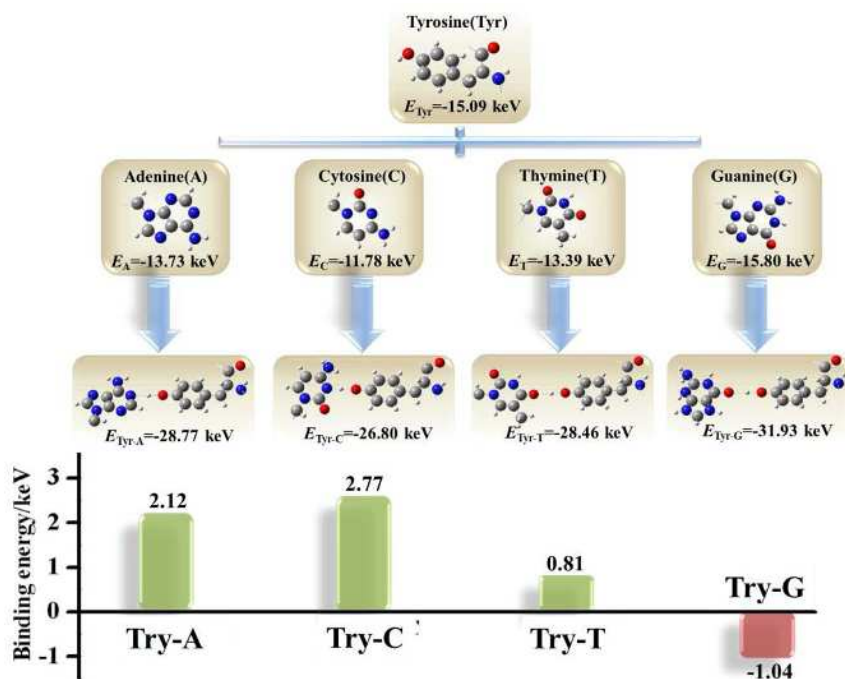


Fig. 2-3.10 The binding energies ( $E_B$ ) of various bases (adenine (A), cytosine (C), thymine (T), guanine (G)) to the hydroxyl-terminated of tyrosine monomer were resulting from DFT calculation models.

### 2-3.3.4 Selectivity, Reproducibility, and Reusability of developed Biosensor

The hybridization specificity of the biosensor was inspected through interaction with various DNA fragments. Fig. 2-3.11 displays the achieved Nyquist diagrams of pDNA/pTyr/SnO<sub>2</sub>-C/GCE after hybridization with various sequences. The results show the value of  $R_{et}$  on NC sequences hybridized electrode (curve b) is close to that on probe electrode (curve a), indicating NC has not been captured on the surface of pDNA/pTyr/SnO<sub>2</sub>-C/GCE because of the entire base-mismatching. However, the  $R_{et}$  value decreases obviously when the biosensor is hybridized with tDNA due to fully complementary sequences (curve e), confirming the pDNA and the complementary tDNA are formed the integrated duplex to facilitate the electro active  $[\text{Fe}(\text{CN})_6]^{3-4-}$  to diffuse to the electrode surface. Moreover, the high selectivity of the biosensor was assessed by a suite of hybridization experiments were performed for the DNA sequences with the various base-mismatch numbers. From the results (curve c and curve d), the  $R_{et}$  values differences of the 3MT and 1MT sequences are 52.8% and 70.5% of that of fully complementary sequences, respectively, and the  $R_{et}$  values decrease with the decrease of the base-mismatch numbers, indicating that the biosensor is capable of identifying the mismatching degree of the target sequences.

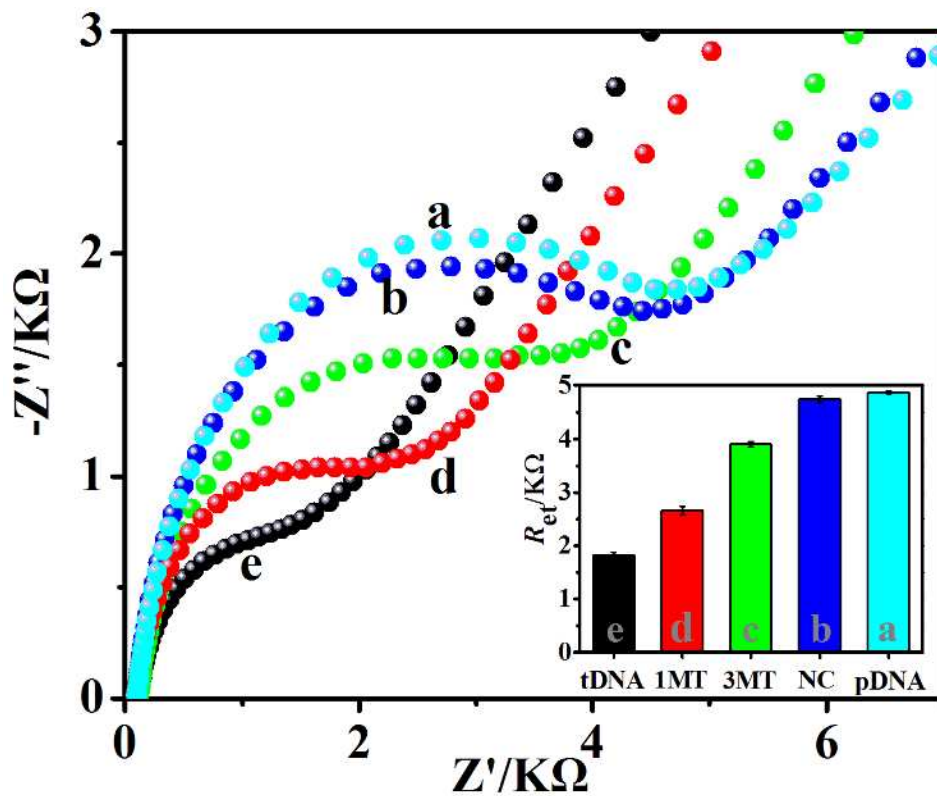


Fig. 3-2.11 Nyquist diagrams of the biosensor before (a) and after hybridization with 10 pM NC (b), 3MT (c), 1MT (d) and tDNA (e). (Inset is the corresponding histogram of  $R_{et}$  values.)

The reproducibility was evaluated by comparing the results of detecting 10 pM tDNA by five parallelly fabricated biosensors (Fig. 2-3.12A). The relative standard deviation (RSD) of the  $\Delta R_{et}$  values obtained from the five independent biosensors was estimated to be 5.2%, showing the developed method of the DNA biosensor preparation and performance analysis is reproducibility. The reusability of the DNA sensor was investigated by unwinding the hybridized biosensor surface in hot water (90 °C) for 10 min, and then cooled rapidly in an ice bath for 5 min. After rinsed with water, the biosensor was hybridized with target again. Such a reusability experiment shows that the hybridization ability of the sensor can be remained at least 5 cycles. Fig. 2-3.12B shows the EIS responses of the reusability electrodes before and after hybridizing with tDNA. The  $R_{et}$  values of the reusability electrode and its hybridized electrode for 5 cycles (curve e and e') are close to those obtained in the initial cycle (curve a and a'), only 7.7 % and 8.4 % signal are lost, respectively.

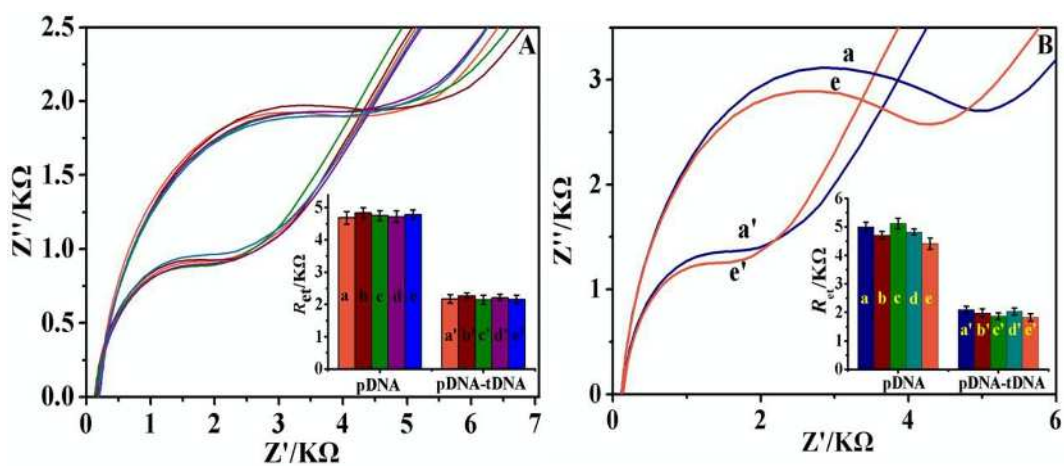


Fig. 2-3.12 EIS responses of (A) pDNA/pTyr/SnO<sub>2</sub>-C modified five independent electrodes hybridized with complementary tDNA (10 pM) (B) before (a, a') and after (e, e') of the regenerated electrodes and its hybridized electrodes for 5 rounds.

### 2-3.3.5 Real soybean samples analysis

In order to testify the practical application of the developed biosensor for CaMV35s promoter gene detection in real samples, the transgenic (TG) soybean samples, non-transgenic (non-TG) soybean samples and blank solution were adopted as examples for analysis and comparison. As shown in Fig. 2-3.13A, after hybridization with DNA extracted from TG soybean, the  $R_{ct}$  value of the biosensor is distinctly decreased (curve d). As compared, the EIS signal variation for blank sample (curve b) and DNA extracted from non-TG soybean sample (curve c) are negligible. The results indicate that the DNA biosensor can effectively differentiate the TG from non-TG soybeans without PCR treatment. To investigate the reliability of the electrochemical biosensor, the homiothermy fluorescence method was also applied to detect the blank sample, standard sample with CaMV35s fragments, and PCR products of DNA extracted from TG soybean samples and non-TG soybean samples. The fluorescence detection results for above four samples are shown in Fig. 2-3.13B. The results show that the fluorescence signals of TG soybean sample (purple dots) obviously exceed the signal line of target threshold, and close to the responses of the standard sample with CaMV35s sequence (red dots), suggesting that the method is responsive to CaMV35s contained TG sample. Whereas the responses of the blank sample (black dots) and non-TG soybean sample (green dots) are obviously lower than the target threshold line. All these results are in accordance with those of the electrochemical biosensor, suggesting the proposed biosensor is reliability and shows the potential application in PCR-free transgenic crops monitoring.

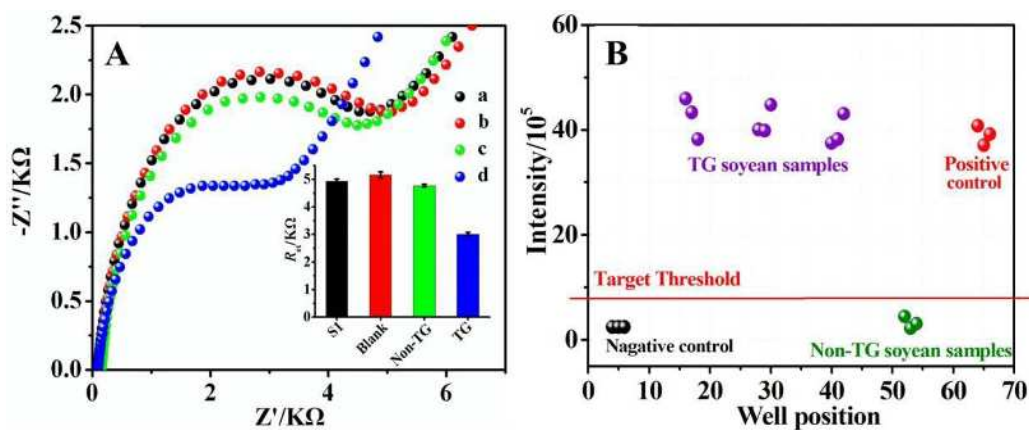


Fig. 2-3.13 (A) Nyquist diagrams of the biosensor before (a) and after incubation in blank buffer (b), and PCR sample from non-TG soybean (c) and TG soybean (d). (Inset is the histogram of  $R_{et}$  values). (B) PCR samples of non-TG soybean and TG soybean detected by homiothermy fluorescence method.

### **2-3.4 Conclusions**

In summary, an inorganic-organic hybrid material consisting SnO<sub>2</sub>-C yolk-shell nanospheres and poly-Tyrosine (pTyr) has been developed for DNA biosensor fabrication. Electrochemical experiments show that the existence of SnO<sub>2</sub>-C in the hybrid matrix remarkably enhances the effective surface area, and the pTyr not only provides abundant carboxyl groups for covalent bonding with pDNA, but also its 4'-hydroxyl group shows hydrogen bonding with the base groups of pDNA. When tDNA was hybridized with the probe DNA, the “signal-off” response in EIS measurement is obtained. The reason is likely related to the change of the state and environment of the biosensor surface before and after hybridization reaction. An ultralow detection limit of 0.53 aM for CaMV35s promoter gene is achieved. Meanwhile, it potentially becomes a convenient tool of PCR-free TG sequences analysis for medical, pabular, and environmental purposes.

## 2-3.5 References

- [1] M. N. Garcia-Casal, J. P. Peña-Rosas, B. Giyose, *Ann. N. Y. Acad. Sci.*, **1390**, 3 (2017).
- [2] Y. Zhang, L. Jing, Q. Bai, W. Shao, Y. Feng, S. Yin, M. Zhang, *Food Qual Prefer.*, **65**, 118 (2018).
- [3] Y. Li, L. Sun, J. Qian, C. Wang, Q. Liu, E. Han, N. Hao, L. Zhang, J. Cai, K. Wang, *Anal. Chim. Acta.*, **948**, 90 (2016).
- [4] J. Liu, H. Xie, B. Zha, W. Ding, J. Luo, C. J. Hu, *Appl. Spectrosc.*, **85**, 119 (2018).
- [5] L. Krejcová, L. Richtera, D. Hýnek, J. Labuda, V. Adam, *Biosens. Bioelectron.*, **97**, 384 (2017).
- [6] F. Zhan, X. Liao, F. Gao, W. Qiu, Q. Wang, *Biosens. Bioelectron.*, **92**, 589 (2017).
- [7] C. L. Manzanares-Palenzuela, J. P. Martín-Clemente, M. J. Lobo-Castañón, B. López-Ruiz, *Talanta*, **164**, 261 (2017).
- [8] F. Gao, X. Cai, X. Wang, C. Gao, S. Liu, F. Gao, Q. Wang, *Sens. Actuators, B*, **186**, 380 (2013).
- [9] M. Faustini, L. Nicole, E. Ruiz-Hitzky, C. Sanchez, *Adv. Funct. Mater.*, **28**, 1704158 (2018).
- [10] J. Han, M. Wang, Y. Hu, C. Zhou, R. Guo, *Prog. Polym. Sci.*, **70**, 52 (2017).
- [11] D. Zheng, Q. Wang, F. Gao, Q. Wang, W. Qiu, F. Gao, *Biosens. Bioelectron.*, **60**, 167 (2014).
- [12] B. B. Jiang, X. F. Sun, L. Wang, S. Y. Wang, R. D. Liu, S. G. Wang, *Chem. Eng. J.*, **311**, 135 (2017).
- [13] B. J. Jongkees, B. Hommel, S. Kühn, L. S. Colzato, *J. Psychiatr. Res.*, **70**, 50 (2015).
- [14] Y. Wang, C. Bi, *J. Mol. Liq.*, **177**, 26 (2013).
- [15] A. Slominski, M. A. Zmijewski, J. Pawelek, *Cell Melanoma Res.*, **25**, 14 (2012).
- [16] F. Li, G. Luo, J. Yu, W. Huang, D. Xu, W. Chen, X. Yu, *J. Alloys Compd.*, **773**, 778 (2019).
- [17] H. Wang, G. Jiang, X. Tan, J. Liao, X. Yang, R. Yuan, Y. Chai, *Inorg. Chem. Commun.*, **95**, 67 (2018).
- [18] N. M. Al-Hada, H. M. Kamari, A. A. Baqer, A. H. Shaari, E. Saion, *Nanomaterials*, **8**, 250 (2018).

- [19] T. J. Jiang, Z. Guo, J. H. Liu, X. J. Huang, *Electrochim. Acta*, **191**, 142 (2016).
- [20] Y. Wei, C. Gao, F. L. Meng, H. H. Li, L. Wang, J. H. Liu, X. J. Huang, *J. Phys. Chem. C*, **116**, 1034 (2011).
- [21] D. Zhou, W. L. Song, L. Z. Fan, *ACS Appl. Mater. Interfaces*, **7**, 21472 (2015).
- [22] Z. Wang, T. Han, T. Fei, S. Liu, T. Zhang, *ACS Appl. Mater. Interfaces*, **10**, 41773 (2018).
- [23] J. Singh, P. Kumari, S. Basu, *J. Photochem. Photobiol. A*, **371**, 136 (2019).
- [24] S. Wang, Q. Liu, H. Li, Y. Li, N. Hao, J. Qian, W. Zhu, K. Wang, *J. Electroanal. Chem.*, **782**, 19 (2016).
- [25] I. Bald, S. Weigelt, X. Ma, P. Xie, R. Subramani, M. Dong, C. Wang, W. Mamdouh, J. Wang, F. Besenbacher, *Phys. Chem. Chem. Phys.*, **12**, 3616 (2010).
- [26] S. Chen, L. Shen, P. A. van Aken, J. Maier, Y. Yu, *Adv. Mater.*, **29**, 1605650 (2017).
- [27] H. Jing, X. Song, S. Ren, Y. Shi, Y. An, Y. Yang, M. Feng, S. Ma, C. Hao, *Electrochim. Acta*, **213**, 252 (2016).
- [28] V. K. Tomer, S. Duhan, *J. Mater. Chem. A*, **4**, 1033 (2016).
- [29] D. Jia, L. Wang, Y. Gao, L. Zou, B. Ye, *J. Electroanal. Chem.*, **764**, 56 (2016).
- [30] S. Cheemalapati, B. Devadas, S. M. Chen, M. A. Ali, F. M. Al-Hemaid, *Anal. Methods*, **6**, 6774 (2014).
- [31] D. Zheng, Q. Wang, F. Gao, Q. Wang, W. Qiu, F. Gao, *Biosens. Bioelectron*, **60**, 167 (2014).
- [32] Y. Yang, F. Gao, X. Cai, X. Yuan, S. He, F. Gao, H. Guo, Q. Wang, *Biosens. Bioelectron*, **74**, 447 (2015).
- [33] L. Shi, Z. Chu, X. Dong, W. Jin, E. Dempsey, *Nanoscale*, **5**, 10219(2013).
- [34] B. Xu, D. Zheng, W. Qiu, F. Gao, S. Jiang, Q. Wang, *Biosens. Bioelectron*, **72**, 175 (2015).
- [35] Q. Wang, R. Liu, X. Yang, K. Wang, J. Zhu, L. He, Q. Li, *Sens. Actuators, B*, **223**, 613 (2016).
- [36] H. Teymourian, A. Salimi, S. Khezrian, *Electroanalysis*, **29**, 409 (2017).
- [37] X. Li, J. Guo, Q. Zhai, J. Xia, G. Yi, *Anal. Chim. Acta*, **934**, 52 (2016).
- [38] X. Chen, C. Y. Hong, Y. H. Lin, J. H. Chen, G. N. Chen, H. H. Yang, *Anal. Chem.*, **84**, 8277 (2012).
- [39] W. Wang, T. Bao, X. Zeng, H. Xiong, W. Wen, X. Zhang, S. Wang, *Biosens. Bioelectron*, **91**, 183 (2017).

- [40] G. Wang, R. Han, X. Su, Y. Li, G. Xu, X. Luo, *Biosens. Bioelectron.*, **92**, 396 (2017).
- [41] A. Benvidi, M. D. Tezerjani, S. Jahanbani, M. M. Ardakani, S. M. Moshtaghioun, *Talanta*, **147**, 621 (2016).
- [42] X. Wang, F. Nan, J. Zhao, T. Yang, T. Ge, K. Jiao, *Biosens. Bioelectron.*, **64**, 386 (2015).
- [43] Y. Ye, J. Gao, H. Zhuang, H. Zheng, H. Sun, Y. Ye, X. Xu, X. Cao, *Microchim. Acta*, **184**, 245 (2017).
- [44] M. Chen, C. Hou, D. Huo, J. Bao, H. Fa, C. Shen, *Biosens. Bioelectron.*, **85**, 684 (2016).
- [45] M. Chen, C. Hou, D. Huo, H. Fa, Y. Zhao, C. Shen, *Sens. Actuators, B*, **239**, 421 (2017).

## **Chapter 3**

# **The functionalization of metal-organic frameworks (MOFs) and their application in electrochemical sensors**

**3-1 Flexible flower-like MOF of  
 $\text{Cu}_2(\text{trans-1,4-cyclohexanedicarboxylic acid})_2$  as the electroactive  
matrix material for label-free and highly sensitive sensing of  
thrombin**

### 3-1.1 Introduction

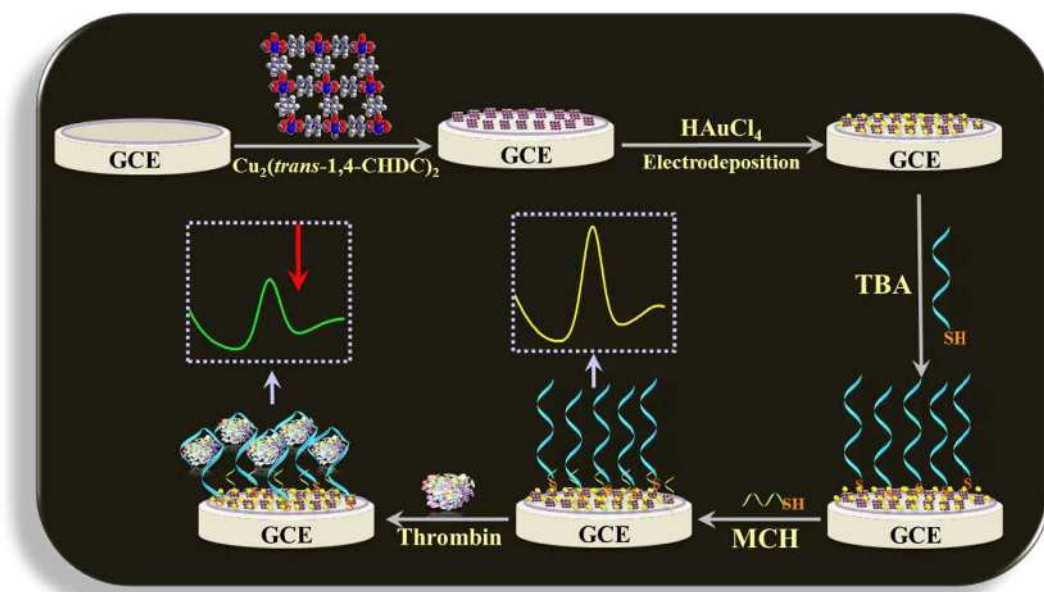
Thrombin is a serine protease and an important component in the process of blood clotting. Its concentration in the blood can be used as a biomarker for the diagnosis of some diseases, such as pulmonary metastases, arterial thrombosis and many diseases caused by abnormal blood clotting [1, 2]. Because of its biological importance, the development of highly selective and sensitive biosensors for thrombin monitoring poses great importance to the basic research.

Aptamer is a type of single-stranded nucleic acid molecule, which is considered to be an effective substitute for antibodies in immunoassay and biotechnology [3, 4]. The aptamer has a high binding affinity to the target molecule due to the folding ability of the aptamer when it binds with the target molecule. Therefore, the aptamer can act as an ideal tool for clinic diagnosis, treatment and sensing [5, 6]. Since the 15-mer thrombin-binding aptamer (TBA) was first proposed in 1992, it has attracted great attention of scientists because of its strong affinity and high selectivity to thrombin [7]. A series of biosensors based on the thrombin aptamer combined with different signal output methods, including chromatometry [8], fluorometry [9], Raman scattering [10], etc., have been widely studied, but the application of the traditional methods are limited because of the high cost of the apparatus and the tedious of the detection process. However, the construction of electrochemical sensor platform based on thrombin aptamer can overcome the above-mentioned unfavorable factors. The electrochemical aptasensor has inherent advantages of rapidity, low cost, portable and simple processing [11, 12]. In addition, the selection of appropriate electrode materials and the design of the rational sensing platform are also important factors for the fabrication of high-performance biosensors. For example, our group has prepared a composite film of yolk-shell structured  $\text{SnO}_2\text{-C}$  and Poly-Tyrosine and used it as an impedimetric “signal-off” platform for sensitive screening of transgenic soybean [13]. Li et al. proposed a signal amplification strategy based on the co-catalysis of hemin/G-quadruplex DNAzyme and  $\text{Cu}_2\text{O-Au}$  nanocomposite [14].

In the past two decades, the research on MOFs has developed rapidly, and a large number of MOFs with various structures have been synthesized, and applied in the fields of gas separation, energy storage and conversion, and electrochemical sensing [15-18]. But the traditional MOFs usually exhibit the disadvantage of poor stability under the operating conditions, through which the framework will be collapsed when the guest solvent is removed. In 1997, Kitagawa and his co-worker [19] first reported a kind of MOFs material whose skeleton structure can be inversely deformed. The discovery of this kind of flexible MOFs breaks the traditional concept that the skeleton rigidity of MOFs materials is unchanged. The discovery attracted the attention of chemists all over the world and this type of MOFs was also regarded as the third generation functional MOFs material [20]. Compared with the rigid MOFs, the hydrophobic groups and pillar-layer structure in the flexible MOFs can effectively avoid the collapse of the framework caused by the substitution of water molecules for organic ligands to coordinate with metal node. As a result, higher thermal and mechanical stability of the flexible MOFs are presented, and the pore structure is maintained after the removal of guest solvents such as water molecules [21, 22].  $\text{Cu}_2(\textit{trans}\text{-}1,4\text{-cyclohexanedicarboxylic acid})_2$  ( $\text{Cu}_2(\text{CHDC})_2$ ) is one of the typical representatives of pillar-layer flexible MOFs. The rigidity of the dimer paddle-wheel  $\text{Cu}_2(\text{COO})_4$  core and the slight elasticity of the -CHDC connector result in the amazing stability of the framework and maintain excellent porosity after solvent removal [23]. In addition, the hydrophobicity of the group of -CHDC further enhances the framework stability in the humid environment.

Herein, we demonstrated a facile assay for label-free thrombin detection based on  $\text{Cu}_2(\text{CHDC})_2$ . The flexible MOF of  $\text{Cu}_2(\text{CHDC})_2$  bearing excellent redox property and large surface area was synthesized by a mild hydrothermal method and coated onto the glassy carbon electrode (GCE) surface, to obtain the electroactive sensing layer. Then the gold nanoparticles (AuNPs) were electrodeposited on the surface of  $\text{Cu}_2(\text{CHDC})_2$  modified electrode. The AuNPs have dual functions in this work, namely, promoting the electrochemical response of  $\text{Cu}_2(\text{CHDC})_2$  layer by its excellent electronic conductivity and acting as the immobilization matrix of bio-probe via Au-S

bond. In addition, the electrodeposited AuNPs on the electrode surface effectively promotes the stability of the interface that is physically modified with  $\text{Cu}_2(\text{CHDC})_2$ . After that, the thrombin aptamer chain was immobilized on the AuNPs surface by the Au-S bonding to form a bio-recognition layer. Thus, an electrochemical aptasensor using TBA as a recognition probe and  $\text{Cu}_2(\text{CHDC})_2$  as an electrochemical indicating material was constructed (Scheme 3-1.1). The proposed thrombin biosensor displays an outstanding performance with wide linear range, ultralow detection limit of 0.01 fM (S/N=3), and favorable specificity. The aptasensor was also successfully applied in the real human serum detection. The results demonstrate that the fabricated aptasensor has a potential application in the clinical diagnosis.



Scheme 3-1.1 Schematic illustration of the fabrication and application of the  $\text{Cu}_2(\text{CHDC})_2$  based electrochemical thrombin biosensor.

## 3-1.2 Experimental

### 3-1.2.1 Reagents and Apparatus

Magnesium chloride ( $\text{MgCl}_2$ ), sodium chloride ( $\text{NaCl}$ ), potassium ferricyanide ( $\text{K}_3\text{Fe}(\text{CN})_6$ ), potassium chloride ( $\text{KCl}$ ), potassium ferrocyanide ( $\text{K}_4\text{Fe}(\text{CN})_6$ ) were provided by Guangdong Xilong Chemical Co., Ltd. (China). N,N-dimethylformamide (DMF), copper nitrate trihydrate ( $\text{Cu}(\text{NO}_3)_2 \cdot 3\text{H}_2\text{O}$ ), *trans*-1,4-cyclohexanedicarboxylic acid ( $\text{H}_2\text{CHDC}$ ) was provided by Aladdin Reagent Co., Ltd. (China). Tris (hydroxymethyl) aminomethane (Tris), 6-mercapto-1-hexanol (MCH), tris (2-carboxyethyl) phosphine hydrochloride (TCEP), thrombin, bovine serum albumin (BSA), hemoglobin (Hb) and trypsin (Try) were obtained from Sigma-Aldrich Reagent Co., Ltd. (China). Chloroauric acid ( $\text{HAuCl}_4 \cdot 4\text{H}_2\text{O}$ ) was obtained from Sinopharm Chemical Reagent Co., Ltd. (China). All the aqueous solutions were prepared with ultrapure water. All the chemicals were of analytical grade and used without further purification.

Thiolated thrombin aptamers (TBA) ( $5'\text{-SH}-(\text{CH}_2)_6\text{-GGT TGG TGT GGT TGG-3}'$ ) was ordered from Sangon Biotech Co., Ltd. (Shanghai, China). The thrombin was prepared with 0.9% NaCl solution and TBA was prepared with mixed Tris buffer that contains 100 mM  $\text{MgCl}_2$ , 100 mM NaCl, 10 mM TCEP, 25 mM Tris-HCl and kept at 4 °C for the following use. The supporting electrolyte for electrochemical measurements was phosphate-buffered solution (PBS) (pH 6.86).

The electrochemical measurements were evaluated using CHI 660E electrochemical workstation in connection with a three-electrode system. The working electrode, auxiliary electrode and reference electrode were bare or modified glass carbon electrode (GCE), platinum wire and Ag/AgCl (3 M KCl), respectively. X-ray diffraction (XRD) patterns of the MOF material were achieved from a Rigaku Miniflex-II diffractometer with Cu  $K\alpha$  radiation (Japan).

Scanning electron microscopy (SEM) images were obtained from JSM-60-10LA

(Japan). The sample for TEM and HRTEM was obtained by grounding the synthesized  $\text{Cu}_2(\text{CHDC})_2$  powder and then dispersing into anhydrous ethanol by strong ultrasonication more than 0.5 h. Transmission electron microscope (TEM) and high-resolution TEM (HRTEM) were recorded on Tecnai G2 F20 (USA). Atomic force microscopy (AFM) characterization on the modified electrode was executed on a CSPM5500 scanning probe microscope (China). Nitrogen adsorption-desorption isotherms were determined by Automated Gas Sorption Analyzer (Autosorb-IQ, USA).

### **3-1.2.2 Synthesis of $\text{Cu}_2(\text{CHDC})_2$**

$\text{Cu}_2(\text{CHDC})_2$  was synthesized based on the reported method with a slight modification [23, 24]. In a typical synthesis, 240.6 mg (1.0 mmol) of  $\text{Cu}(\text{NO}_3)_2 \cdot 3\text{H}_2\text{O}$  and 172.2 mg (1.0 mmol) of  $\text{H}_2\text{CHDC}$  were dissolved in 30 mL DMF. The solution was shifted to the round bottom flask and refluxed at 130 °C for 24 h. After cooling to the room temperature, the resulting blue precipitate i.e., the product of  $\text{Cu}_2(\text{CHDC})_2$  was washed with DMF and acetone several times and dried under vacuum at 80 °C .

### **3-1.2.3 Fabrication of the biosensing interface**

Prior to the experiment, the bare GCE was mechanically polished with alumina powder as previously reported [25]. Followed by, 1.0 mg of synthesized  $\text{Cu}_2(\text{CHDC})_2$  was dispersed in 10 mL ultrapure water by ultrasonication, an uniform suspension was prepared. Then, 10  $\mu\text{L}$  suspension was coated onto the cleaned GCE surface for dryness at room temperature. The  $\text{Cu}_2(\text{CHDC})_2$  modified electrode ( $\text{Cu}_2(\text{CHDC})_2/\text{GCE}$ ) was further electrochemically scanned in 0.5 mM  $\text{HAuCl}_4$  solution for 30 cycles with scan rate of 100  $\text{mV s}^{-1}$  within the potential range from -0.5 to 0 V. Subsequently, the electrode was soaked into 1  $\mu\text{M}$  TBA solution for 1 h at 37 °C to immobilize the probe DNA by the Au-S bond to form the sensing platform of TBA/AuNPs/ $\text{Cu}_2(\text{CHDC})_2/\text{GCE}$ . Finally, the uncovered AuNPs active site on the

electrode surface was blocked by MCH for 2 h, and the prepared electrode was named as MCH/TBA/AuNPs/Cu<sub>2</sub>(CHDC)<sub>2</sub>/GCE.

### 3-1.2.4 Thrombin binding and electrochemical measurements

The recognition reaction of the prepared aptasensor to thrombin was inspected by immersing MCH/TBA/AuNPs/Cu<sub>2</sub>(CHDC)<sub>2</sub>/GCE into a thrombin solution with expected concentrations and gently shaken at 37 °C for 30 min. The electrode was then rinsed with PBS buffer and water to remove the unreacted thrombin. The process was also used for the reaction of the aptasensor with the other control proteins. The electrochemical characterization was performed in 1.0 mM [Fe(CN)<sub>6</sub>]<sup>3-/4-</sup> solution containing 0.1 M KCl by cyclic voltammetry (CV) and electrochemical impedance spectra (EIS). The scan range of CV was from -0.2 to +0.6 V with the scan rate of 0.10 V s<sup>-1</sup>. The EIS was executed at a potential of +0.227 V, a frequency range of 10<sup>5</sup>~0.01 Hz and a voltage amplitude of 5 mV. The electrochemical behavior of the aptasensor and its recognition to thrombin detection were obtained from CV and differential pulse voltammetry (DPV) in the PBS buffer (pH 6.86). The response was recorded within the potential range from -0.3 V to +0.4 V.

## 3-1.3 Results and Discussion

### 3-1.3.1 Physical Characterizations of Cu<sub>2</sub>(CHDC)<sub>2</sub>

Fig. 3-1.1A reveals the XRD pattern of the synthesized Cu<sub>2</sub>(CHDC)<sub>2</sub>. From the results, all the diffraction peaks correspond to the triclinic structure of Cu<sub>2</sub>(CHDC)<sub>2</sub> (CCDC No.: 269992) as reported in the literature [23, 24], showing the successful synthesis of the Cu<sub>2</sub>(CHDC)<sub>2</sub>. From the XRD result, its crystal structure is depicted in the inset of Fig. 3-1.1A. Fig. 3-1.1B displays the surface area characterization of the

sample by N<sub>2</sub> adsorption-desorption isotherms at 77 K. It is testified that the sample shows a typical type I curve, indicating the presence of microporous in the sample. According to the corresponding pore size distribution curve (inset of Fig. 3-1.1B), the small pore size of 3.24 nm with high uniformity was achieved. From the Brunner-Emmet-Teller (BET) method, the specific surface area of the product was estimated to be 237.36 m<sup>2</sup>g<sup>-1</sup>, which indicates that the Cu<sub>2</sub>(CHDC)<sub>2</sub> has a high specific surface area.

The morphologies of the Cu<sub>2</sub>(CHDC)<sub>2</sub> were investigated by SEM, and the results are presented in Fig. 3-1.1C and Fig. 3-1.1D. From the SEM images, the hierarchical flower-like shape for the synthesized Cu<sub>2</sub>(CHDC)<sub>2</sub> is observed. The high-resolution SEM image further shows that the Cu<sub>2</sub>(CHDC)<sub>2</sub> nanoflower contains lots of nanoflower contains lots of nanosheets. Such a nanosheet assembly structure contributed to the large surface area of the material. After grinding and strong dispersing into anhydrous ethanol by strong ultrasonication, the detail of nanocluster was further revealed by the TEM, and the result is shown in Fig. 3-1.1E. It was found that the material showed the characteristic of semitransparency, confirming its flaky property. The HRTEM image displays obvious lattice fringes with the lattice spacing of about 0.212 nm (Fig. 3-1.1F), which can be assigned to the (1-40) lattice plane of Cu<sub>2</sub>(CHDC)<sub>2</sub>.

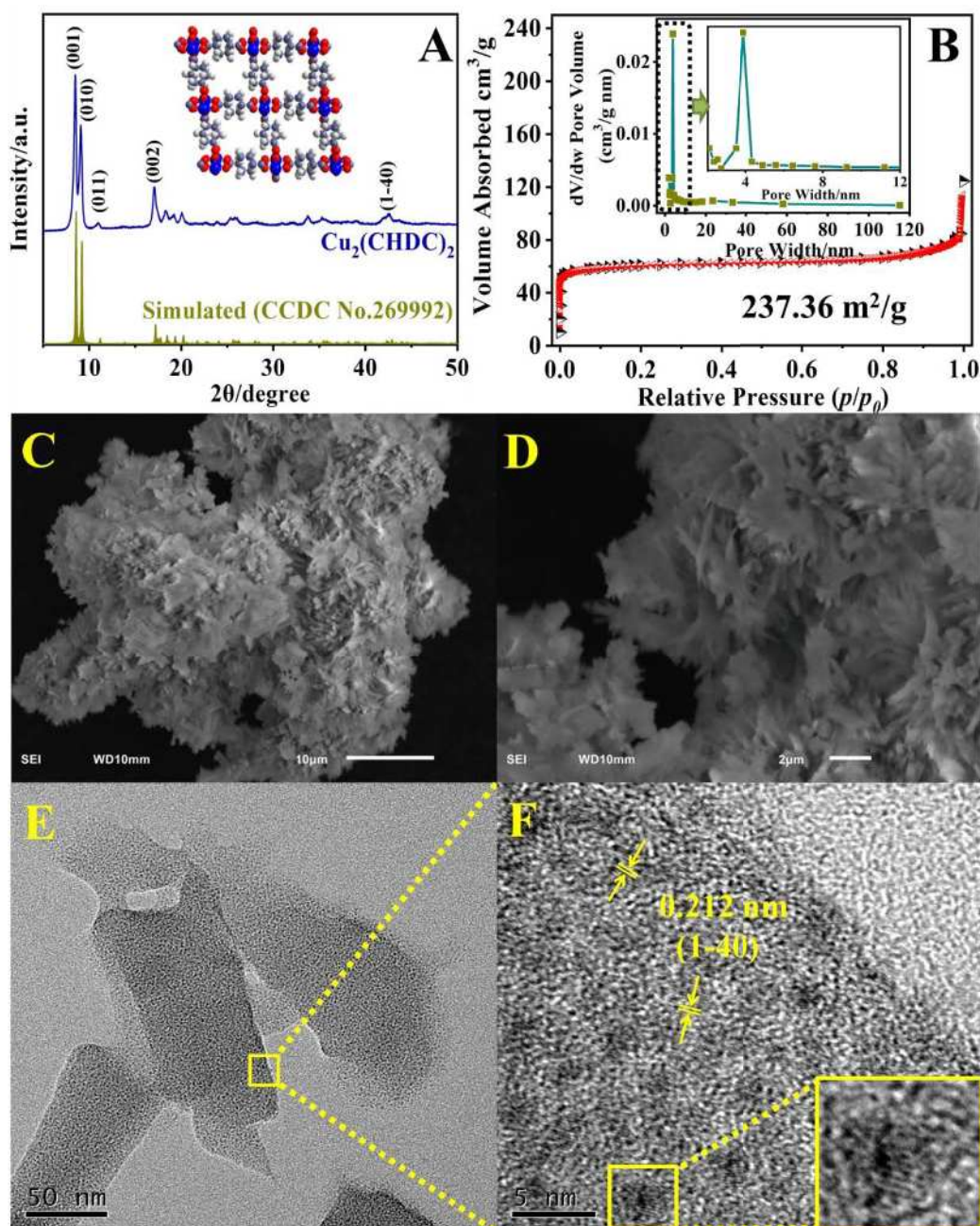


Fig. 3-1.1 XRD pattern and crystal structure (inset) (A),  $\text{N}_2$  adsorption-desorption isotherms and the pore size distribution curve (inset) (B) of the  $\text{Cu}_2(\text{CHDC})_2$ , SEM (C, D), TEM (E), and HRTEM with enlarged lattice fringes part (inset) (F) of  $\text{Cu}_2(\text{CHDC})_2$ .

### 3-1.3.2 AFM and electrochemical characterization of the aptasensor

Layer-by-layer construction of the aptasensor and its effective capture toward the thrombin are verified by the atomic force microscopy (AFM) technique. Fig. 3-1.2 shows the three-dimensional images of  $\text{Cu}_2(\text{CHDC})_2/\text{GCE}$  (A),  $\text{AuNPs}/\text{Cu}_2(\text{CHDC})_2/\text{GCE}$  (B),  $\text{MCH}/\text{TBA}/\text{AuNPs}/\text{Cu}_2(\text{CHDC})_2/\text{GCE}$  (C), and  $\text{Thrombin}/\text{MCH}/\text{TBA}/\text{AuNPs}/\text{Cu}_2(\text{CHDC})_2/\text{GCE}$  (D). As can be seen from Fig. 3-1.2A-a, the surface of  $\text{Cu}_2(\text{CHDC})_2/\text{GCE}$  is rough and some hill-like heaves are observed from the 3D images, suggesting the modification of  $\text{Cu}_2(\text{CHDC})_2$  on the electrode surface. The representative height (H) between the summit and the valley was determined to be 573.9 nm, as determined from the top-viewed image (Fig. 3-1.2A-b) and the cross-sectional image (Fig. 3-1.2A-c). After AuNPs were electrodeposited, the electrode surface changed much smoother, and the size of the “hill” become smaller (Fig. 3-1.2B-a). This can be explained by the deposition of small-sized AuNPs on the  $\text{Cu}_2(\text{CHDC})_2/\text{GCE}$ , which increased the uniformity of the electrode surface. This result was also verified by the smaller H value of 537.1 nm as found in top-viewed (Fig. 3-1.2B-b) and cross-sectional images (Fig. 3-1.2B-c). When the TBA strand and MCH were assembled on the electrode, the peaks increased dramatically, and the H value was increased to 718.5 nm, suggesting that the 1D strand-shaped TBA had been successfully grafted on  $\text{AuNPs}/\text{Cu}_2(\text{CHDC})_2/\text{GCE}$  (Fig. 3-1.2C). These changes demonstrate that it is feasible to construct aptasensor by layer-by-layer assembly strategy. After the sensor was hybridized with thrombin, the surface of the electrode changed obviously. Some ellipsoidal heaves with large size appeared. The top-viewed image shows that there are some gelatinous particles are present, and the H value was further increased to 776.2 nm (Fig. 3-1.2D). This suggests that the bio-macromolecules of thrombin are effectively captured by the aptasensor.

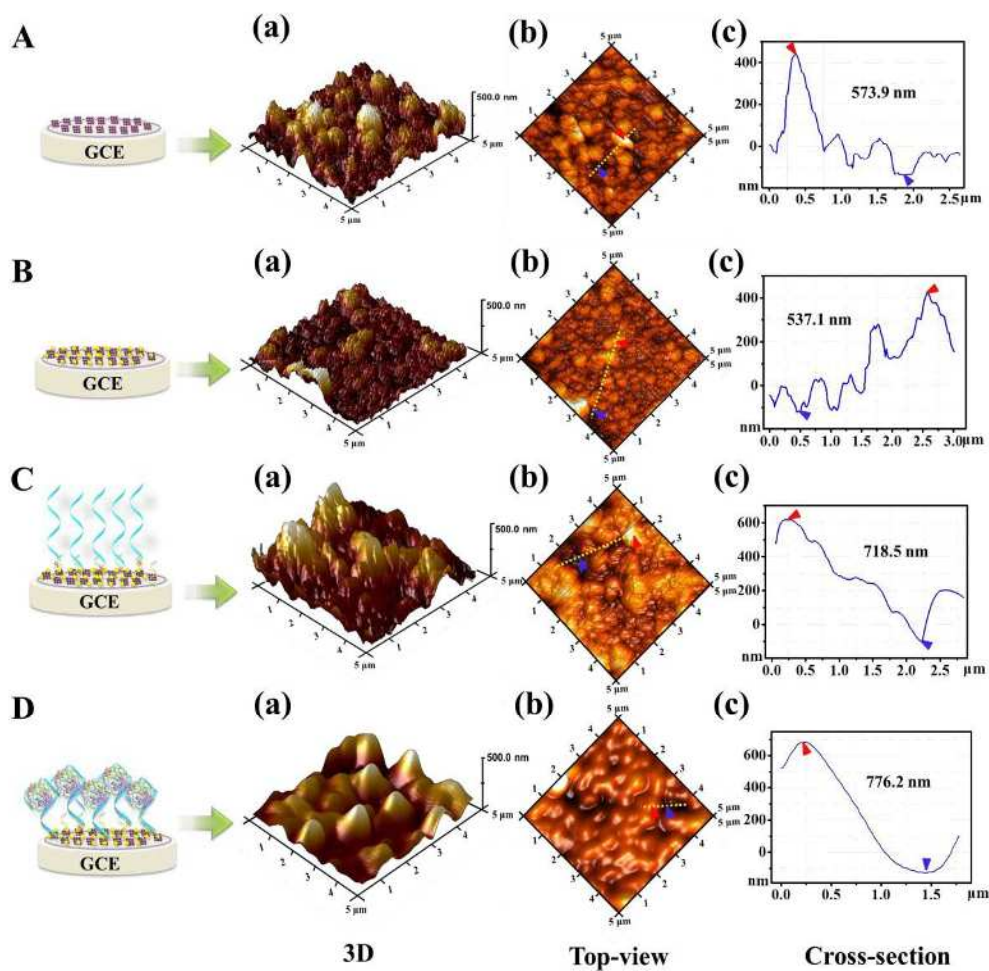


Fig. 3-1.2 Three-dimensional (3D) (a), top-viewed (b), and corss-sectional (c) AFM images of  $\text{Cu}_2(\text{CHDC})_2/\text{GCE}$  (A),  $\text{AuNPs}/\text{Cu}_2(\text{CHDC})_2/\text{GCE}$  (B),  $\text{MCH}/\text{TBA}/\text{AuNPs}/\text{Cu}_2(\text{CHDC})_2/\text{GCE}$  (C), and  $\text{Thrombin}/\text{MCH}/\text{TBA}/\text{AuNPs}/\text{Cu}_2(\text{CHDC})_2/\text{GCE}$  (D).

Fig. 3-1.3A displays the CVs of different electrodes within the potential range from -0.2 V to +0.6 V using  $[\text{Fe}(\text{CN})_6]^{3-/4-}$  as an electroactive probe. A pair of reversible redox peaks were observed at bare GCE (curve a), suggesting that the bare GCE has a good electron transfer process for  $[\text{Fe}(\text{CN})_6]^{3-/4-}$ . However, the redox peak currents of  $[\text{Fe}(\text{CN})_6]^{3-/4-}$  decreased remarkably when the GCE was modified with  $\text{Cu}_2(\text{CHDC})_2$  (curve b). This can be explained by two reasons: (1) the uncoordinated carboxylic group bearing negative charge impeded the  $[\text{Fe}(\text{CN})_6]^{3-/4-}$  diffuses to the electrode surface; (2) The  $\text{Cu}_2(\text{CHDC})_2$  film with poor conductivity hinders the electron transfer kinetics of  $[\text{Fe}(\text{CN})_6]^{3-/4-}$ . Then when the AuNPs were deposited on the surface of the  $\text{Cu}_2(\text{CHDC})_2/\text{GCE}$ , the high conductivity of AuNPs promoted the electron transfer process, causing an obvious increase of redox signal of  $[\text{Fe}(\text{CN})_6]^{3-/4-}$  (curve c). After the TBA was assembled on AuNPs/ $\text{Cu}_2(\text{CHDC})_2/\text{GCE}$  by Au-S bond, the redox peak currents of  $[\text{Fe}(\text{CN})_6]^{3-/4-}$  decreases again and the redox potential difference is enlarged obviously (curve d), which can be explained in term of the electrostatic repulsion between the phosphate skeleton of TBA and  $[\text{Fe}(\text{CN})_6]^{3-/4-}$ . After the electrode was grafted with MCH, the redox signal of  $[\text{Fe}(\text{CN})_6]^{3-/4-}$  further decreases, indicating the remaining active sites had been successfully closed (curve e). Finally, the fabricated aptasensor was immersed in the solution containing thrombin, the peak current signal on the incubated aptasensor was further decreased (curve f), indicating that the TBA strands on the biosensor surface successfully captured the thrombin in the solution, and the diffusion of the signal probe of  $[\text{Fe}(\text{CN})_6]^{3-/4-}$  was further hindered by the bio-macromolecules of thrombin that covered on the sensor surface.

In this work, the assemble process of the sensing interface was also investigated by EIS and the obtained Nyquist plots are presented in Fig. 3-1.3B. An equivalent circuit model was utilized to fit the impedance results (Fig. 3-1.3B, inset), where  $R_s$  is the solution resistance,  $R_{ct}$  is the charge transfer resistance at the electrode/electrolyte interface,  $Q_{dl}$  represents the double-layer capacitance, and  $W$  represents the Warburg impedance base on mass transfer to the electrode surface. The fitting results display that the equivalent circuit model (solid lines) is consistent with the actual

experimental data (dotted lines). The values of all the elements in the equivalent circuit model are expressed in Table 2.1. A minimum  $R_{ct}$  (0.46 k $\Omega$ ) on bare GCE is observed (curve a), which explained that the electron transfer of  $[\text{Fe}(\text{CN})_6]^{3-/4-}$  on the bare GCE is unhindered [26]. After immobilizing  $\text{Cu}_2(\text{CHDC})_2$  on the GCE surface, a conspicuous increase of semicircle diameter is found for the Nyquist plot in the high-frequency region (curve b). The  $R_{ct}$  value is obtained to be 8.9 k $\Omega$ , indicating that the electron transfer of  $[\text{Fe}(\text{CN})_6]^{3-/4-}$  is seriously restrained by the  $\text{Cu}_2(\text{CHDC})_2$  film due to its poor conductivity and the repulsion force by the residual carboxylic groups. When the  $\text{Cu}_2(\text{CHDC})_2$  modified electrode was anchored with AuNPs, the  $R_{ct}$  is sharply decreased to 1.8 k $\Omega$  (curve c) attribute to the excellent electrical conductivity of AuNPs, which also indicates that AuNPs has been successfully assembled on the modified electrode surface. After TBA was grafted on the AuNPs/ $\text{Cu}_2(\text{CHDC})_2$ /GCE surface, the  $R_{ct}$  value is markedly increased to 2.1 k $\Omega$  (curve d), which is attributed to the diffusion kinetics barrier between negatively charged phosphate backbones and  $[\text{Fe}(\text{CN})_6]^{3-/4-}$ . When the redundant active sites on AuNPs have been blocked with MCH, the  $R_{ct}$  value is further raised to 3.2 k $\Omega$  (curve e). Upon interaction of the aptamer with target thrombin molecules, the  $R_{ct}$  value dramatically increased to 6.7 k $\Omega$  (curve f), suggesting that the thrombin was captured with the TBA strand, and then further hindered the approaching of the  $[\text{Fe}(\text{CN})_6]^{3-/4-}$  to the sensor surface. All of results suggested that the sensing interface had been constructed successfully, and is feasible for target recognition.

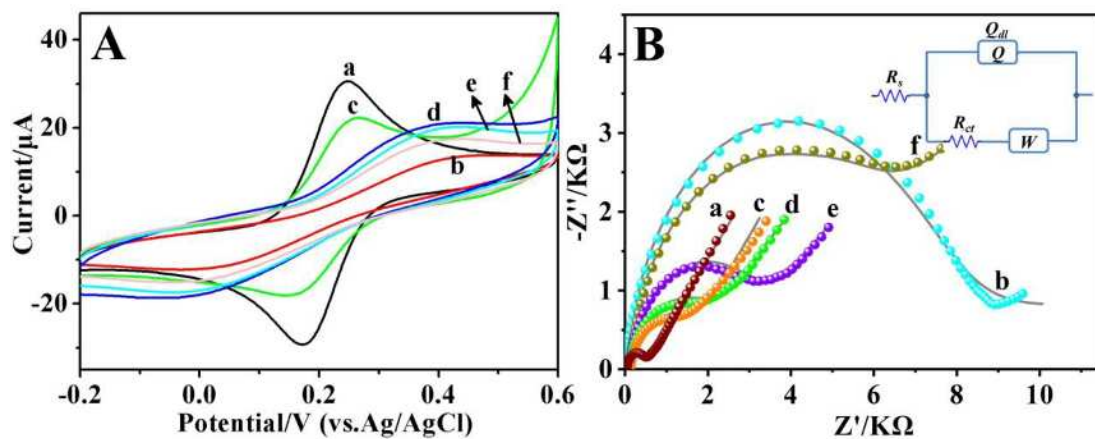


Fig. 3-1.3 CVs (A) and Nyquist plots (B) of 1.0 mM  $[\text{Fe}(\text{CN})_6]^{3-/4-}$  with 0.1 M KCl on bare GCE (a),  $\text{Cu}_2(\text{CHDC})_2/\text{GCE}$  (b), AuNPs/ $\text{Cu}_2(\text{CHDC})_2/\text{GCE}$  (c), TBA/AuNPs/ $\text{Cu}_2(\text{CHDC})_2/\text{GCE}$  (d), MCH/TBA/AuNPs/ $\text{Cu}_2(\text{CHDC})_2/\text{GCE}$  (e), thrombin/MCH/TBA/AuNPs/ $\text{Cu}_2(\text{CHDC})_2/\text{GCE}$  (f).

Table 3-1.1 Values of the equivalent circuit elements were obtained by fitting the experimental results for the different modified electrodes.

<b>Electrode</b>	$R_s$ ( $\Omega \text{ cm}^2$ )	$Q_{dl}$ ( $\mu\text{F cm}^2$ )	$n$	$R_{ct}$ ( $\text{k}\Omega \text{ cm}^2$ )	$W$ ( $\text{m}\Omega \text{ cm}^2$ )
GCE	105.2	2.728	0.800	0.46	0.371
$\text{Cu}_2(\text{CHDC})_2/\text{GCE}$	94.3	7.455	0.894	8.92	0.147
$\text{AuNPs}/\text{Cu}_2(\text{CHDC})_2/\text{GCE}$	114.5	3.640	0.688	1.83	0.322
$\text{TBA}/\text{AuNPs}/\text{Cu}_2(\text{CHDC})_2/\text{GCE}$	91.8	13.37	0.809	2.09	0.360
$\text{MCH}/\text{TBA}/\text{AuNPs}/\text{Cu}_2(\text{CHDC})_2/\text{GCE}$	94.2	7.036	0.841	3.23	0.361
thrombin/ $\text{MCH}/\text{TBA}/\text{AuNPs}$ $/\text{Cu}_2(\text{CHDC})_2/\text{GCE}$	103.7	6.631	0.841	6.77	0.331

### 3-1.3.3 Electrochemical behavior of the aptasensor

Fig. 3-1.4A displays the CV responses of various modified electrodes in 0.01 M PBS (pH 6.86) with a scan rate of  $0.10 \text{ V s}^{-1}$ . A pair of redox peaks with the peak potentials of 0.01 V and -0.28 V are observed on the  $\text{Cu}_2(\text{CHDC})_2/\text{GCE}$  (curve a). According to the previously reported literature [12], the current response can be attributed to the redox process of Cu(II)/Cu(I) couple from  $\text{Cu}_2(\text{CHDC})_2$ , and the abundant  $\text{Cu}^{2+}$  in the MOFs affords high electrochemical response. This result suggests that the  $\text{Cu}_2(\text{CHDC})_2$  presented a well-behaved redox process after modified on the bare GCE. When the AuNPs were electrodeposited on the surface of  $\text{Cu}_2(\text{CHDC})_2$  modified GCE, the current response of redox peaks distinctly increased (curve b), indicating the AuNPs on the  $\text{Cu}_2(\text{CHDC})_2/\text{GCE}$  effectively improved the electrochemical signal of  $\text{Cu}_2(\text{CHDC})_2$ . So it is concluded that the AuNPs have two functions in this work, namely, the immobilization platform of TBA probe and the electrocatalyst for the electrochemical response of  $\text{Cu}_2(\text{CHDC})_2$ . While TBA was assembled on the AuNPs/ $\text{Cu}_2(\text{CHDC})_2/\text{GCE}$ , the electrochemical response was obviously decreased (curve c). This result indicates that TAB covers part of the surface of AuNPs. In addition, the redox peak potentials of the  $\text{Cu}_2(\text{CHDC})_2$  shift positively upon TBA modification. It is likely related to the electrode microenvironment variation. For example, the modification of TBA on the electrode surface changed the concentrations and acidity of the electrolyte around the electroactive  $\text{Cu}_2(\text{CHDC})_2$  layer, and as a result the redox process become much more difficult, leading to the positive shift of the redox peak potential of the  $\text{Cu}_2(\text{CHDC})_2$ . After the residual sites were blocked with MCH, the current response of redox peaks was further decreased.

Fig. 3-1.4B displays the CV responses of the aptasensor in 0.01 M PBS (pH 6.86) with different scan rate ( $v$ ). The redox peaks increase gradually with increase of the scan rate, a well correlation can be achieved between the oxidation peak currents ( $I_{\text{pa}}$ ) and the scan rate ( $v$ , inset) with the linear regression equation of  $I_{\text{pa}} (\mu\text{A}) =$

$-0.43+122.93 v (V s^{-1}) (R=0.998)$ , which confirms that the electrochemical reaction of the sensing material on the electrode interface undergone an adsorption-controlled process [27]. It is of note that the oxidation peak of the sensing interface is much stronger than the reduction one, the oxidation peak signal was selected as the analytical signal for the following sensing analysis evaluation.

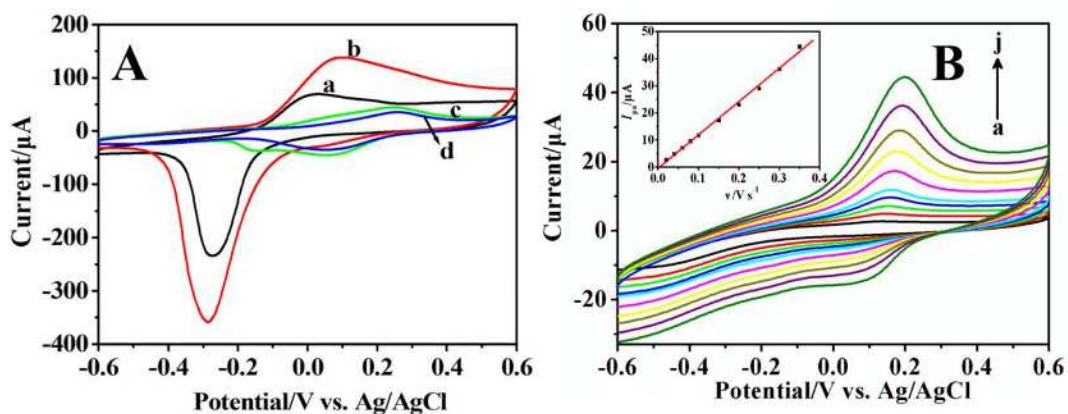


Fig. 3-1.4 (A) The CVs were recorded in 0.01 M PBS (pH 6.86) with a scan rate of  $0.10 \text{ V s}^{-1}$  on  $\text{Cu}_2(\text{CHDC})_2/\text{GCE}$  (a),  $\text{AuNPs}/\text{Cu}_2(\text{CHDC})_2/\text{GCE}$  (b),  $\text{TBA}/\text{AuNPs}/\text{Cu}_2(\text{CHDC})_2/\text{GCE}$  (c),  $\text{MCH}/\text{TBA}/\text{AuNPs}/\text{Cu}_2(\text{CHDC})_2/\text{GCE}$  (d). (B) The CVs of  $\text{MCH}/\text{TBA}/\text{AuNPs}/\text{Cu}_2(\text{CHDC})_2/\text{GCE}$  in 0.01 M PBS (pH 6.86) with different scan rates (a-j: 0.02, 0.04, 0.06, 0.08, 0.10, 0.15, 0.20, 0.25, 0.30,  $0.35 \text{ V s}^{-1}$ ). (Inset: the linear relationship of  $I_{\text{pa}}$  with scan rates of  $v$ ).

### 3-1.3.4 Optimization of experimental conditions

In order to obtain the optimal analytical signal, the assay conditions including the cast amount of  $\text{Cu}_2(\text{CHDC})_2$  on the surface electrode, electrodeposition cycles of AuNP, the bonding time of TBA ( $t_{\text{TBA}}$ ), the TBA concentration ( $C_{\text{TBA}}$ ) and the binding time of thrombin ( $t_{\text{thrombin}}$ ) were optimized. The dependence of the DPVs on the cast amount of  $\text{Cu}_2(\text{CHDC})_2$  ( $V_{\text{Cu}_2(\text{CHDC})_2}$ ) on the electrode surface and the corresponding oxidation peak currents ( $I_{\text{pa}}$ ) versus  $V_{\text{Cu}_2(\text{CHDC})_2}$  is shown in Fig. 3-1.5A. The figure revealed that the  $I_{\text{pa}}$  values enhanced with an increase of the cast amount of  $\text{Cu}_2(\text{CHDC})_2$ , suggesting that the electrochemical response of the electrode is related to the amount of the modified  $\text{Cu}_2(\text{CHDC})_2$ . When the cast volume increases from 10  $\mu\text{L}$  to 14  $\mu\text{L}$ , the  $I_{\text{p}}$  values reach to the constant values, indicating that the cast amount of  $\text{Cu}_2(\text{CHDC})_2$  on the bare electrode is saturation. So 10  $\mu\text{L}$  is used as the best modification amount of  $\text{Cu}_2(\text{CHDC})_2$ .

The deposition amount of AuNPs was investigated by monitoring the CV curve during electrodeposition. From Fig. 3-1.5B, it was found that the redox current tends to be constant when the CV scan cycles increases to 30 cycles, suggesting that the electrodeposited AuNPs reach to saturation on the electrode surface. Additionally, the redox current of AuNPs/ $\text{Cu}_2(\text{CHDC})_2$ /GCE in the 0.1 M PBS (pH 6.86) reaches to the maximum value when the deposition cycles reach 30 cycles, and then kept constant (Fig. 3-1.5C). Therefore, a 30-cycle CV scan is adopted for electrodeposition of AuNPs.

The optimal assembly time of TBA ( $t_{\text{TBA}}$ ) on AuNPs/ $\text{Cu}_2(\text{CHDC})_2$ /GCE was investigated by immersing the AuNPs/ $\text{Cu}_2(\text{CHDC})_2$ /GCE into 1  $\mu\text{M}$  TBA solution for a different time in the range from 10 to 70 min. The result shows that the DPV peak currents ( $I_{\text{p}}$ ) gradually decrease with time increasing from 10 to 60 min (Fig. 3-1.5D), and then the  $I_{\text{p}}$  value slightly changes with a further increase of  $t_{\text{TBA}}$ , indicating the immobilization of TBA on the electrode is completed. Thus, 60 min is chosen as the optimal self-assembly time between TBA and AuNPs. The effect of  $C_{\text{TBA}}$  was shown in Fig. 3-1.5E. The figure displays that the DPV response declines with increasing  $C_{\text{TBA}}$  from 0.2 to 1.0  $\mu\text{M}$ , when  $C_{\text{TBA}}$  reaches to 1.2  $\mu\text{M}$ , the peak current tends to stability. Therefore, the 1.0  $\mu\text{M}$  was chosen as the optimal concentration of TBA.

The influence of the incubation time in thrombin ( $t_{\text{thrombin}}$ ) solution on the analytical signal was also evaluated. Fig. 3-1.5F shows the DPV signals of TBA/AuNPs/Cu<sub>2</sub>(CHDC)<sub>2</sub>/GCE upon incubation with 0.1 pM thrombin at 37 °C. It can be found that the DPV responses gradually decrease when  $t_{\text{thrombin}}$  increases from 0 min to 30 min, proving that increasing amounts of thrombin were captured by TBA. When the incubation time is more than 30 min, the  $I_p$  value is almost constant, indicating a binding saturation on the sensor surface. So, 30 min is chosen as the reaction time of thrombin with the biosensor in the following test.

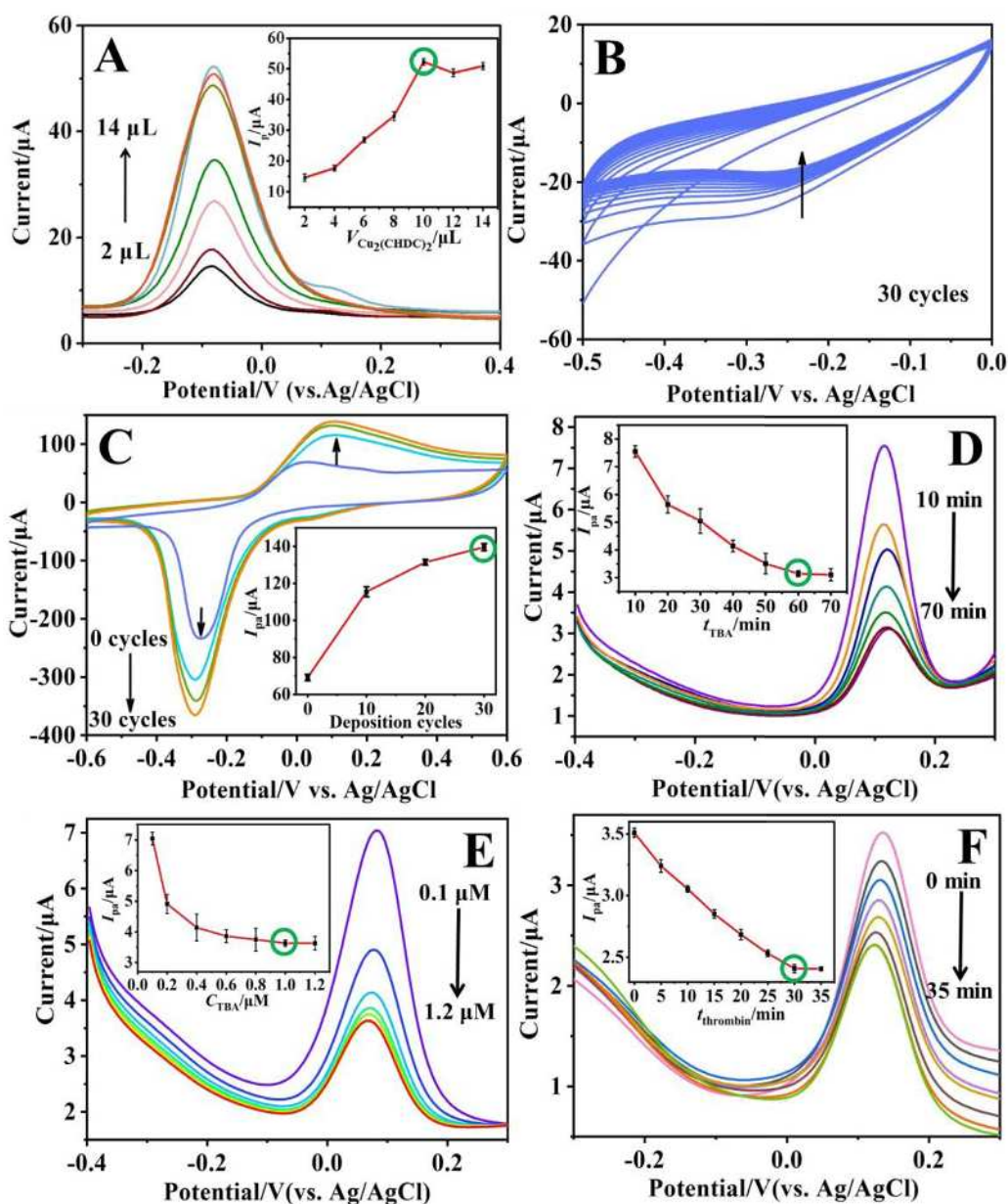


Fig. 3-1.5 Effect of the cast amounts ( $V$ ) of  $\text{Cu}_2(\text{CHDC})_2$  on the DPV response of the modified GCE in the 0.01 M PBS (pH 6.86) (A), the CV responses of AuNPs modified on the  $\text{Cu}_2(\text{CHDC})_2/\text{GCE}$  by electrochemically scanned in 0.5 mM  $\text{HAuCl}_4$  solution for 30 cycles (B) and effect of the AuNPs deposition cycles on the  $\text{Cu}_2(\text{CHDC})_2/\text{GCE}$  in the 0.01 M PBS (pH 6.86) (C), effect of the bonding time of TBA (D), the concentration of TBA (E) and the incubation time of thrombin (F) on the DPV response of the modified GCE in the 0.01 M PBS (pH 6.86).

### 3-1.3.5 Analytical performance of the aptasensor

Under the optimized conditions, the analytical performance of the aptasensor was investigated by interaction with various concentrations of thrombin. As shown in Fig. 3-1.6A, the DPV response of the oxidation peak declined with the increase of thrombin concentrations ( $C_{\text{thrombin}}$ ). The inhibition of the electrochemical response of the aptasensor after binding with the thrombin is also likely caused by the blocking of approaching of electrolyte ion to the electroactive  $\text{Cu}_2(\text{CHDC})_2$  layer due to the formation of the 3D spatial structure of the TBA-thrombin complex [28]. This result also implies that the capture of the biosensor to thrombin can be readily reflected by the electrochemical signal variation of the electrode-confined  $\text{Cu}_2(\text{CHDC})_2$  layer. Fig. 3-1.6B displays the difference ( $\Delta I_p$ ) of DPV responses of the aptasensor before and after hybridization with thrombin varied proportionally with logarithmic concentration of thrombin ( $\lg C_{\text{thrombin}}$ ) from 0.01 fM to 10 nM. The calibration curve was identified as  $\Delta I_p(\mu\text{A})=3.089+0.157\lg C_{\text{thrombin}}(\text{M})$  ( $R=0.995$ ), and the detection limit was identified for 0.01 fM, which exhibited better performance than many other reports as listed in Table 3-1.2. The outstanding performance of the sensor may be attributed to the excellent electrochemical behavior of  $\text{Cu}_2(\text{CHDC})_2$  and its high surface area for TBA immobilization and thrombin capture.

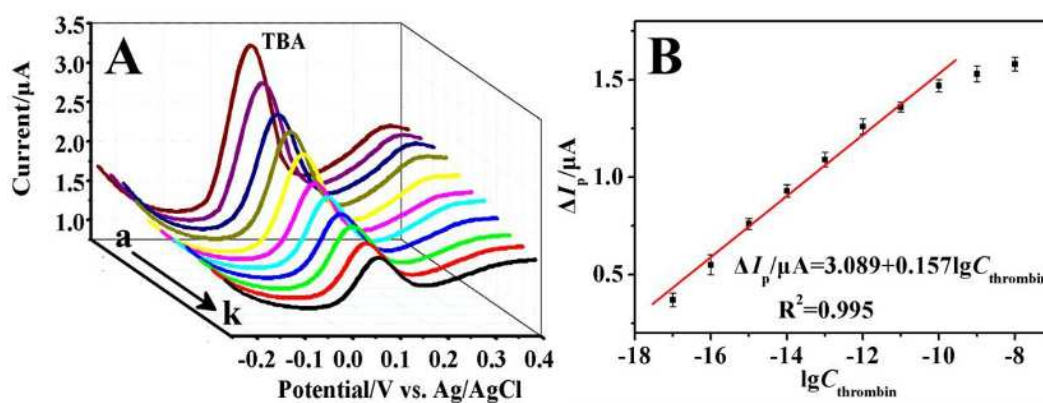


Fig. 3-1.6 (A) DPV responses of MCH/TBA/AuNPs/Cu<sub>2</sub>(CHDC)<sub>2</sub>/GCE in the 0.01 M PBS (pH 6.86) before (a) and after incubated with 0.01 fM (b), 0.1 fM (c), 1.0 fM (d), 10.0 fM (e), 0.1 pM (f), 1.0 pM (g), 10 pM (h), 0.1 nM (i), 1 nM (j), and 10 nM (k) thrombin. (B) Linear relationship of peak currents ( $\Delta I_p$ ) versus the logarithm of thrombin concentration ( $\lg C_{\text{thrombin}}$ ).

Table 3-1.2 Comparison of the proposed aptasensor with other  
TBA-based electrochemical thrombin aptasensors

Electrode materials	Indicator	Method	Linear range	LOD	Ref.
Cu <sup>2+</sup> -L-cys/AuNPs/TBA-TSS/MCH/AuE	Lable-free	DPV	100 fM-2.0 μM	21 fM	[1]
Cu <sub>2</sub> O-AuNPs-BSA/NH <sub>2</sub> -TBA/AuNPs/GCE	Lable-free	CA	100 fM- 20 nM	23 fM	[14]
TBA/PDA/AgNPs/GCE	MB	DPV	0.1 pM -5.0 nM	36 fM	[29]
MNP-TBA1/HAP-TBA2/GCE	Na <sub>2</sub> MoO <sub>4</sub>	SWV	0.1 fM-1 nM	0.03 fM	[30]
MB-HCR/TBA/Pt/Fe-MIL-88-NH <sub>2</sub> /AuE	MB	DPV	1 fM-10 nM	0.33 fM	[31]
TBA/PDA@Gr/GCE	[Fe(CN) <sub>6</sub> ] <sup>3-/4-</sup>	DPV	0.1 fM-0.1 pM	0.1 fM	[32]
3D-NGO/NGQD-Chitosan/GCE	K <sub>2</sub> S <sub>2</sub> O <sub>8</sub>	ECL	1 fM-1 nM	0.25 fM	[33]
MCH/TBA/AuNPs/Cu <sub>2</sub> (CHDC) <sub>2</sub> /GCE	Lable-free	DPV	10 aM-10 pM	0.027 fM	This work.

**Note:** TBA: thrombin aptamer; BSA: bovine serum albumin; AuNPs gold nanoparticles; GO: graphene oxide; AgNPs: silver nanoparticles; GCE: glassy carbon electrode; PDA: polydopamine. MNP: magnetic nanoparticle; HAP: Hydroxyapatite; CA: Chronoamperometry; AuE: Au electrode; L-cys: L-cysteine; TSS: thiolated supporting sequence; MCH: 6-mercapto-1-hexanol; MB: methylene blue; HCR: hybridization chain reaction; PDA: polydopamine; Gr: graphene; ECL: Electrochemiluminescent; 3D-NGO: Three-dimensional nitrogen-doped graphene oxide; NGQD: nitrogen-doped graphene quantum dots.

### 3-1.3.6 Selectivity, reproducibility, and stability of the aptasensor

Furthermore, the selectivity, reproducibility, and stability of the prepared aptasensor were investigated. The electrochemical responses of the aptasensor for thrombin and other proteins including bovine serum albumin (BSA), hemoglobin (Hb), and trypsin (Try) was examined. When the biosensor was applied for the determination of 0.1 nM thrombin, and the mixed solution containing 0.1 nM thrombin, 1 nM BSA, Hb, and Tyr, respectively, the obvious current changes and the similar  $\Delta I_p$  values were achieved (Fig. 3-1.7A). However, a faint DPV response variation was obtained when the aptasensor was reacted with only 1 nM BSA, Hb, or Tyr under the same experimental condition, suggesting that the aptasensor maintains outstanding selectivity for the thrombin in the presence of the common interfering species.

In order to inspect the reproducibility of the aptasensor, seven different TBA/AuNPs/Cu<sub>2</sub>(CHDC)<sub>2</sub> modified electrodes were prepared at the same conditions. Fig. 3-1.7B shows that the nearly equal  $\Delta I_p$  values were achieved when the seven parallel fabricated electrodes before and after interaction with 0.1 nM thrombin, and the relative standard deviation (RSD) of  $\Delta I_p$  values was identified to be 1.01%, indicating high reproducibility of the constructed thrombin aptasensor. The good stability of the aptasensor was testified through the change of DPV response before and after storing the aptasensor at 4 °C for four weeks, and only a small change of 2.94% in peak current was obtained.

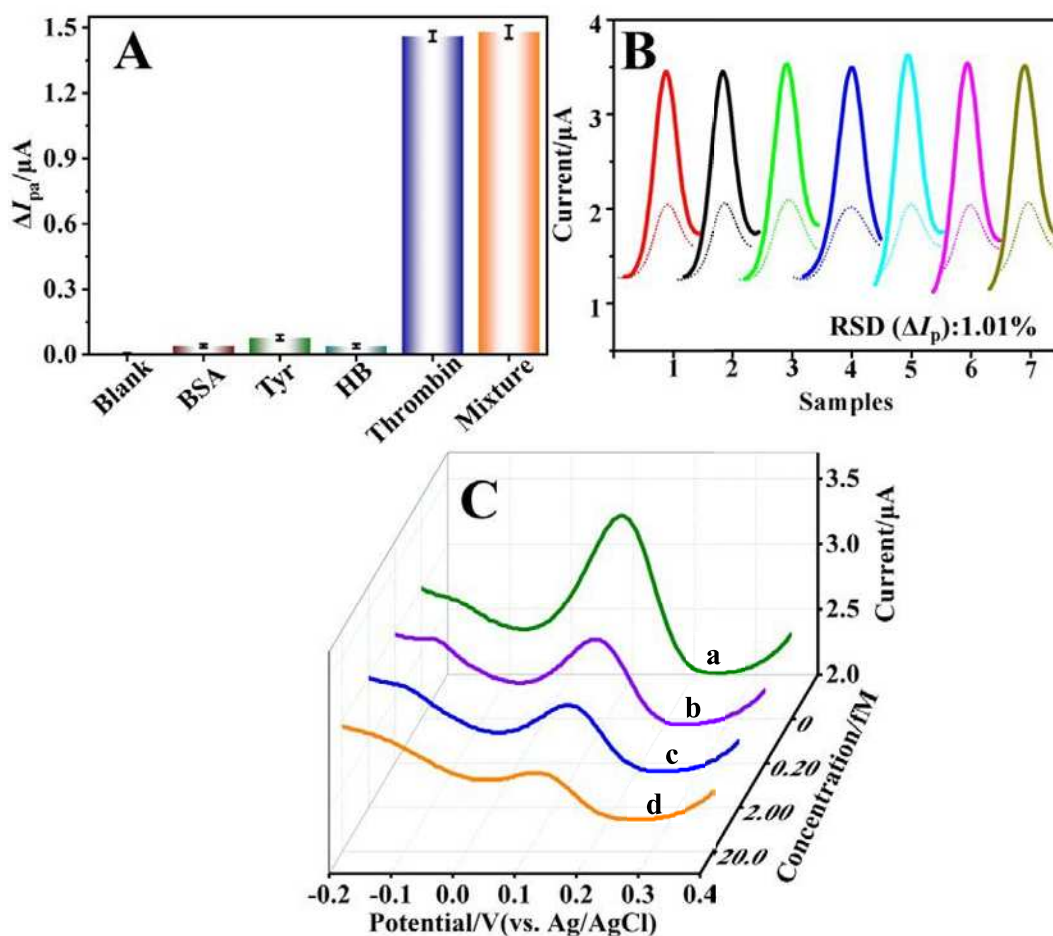


Fig. 3-1.7 (A) Selectivity analysis of the aptasensor tested in a blank solution, 1 nM BSA, Hb, Tyr, 0.1 nM thrombin, and the mixture samples containing 0.1 nM thrombin and BSA, Hb, and Tyr at concentrations of 1 nM in the 0.01 M PBS (pH 6.86). (B) Reproducibility of seven aptasensors for detection of 0.1 nM thrombin. (C) DPV responses of the aptasensor incubated with various concentrations of 0 (a), 0.20 (b), 2.00 (c), 20.0 (d) fM thrombin in human serum sample in the 0.01 M PBS (pH 6.86).

### **3-1.3.7 Analysis of real sample**

The standard addition method is performed to estimate the analytical capacity of the fabricated thrombin aptasensor in real samples [34]. The assay was performed by diluting various concentrations of thrombin solutions in human serum samples, and the sample was obtained from Zhangzhou Affiliated Hospital of Fujian Medical University. Thereafter, the fabricated aptasensor was incubated in the samples that were 100-fold diluted with 0.9% sodium chloride (NaCl) solution. Fig. 3-1.7C shows the DPV responses of the aptasensor applied for determination of the human serum samples including 0 (a), 0.20 (b), 2.00 (c), 20.0 (d) fM thrombin, respectively, and the current signal decrease with the increasing concentration of thrombin as expected. Results of analysis are exhibited in Table 3-1.3, and the recovery is determined to be between 96.0% and 102.1%, which represents that the developed aptasensor is credible for thrombin in complex biological samples.

Table 3-1.3 Determination of thrombin in serum samples using the developed aptasensor<sup>a</sup>

Serum samples	Added (fM)	Found (fM)	Recovery (%)
1	0.20	0.192	96.0
2	2.00	1.950	97.5
3	20.0	20.42	102.1

<sup>a</sup>Mean values of three measurements.

### 3-1.4 Conclusion

A flexible metal-organic frameworks (MOFs) of  $\text{Cu}_2(\text{CHDC})_2$  present high thermal and mechanical stability based on its dimer paddle-wheel  $\text{Cu}_2(\text{COO})_4$  core and its slight elasticity and hydrophobicity of the -CHDC connector. It was synthesized by a facile hydrothermal method, the physical characterization reveals high surface area by its nanocluster-assembled structure. Due to the signal of the Cu(II) from MOFs can be directly detected without the modification of electroactive tags and its excellent electrochemical activity, amazing stability, rich active sites, a label-free electrochemical aptasensor with simplified construction steps is proposed and used for ultrasensitive detection of thrombin. The proposal thrombin aptasensor displays excellent performance with wide linear range, ultralow detection limit, excellent stability and favorable reproducibility. In addition, the sensor had been successfully applied to detect thrombin in complex matrix of the human serum, which indicates that it can be potentially used for the clinical diagnosis and monitoring. Unfortunately, the reusability of the proposed thrombin aptasensor is feeble, which is likely due to the strong affinity of between the aptamer and the target thrombin molecules. In addition, the signal-off mechanism of biosensor after interaction with thrombin is still not clear, which makes it difficult to extend its application and extensively optimize the analytical performance.

### 3-1.5 Reference

- [1] J. Song, S. L. Li, F. Gao, Q. X. Wang, Z. Y. Lin, *Chem. Commun.*, **55**, 905 (2019).
- [2] T. X. Lin, P. X. Lai, J. Y. Mao, H. W. Chu, B. Unnikrishnan, A. Anand, C. C. Huang, *Front. Chem.*, **7**, 280 (2019).
- [3] N. Pourreza, M. Ghomi, *Anal. Chim. Acta.*, **1079**, 180 (2019).
- [4] T. Funck, T. Liedl, W. Bae, *Appl. Sci.*, **9**, 3006 (2019).
- [5] D. Sun, J. Lu, L. Zhang, Z. Chen, *Anal. Chim. Acta.*, **1082**, 1 (2019).
- [6] F. Ghorbani, H. Abbaszadeh, J. E. N. Dolatabadi, L. Aghebati-Maleki, M. Yousefi, *Biosens. Bioelectron.*, **142**, 11484 (2019).
- [7] L. Pol, L. K. Acosta, J. Ferré-Borrull, L. F. Marsal, *Sens.*, **19**, 4543 (2019).
- [8] X. F. Wang, B. H. Zhang, X. Q. Lu, P. Wang, *Kidney Blood Pressure Res.*, **43**, 1231 (2018).
- [9] L. Saa, B. Díez-Buitrago, N. Briz, V. Pavlov, *Microchim. Acta.*, **186**, 657 (2019).
- [10] C. Li, P. Fan, A. Liang, Z. Jiang, *Mater. Sci. Eng., C*, **99**, 1399 (2019).
- [11] Z. Shi, G. Li, Y. Hu, *Chin. Chem. Lett.*, **30**, 1600 (2019).
- [12] Y. Z. Yang, Q. X. Wang, W. W. Qiu, H. X. Guo, F. Gao, *J. Phys. Chem. C*, **120**, 9794 (2016).
- [13] W. W. Qiu, F. Gao, F. Gao, Z. Y. Lin, Q. X. Wang, *J. Phys. Chem. C*, **123**, 18685 (2019).
- [14] S. Chen, P. Liu, K. Su, X. Li, Z. Qin, W. Xu, J. Chen, C. R. Li, J. F. Qiu, *Biosens. Bioelectron.*, **99**, 338 (2018).
- [15] Y. Xu, Q. Li, H. Xue, H. Pang, *Coord. Chem. Rev.*, **376**, 292 (2018).
- [16] H. Molavi, A. Shojaei, *ACS Appl. Mater. Interfaces*, **11**, 9448 (2019).
- [17] M. Eddaoudi, J. Kim, N. L. Rosi, D. T. Vodak, J. Wachter, M. O'keeffe, O. M. Yaghi, *Science*, **295**, 469 (2002).
- [18] W. Mori, S. Takamizawa, C. N. Kato, T. Ohmura, T. Sato, *Microporous Mesoporous Mater.*, **73**, 31 (2004).

- [19] K. Seki, M. Kondo, T. Yoshitomi, H. Matsuzaka, S. Kitagawa, *Angew. Chem. Int. Ed.*, **36**, 1725 (1997).
- [20] A. Schneemann, V. Bon, I. Schwedler, I. Senkovska, S. Kaskel, R.A. Fischer, *Chem. Soc. Rev.*, **43**, 6062 (2014).
- [21] Z. J. Lin, J. Lü, M. Hong, R. Cao, *Chem. Soc. Rev.*, **43**, 5867 (2014).
- [22] F. ZareKarizi, M. Joharian, A. Morsali, *J. Mater. Chem. A*, **6**, 19288 (2018).
- [23] H. Kumagai, M. Akita-Tanaka, K. Inoue, K. Takahashi, H. Kobayashi, S. Vilminot, M. Kurmoo, *Inorg. Chem.*, **46**, 5949 (2007).
- [24] K. Seki, S. Takamizawa, W. Mori, *Chem. Lett.*, **20**, 122 (2001).
- [25] F. Gao, Q. X. Wang, N. N. Gao, Y. Z. Yang, F. X. Cai, M. Yamane, H. Tanaka, *Biosens. Bioelectron.*, **97**, 238 (2017).
- [26] F. Gao, X.L. Cai, X. Wang, C. Gao, S. Liu, F. Gao, Q.X. Wang, *Sens. Actuators, B*, **186**, 380 (2013).
- [27] R. Hajian, Z. Tayebi, N. Shams, *J. Pharm. Anal.*, **7**, 27 (2017).
- [28] T. Wang, C. Chen, L.M. Larcher, R.A. Barrero, R.N. Veedu, *Biotechnol. Adv.*, **37**, 28 (2019).
- [29] Q. Xu, G. Wang, M. Zhang, G. Xu, J. Lin, X. Luo, *Microchim. Acta.*, **185**, 253 (2018).
- [30] Y. Zhang, J. Xia, F. Zhang, Z. Wang, Q. Liu, *Sens. Actuators, B*, **267**, 412 (2018).
- [31] T. Cheng, X. Li, P. Huang, H. Wang, M. Wang, W. Yang, *Microchim. Acta.*, **186**, 94 (2019).
- [32] F. Zhang, Z. Liu, Y. Han, L. Fan, Y. Guo, *Anal. Methods*, **10**, 5547 (2018).
- [33] Y.N. Khonsari, S. Sun, *Microchim. Acta.*, **185**, 430 (2018).
- [34] W.W. Qiu, H. Tanaka, F. Gao, Q.X. Wang, M.Q. Huang, *Adv. Powder Technol.*, **30**, 2083 (2019).

**3-2 A strategy for the construction of a reusable electrochemical aptasensor using UiO-66 as signal amplified platform**

### 3-2.1 Introduction

Ochratoxin A (OTA), as a mycotoxin produced by various *Aspergillus ochraceus* and *Penicillium verrucosum*, widely exists in many foods, including wheat, corn, coffee, beer, nuts and so on [1, 2]. The pathological researches show that OTA is a serious endangers to human and animal health due to its hepatotoxicity, nephrotoxicity and carcinogenicity. It was classified as a 2B carcinogen by the United Nations Cancer Organization. So it is of great significance to establish a rapid and sensitive method for the detection of OTA. The general analysis methods of OTA include mass spectrometry (MS) [3], high performance liquid chromatography (HPLC) [4], enzyme-linked immunosorbent assay (ELISA) [5] and so on. However, these traditional methods cannot meet the requirements of real-time and rapid detection because of their complicated sample pretreatment process, high cost, expensive instrument, and time-consuming process [6, 7].

Electrochemical biosensor is a kind of sensor which can rapidly sense or respond to biological or chemical substances [8, 9]. In the past decade, the electrochemical aptasensor as a branch of biosensor has received considerable attention in various fields due to its advantages of its high affinity to target, easy synthesis of aptamer probe, wide applicable targets from the small molecule to the cell, and inherent advantages of electrochemistry such as high sensitivity, fast response, simple operation, low cost [10, 11]. In a typical electrochemical aptasensor, the aptamer probe, namely the molecular recognition receptor, is fixed on the surface of the basic electrode, and the recognition reaction is then converted into the readable electrochemical signals of concentration or bio-activity of the analytes [12, 13]. However, these traditional electrochemical aptasensors also have some defects. First, the commercially purchased or home-made electroactive aptamer probes are usually single-point labeled with electroactive methylene blue (MB) [14, 15] and ferrocene (Fc) [16, 17] molecules, resulting in limited signal output as well as low sensitivity. In addition, the reusability of the traditional sensor is feeble because of the strong

affinity between the aptamer probe and the target molecule [18]. Therefore, it is still a great challenge to develop a new strategy to overcome the above-mentioned shortcomings of traditional electrochemical aptasensors.

Metal-organic framework (MOF) is a new type of nanomaterials, which are widely used in many fields, including the preparation of functional biosensors due to its good three-dimensional structure, high specific surface area and porosity, and a variety of chemical functions [19, 20]. Based on its high surface area and abundant metal active sites, the functional modification of the external surface of MOFs is considered to be a popularized strategy to further expand its application [21, 22]. A typical example is that Zr-based MOF, such as UiO-66 (UiO-66 is obtained by connecting  $Zr_6O_4(OH)_4$  inorganic cornerstones with 1,4-benzene-dicarboxylate (BDC) as linker resulting in a cubic MOF), shows a high affinity for phosphate groups ( $-PO_4^{3-}$ ) by forming the Zr-O-P coordination bonds, enabling the effective and highly selective accumulation of phosphate-contained biomolecules [23]. On the basis of this feature, Mirkin et al. [24] realized the surface functionalization of UiO-66 nanoparticles with  $-PO_4^{3-}$ -terminated DNA, and used it as a probe to detect cellular endotoxin. In addition, Sun et al. [25] developed a label-free electrochemical biosensor for the sensitive analysis of glioblastoma-derived exosomes based on the adsorption of MB-encapsulated Zr-MOF the surface of the exosomes by the interaction of  $Zr^{4+}$  with the intrinsic phosphate groups outside of exosomes.

Inspired by these, an ingenious, sensitive and reusable electrochemical aptamersensor for OTA has been proposed in this work on the basis of interaction between the Zr-O-P clusters and the signal amplification effect of UiO-66 due to its large surface area and rich active sites. In the design, the OTA binding aptamer (OBA) was confined on the electrode surface via hybridization with the supporting complementary strands. Then the UiO-66 was *in-situ* assembled on the terminal of OBA by Zr-O-P coordination bond. Followed by, a large amount of probe sequences tagged with electroactive methylene blue (MB) were also *in-situ* coordination-assembled on the UiO-66 surface through coordination with the residual  $Zr^{4+}$  center. Thus, a biosensing interface with strong electrochemical response was

constructed. Upon interaction with target OTA, the OBA bearing the signal carrier of UiO-66 and the signal strands were released from the sensor surface, realizing monitoring of the OTA. In addition, because the strategy is designed on the basis of the auxiliary strand-based competitive binding strategy, the biosensing interface can be easily realized for next round of reconstruction after OTA analysis. And the aptasensor is also successful for the analysis of OTA in wine samples, showing its great potential for the food safety monitoring.

## 3-2.2 Experimental

### 3-2.2.1 Reagents and Apparatus

Zirconium tetrachloride ( $ZrCl_4$ ), 1, 4-benzenedicarboxylic acid ( $H_2BDC$ ) was provided by Aladdin Reagent Co., Ltd. (China). Potassium chloride (KCl), potassium ferricyanide ( $K_3Fe(CN)_6$ ), potassium ferrocyanide ( $K_4Fe(CN)_6$ ), magnesium chloride ( $MgCl_2$ ), sodium chloride (NaCl), *N, N*-dimethylformamide (DMF), formic acid (99%), dichloromethane ( $CH_2Cl_2$ ) were obtained from Guangdong Xilong Chemical Co., Ltd. (China). Tris (2-carboxyethyl) phosphine hydrochloride (TCEP), 6-mercapto-1-hexanol (MCH), OTA, ochratoxin B (OTB), aflatoxin B1 (AFB1) and zearalenone (ZEN) were purchased from Sigma-Aldrich reagent Co., Ltd. (China). All aqueous solutions were prepared in ultrapure water, which was obtained from a Milli-Q water purifying system (18  $M\Omega \cdot cm$ ). All the chemicals were of analytical grade and used without further purification.

Thiolated supporting sequence (TSS, 5'-SH-( $CH_2$ )<sub>6</sub>-GGG TGT CCG ATG CTC CCT TTA CGC CAC CCA-3') that partial complementary to the OTA aptamer, phosphate-terminated OTA binding aptamers (OBA) (5'- $PO_4^{3-}$ -GAT CGG GTG TGG GTG GCG TAA AGG GAG CAT CGG ACA-3'), the MB-labeled strand (DLS) bearing 5'-phosphate ( $PO_4^{3-}$ ) (5'- $PO_4^{3-}$ -( $CH_2$ )<sub>6</sub>-TTG-CAA-MB-3'), methylene

blue-terminated OTA aptamer (MOBA) (5'-MB-GAT CGG GTG TGG GTG GCG TAA AGG GAG CAT CGG ACA-3') were purchased from Sangon Biotech Co., Ltd. (Shanghai, China). The reserve liquid of OTA was prepared with absolute ethanol and all the oligonucleotides were prepared with mixed Tris buffer solution containing 100 mM NaCl, 100 mM MgCl<sub>2</sub>, 10 mM TCEP, 25 mM Tris-HCl and kept at 4 °C for further use. 0.1 M phosphate-buffered saline (PBS, pH 6.86) was used as supporting electrolyte for electrochemical measurements.

Electrochemical measurements were carried out on a CHI 660E electrochemical analyzer (China) in connection with a conventional three-electrode system: the modified gold electrode (AuE) as working electrode, a platinum wire as auxiliary electrode and an Ag/AgCl (3 M KCl) as reference electrode. Powder X-ray diffraction (XRD) patterns of the materials were obtained from a Rigaku Miniflex-II diffractometer with a Ni-filtered Cu K $\alpha$  radiation (30 kV and 15 mA, Japan). Nitrogen adsorption-desorption isotherms were determined by Belsorp-MAX (Japan). Morphology of the UiO-66 was recorded on JEOL JSM-5600F Field-Emission Scanning Electron Microscopy (SEM, Japan).

### **3-2.2.2 Synthesis of UiO-66 nanoparticles**

UiO-66 was synthesized via a simple solvothermal method as reported in literature [26] with a slight modification. In brief, ZrCl<sub>4</sub> (233.0 mg, 1.0 mmol) and H<sub>2</sub>BDC (166.1 mg, 1.0 mmol) were dissolved in 15 mL of DMF. The mixture was then transferred into a 30 mL vial and 7.0 mL formic acid was added. After sonication to obtain a homogeneous solution, the vial was heated at 120 °C for 24 h in an oil bath. Afterwards, the vial was cooled to the room temperature, and the resulting precipitate was washed with DMF and acetone several times. After the white precipitate was dried under vacuum at room temperature for 1 h, the obtained powder was stirred in 100 mL CH<sub>2</sub>Cl<sub>2</sub> for 24 h to remove residual DMF from UiO-66 holes. Finally, the cleaned product was collected by filtration and washed with CH<sub>2</sub>Cl<sub>2</sub> several times and

dried at 80 °C for 1 h in vacuum to give the cleaned product of UiO-66 with formula of  $[\text{Zr}_6\text{O}_4(\text{OH})_4(\text{BDC})_6]$ .

### 3-2.2.3 Fabrication of the biosensing interface

Prior to experiment, the AuE was carefully polished with 1.0, 0.3, and 0.05  $\mu\text{m}$  alumina powder to obtain a mirror electrode surface. Then, the electrode was ultrasonicated in ultrapure water, mixture of water and ethanol ( $V_{\text{water}}: V_{\text{ethanol}} = 1:1$ ) and ultrapure water for 5 min, respectively. Subsequently, the cleaned electrode was activated in Piranha solution ( $V_{30\% \text{ H}_2\text{O}_2}: V_{98\% \text{ H}_2\text{SO}_4} = 7:3$ ) for 20 min. Followed by, the electrodes were scanned from -0.2 to 1.6 V at 100  $\text{mV s}^{-1}$  in 0.5 M  $\text{H}_2\text{SO}_4$  until steady curves were achieved [18]. Afterward, the AuE was washed thoroughly with ultrapure water and dried by nitrogen.

Subsequently, the TSS modified AuE (TSS/AuE) was prepared by immersing the cleaned AuE into 1.0  $\mu\text{M}$  TSS solution at room temperature for 24 h, through which the TSS was confined on the cleaned AuE through strong Au-S assembly chemistry. Then, the modified electrode was incubated in 10 mM MCH for 3 h to passivate the unmodified region of electrode, and the obtained electrode was denoted as TSS/MCH/AuE. The hybridization of TSS with partial complementary aptamer sequence of OBA was performed by soaking the TSS/MCH/AuE in 1.0 mM OBA solution for 30 min at 42 °C. Then the electrode was washed with PBS buffer to remove the non-specifically adsorbed OBA, and the hybridized electrode (OBA-TSS/MCH/AuE) was obtained. Thereafter, the electrode was immersed into a homogeneous UiO-66 suspension (5.0  $\text{mg/mL}$ ) for 2.5 h at 37 °C with shaking. Through this step, the UiO-66 was assembled on the electrode surface via specific coordination with  $5'\text{-PO}_4^{3-}$  on OBA. After washing with water to remove the non-specific adsorbed UiO-66, the electrode was further immersed in 1  $\mu\text{M}$  DLS solution, and reacted under shaking overnight. After this, NaCl solution was slowly added to the DLS solution to a final concentration of 0.5 M to reduce electrostatic

repulsion of immobilized DLS strands toward the DLS in solution, through which a higher density of DLS can be loaded on the UiO-66 [24]. Finally, the electrode was washed with PBS buffer and ultrapure water, and thus the DLS loaded sensing interface was prepared, which was named as DLS/UiO-66/OBA-TSS/MCH/AuE.

### **3-2.2.4 OTA binding and electrochemical measurements**

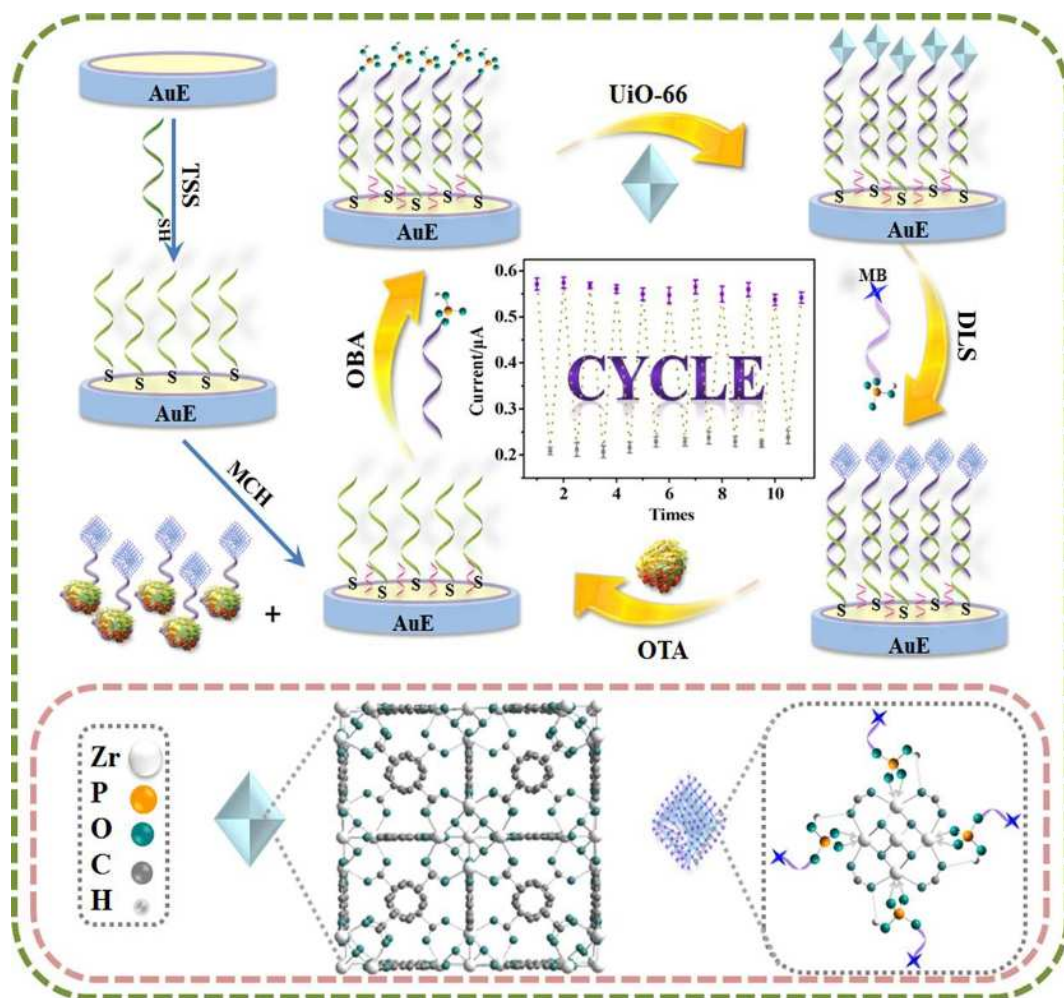
The recognition of the aptasensor for OTA was investigated by incubating DLS/UiO-66/OBA-TSS/MCH/AuE into the OTA solution with desired concentrations for 20 min under 37 °C with gentle shaking. After the reaction finished, the electrode was rinsed with Tris buffer and electrochemically measured in 0.1 M PBS buffer with the techniques of cyclic voltammetry (CV) and square wave voltammetry (SWV). The electrochemical characterization on the fabrication of the aptasensor was carried out in 1.0 mM  $[\text{Fe}(\text{CN})_6]^{3-/4-}$  solution containing 0.1 M KCl via cyclic voltammetry (CV) and electrochemical impedance spectra (EIS). The scan range of CV was from -0.2 to +0.6 V and the scan rate was 100 mV s<sup>-1</sup>. The EIS was collected at a potential of +0.197 V in the frequency range of 0.01~10<sup>5</sup> Hz with the voltage amplitude of 5 mV.

## **3-2.3 Results and Discussion**

### **3-2.3.1 Design concept and sensing mechanism of the aptasensor**

The rational, sensitive and reusable electrochemical aptasensors have important and extensive application value in many fields, such as food safety, environmental monitoring, clinical diagnosis and so on. To achieve this purpose, a novel electrochemical aptasensor for OTA, a highly carcinogenic and teratogenic food pollutant, was designed and constructed on the basis of using *in-situ*

coordination-assembled UiO-66 as signal amplification platform and MB-labeled strands (DLS) as the signal marker (Scheme 3-2.1). First, the thiol-modified supporting strand (TSS) that partial complementary to the OTA-binding aptamer (OBA) was immobilized on the AuE surface by the Au-S bond, and the OBA with 5'-PO<sub>4</sub><sup>3-</sup> is then anchored by the hybridization reaction. Furthermore, the MOF of UiO-66 was directly assembled on the electrode surface through the specific and strong coordination between Zr<sup>4+</sup> and PO<sub>4</sub><sup>3-</sup>, in which no extra cross-linking agents was needed. Follow by, large amounts of electroactive MB-labeled strands (DLSs) were further anchored on the electrode surface through the coordination between the residual Zr<sup>4+</sup> of UiO-66 and 5'-PO<sub>4</sub><sup>3-</sup> on DLS. It is of notice that the UiO-66 as a porous MOF material has large surface area and rich active site of Zr<sup>4+</sup>, enable the loading amount of DLS as well as the signal intensity of the sensor substantially enhanced. This is beneficial to the improvement of the analytical sensitivity of the biosensor. When the analyte of OTA is present in the detected solution, the OBAs with the signal probes release from the electrode surface. As a result, the redox signal of the sensor decreases. When all aptamer stands are released from the electrode surface, the electrode can be reconstructed and analyzed. The proposed strategy exhibits the advantages of easy fabrication by Zr<sup>4+</sup>-PO<sub>4</sub><sup>3-</sup> coordination, high sensitivity from signal amplification of UiO-66, and excellent reusability upon analytical process.



Scheme 3-2.1 Schematic illustration of the fabrication of the sensitive OTA aptasensor and the sensing application of the reusable aptasensor

### 3-2.3.2 Characterizations of UiO-66

Fig. 3-2.1A reveals the typical XRD pattern of the synthesized UiO-66 nanoparticles. The result shows that all diffraction peaks match well with a pure phase of simulated UiO-66 as reported in the literature [27], demonstrating the successful synthesis of UiO-66. Fig. 3-2.1B displays the specific surface area characterization of the sample by  $N_2$  adsorption isotherms at 77 K. It is observed that the sample shows a typical type I curve, indicating the presence of microporous in the sample. According to the corresponding pore size distribution curve and the crystal structure (inset of Fig. 3-2.1B), the pore size of the tetrahedral cages of 0.72 nm (violet ball) and the octahedral cages of 1.27 nm (green ball) were achieved, respectively, which is well consistent with the previously reported results [28]. From the Brunner-Emmet-Teller (BET) method, the specific surface area of the product was estimated to be  $975.01 \text{ m}^2 \text{ g}^{-1}$ , which indicates that the UiO-66 has a high specific surface area. The morphologies of the UiO-66 nanoparticles were investigated by SEM, and the results are presented in Fig. 3-2.1C and Fig. 3-2.1D. From Fig. 3-2.1C, the UiO-66 particles with uniform and well-defined octahedral morphology are observed. From the high-resolution SEM image (Fig. 3-2.1D), the sharp edges and the smooth surface are observed, suggesting that the as-synthesized material has good crystallinity and high purity.

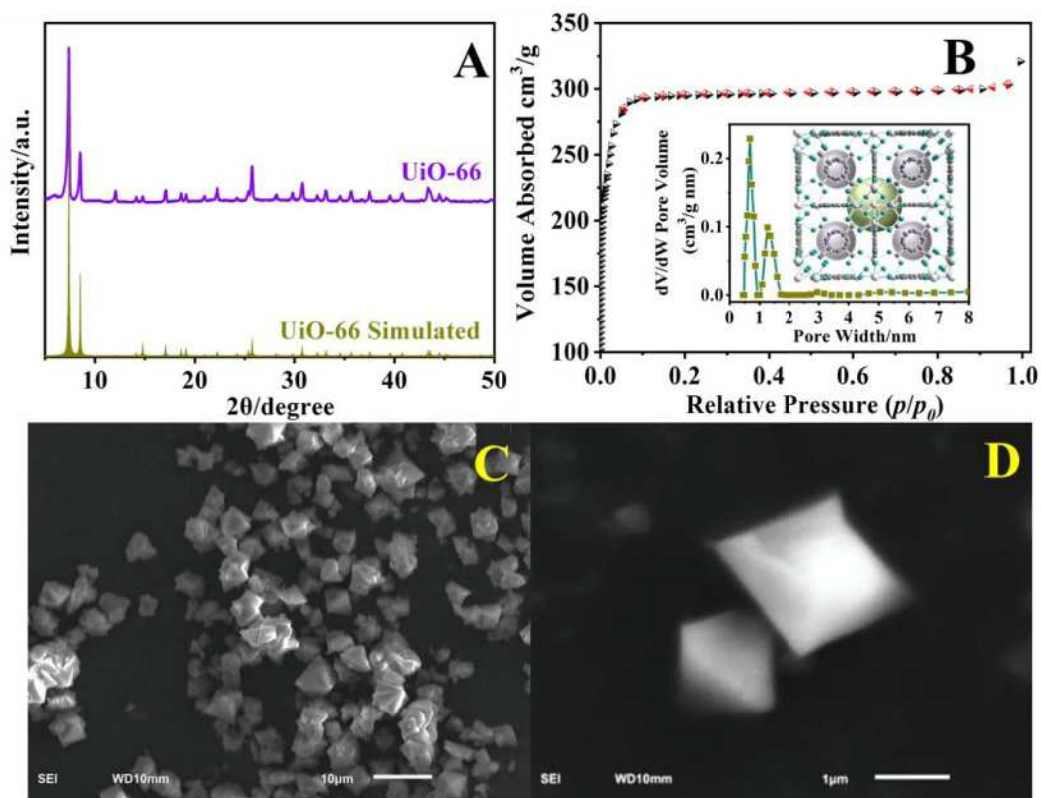


Fig. 3-2.1 XRD pattern (A), N<sub>2</sub> adsorption–desorption isotherms (B), the pore size distribute and the crystal structure (inset, B), and SEM (C, D) images of UiO-66 nanoparticles.

### 3-2.3.3 Electrochemical characterization on the preparation of the aptasensor

Fig. 3-2.2A displays the CVs of different modified electrodes within potential range from -0.2 V to 0.6 V using  $[\text{Fe}(\text{CN})_6]^{3-/4-}$  as electroactive probes. It is observed that a pair of reversible redox peaks at bare AuE (curve a), suggesting bare AuE has good electron transfer of  $[\text{Fe}(\text{CN})_6]^{3-/4-}$ . However, the redox peak currents of  $[\text{Fe}(\text{CN})_6]^{3-/4-}$  decrease remarkably and the redox potential difference increases obviously when the AuE was modified with TSS (curve b), suggesting TSS has been confined on the AuE through Au-S bond, and the negatively charged TSS electrostatically repulsed approaching of  $[\text{Fe}(\text{CN})_6]^{3-/4-}$  to the electrode surface. After TSS/AuE was passivated with MCH, the peak currents of  $[\text{Fe}(\text{CN})_6]^{3-/4-}$  further decrease (curve c). When the aptamer of OBA was hybridized with TSS on the electrode surface, the peak current of  $[\text{Fe}(\text{CN})_6]^{3-/4-}$  shows further decreases and the redox potential difference also increases (curve d), which can be attributed to the increase of electrostatic repulsion force and steric hindrance effect of electrode surface caused by the formation of DNA duplex. When UiO-66 was assembled on 5'- $\text{PO}_4^{3-}$  terminal of OBA by the coordination bonding, the current response decreases dramatically again because the poor electroconductivity of UiO-66 hindered the electron transfer of  $[\text{Fe}(\text{CN})_6]^{3-/4-}$  on the sensor surface (curve e). Afterward, when numerous DLS was attached on the surface of UiO-66 also by the coordination bond, the lowest current signal and the largest redox potential can be observed, confirming that the signal strands have been successfully anchored on the electrode surface.

Additionally, the fabrication process of the sensing interface was also characterized by EIS and the obtained Nyquist plots are presented in Fig. 3-2.2B. An equivalent circuit model was utilized for fitting of impedance results (Fig. 3-2.2B, inset), where  $R_s$  is the solution resistance,  $Q_{\text{dl}}$  is the double-layer capacitance,  $R_{\text{ct}}$  represents the charge transfer resistance at the electrode/electrolyte interface,  $W$  is the Warburg impedance due to mass transfer to the electrode surface. The fitting results (solid lines)

display that the equivalent circuit model is consistent with the real experimental data (dotted curves). The values of all the elements in the equivalent circuit model are listed in Table 3-2.1. A linear part is obtained on bare AuE (curve a), which shows that the electrochemical response of  $[\text{Fe}(\text{CN})_6]^{3-/4-}$  on the bare AuE is mainly controlled by a diffusion procedure. After TSS has been immobilized onto the AuE, an obvious increase in the Nyquist plots have been displayed and the  $R_{\text{ct}}$  value of 7.9  $\text{k}\Omega$  (curve b) is recorded, suggesting electron transfer is hindered because of the electrostatic repulsion between DNA and  $[\text{Fe}(\text{CN})_6]^{3-/4-}$ . Then, the TSS/AuE has been modified with MCH, the unoccupied part of the AuE is further blocked and the  $R_{\text{ct}}$  value is raised to 9.9  $\text{k}\Omega$  (curve c). When the hybridization of TSS with partial complementary aptamer sequence OBA was performed, the  $R_{\text{ct}}$  value is dramatically increase to 12.2  $\text{k}\Omega$  (curve d), confirming the kinetics barrier effect between  $[\text{Fe}(\text{CN})_6]^{3-/4-}$  and double-stranded DNA is further enhanced. After that, UiO-66 is assembled on to the OBA with phosphate terminal through coordination bonding, and the EIS response is further increased to 16.3  $\text{k}\Omega$  due to the poor conductivity of UiO-66. Finally, the signal sequence labeled with MB is modified on the surface of UiO-66, and the electrostatic repulsion between a large number of negatively charged phosphate skeletons and  $[\text{Fe}(\text{CN})_6]^{3-/4-}$  greatly hinders the electron transfer, resulting in a sharp increase in  $R_{\text{ct}}$  value to 24.7  $\text{k}\Omega$ . All experimental results suggested that the sensing interface had been successfully fabricated.

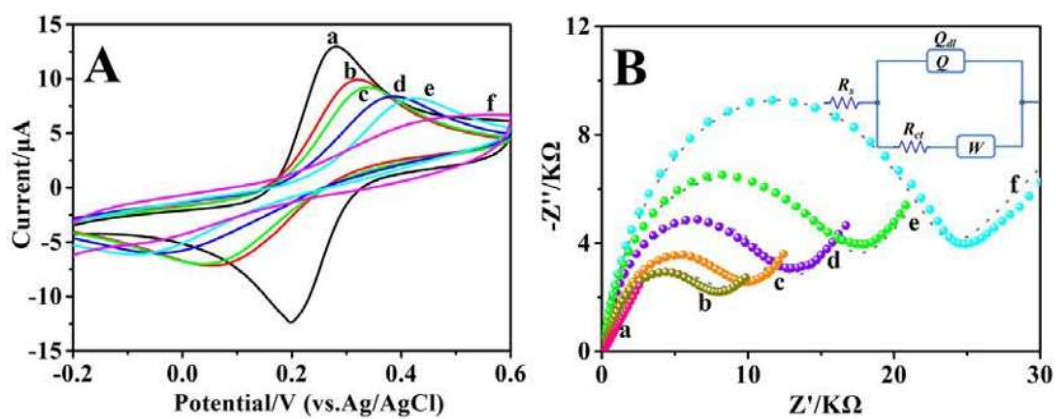


Fig. 3-2.2 Cyclic voltammograms (A) and EIS responses (B) of 1.0 mM  $[\text{Fe}(\text{CN})_6]^{3-/4-}$  with 0.1 M KCl on (a) bare AuE, (b) TSS/AuE, (c) TSS/MCH/AuE, (d) OBA-TSS/MCH/AuE, (e) UiO-66/OBA-TSS/MCH/AuE, (f) DLS/UiO-66/OBA-TSS/MCH/AuE.

Table 3-2.1 Values of the equivalent circuit elements obtained by fitting the experimental results for the different modified electrodes

Electrode	$R_s$ ( $k\Omega\text{ cm}^2$ )	$Q_{dl}$ ( $\mu\text{F cm}^2$ )	$n$	$R_{ct}$ ( $k\Omega\text{ cm}^2$ )	$W$ ( $m\Omega\text{ cm}^2$ )
AuE	0.011	0.003	1.000	0.15	0.128
TSS/AuE	0.136	2.278	0.800	7.9	0.136
TSS/MCH/AuE	0.131	2.260	0.800	9.9	0.322
OBA-TSS/MCH/AuE	0.115	1.084	0.868	12.2	0.360
UiO-66/OBA-TSS/MCH/AuE	0.087	1.030	0.866	16.3	0.361
DLS/UiO-66/OBA-TSS/MCH/AuE	0.183	0.914	0.800	24.7	0.144

### 3-2.3.4 Electrochemical behavior of the UiO-66-based aptasensor and its feasibility for OTA recognition

Fig. 3-2.3A displays the CV responses of different modified electrodes in 0.01 M PBS (pH 6.86) with a scan rate of  $0.10 \text{ V s}^{-1}$ . It can be seen from the figure that no obvious redox peaks was observed for UiO-66/OBA-TSS/MCH/AuE (curve a), suggesting that the modification layer of UiO-66/OBA-TSS is electrochemically inactive in PBS. After the UiO-66 modified electrode was incubated in DLS solution, a pair of well-defined redox peaks with the potential of  $-0.228 \text{ V}$  and  $-0.271 \text{ V}$  that corresponding to the redox reaction of MB is clearly observed (curve b), suggesting that MB-contained signal sequence has been successfully tethered on UiO-66 through the coordination between  $5'\text{-PO}_4^{3-}$  and  $\text{Zr}^{4+}$ . As a comparison, the OTA aptamer with 5'-tagged MB (MOBA) was also utilized for hybridization reaction. The electrochemical test shows that only a pair of faint redox peaks is observed on the hybridized electrode (curve c). Therefore, from the signal difference, it can be concluded that the UiO-66 in combining with the specific  $\text{PO}_4^{3-}\text{-Zr}^{4+}$  chemistry can effectively amplify the probe signal of the aptasensor.

The CV investigations of the fabricated aptasensor at different scan rates ( $v$ ) were also performed. Fig. 3-2.3B displays the CV responses of DLS/UiO-66/OBA-TSS/MCH/AuE in 0.01 M PBS (pH 6.86) with the scan rate ( $v$ ) ranging from  $0.02$  to  $0.35 \text{ V s}^{-1}$ . It is found that the redox peaks enhanced gradually with increase of the scan rate. The redox peak currents ( $I_p$ ) correlate well with the scan rate ( $v$ ) (Fig. 3-2.3C), and the linear regression equations of  $I_{pa}(\mu\text{A})=-0.012+1.223 v (\text{V s}^{-1})$  ( $R^2=0.999$ ) and  $I_{pc}(\mu\text{A})=-0.067-1.117 v (\text{V s}^{-1})$  ( $R^2=0.999$ ), respectively. The results also suggest that the electrochemical reaction of the aptasensor is an adsorption-controlled process [29], which confirms that the signal sequence have been assembled on the electrode surface by the expected coordination with the UiO-66. In order to further explore whether the adoption of UiO-66 will affect the recognition reaction of OBA to the target OTA, the electrochemical

response variation of the constructed aptasensor upon reaction with OTA was investigated by square wave voltammetry (SWV), and the results are displayed as Fig. 3-2.3D-a. It is found that after interaction with 2.0  $\mu\text{M}$  OTA, the oxidation peak (brown curve) of the aptasensor decreases by 4.6  $\mu\text{A}$  (74.0%) with respect to that of the pristine electrode (violet curve), showing that the developed aptasensor is feasible for recognition of target OTA with significant signal change. Comparatively, the response of MOBA-hybridized aptasensor only shows a decrease of 0.4  $\mu\text{A}$  (21.9%) in oxidation peak after interaction with 2.0  $\mu\text{M}$  OTA (Fig. 3-2.3D-b). Therefore, from the comparative experiments, it can be concluded that the aptasensor based on the use of UiO-66 as the signal-amplification platform not only inherits the excellent target recognition ability of the aptamer, but also greatly increased the analytical signal intensity of the sensor.

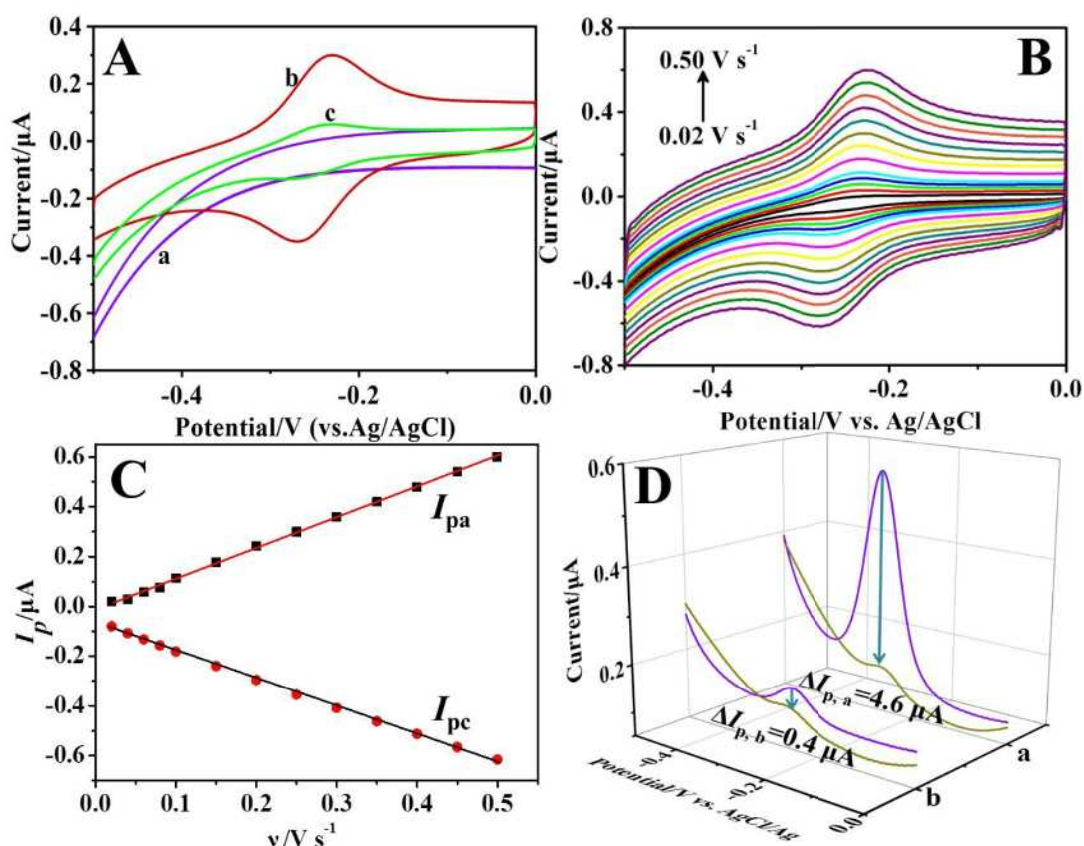


Fig. 3-2.3 (A) The CVs of (a) UiO-66/OBA-TSS/MCH/AuE, (b) DLS/UiO-66/OBA-TSS/MCH/AuE, (c) MOBA-TSS/MCH/AuE in 0.01 M PBS (pH 6.86) with a scan rate of  $0.10 \text{ V s}^{-1}$ . (B) The CVs of DLS/UiO-66/OBA-TSS/MCH/AuE in 0.01 M PBS (pH 6.86) with different scan rates (a-j: 0.02, 0.04, 0.06, 0.08, 0.10, 0.15, 0.20, 0.25, 0.30, 0.35  $\text{V s}^{-1}$ ). (C) the corresponding linear relationship of redox peak currents ( $I_{pa}$ ) with scan rates  $v$  ( $\text{V s}^{-1}$ ). (D) The SWV responses of absence (curve violet) and presence (curve brown) of 2.0  $\mu\text{M}$  OTA on the DLS/UiO-66/OBA-TSS/MCH/AuE (a) and MOBA-TSS/MCH/AuE (b) in 0.01 M PBS (pH 6.86)

### 3-2.3.5 Optimization of experimental conditions

As concern of the optimal condition to obtain the best analytical performance, the experimental conditions including modification concentration and time of UiO-66 on the surface of OBA-TSS/MCH/AuE, and the assembling of concentration and time of DLS on UiO-66/OBA-TSS/MCH/AuE surface were optimized. On the process of the DLS/UiO-66/OBA-TSS/MCH/AuE aptasensor fabrication, the relationship between the SWV oxidation peak currents ( $I_{pa}$ ) versus the modification concentration of UiO-66 ( $C_{UiO-66}$ ) is showed in Fig. 3-2.4A. It is observed that the  $I_{pa}$  values stepped up with increase of the concentration of UiO-66 from 0.2 g/L to 10 g/L, suggesting the signal amplification effect of the sensor increases with the increase of the modification amount of UiO-66. When the immobilized concentration of UiO-66 reaches to 10 g/L, the  $I_p$  value changes faintly, therefore, 5 g/L UiO-66 dispersion was identified as the optimal concentration. The optimal bonding time of UiO-66 ( $t_{UiO-66}$ ) on the aptasensor surface was investigated by immersing the OBA-TSS/MCH/AuE into 5 g/L UiO-66 for different time in the range from 0.5 to 3 h. The results show that the SWV peak currents ( $I_{pa}$ ) achieve stability on the prepared aptasensor at the bonding time of 2.5 h for UiO-66 (Fig. 3-2.4B), indicating that the binding UiO-66 on the electrode reaches equilibrium.

In addition, the assembling of concentration ( $C_{DLS}$ ) and time of DLS ( $t_{DLS}$ ) on UiO-66/OBA-TSS/MCH/AuE surface are also important parameters for obtaining high readable signal. Fig. 3-2.4C displays the influence of  $C_{DLS}$  on the signal intensity of the aptasensor. Obviously, the electrochemical responses enhance with the increase of  $C_{DLS}$  from 2  $\mu$ M to 10  $\mu$ M, and then level off in 12  $\mu$ M DLS, suggesting that 10  $\mu$ M is the optimal concentration of DLS for assembly reaction. Fig. 3-2.4D shows the relationship between the SWV peak currents ( $I_p$ ) and the incubation time ( $t_{DLS}$ ) of UiO-66/OBA-TSS/MCH/AuE in 10  $\mu$ M DLS solution. It can be seen that the electrochemical signal gradually increases with prolonging of the binding time of modification DLS on the UiO-66/OBA-TSS/MCH/AuE surface, and the highest current signal is achieved at the incubated time of 10 h. So, the incubation of UiO-66/OBA-TSS/MCH/AuE in 10  $\mu$ M DLS for 10 h was adopted for DLS assembly in the following experiment.

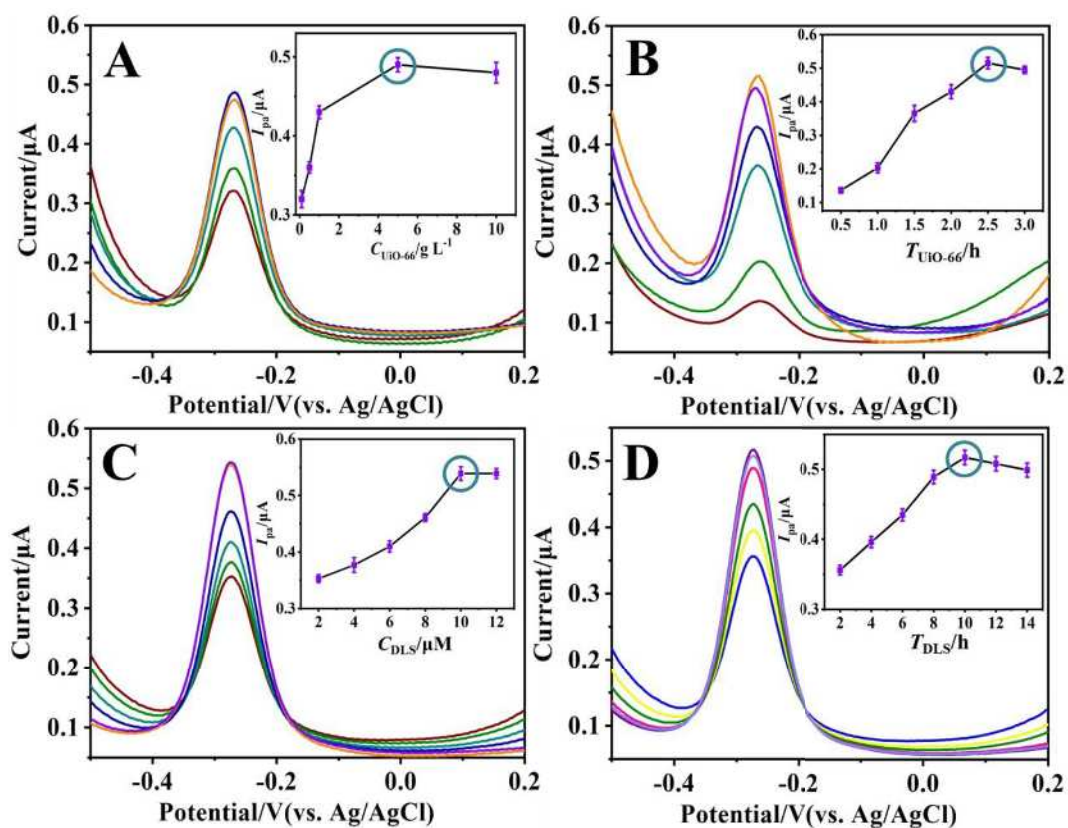


Fig. 3-2.4 Effect of the concentration (A) and the bonding time of UiO-66 (B), the concentration (C) and the incubation time (D) of DLS on the SWV response of the modified AuE in the 0.01 M PBS (pH 6.86).

### 3-2.3.6 Analytical performance of the aptasensor

The proposed aptasensor (DLS/UiO-66/OBA-TSS/MCH/AuE) was fabricated under the optimal experiment conditions and the quantitative analytical performance of the prepared aptasensor was inspected with various concentration of OTA by SWV. Fig. 3-2.5A shows that the SWV curves of the aptasensor upon interaction with increase amount of OTA. The results demonstrate that the characteristic oxidation peaks of the MB groups gradually decline with increasing of the OTA concentration, which indicates that increasing amount of OTA has interacted with OBA, and caused the release of OBA strands with the electroactive moiety of DLS/UiO-66 from aptasensor surface. The decreasing value ( $\Delta I_p$ ) from the SWV measurements displays a good linear relationship with the logarithm of the OTA concentration ( $\lg C_{OTA}$ ) ranging from 0.1 fM to 2.0  $\mu$ M (Fig. 3-2.5B). The regression equation was identified as  $\Delta I_p(\mu A)=0.377+0.01811\lg C_{OTA}$  (M) with a correlation coefficient of  $R^2=0.992$ . The detection limit is estimated to be 0.079 fM ( $3\delta$ ). Through comparison, it is found that the analytical performance of the UiO-66-based biosensor over performed that of the previously reported strategies (Table 3-2.2). The superiority of our sensor can be attributed to the signal amplification platform of the UiO-66: (1) The strong and specific coordination between the  $PO_4^{3-}$  and the  $Zr^{4+}$  center lead to effective assembly of UiO-66 on the  $-PO_4^{3-}$  modified OTA aptamer; (2) The UiO-66 platform bearing large surface and rich active site of  $Zr^{4+}$  can capture large amount of electroactive signal probe also by the direct coordination, which enhances the readable signal intensity of the developed aptasensor.

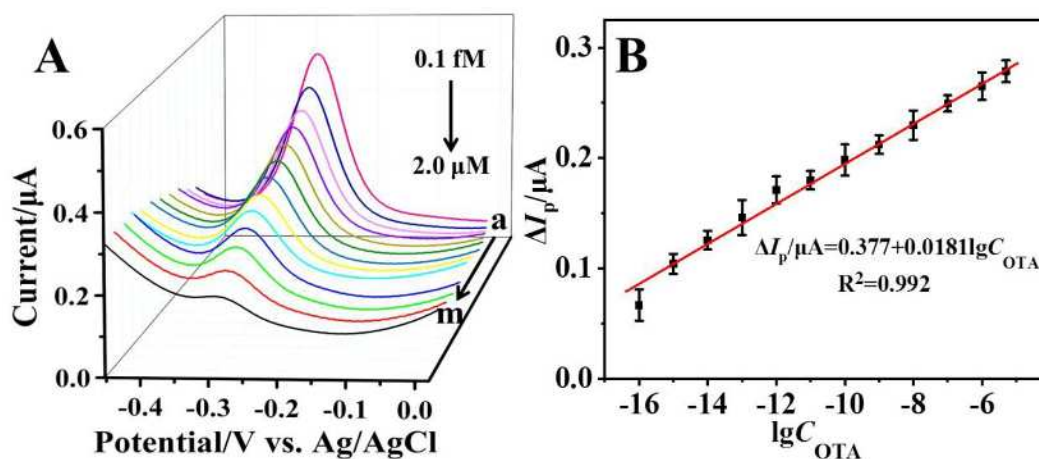


Fig. 3-2.5 (A) SWV responses of DLS/UiO-66/OBA-TSS/MCH/AuE in the 0.01 M PBS (pH 6.86) incubated with 0 M (a), 0.1 fM (b), 1.0 fM (c), 10.0 fM (d), 0.1 pM (e), 1.0 pM (f), 10 pM (g), 0.1 nM (h), 1.0 nM (i), 10.0 nM (j), 0.1  $\mu$ M (k), 1.0  $\mu$ M (l) and 2.0  $\mu$ M (m) of OTA. (B) Linear relationship of the different peak currents ( $\Delta I_p$ ) versus the logarithm of OTA concentration ( $\lg C_{\text{OTA}}$ ).

Table 3-2.2 Comparison of the proposed aptasensor with other  
OBA-based electrochemical OTA aptasensors

Electrode materials	Indicator	Method	Linear range	LOD	Ref.
TCA/drDNA-AuNPs/HA/GCE	label-free	DPV	2.5 pM-2.5 nM	1.24 pM	[1]
MB/OTA/hDNA/Apt/MCH/cDNA/AuE	MB	ACV	24 pM-24 nM	8.2 pM	[2]
Janus/COOH-GN/GCE	label-free	DPV	10 fM-10 nM	3.3 fM	[30]
PEDOT-AuNFs/GOS/GCE	label-free	CV	24 pM-49 nM	12 pM	[31]
AuNP@CuCoPBA/GCE	label-free	EIS	0.12 pM-25 pM	12.9 fM	[32]
BSA/anti-OTA/PdNPs/CFE	label-free	DPV	1.2 nM-50 nM	0.24 nM	[33]
Th-Au octahedra-dsDNA/SA-GR/GCE	TH	DPV	2.5 pM-12 nM	0.32 pM	[34]
DLS/UiO-66/OBA-TSS/MCH/AuE	MB	SWV	0.1 fM-2 μM	0.079 fM	This work.

Note: COOH-GN: Carboxylated grapheme; GCE: glassy carbon electrode; DPV: differential pulse voltammetry; TCA: trithiocyanuric acid; HA: hairpin aptamer; hDNA: complementary helper DNA; Apt: aptamer; MCH: 6-mercapto-1-hexanol; cDNA: complementary DNA; ACV: alternating current voltammetry; PEDOT: poly (3,4-ethylenedioxy thiophene); AuNFs: gold nanoflowers; GOS: graphene oxide sponge; PBA: Prussian Blue analogue; BSA: bovine serum albumin; CFE: carbon felt electrode; PdNPs: palladium nanoparticles; Th: thionine; GR: graphene; SA: streptavidin.

### 3-2.3.7 Regeneration and Specificity of the aptasensor

In traditional aptasensor, the target analytes was analyzed through interacting with the aptamer that directly immobilized on electrode surface, which resulted in the difficulty of regeneration of the aptasensor. Alternatively, the auxiliary strand-based competitive binding strategy can facilely overcome this deficiency [18]. In this strategy, the aptamer strand with the electroactive signal tag of DLS/UiO-66 was attached on the electrode through hybridizing with the electrode-confined supporting strands, showing its possibility for regeneration after analysis. In order to explore the feasibility of this strategy, the prepared aptasensor was reacted with 2.0  $\mu\text{M}$  OTA. Then, the electrode was washed with Tris buffer and distilled water several times to remove the non-specific adsorbed OTA and aptamer stands on the electrode surface. The sensor was reassembled with OBA, UiO-66, DLS, and was used to detect OTA again. Fig.3-2.6A shows the SWV responses of the aptasensor before (violet curves) and after interaction with 2.0  $\mu\text{M}$  OTA (black curves) for 11 cycles. The results show that the regenerated aptasensor still retains the original and excellent capacity to detect the target. Fig.3-2.6B shows the peak currents ( $I_p$ ) of the aptasensor for OTA binding and regeneration cycles, and the relative standard deviation (RSD) of the SWV responses of aptasensor before (dots violet) and after interaction with 2.0  $\mu\text{M}$  OTA (dots grey) were calculated to be 1.25 % and 1.77 %, respectively, indicating that the proposed aptasensor assembly strategy has an outstanding reusability.

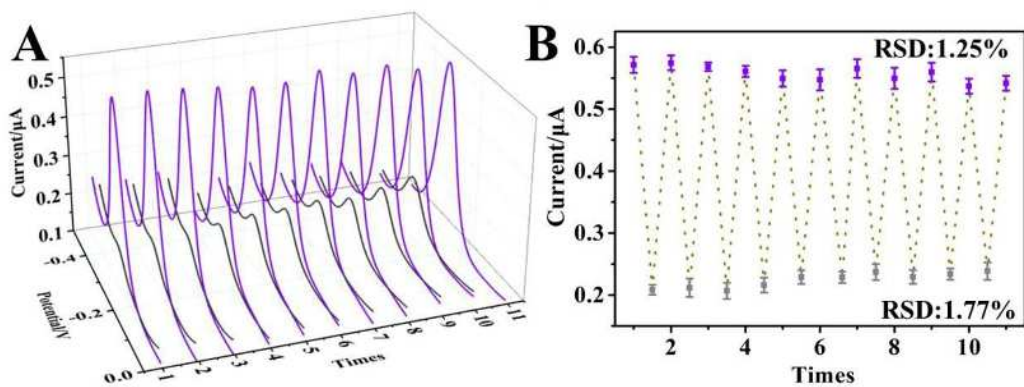


Fig. 3-2.6 (A) Graphic shows the SWV responses of the cycles of the aptasensor before (violet curves) and after toward 2.0  $\mu\text{M}$  OTA (black curves) and the reassembly results. (B) Peak currents ( $I_p$ ) of the aptasensor for OTA binding and regeneration cycles.

The specificity is one of the important indexes to evaluate the practical application performance of a sensor. In order to investigate the specificity of the aptasensor, 100 nM ochratoxin B (OTB), aflatoxin B1 (AFB1) and zearalenone (ZEN) were used as control samples for interaction. Fig. 3-2.7A displays the histograms of the specificity test result of the sensor with parallel three measurements for each sample. It is found that there is only a feeble current change ( $\Delta I_p$ ) after interaction with these controls, which is obviously different from the result on the aptasensor upon interaction with 10 nM OTA. In addition, when the aptasensor was immersed in the mixture solution including 10 nM OTA and other three possible interfering substances with the concentrations of 100 nM, the obtained  $\Delta I_p$  is also similar to that of OTA alone, which shows that the sensor has high selectivity for OTA.

### **3-2.3.8 Analysis of real sample**

In order to prove the applicability of the proposed aptasensor in real samples, the sensor was applied for determination of different concentrations of OTA in red wine samples by standard addition method. The result shows that the current response decreased with the increase of OTA concentration from 10 pM to 100 nM in red wine samples (Fig. 3-2.7B). The recovery was obtained in the range of 95.8%-104%, and the relative standard deviation (RSD) of the three parallel test results was less than 4.74% (Table 3-2.3), implying that the sensor is feasible for safety valuation in real sample.

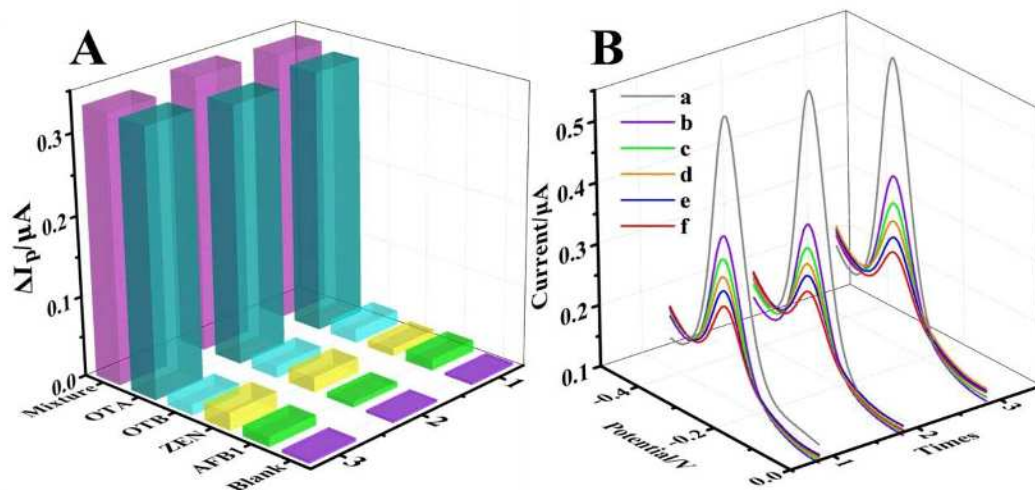


Fig. 3-2.7 (A) Specificity evaluation of the aptasensor by testing in a blank solution, 100 nM OTB, AFB1, ZEN, 10 nM OTA, and the mixture samples containing 10 nM OTA and OTB, AFB1, and ZEN at concentrations of 100 nM in the 0.01 M PBS (pH=6.86). (B) SWV responses of the aptasensor before (a) and after incubated with various concentrations 10 pM (b), 100 pM (c), 1 nM (d), 10 nM (e), and 100 nM (f) OTA in the red wine samples.

Table 3-2.3 Determination of OTA in red wine samples using the developed aptasensor <sup>a</sup>

<b>Red wine samples</b>	<b>Added</b>	<b>Found</b>	<b>Recovery (%)</b>	<b>RSD (%)</b>
1	10 pM	10.4 pM	104	1.95
2	100 pM	97.3 pM	97.3	3.42
3	1.0 nM	1.02 nM	102	3.09
4	10.0 nM	9.89 nM	98.9	4.74
5	100 nM	95.8 nM	95.8	4.40

<sup>a</sup> Mean values of three measurements.

### 3-2.4 Conclusions

In summary, a rational, sensitive and reusable electrochemical aptamer sensing strategy was proposed based on the *in-situ* coordination-assembled UiO-66 as signal amplification platform. Using OTA as a detection model, the analytical performance of the proposed aptasensor was investigated. The result shows that the UiO-66-based aptasensor not only inherits the excellent target recognition ability of the aptamer chemistry, but also greatly increases the analytical signal intensity of the sensor. As a result, a wide range, ultralow detection, and excellent specificity are obtained for the aptasensor. In addition, because the aptasensor is designed on the basis of the auxiliary strand-based competitive combination binding strategy, and therefore an outstanding reusability was achieved for the aptasensor. The aptasensor was also successfully applied for OTA determination in the red wine samples, demonstrating a promising prospect in food safety monitoring. In summary, based on the strong and specific  $\text{Zr}^{4+}$ - $\text{PO}_4^{3-}$  and the advantages of UiO-66 bearing rich active site and large surface area, the proposed strategy has the potential to construct a rational, excellent analytical performance and reusable aptamer biosensors, and it is expected to be applied to the detection of a variety of biomolecules.

### 3-2.5 References

- [1] X. Wang, Y. Shan, M. Gong, X. Jin, M. Jiang and J. Xu, *Sensors and Actuators B: Chemical*, **281**, 595-601 (2019).
- [2] C. Zhu, D. Liu, Y. Li, X. Shen, S. Ma, Y. Liu and T. You, *Biosens. Bioelectron.*, **150**, 111814 (2020).
- [3] Z. Tang, X. Liu, B. Su, Q. Chen, H. Cao, Y. Yun and B. D. Hammock, *Journal of hazardous materials*, **387**, 121678 (2020).
- [4] A. M. A. Alsharif, Y. M. Choo, G. H. Tan and L. B. Abdulra'uf, *Analytical Letters*, **52**, 1976-1990 (2019).
- [5] Z. Sun, X. Wang, Z. Tang, Q. Chen and X. Liu, *Ecotoxicology and environmental safety*, **171**, 382-388 (2019).
- [6] C. Sun, X. Liao, P. Huang, G. Shan, X. Ma, L. Fu and W. Kong, *Food Chemistry*, **315**, 126289 (2020).
- [7] P. P. Li, Y. Cao, C. J. Mao, B. K. Jin and J. J. Zhu, *Anal. Chem.*, **91**, 1563-1570 (2019).
- [8] J. Chang, X. Wang, J. Wang, H. Li and F. Li, *Analytical chemistry*, **91**, 3604-3610 (2019).
- [9] N. Colozza, K. Kehe, G. Dionisi, T. Popp, A. Tsoutsouloupoulos, D. Steinritz and F. Arduini, *Biosens. Bioelectron.*, **129**, 15-23 (2019).
- [10] J. Yi, Z. Liu, J. Liu, H. Liu, F. Xia, D. Tian and C. Zhou, *Biosens. Bioelectron.*, **148**, 111827 (2020).
- [11] Y. Li, D. Liu, C. Zhu, X. Shen, Y. Liu and T. You, *Journal of Hazardous Materials*, **387**, 122001 (2020).
- [12] Y. Duan, N. Wang, Z. Huang, H. Dai, L. Xu, S. Sun and M. Lin, *Materials Science and Engineering: C*, **108**, 110501 (2020).
- [13] Z. Han, Z. Tang, K. Jiang, Q. Huang, J. Meng, D. Nie and Z. Zhao, *Biosens. Bioelectron.*, **150**, 111894 (2020).
- [14] R. H. Ren, K. Shi, J. M. Yang, R. Yuan and Y. Xiang, *Sens. Actuators, B*, **258**,

783-788 (2018)

- [15] N. Hong, L. Cheng, B. G. Wei, C. D. Chen, L. L. He, D. R. Kong, J. X. Ceng, H. F. Cui and H. Fan, *Biosens. Bioelectron.*, **91**, 110–114 (2017).
- [16] X. Y. Zhang, C. X. Song, K. Yang, W. W. Hong, Y. Lu, P. Yu and L. Q. Mao, *Anal. Chem.*, **90**, 4968–4971 (2018).
- [17] X. L. Zhang, Z. H. Yang, Y. Y. Chang, M. Qing, R. Yuan and Y. Q. Chai, *Anal. Chem.*, **90**, 9538–9544 (2018).
- [18] J. Song, S. Li, F. Gao, Q. Wang and Z. Lin, *Chemical communications*, **55**, 905-908 (2019).
- [19] M. Bagheri and M. Y. Masoomi, *ACS Applied Materials & Interfaces*, **12**, 4625 (2020).
- [20] D. Giliopoulos, A. Zamboulis, D. Giannakoudakis, D. Bikiaris and K. Triantafyllidis, *Molecules*, **25**, 185 (2020).
- [21] S. Wang, C. M. McGuirk, A. d'Aquino, J. A. Mason and C. A. Mirkin, *Advanced Materials*, **30**, 1800202 (2018).
- [22] Y. Pang, Y. Fu, C. Li, Z. Wu, W. Cao, X. Hu and Q. Li, *Nano Letters*, **20**, 829 (2020).
- [23] Y. Li, M. Hu, X. Huang, M. Wang, L. He, Y. Song and M. Du, *Sensors and Actuators B: Chemical*, **306**, 127608 (2020).
- [24] S. Wang, C. M. McGuirk, M. B. Ross, S. Wang, P. Chen, H. Xing and C. A. Mirkin, *Journal of the American Chemical Society*, **139**, 9827-9830 (2017).
- [25] Z. Sun, L. Wang, S. Wu, Y. Pan, Y. Dong, S. Zhu and G. Li, *Anal. Chem.*, **92**, 3819 (2020).
- [26] Z. Hu, A. Nalaparaju, Y. Peng, J. Jiang and D. Zhao, *Inorganic chemistry*, **55**, 1134-1141 (2016).
- [27] L. Shen, R. Liang, M. Luo, F. Jing and L. Wu, *Physical Chemistry Chemical Physics*, **17**, 117-121 (2015).
- [28] M. J. Katz, Z. J. Brown, Y. J. Colón, P. W. Siu, K. A. Scheidt, R. Q. Snurr and O. K. Farha, *Chemical Communications*, **49**, 9449-9451 (2013).
- [29] R. Hajian, Z. Tayebi, N. Shams, *J. Pharm. Anal.*, **7**, 27 (2017).

- [30] Y. J. Yang, Y. Zhou, Y. Xing, G. M. Zhang, Y. Zhang, C. H. Zhang and S. M. Shuang, *Talanta*, **199**, 310-316 (2019).
- [31] P. Wang, L. Wang, M. Ding, M. Pei and W. Guo, *Analyst*, **144**, 5866-5874 (2019)
- [32] C. Gu, L. Yang, M. Wang, N. Zhou, L. He, Z. Zhang and M. Du, *Microchimica Acta*, **186**, 343 (2019).
- [33] K. Kunene, M. Weber, M. Sabela, D. Voiry, S. Kanchi, K. Bisetty and M. Bechelany, *Sensors and Actuators B: Chemical*, **305**, 127438 (2020).
- [34] M. Wei, S. Yue, W. Zhang and X. Li, *Analytical Methods*, **12**, 317-323 (2020).

## **Chapter 4**

### **General Conclusion and Scope**

## **Chapter 4.1**

### **General Conclusions**

#### **Chapter 2: The functionalization of metal-oxide and their application for electrochemical sensors**

##### **2-1 Synthesis of porous nanododecahedron Co<sub>3</sub>O<sub>4</sub>/C and its application for nonenzymatic electrochemical detection of nitrite**

Porous nanododecahedron of Co<sub>3</sub>O<sub>4</sub>/C nanocomposites was synthesized by calcination of the Co-based MOF (ZIF-67) in air at 400 °C and was used for fabricating a highly sensitive and low oxide potential nitrite ion (NO<sub>2</sub><sup>-</sup>) sensor. The structure and morphology characterization show that ZIF-67 behaves as an ideal sacrificial template and converted to Co<sub>3</sub>O<sub>4</sub>/C with regular shape. Electrochemical analysis shows that the excellent electrocatalysis performance toward the oxidation of NO<sub>2</sub><sup>-</sup> based on the synergy of Co<sub>3</sub>O<sub>4</sub> and carbon in the nanocomposite. At NO<sub>2</sub><sup>-</sup> concentration from 2 nM to 8 mM, a fast response time within 3 s is revealed and 1.21 nM of ultralow detection limit is achieved as the steady-state current signal linear increase. Using the nanocomposite acts as an electrochemical sensing material for determination of NO<sub>2</sub><sup>-</sup> in the real samples, the results are satisfactory.

##### **2-2 Synthesis of ZrO<sub>2</sub>/C using UiO-67 as template and its high sensitivity for heavy metal ions**

A thin nanosheet structure of ZrO<sub>2</sub>/C was prepared using UiO-67 with a flat cuboid structure as precursor. The peculiar and fluffy structures endowed materials with high surface areas that tremendously improved the adsorption capacity of electrode materials for heavy metal ions. Thus, ZrO<sub>2</sub>/C acts as an electrode material was used to simultaneous detection of Pb(II) and Cd(II) in 0.1 M HAc-NaAc buffer by differential

pulse anodic stripping voltammetry (DPASV). Under the optimal conditions, the results show that prepared sensor has the high sensitivity, good stability and low interference of the detection for two metal ions, and the limit detections for Pb(II) and Cd(II) of 0.007  $\mu\text{A}$  and 0.019  $\mu\text{A}$  were estimated, respectively. Furthermore, it was also successfully applied for the detection of trace Pb(II) and Cd(II) in real water samples with a satisfactory result.

### **2-3 Yolk-shell-structured SnO<sub>2</sub>-C and poly-tyrosine composite films as an impedimetric “Signal-Off” sensing platform for transgenic soybean screening**

The yolk-shell structured SnO<sub>2</sub>-C nanospheres have been prepared by a hydrothermal reaction of SnCl<sub>2</sub>·2H<sub>2</sub>O and glucose, followed by carbonization under 500 °C in air condition. Then an inorganic/organic hybrid film bearing SnO<sub>2</sub>-C and polytyrosine (pTyr) is fabricated by electro-polymerization of SnO<sub>2</sub>-C modified electrode in tyrosine solution. The modified electrode is utilized as a supporting platform for covalent immobilization of cauliflower mosaic virus 35s (CaMV35s) promoter gene fragments to construct an electrochemical DNA sensor. Chronocoulometric experiments show that the loading density of probe DNA (pDNA) and hybridization efficiency are determined to be as high as 4.54×10<sup>13</sup> strands cm<sup>-2</sup> and 83.2%, respectively. Upon hybridization with target DNA (tDNA), the probe DNA that lied flat on the electrode surface through hydrogen bonding with pTyr is erected, reducing the charge repulsion and steric hindrance for [Fe(CN)<sub>6</sub>]<sup>3-/4-</sup> diffusion. So a “signal-off” response strictly dependent on hybridization reaction is achieved in electrochemical impedance spectroscopy. The response mechanism is predicted by theoretical calculation. Owing to the high probe density and hybridization efficiency of the sensor, a wide kinetic linear ranging from 1.0 aM to 100 pM and an ultralow detection limit of 0.53 aM for target sequence are obtained. The biosensor also presents high recognition ability toward the DNA samples extracted from real transgenic and non-transgenic soybeans, showing great promising of the biosensor for facile monitoring of transgenic product.

### **Chapter 3: The functionalization of metal-organic frameworks (MOFs) and their application for electrochemical sensors**

#### **3-1 Flexible flower-like MOF of $\text{Cu}_2(\text{trans-1,4-cyclohexanedicarboxylic acid})_2$ as the electroactive matrix material for label-free and highly sensitive sensing of thrombin**

A flexible metal-organic framework (MOF) of  $\text{Cu}_2(\text{trans-1,4-cyclohexanedicarboxylic acid})_2$  ( $\text{Cu}_2(\text{CHDC})_2$ ) presents high thermal and mechanical stability based on its dimer paddle-wheel  $\text{Cu}_2(\text{COO})_4$  core and slight elasticity of the -CHDC connector, and therefore shows a promising application in electrochemistry. Herein, the flexible MOF was synthesized by a facile hydrothermal method, and the physical characterization shows that the  $\text{Cu}_2(\text{CHDC})_2$  displays a flower-like shape with a large surface area of  $237.36 \text{ m}^2 \text{ g}^{-1}$ . Then a signal-off aptasensor using thrombin as the target model was constructed that  $\text{Cu}_2(\text{CHDC})_2$  as the signal platform and in-situ electrodeposited gold nanoparticles as signal amplification and aptamer immobilization matrix. The proposed thrombin aptasensor displays excellent performance with wide linear range, ultralow detection limit of  $0.01 \text{ fM}$  ( $\text{S/N}=3$ ), and favorable specificity. Also, the aptasensor was applied for determination of thrombin in the human serum samples, the satisfying results are achieved. The results imply that the proposed sensor can be potentially used for the early diagnosis of disease and clinical monitoring.

#### **3-2 A strategy for the construction of a reusable electrochemical aptasensor using UiO-66 as signal amplified platform**

Direct, strong and specific coordination between  $\text{Zr}^{4+}$  and phosphate group ( $-\text{PO}_4^{3-}$ ) provides a new avenue to construct Zr-MOF-based high-performance electrochemical biosensors. In this work, a rational, sensitive and reusable electrochemical aptasensing strategy for Ochratoxin A (OTA) was proposed using *in-situ* coordination-assembled UiO-66 as signal amplification platform in the design, the OTA aptamer was

pre-hybridized with supporting strands that immobilized on the gold electrode surface. Then the classic Zr-MOF of UiO-66 was *in-situ* immobilized on the terminal of OTA aptamer through coordination between  $Zr^{4+}$  and  $5'-PO_4^{3-}$  modified on OTA aptamer. Furthermore, the signal probe with electroactive tag of methylene blue was *in-situ* assembled on UiO-66 also by the Zr-O-P bond. Because of large surface area and rich active sites of  $Zr^{4+}$ , the comparative assay shows that the UiO-66 greatly enhances the analytical performance of the aptasensor. A wide range from 0.1 fM to 2.0  $\mu$ M and an ultralow detection limit of 0.079 fM (S/N = 3) for target OTA were achieved. In addition, because the aptasensor was designed on the basis of the auxiliary strand-based competitive binding strategy, 11 times reusability of the aptasensor can be realized in accompany with the detection process. The aptasensor can also be applied for detection of OTA in the red wine sample, demonstrating a promising prospect of the biosensor for food safety monitoring.

## Chapter 4.2

### Scope

Recently, people have devoted themselves to developing advanced materials with excellent electrochemical properties to modify common working electrodes. Metal oxide, MOFs and their derivatives have attracted great attention in the application field of electrochemical sensor modification materials because of their high surface area, high catalytic activity and strong adsorption capacity, *etc.*

In chapter 2, the author has synthesized the metal oxide-carbon nanocomposites ( $\text{Co}_3\text{O}_4/\text{C}$ ,  $\text{ZrO}_2/\text{C}$  and  $\text{SnO}_2/\text{C}$ ) through heat treatment. Due to the introduction of carbon materials, the electrical conductivity of these metal oxides is effectively improved. They are all used as ideal electrode materials to detect  $\text{NO}_2^-$ , heavy metal ions and DNA. Therefore, in the future research, more functionalize metal oxides will be planned to synthesis through recombining metal oxides and some functional materials such as graphene, carbon nanotube, gold nanoparticles, *etc.* Then using these metal oxide composites as sensing materials in electrochemical sensing detection.

In chapter 3-1, the author has synthesized a flexible MOF of  $\text{Cu}_2(\text{trans-1,4-cyclohexanedicarboxylic acid})_2$  ( $\text{Cu}_2(\text{CHDC})_2$ ) and using it as a signal platform to fabricate a sensitive free-label aptasensor for thrombin detection due to its electrochemical redox active and high surface area. However, it is a pity that the switching properties of flexible MOFs multitudinous dynamic behaviors, for example, the expansion/shrinkage of the framework, the opening/closing of pores, or the reversible change of the physicochemical properties, have not been fully utilized and discussed in this study. The reversible change of flexible MOF structure was depends on a variety of subtle parameters, including temperature, pH, pressure, electromagnetic irradiation or adsorption of guest molecules and so on. It inspires us

to further design a more reasonable and widely used electrochemical sensing interface for temperature effect, pressure effect, solvent effect, *etc.* due to the specific switching properties of flexible MOF.

In chapter 3-2, Zr-based MOFs and its derivatives were synthesized, and the authors marvel at the excellent biocompatibility and strong adsorption capacity of this kind of materials. Based on the excellent biocompatibility of UiO-66, the DNA strands were successfully stably modified on the surface of UiO-66, an Ochratoxin A (OTA) aptasensor was constructed for quantitative detection OTA. Therefore, bases on the characteristic of the strong and stable Zr-P-O coordination between Zr-based MOFs and DNA, devoting to the design and construction of various types of MOFs-based electrochemical biosensors is the focus of our next work.

## Acknowledgments

The author is sincerely grateful to Professor Hidekazu Tanaka for his great help during the course of the studies, and sincerely grateful to Professor Makoto Handa, Dr. Yusuke Kataoka and Dr. Aohan Wang of Shimane University for their kind help during my studying in Japan.

The author wishes to thank the students of Natsumi Yano, Mayoka Yamane, Mirai Suganuma, Ryohei Shibata, Tomokazu Tahara, Hisayuki Nozato, Yuko Ishizaki, *etc.* for their warm help in the laboratory of Shimane University.

The author would like to thanks to all the workmates of inorganic chemistry group and Professor Qingxiang Wang of Minnan Normal University for their help during the course of the study.

The author sincerely acknowledges to the students of Juan Song, Shuping Lai, Yan Lu and Weimin Lu of Minnan Normal University for their help in the experiments.

Finally, the author gratefully acknowledges to her mother, her husband and her daughter for their selfless support.

# Appendix

## List of Figures

### Chapter 1

Fig. 1.1 Schematic diagram of three-electrode electrochemical workstation

Fig. 1.2 Schematic diagram of the principle of electrochemical biosensor

Fig. 1.3 Schematic diagram of the mainly MOFs-derived materials

Fig. 1.4 Schematic illustration of postsynthetic modification of MOFs external surfaces through covalent bonds (top) and coordinative bonds (bottom) on the MOFs surface

### Chapter 2

Fig. 2-1.1 (A) XRD pattern of ZIF-67, (B) XRD pattern, and (C)  $N_2$  adsorption-desorption isotherms of  $Co_3O_4/C$  obtained at 300 °C, 400 °C, 500 °C.

Fig. 2-1.2 SEM images of (A) ZIF-67, and Low-magnification TEM images  $Co_3O_4$  products obtained at (B) 300 °C, (C, E) 400 °C, and (D) 500 °C. (F) HRTEM image of  $Co_3O_4$  formed at 400 °C.

Fig. 2-1.3 (A) Full XPS spectrum of  $Co_3O_4/C$  prepared at 400 °C. Result of curve fitting of (B) Co 2p, (C) O 1s, and (D) C 1s spectra.

Fig. 2-1.4 (A) CVs for three products were obtained at 300 °C (a), 400 °C (b), and 500 °C (c) modified GCE in the solution of 1 mM  $Fe(CN)_6^{3-/4-}$  containing 0.1 M KCl, inset: EIS characterization for different modified GCE. (B) CVs of the GCE before (a) and after modification with different volume ratio of  $Co_3O_4/C$  nanoparticles to CS in the composite membrane (b-d). (C) Histograms of oxidation peak current ( $I_{pa}$ ) of  $Co_3O_4/C$  for  $NO_2^-$  in the solution of PBS, NaOH, B-R and NaAc-HAc. (D) Histograms of oxidation peak current ( $I_{pa}$ ) of  $Co_3O_4/C$  for  $NO_2^-$  versus pH values of NaAc-HAc buffer.

Fig. 2-1.5 CVs of GCE (A), CS/GCE (B), and  $Co_3O_4/C$ -CS/GCE (C) in NaAc-HAc (pH 4.5) buffer without (a) and with (b) 1.0 mM  $NO_2^-$ . (D)  $Co_3O_4/C$ -CS/GCE measured in NaAc-HAc (pH 4.5) containing various concentrations of  $NO_2^-$ .

Fig. 2-1.6 (A) CV responses of the  $\text{Co}_3\text{O}_4/\text{C-CS}/\text{GCE}$  investigated in the buffer solution with 0.2 mM  $\text{NO}_2^-$  at various  $v$ . Inset: Plot of  $I_{pa}$  vs.  $v^{1/2}$ . (B) Chronoamperograms of  $\text{Co}_3\text{O}_4/\text{C-CS}/\text{GCE}$  without and with different  $\text{NO}_2^-$  concentrations in NaAc-HAc (pH 4.5) analyzed at 0.85 V. (C) Plots of  $I_{cat}$  vs  $t^{-1/2}$ . (D) Plot of  $I_{cat}/I_L$  vs.  $t^{1/2}$ .

Fig. 2-1.7 (A) Chronoamperometric currents of the  $\text{Co}_3\text{O}_4/\text{C-CS}/\text{GCE}$  upon unremitting injections of 0.05 mM  $\text{NO}_2^-$  in NaAc-HAc (pH 4.5) at various potentials. (B) Chronoamperometric responses of the  $\text{Co}_3\text{O}_4/\text{C-CS}/\text{GCE}$  upon unremitting injections of  $\text{NO}_2^-$  at the applied potential of 0.85 V. Inset a is the amplified  $I-t$  curve in the low concentration of  $\text{NO}_2^-$ . Inset b is response time of the sensor upon injection of  $\text{NO}_2^-$ . (C) Calibration plots for the  $\text{Co}_3\text{O}_4/\text{C-CS}/\text{GCE}$  with  $\text{NO}_2^-$  concentrations of 2.0 nM to 1.0 mM and 1.0 to 8.0 mM. The inset displays an amplified calibration curve with  $\text{NO}_2^-$  concentrations ranging from 2.0 nM to 1.0 mM. (D) Amperometric response of  $\text{Co}_3\text{O}_4/\text{C-CS}/\text{GCE}$  to 0.05 mM  $\text{NO}_2^-$  in the presence of 0.1 mM DA, UA, AA, Glu,  $\text{H}_2\text{O}_2$ ,  $\text{NO}_3^-$ ,  $\text{Na}^+$ ,  $\text{K}^+$ ,  $\text{Mg}^{2+}$ ,  $\text{Zn}^{2+}$ .

Fig. 2-1.8 (A) Amperometric current with 0.05 mM  $\text{NO}_2^-$  over a long time-period of 10000 s. Inset: the stability of the sensor to  $\text{NO}_2^-$  measured every other day for 4 weeks. (B) Reproducibility of five  $\text{Co}_3\text{O}_4/\text{C-CS}/\text{GCE}$ s for detection of 0.05 mM  $\text{NO}_2^-$ . Inset: Repeatability of  $\text{Co}_3\text{O}_4/\text{C-CS}/\text{GCE}$  for detection 0.05 mM  $\text{NO}_2^-$  seven times.

Fig. 2-1.9 Chronoamperometric responses recorded at  $\text{Co}_3\text{O}_4/\text{C-CS}/\text{GCE}$  upon injection of real samples and followed by continuous injections of 0.02 mM  $\text{NO}_2^-$  in HAc-NaAc (pH 4.5) buffer

Fig. 2-2.1 (A) XRD pattern (A) and  $\text{N}_2$  adsorption–desorption isotherms (B) of UiO-67 particles.

Fig. 2-2.2 (A) XRD pattern of UiO-67 (a), UiO-67-200 (b), UiO-67-300 (c),  $\text{ZrO}_2/\text{C}$  (d), UiO-67-500 (e) and SEM images of UiO-67 (B), UiO-67-200 (C), UiO-67-300 (D),  $\text{ZrO}_2/\text{C}$  (E), UiO-67-500 (F).

Fig. 2-2.3 (A) Full XPS spectrum of  $\text{ZrO}_2/\text{C}$  prepared at 400 °C. Result of curve fitting of (B) Zr 3d, (C) C 1s, and (D) O 1s spectra.

Fig. 2-2.4 DPASVs responses (A) and histogram of stripping peak currents ( $I_p$ ) (B) for 1.0  $\mu\text{M}$  each of Pb(II) and Cd(II) on bare (a), Nafion (b), UiO-67-200/Nafion (c), UiO-67-300/Nafion (d),  $\text{ZrO}_2/\text{C}/\text{Nafion}$  (e), UiO-67-500/Nafion (f), and UiO-67/Nafion (g) modified GCE in 0.1 M HAc-NaAc buffer (pH 4.5).

Fig. 2-2.5 The DPASV responses (a) and point plots of stripping peak currents ( $I_p$ ) (B) of pH value of 0.1 M HAc-NaAc buffer (A), deposition potential (B), and deposition time (C) of the UiO-67-400/Nafion/GCE for 1.0  $\mu\text{M}$  each of Pb(II) and Cd(II).

Fig. 2-2.6 DPASV response of the  $\text{ZrO}_2/\text{C}/\text{Nafion}/\text{GCE}$  at 0.1, 0.2, 0.4, 0.5, 0.8, 1.0 and 1.2  $\mu\text{M}$  Pb(II) in the presence of 0.5  $\mu\text{M}$  Cd(II) (A), and 0.1, 0.2, 0.4, 0.5, 0.8, 1.0 and 1.2  $\mu\text{M}$  Cd(II) in the presence of 0.5  $\mu\text{M}$  Pb(II) (B) in 0.1 M HAc-NaAc buffer (pH 4.5).

Fig. 2-2.7 (A) DPASV response for the simultaneous analysis of Pb(II) and Cd(II) in the different concentration from 0.01 to 2.0  $\mu\text{M}$  and 0.05 to 5.0  $\mu\text{M}$  on  $\text{ZrO}_2/\text{C}/\text{Nafion}/\text{GCE}$  in 0.1 M HAc-NaAc buffer (pH 4.5), (B) The calibration curves of Pb(II), (C) the calibration curves of Cd(II).

Fig. 2-2.8 DPASV responses (A) and histogram of stripping peak currents ( $I_p$ ) of interference experiments for simultaneous detection of Pb(II) and Cd(II) without (curve orange) and with (curve green) different metal ions (5-fold concentration) under optimal conditions. DPASVs responses (C) and the point plot of stripping peak currents ( $I_p$ ) (D) for simultaneous detection of 0.5  $\mu\text{M}$  Pb(II) and Cd(II) on the  $\text{ZrO}_2/\text{C}/\text{Nafion}/\text{GCE}$  in 0.1 M HAc-NaAc buffer (pH 4.5).

Fig. 2-2.9 DPASV responses recorded at  $\text{ZrO}_2/\text{C}/\text{Nafion}/\text{GCE}$  upon injection of real samples and followed by continuous injections of Pb(II) and Cd(II) in HAc-NaAc (pH 4.5) buffer.

Fig. 2-3.1 (A) XRD patterns of  $\text{SnO}_2\text{-C}$  and its precursor, (B) C 1s, (C) O 1s and (D) Sn 3d XPS spectra of  $\text{SnO}_2\text{-C}$ .

Fig. 2-3.2 SEM(A) and TEM(B) images for  $\text{SnO}_2\text{-C}$  precursor

Fig. 2-3.3 SEM images (A-B), TEM images (C-D), and HRTEM image (E) for yolk-shell  $\text{SnO}_2\text{-C}$  structure nanospheres, EDX element mapping (F) of  $\text{SnO}_2\text{-C}$  nanospheres reveals the elemental distribution of C, O, and Sn.

Fig. 2-3.4 EDX spectra of yolk (A) and shell (B) for  $\text{SnO}_2\text{-C}$  nanospheres

Fig. 2-3.5 (A) Continuously scanned CVs of  $\text{SnO}_2\text{-C}/\text{GCE}$  and GCE (inset) in the mixture solution of  $1.0 \times 10^{-4}$  M Tyr and 0.1 M KCl with the scan rate of  $100 \text{ mV s}^{-1}$ . (B) Proposed growth mechanism of pTyr on  $\text{SnO}_2\text{-C}$  by electro-polymerization.

Fig. 2-3.6 Cyclic voltammograms (A) and Nyquist diagrams (B) of 1.0 mM  $[\text{Fe}(\text{CN})_6]^{3-/4-}$  (1:1) with 0.1 M KCl at bare GCE (a), pTyr/GCE (b),  $\text{SnO}_2\text{-C}/\text{GCE}$  (c), pTyr/ $\text{SnO}_2\text{-C}/\text{GCE}$  (d), and pDNA/pTyr/ $\text{SnO}_2\text{-C}/\text{GCE}$  (e). Inset in image B shows the

equivalent circuit diagram of the modified electrodes.

Fig. 2-3.7 (A) Chronocoulometric curves of pDNA/pTyr/SnO<sub>2</sub>-C/GCE in 10 mM pH 8.0 Tris-HCl without (a) and with (b) 50 μM RuHex. The chronocoulometric curve (c) is pDNA/pTyr/SnO<sub>2</sub>-C/GCE after hybridization with 0.1 nM tDNA in 10 mM pH 8.0 Tris-HCl with 50 μM RuHex. (B) The same test was matched at pDNA/pTyr/GCE. (C) Schematic illustration of larger surface to accommodate the tDNA for hybridization.

Fig. 2-3.8 Effect of (A) amount of SnO<sub>2</sub>-C, (B) immobilization time ( $t_{\text{DNA}}$ ) of pDNA at pTyr/SnO<sub>2</sub>-C/GCE, (C) hybridization time ( $t_{\text{H}}$ ), (D) hybridization temperature ( $T_{\text{H}}$ ) of tDNA on pDNA/pTyr/SnO<sub>2</sub>-C/GCE on the  $R_{\text{et}}$ . The electrolyte is a 1.0 mM [Fe(CN)<sub>6</sub>]<sup>3-/4-</sup> (1:1) with 0.1 M KCl. The Hybridization concentration of tDNA is 10 pM.

Fig. 2-3.9 (A) Nyquist diagrams of pDNA/pTyr/SnO<sub>2</sub>-C/GCE before (a) and after hybridization with 1.0 aM (b), 10 aM (c), 100 aM (d), 1.0 fM (e), 10 fM (f), 100 fM (g), 1.0 pM (h), 10 pM (i), 100 pM (j), 1.0 nM (k) tDNA in 1.0 mM [Fe(CN)<sub>6</sub>]<sup>3-/4-</sup> (1:1) with 0.1 M KCl solution. (B) The calibration curve for  $\Delta R_{\text{et}}$  values versus the logarithm of tDNA concentrations ( $\lg C$ ). (C) The illustration of the hydrogen bonding effect before and after hybridization reaction.

Fig. 2-3.10 The binding energies ( $E_{\text{B}}$ ) of various bases (adenine (A), cytosine (C), thymine (T), guanine (G)) to the hydroxyl-terminated of tyrosine monomer were resulting from DFT calculation models.

Fig. 2-3.11 Nyquist diagrams of the biosensor before (a) and after hybridization with 10 pM NC (b), 3MT (c), 1MT (d) and tDNA (e). (Inset is the corresponding histogram of  $R_{\text{et}}$  values.)

Fig. 2-3.12 EIS responses of (A) pDNA/pTyr/SnO<sub>2</sub>-C modified five independent electrodes hybridized with complementary tDNA (10 pM) (B) before (a, a') and after (e, e') of the regenerated electrodes and its hybridized electrodes for 5 rounds.

Fig. 2-3.13 (A) Nyquist diagrams of the biosensor before (a) and after incubation in blank buffer (b), and PCR sample from non-TG soybean (c) and TG soybean (d). (Inset is the histogram of  $R_{\text{et}}$  values). (B) PCR samples of non-TG soybean and TG soybean detected by homiothermy fluorescence method.

### Chapter 3

Fig. 3-1.1 XRD pattern and crystal structure (inset) (A),  $N_2$  adsorption-desorption isotherms and the pore size distribution curve (inset) (B) of the  $Cu_2(CHDC)_2$ , SEM (C, D), TEM (E), and HRTEM (F) and an enlarged image of lattice stripes (inset) images of  $Cu_2(CHDC)_2$ .

Fig. 3-1.2 Three-dimensional (3D) (a), top-viewed (b), and cross-sectional (c) AFM images of  $Cu_2(CHDC)_2/GCE$  (A),  $AuNPs/Cu_2(CHDC)_2/GCE$  (B),  $MCH/TBA/AuNPs/Cu_2(CHDC)_2/GCE$  (C), and  $Thrombin/MCH/TBA/AuNPs/Cu_2(CHDC)_2/GCE$  (D).

Fig. 3-1.3 CVs (A) and Nyquist plots (B) of  $1.0\text{ mM } [Fe(CN)_6]^{3-/4-}$  with  $0.1\text{ M KCl}$  on bare GCE (a),  $Cu_2(CHDC)_2/GCE$  (b),  $AuNPs/Cu_2(CHDC)_2/GCE$  (c),  $TBA/AuNPs/Cu_2(CHDC)_2/GCE$  (d),  $MCH/TBA/AuNPs/Cu_2(CHDC)_2/GCE$  (e),  $thrombin/MCH/TBA/AuNPs/Cu_2(CHDC)_2/GCE$  (f).

Fig. 3-1.4 (A) The CVs were recorded in  $0.01\text{ M PBS (pH 6.86)}$  with a scan rate of  $0.10\text{ V s}^{-1}$  on  $Cu_2(CHDC)_2/GCE$  (a),  $AuNPs/Cu_2(CHDC)_2/GCE$  (b),  $TBA/AuNPs/Cu_2(CHDC)_2/GCE$  (c),  $MCH/TBA/AuNPs/Cu_2(CHDC)_2/GCE$  (d). (B) The CVs of  $MCH/TBA/AuNPs/Cu_2(CHDC)_2/GCE$  in  $0.01\text{ M PBS (pH 6.86)}$  with different scan rates (a-j:  $0.02, 0.04, 0.06, 0.08, 0.10, 0.15, 0.20, 0.25, 0.30, 0.35\text{ V s}^{-1}$ ). (Inset: the linear relationship of  $I_{pa}$  with scan rates  $v$  ( $\text{V s}^{-1}$ )).

Fig. 3-1.5 Effect of the cast amounts (V) of  $Cu_2(CHDC)_2$  on the DPV response of the modified GCE in the  $0.01\text{ M PBS (pH 6.86)}$  (A), the CV responses of  $AuNPs$  modified on the  $Cu_2(CHDC)_2/GCE$  by electrochemically scanned in  $0.5\text{ mM HAuCl}_4$  solution for 30 cycles (B) and effect of the  $AuNPs$  deposition cycles on the  $Cu_2(CHDC)_2/GCE$  in the  $0.01\text{ M PBS (pH 6.86)}$  (C), effect of the bonding time of TBA (D), the concentration of TBA (E) and the incubation time of thrombin (F) on the DPV response of the modified GCE in the  $0.01\text{ M PBS (pH 6.86)}$ .

Fig. 3-1.6 (A) DPV responses of  $MCH/TBA/AuNPs/Cu_2(CHDC)_2/GCE$  in the  $0.01\text{ M PBS (pH 6.86)}$  before (a) and after incubated with  $0.01\text{ fM}$  (b),  $0.1\text{ fM}$  (c),  $1.0\text{ fM}$  (d),  $10.0\text{ fM}$  (e),  $0.1\text{ pM}$  (f),  $1.0\text{ pM}$  (g),  $10\text{ pM}$  (h),  $0.1\text{ nM}$  (i),  $1\text{ nM}$  (j), and  $10\text{ nM}$  (k)

thrombin. (B) Linear relationship of peak currents ( $\Delta I_p$ ) versus the logarithm of thrombin concentration ( $\lg C_{\text{thrombin}}$ ).

Fig. 3-1.7 (A) Selectivity analysis of the aptasensor tested in a blank solution, 10 pM BSA, Hb, Try, 1 pM thrombin, and the mixture samples containing 1 pM thrombin and BSA, Hb, and Try at concentrations of 10 pM in the 0.01 M PBS (pH 6.86). (B) Reproducibility of seven aptasensors was investigated before and after interacted with 0.1 nM thrombin. (C) DPV responses of the aptasensor incubated with various concentrations of 0 (a), 0.20 (b), 2.00 (c), 20.0 (d) fM thrombin in human serum sample in the 0.01 M PBS (pH 6.86).

Fig. 3-2.1 XRD pattern (A),  $N_2$  adsorption–desorption isotherms (B), the pore size distribute and the crystal structure (inset, B), and SEM (C, D) images of UiO-66 particles.

Fig. 3-2.2 Cyclic voltammograms (A) and EIS responses (B) of 1.0 mM  $[\text{Fe}(\text{CN})_6]^{3-/4-}$  with 0.1 M KCl on (a) bare AuE, (b) TSS/AuE, (c) TSS/MCH/AuE, (d) OBA-TSS/MCH/AuE, (e) UiO-66/OBA-TSS/MCH/AuE, (f) DLS/UiO-66/OBA-TSS/MCH/AuE.

Fig. 3-2.3 (A) The CVs of (a) UiO-66/OBA-TSS/MCH/AuE, (b) DLS/UiO-66/OBA-TSS/MCH/AuE, (c) TSS/MCH/AuE, (d) MOBA-TSS/MCH/AuE in 0.01 M PBS (pH 6.86) with a scan rate of  $0.10 \text{ V s}^{-1}$ . (B) The CVs of DLS/UiO-66/OBA-TSS/MCH/AuE in 0.01 M PBS (pH 6.86) with different scan rates (a-j: 0.02, 0.04, 0.06, 0.08, 0.10, 0.15, 0.20, 0.25, 0.30,  $0.35 \text{ V s}^{-1}$ ). (C) the corresponding linear relationship of redox peak currents ( $I_{pa}$ ) with scan rates  $v$  ( $\text{V s}^{-1}$ ). (D) The SWV responses of absence (curve violet) and presence (curve brown) 2.0  $\mu\text{M}$  OTA on the DLS/UiO-66/OBA-TSS/MCH/AuE (a) and MOBA-TSS/MCH/AuE (b) in 0.01 M PBS (pH 6.86)

Fig. 3-2.4 Effect of the concentration (A) and the bonding time of UiO-66 (B), the concentration (C) and the incubation time (D) of DLS on the SWV response of the modified AuE in the 0.01 M PBS (pH 6.86).

Fig. 3-2.5 (A) SWV responses of DLS/UiO-66/OBA-TSS/MCH/AuE in the 0.01 M PBS (pH 6.86) incubated with 0 M (a), 0.1 fM (b), 1.0 fM (c), 10.0 fM (d), 0.1 pM (e), 1.0 pM (f), 10 pM (g), 0.1 nM (h), 1.0 nM (i), 10.0 nM (j), 0.1  $\mu$ M (k), 1.0  $\mu$ M (l) and 2.0  $\mu$ M (m) of OTA. (B) Linear relationship of the different peak currents ( $\Delta I_p$ ) versus the logarithm of OTA concentration ( $\lg C_{OTA}$ ).

Fig. 3-2.6 (A) Graphic shows the SWV responses of the cycles of the aptasensor before (violet curves) and after toward 2.0  $\mu$ M OTA (black curves) and the reassembly results. (B) Peak currents ( $I_p$ ) of the aptasensor for OTA binding and regeneration cycles.

Fig. 3-2.7 (A) Specificity evaluation of the aptasensor by testing in a blank solution, 100 nM OTB, AFB1, ZEN, 10 nM OTA, and the mixture samples containing 10 nM OTA and OTB, AFB1, and ZEN at concentrations of 100 nM in the 0.01 M PBS (pH=6.86). (B) SWV responses of the aptasensor before (a) and after incubated with various concentrations 10 pM (b), 100 pM (c), 1 nM (d), 10 nM (e), and 100 nM (f) OTA in the red wine samples.

## List of Tables

### Chapter 2

Table 2-1.1 Comparisons of Analytical Performance of  $\text{NO}_2^-$  on Electrode Modified with Different Materials<sup>a</sup>

Table 2-1.2 Recovery data for  $\text{NO}_2^-$  determination in real samples on  $\text{Co}_3\text{O}_4/\text{C-CS}/\text{GCE}$

Table 2-2.1 Comparison of the proposed sensors for the determination of Pb(II) and Cd(II).

Table 2-2.2 Determination of Pb(II) and Cd(II) in different water samples (n = 3).

Table 2-3.1 Values of the equivalent circuit elements obtained by fitting the experimental results for the different modified electrodes

Table 2-3.2 Analytical performance of DNA biosensors designed with different inorganic material or organic polymer composites as probe immobilization matrix

### Chapter 3

Table 3-1.1 Values of the equivalent circuit elements were obtained by fitting the experimental results for the different modified electrodes.

Table 3-1.2 Comparison of the proposed aptasensor with other TBA-based electrochemical thrombin aptasensors

Table 3-1.3 Determination of thrombin in serum samples using the developed aptasensor<sup>a</sup>

Table 3-2.1 Values of the equivalent circuit elements obtained by fitting the experimental results for the different modified electrodes

Table 3-2.2 Comparison of the proposed aptasensor with other OBA-based

electrochemical OTA aptasensors

Table 3-2.3 Determination of OTA in red wine samples using the developed aptasensor <sup>a</sup>

## List of Schemes

### Chapter 2

Scheme 2-1.1 Schematic synthesis of  $\text{Co}_3\text{O}_4/\text{C}$  and its application as a nonenzymatic electrocatalyst for nitrite

Scheme 2-2.1 Schematic diagram for synthesis of  $\text{ZrO}_2/\text{C}$  and the adsorption-release model illustrating the electrochemical stripping behaviors

Scheme 2-3.1 Schematic illustration for preparation procedure of DNA biosensor and its application for monitoring transgenic soybean sample.

### Chapter 3

Scheme 3-1.1 Schematic illustration of the fabrication and application of the  $\text{Cu}_2(\text{CHDC})_2$  based electrochemical thrombin biosensor

Scheme 3-2.1 Schematic illustration of the fabrication of the sensitive OTA aptasensor and the sensing application of the reusable aptasensor

## List of Publications

- (1) Synthesis of porous nanododecahedron  $\text{Co}_3\text{O}_4/\text{C}$  and its application for nonenzymatic electrochemical detection of nitrite  
W. Qiu, H. Tanaka, F. Gao, Q. Wang  
*Advanced Powder Technology*, **30**, 2083-2093 (2019).
- (2) Yolk–Shell-Structured  $\text{SnO}_2\text{-C}$  and Poly-Tyrosine Composite Films as an Impedimetric “Signal-Off” Sensing Platform for Transgenic Soybean Screening  
W. Qiu, F. Gao, F. Gao, Z. Lin, Q. Wang  
*The Journal of Physical Chemistry, C*, **123**, 18685-18692 (2019).
- (3) Flexible flower-like MOF of  $\text{Cu}_2(\text{trans-1,4-cyclohexanedicarboxylic acid})_2$  as the electroactive matrix material for label-free and highly sensitive sensing of thrombin  
W. Qiu, Q. Wang, N. Yano, Y. Kataoka, M. Handa, F. Gao, H. Tanaka  
*Electrochimica Acta*, **353**, 136611 (2020).